Experimental and Modeling Study of Zinc-Cerium Redox Flow Batteries

by

Kiana Amini

A thesis
presented to the University of Waterloo
in fulfillment of the
thesis requirement for the degree of
Doctor of Philosophy
in
Chemical Engineering (Nanotechnology)

Waterloo, Ontario, Canada, 2021

Examining Committee Membership

The following served on the Examining Committee for this thesis. The decision of the Examining Committee is by majority vote.

External Examiner:	Dr. Adam Weber Energy Conversion Group, Lawrence Berkeley National Laboratory
Supervisor:	Prof. Mark Pritzker Dept. of Chemical Engineering, University of Waterloo
Internal Member:	Prof. Michael Pope Dept. of Chemical Engineering, University of Waterloo
Internal Member:	Prof. Jeff Gostick Dept. of Chemical Engineering, University of Waterloo
Internal-External Member:	Prof. Rodney Smith Dept. of Chemistry, University of Waterloo

Author's Declaration

I hereby declare that I am the sole author of this thesis. This is a true copy of the thesis, including any required final revisions, as accepted by my examiners.

I understand that my thesis may be made electronically available to the public.

Statement of Contribution

The body of this thesis is based upon a combination of published and unpublished studies.

1. **Kiana Amini**, Jeff Gostick, and Mark D. Pritzker. "Metal and metal oxide electrocatalysts for redox flow batteries." Advanced Functional Materials 30.23 (2020): 1910564.

   Parts of Chapter 1 and Chapter 2 are from the above review paper. I am the first author of the paper and was responsible for the investigation, analysis and writing of all drafts. Professor Gostick and Professor Pritzker reviewed and edited the manuscript.

2. **Kiana Amini**, and Mark D. Pritzker. "*In situ* polarization study of zinc–cerium redox flow batteries." Journal of Power Sources 471 (2020): 228463.

   Chapter 3 consists of the above paper. I am the first author of the paper and was responsible for investigation, methodology, data curation and writing of all drafts. Professor Pritzker was responsible for supervision, validation and editing the manuscript.

3. **Kiana Amini**, and Mark D. Pritzker. "Life-cycle analysis of zinc-cerium redox flow batteries." Electrochimica Acta 356 (2020): 136785.

   Chapter 4 consists of the above paper. I am the first author of the paper and was responsible for investigation, methodology, data curation and writing of all drafts. Professor Pritzker was responsible for supervision, validation and editing the manuscript.

4. **Kiana Amini**, and Mark D. Pritzker. "Electrodeposition and electrodissolution of zinc in mixed methanesulfonate-based electrolytes." Electrochimica Acta 268 (2018): 448-461.

   Chapter 5 consists of the above paper. I am the first author of the paper and was responsible for investigation, methodology, data curation and writing of all drafts. Professor Pritzker was responsible for supervision, validation and editing the manuscript.

5. **Kiana Amini**, and Mark D. Pritzker. "Improvement of zinc-cerium redox flow batteries using mixed methanesulfonate-chloride negative electrolyte." Applied Energy 255 (2019): 113894.

   Chapter 6 consists of the above paper. I am the first author of the paper and was responsible for investigation, methodology, data curation and writing of all drafts. Professor Pritzker was responsible for supervision, validation and editing the manuscript.

6. **Kiana Amini**, and Mark D. Pritzker. "Two-dimensional transient model for a zinc-cerium redox flow battery validated by extensive experimental data." Submitted.

   Chapter 7 consists of the above paper. I am the first author of the paper and was responsible for investigation, methodology, data curation and writing of all drafts. Professor Pritzker was responsible for supervision, validation and editing the manuscript.

Abstract

Redox flow batteries (RFBs) are one of the most promising energy storage technologies that are expected to have an increasing market size in the near future due to their scalability, safety, long-life and system flexibility. The development of RFBs will facilitate the utilization of clean renewable sources of energy, such as sun and wind power, by resolving their intermittency problem. RFBs are also capable of enhancing the stability of the electrical grid by storing the excess electrical power and releasing it during peak hours of electricity demand. Among different types of RFBs, those based on zinc and cerium metals are attractive since they offer a large open-circuit cell voltage and thus have the potential to provide high output energy density. Motivated by these advantages, the present work is focused on the improvement of zinc-cerium RFBs through both experimental and modeling studies.

In this work, *in situ* polarization and electrochemical impedance spectroscopy measurements were combined to accurately identify the sources of voltage loss in each half-cells of the zinc-cerium RFBs during battery operation. This analysis revealed that the kinetic losses at the zinc negative half-cell are responsible for most of the voltage drop at low and intermediate current densities, while limitations to the mass transfer of Ce(IV)/Ce(III) on the positive side are the main reasons for the sharp potential drop at high current densities. At 50% state of the charge, the exchange current density for zinc oxidation was estimated to be $\approx 7.4\ \mathrm{mA\,cm^{-2}}$, while the corresponding value for cerium reduction was found to be $\approx 24.2\ \mathrm{mA\,cm^{-2}}$, confirming that the slower kinetics of the negative half-cell limited the battery performance at low and mid-range current densities. Next, extensive life-cycle analyses were performed to pinpoint the exact cause of the battery capacity fade over multi-cycle experiments. Combination of *in situ* monitoring of the half-cell electrode potentials and colorimetric titration revealed that the combination of hydrogen evolution side reaction (HER) in the negative half-cell, crossover of protons, and accumulation of Ce(IV) in the positive electrolyte results in the eventual capacity fade of the system.

The research contributions outlined above underpin the rest of the work, where a novel electrolyte is designed to increase the kinetic rate of the Zn/Zn(II) redox reaction and enhance the charge and voltage efficiency of the zinc redox reaction and consequently the full-cell battery at low and intermediate current densities. Extensive half-cell potentiometric and galvanostatic electrochemical techniques revealed that the amount of zinc deposited, charge, voltage and energy efficiencies of Zn/Zn(II) always remain significantly higher in an alternative mixed methanesulfonate-chloride negative electrolyte compared to the conventional methanesulfonic acid (MSA) solutions. Given these promising half-cell studies, the electrolyte was further tested in a bench-scale zinc-cerium RFB and the results

showed that a zinc-cerium RFB with this new electrolyte has a significantly longer life and notably higher charge and voltage efficiencies compared to conventional zinc-cerium RFBs. Whereas the battery containing pure MSA negative electrolyte was able to operate for $\approx$ 42 h with 97 cycles at a current density of 25 $\mathrm{mA\,cm^{-2}}$, it was able to operate for more than 75 h with 166 cycles when mixed MSA-chloride was used on the negative side.

Lastly, to simulate the operation of zinc-cerium RFBs, a two-dimensional transient model accounting for three modes of transport (migration, diffusion and convection) coupled with electrode kinetics was developed. The developed model was validated against the above-described extensive set of experimental data. This included full-cell voltages, positive and negative electrode potentials monitored via reference electrodes inserted into the battery set-up and Ce(IV) concentrations in the positive electrolyte measured by colorimetric titration over multi-cycle experiments. This was the most comprehensive comparison carried out between the output of an RFB model and experimental data extracted during operation of a redox flow battery. The validated model was then used to predict the cell voltages and limiting redox reactions during battery operation for different model parameters to provide a direction toward improving the performance of zinc-cerium RFBs.

Acknowledgements

First and foremost, I would like to express my sincere gratitude to my supervisor, Professor Mark Pritzker, for his continuous support, encouragement, positiveness and patience throughout the course of my PhD studies. I thank you for always willing to assist in any way possible throughout this project and to generously share your time and immense knowledge with me. I truly could not have imagined having a better advisor and mentor for my PhD studies.

I would also like to thank Professor Jeff Gostick, for his helpful comments, valuable advice and continuous support. Thank you very much for giving me the opportunity to collaborate with you. I hope that I can pay it forward by supporting other students in the future. I would like to further thank him and other members of my PhD examination committee, Professor Michael Pope, Professor Rodney Smith and Dr. Adam Weber for their time in reviewing my thesis and for their valuable feedback.

I also thank my colleagues, lab-mates and office-mates for their academic and emotional support and for all the fun moments we had together during this time. I am also grateful for the support of all the staff at Chemical Engineering Department, particularly the support from Judy Caron. Thank you for being approachable and welcoming.

I am grateful for the love and support of my amazing family and friends. My special thanks goes to my parents, Keykavoos Amini and Fereshteh Aghahosseini, for always believing in me and for continuously encouraging me to go after my dreams. I am grateful for everything you have done for me. Without your support, I would not have come this far. I further thank my kind brother, Kiasam Amini, for always cheering me on.

Last but not least, I like to thank my fiancée, Dr. Bijan Sakhdari, for his love, patience, support and encouragement. Thanks for always being there for me through thick and thin.

Dedication

This thesis is dedicated to Bijan, for his love, his encouragement and his constant support.

Table of Contents

List of Figures

List of Tables

Nomenclature

Parameters

α	Transfer coefficient for main reactions
β'	Transfer coefficient for side reactions
β_a	Anodic Tafel Constant ($\mathrm{V\,decade^{-1}}$)
β_c	Cathodic Tafel Constant ($\mathrm{V\,decade^{-1}}$)
ϵ	Electrode porosity
η	Overpotential (V)
μ	Dynamic viscosity ($\mathrm{kg\,m^{-1}\,s^{-1}}$)
ν	Stochiometric coefficient
ϕ_e	Ionic potential (V)
ϕ_s	Electronic potential (V)
ρ	Fluid density ($\mathrm{kg\,m^{-3}}$)
σ_s	Conductivity of the Solid Material ($\mathrm{S\,m^{-1}}$)
σ_s^{eff}	Effective conductivity of the Solid Material ($\mathrm{S\,m^{-1}}$)
σ_m	Membrane conductivity ($\mathrm{S\,m^{-1}}$)
$\vec{P}$	Pressure vector (Pa)
$\vec{v}$	Velocity ($\mathrm{m\,s^{-1}}$)

a	Specific surface area (m^{-1})
c	Concentration ($\mathrm{mol\,m}^{-3}$)
D	Diffusion coefficient ($\mathrm{m}^2\,\mathrm{s}^{-1}$)
D_{eff}	Effective diffusion coefficient ($\mathrm{m}^2\,\mathrm{s}^{-1}$)
E_{co}	Crossover potential (V)
E_{nu}	Nucleation potential (V)
F	Faraday's constant ($\mathrm{C\,mol}^{-1}$)
H	Electrode height (m)
I	Current (A)
i	Current density ($\mathrm{A\,m}^{-2}$)
i_0	Exchange current density ($\mathrm{A\,m}^{-2}$)
i_{app}	Applied current density ($\mathrm{A\,m}^{-2}$)
k_m	Mass transfer coefficient ($\mathrm{m\,s}^{-1}$)
k_{kc}	Intrinsic permeability of the porous media (m^2)
L_f	Flow channel thickness (m)
L_m	Membrane thickness (m)
L_w	Electrode width (m)
N	Flux ($\mathrm{mol\,m}^{-3}\,\mathrm{s}^{-1}$)
Q	Flow rate ($\mathrm{L\,s}^{-1}$)
R	Gas constant ($\mathrm{J\,mol}^{-1}\,\mathrm{K}^{-1}$)
S	Source term ($\mathrm{mol\,m}^{-3}\,\mathrm{s}^{-1}$)
T	Temperature (K)
t	Time (s)

V_e Tank volume (m^3)

z Charge number

I_{ac} Anodic peak current density ($mA\,cm^{-2}$)

Q_{an} Anodic charge ($mA\,s$)

Subscripts

a Property related to the anodic half-cell

b Bulk property

c Property related to the cathodic half-cell

$Ce(III)$ Property related to Ce(III)

$Ce(IV)$ Property related to Ce(IV)

ct Charge transfer

e Electrolyte property

f Property related to the fixed sulfonate ions in Nafion

H_2 Property related to HER

in Property related to the inlet

j Ions in the positive electrolyte

k Ions in the negative electrolyte

m Membrane property

neg Property related to the negative half-cell

O_2 Property related to OER

out Property related to the outlet

pos Property related to the positive half-cell

r Redox reaction

ref	Reference value
s	Surface property
Zn	Property related to Zn
$Zn(II)$	Property related to Zn(II)

Chapter 1

Introduction and Research Objectives

1.1 Introduction

According to the U.S. National Oceanic and Atmospheric Administration (NOAA), the hottest July on Earth in recorded history occurred in 2019 [1]. The need to decarbonize the world economy has become so clear that the general public in many countries has named global climate change as a major threat to their nation, as reflected in a recent survey conducted by the Pew Research Center [2]. From an engineering standpoint, it is apparent that any renewable energy system will require large-scale energy storage. A reliable storage unit should be able to store the energy obtained from intermittent renewable sources such as solar and wind power and discharge it as required. The development of efficient energy storage systems will also enhance the performance and robustness of the electrical grid by storing the excess electrical power when energy demand is low and releasing it during on-peak periods (i.e., load balancing) [3]. A cost-effective energy storage device can also be used for peak shaving at industrial and commercial sites to significantly reduce utility costs [3]. It can also serve as an uninterruptible power supply (UPS) to provide electrical power to a load when the main power source fails [3].

Current viable and cost-effective devices for grid-scale energy storage applications are pumped-hydro and compressed-air [4]. These systems have a long life and require low maintenance. However, they are restricted to locations with very large elevation differences [4]. On the other hand, electrochemical energy storage devices such as batteries are scalable and adaptable in terms of location of installation. Hence, a tremendous amount of research

is currently focused on the development of cheap, safe and efficient electrochemical energy storage systems.

One of the most promising technologies for electrochemical energy storage devices are redox flow batteries (RFBs) [5]. In contrast to conventional batteries in which the electroactive species are stored inside the cell and constitute the electrode, the electrochemically active species for each electrode in an RFB are dissolved in electrolytes and stored in separate external tanks. The electrolytes are then pumped through the cell containing the electrodes, on which the redox reactions occur [5]. The negative and positive half-cells usually are separated into different compartments by an ion-exchange membrane to prevent cross-over of the electroactive species. Figure 1.1 shows a schematic of a typical redox flow battery.

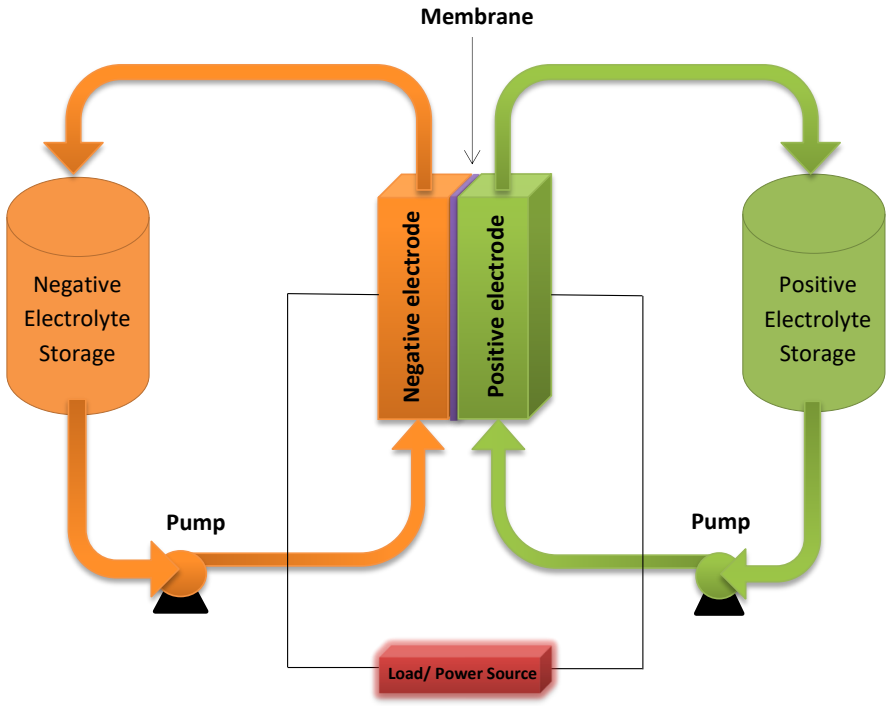

Figure 1.1: Schematic of a redox flow battery.

Since the active materials in RFBs are stored in electrolytes and not internally in the electrodes, the cell energy and power can be scaled up independently [4]. The power

of RFBs is controlled by the size of the electrodes in the cell, while the energy density of the battery is determined by the size of the external storage tanks and electrolyte volume [4]. Additionally, storage of the electroactive species in the electrolyte rather than the electrodes usually enables RFBs to operate for a longer life with less maintenance than conventional static batteries since the electrode is not undergoing any chemical or physical change during operation. To date, several redox reactions involving different chemistries have been combined and tested to achieve stable, high efficiency and long-life RFBs [6,7]. Among these chemistries, RFBs based on V(II)/V(III) negative and V(IV)/V(V) positive redox reactions have been the most extensively explored and commercially developed due to the advantage of having the same species (vanadium) on both half-cells of the battery [8,9]. Nevertheless, all-vanadium RFBs exhibit a comparably low open-circuit voltage (OCV) ($\sim$ 1.26 V) [10].

Another type of redox flow battery is one in which an active material is deposited on one of the electrodes during cell operation [11]. A flow battery with such design is categorized as a hybrid redox flow battery. The power and energy are not completely independent in hybrid RFBs, thereby removing one of the important advantages of an all-liquid redox flow battery. However, hybrid RFBs retain most of the other advantages. Hybrid RFBs have been developed with different chemistries each of which can provide an additional feature that does not exist in all-liquid RFBs.

Among hybrid RFBs, zinc-based flow batteries have gained a great deal of attention due to the availability and low price of zinc and the successful use of zinc electrodes in many other batteries. More importantly, the zinc redox couple provides a large negative potential (-0.76 V versus standard hydrogen electrode (SHE)) in aqueous media with a two-electron transfer reaction. When zinc is combined with cerium, which has a standard potential of 1.64 V versus SHE, the battery can generate an open-circuit potential of 2.4 V, which is one of the highest open-circuit voltages among the currently known aqueous RFBs [11]. In zinc/cerium RFBs, methanesulfonic acid (MSA) is used as the supporting electrolyte on both the negative and positive sides of the cell [12]. During charge, Zn(II) deposits from the solution onto the negative electrode. During discharge, this reaction is reversed and the zinc deposit dissolves back into the electrolyte to form Zn(II) and release 2 electrons [12]:

$$\mathrm{Zn(II)} + 2\,\mathrm{e}^- \underset{\text{discharge}}{\overset{\text{charge}}{\rightleftharpoons}} \mathrm{Zn} \qquad\qquad \mathrm{E} = -0.757\,\mathrm{V\,vs\cdot\,SHE}.$$

On the positive side, oxidation of Ce(III) to Ce(IV) occurs during charge and the reverse reaction during discharge:

$$\mathrm{Ce(III)} \underset{\text{discharge}}{\overset{\text{charge}}{\rightleftharpoons}} \mathrm{Ce(IV)} + \mathrm{e^-} \qquad \mathrm{E} = 1.643 \text{ V vs. SHE (in MSA solution).}$$

Thus, the overall reaction in a zinc-cerium RFB is:

$$\mathrm{Zn(II)} + 2\,\mathrm{Ce(III)} \underset{\text{discharge}}{\overset{\text{charge}}{\rightleftharpoons}} \mathrm{Zn} + 2\,\mathrm{Ce(IV)}. \qquad \mathrm{E} = 2.4 \text{ V}.$$

Despite its advantages, zinc-cerium RFBs face several challenges and unknown performance factors that must be addressed before they become a viable option on a commercial scale. In terms of the performance challenges, hydrogen evolution and oxygen evolution side reactions can occur on the negative and positive electrodes, respectively, due to the large negative and positive electrode potentials, which results in a lower charge efficiency and wasted energy. Reduction of the rates of these side reactions is therefore highly beneficial for improving the battery efficiency. Additionally, due to the highly oxidative environment in the positive compartment, expensive porous platinized titanium electrodes are required on that side since cheaper carbon-based electrodes are susceptible to deterioration in the highly acidic and oxidative environment. In terms of unknown performance factors, knowledge is lacking regarding the sources of voltage loss in the battery and the contribution of the negative and positive electrodes to the loss of voltage efficiency. Secondly, the reasons behind the capacity fade of the battery over multi-cycle experiments are not understood. Accurate identification of the sources of performance loss over multi-cycle experiments is crucial for optimizing battery performance and elucidating the pathways that enhance system efficiency. Finally, no multi-physics model for zinc-cerium RFBs has been developed to date. These models are required for optimal design and scale-up of redox flow batteries.

1.2 Research Objectives

The main objective of this work is to offer a detailed description of the sources of performance loss in zinc-cerium RFBs and further provide novel solutions to address the identified problems. To this end, the specific objectives of this experimental and computational study are as follows:

- Experimental studies
  - Investigate the sources of voltage loss in zinc-cerium RFBs and decouple the contribution of negative and positive redox reactions to the overall voltage loss in the battery.

  - Identify the cause of battery capacity fade and monitor the evolution in performance of the negative and positive redox reactions over the course of the battery life-cycle.
  - Investigate the use of mixed-acid electrolytes as a possible solution to enhance the kinetic of zinc redox reaction on the negative side of a zinc-cerium RFBs during charge.
  - Evaluate the mixed-acid electrolyte with optimum composition in a lab-scale zinc-cerium RFB and compare the performance in terms of charge, voltage and energy efficiency with conventional zinc-cerium RFBs.

- Computational modeling

  - Develop a transient multi-physics model including all three modes of transport (migration, diffusion and convection) coupled with a kinetic model to simulate the operation of zinc-cerium redox flow batteries.
  - Validate the model using the extensive experimental data obtained as part of the previous objectives.
  - Employ the validated model to predict the cell voltages and limiting redox reactions during battery operation for different model parameters to provide a guide to further improve the performance of zinc-cerium RFBs.

1.3 Outline

The content of this thesis is presented in 8 chapters as shown in Figure 1.2. The present chapter provided an introduction to redox flow batteries and discussed the objectives of this project. Chapter 2 provides a comprehensive literature review of redox flow batteries including the history of RFBs, different types of RFBs and recent developments in the field with particular attention to zinc-cerium RFBs. Chapter 3 presents an *in situ* investigation of the sources of voltage loss during discharge of a zinc-cerium redox flow battery and the contributions of each side to the overall voltage loss. Chapter 4 examines the role of the negative and positive redox reactions in the capacity fade of the battery over multi-cycle experiments. Chapter 5 describes a detailed half-cell study on the use of alternative mixed methanesulfonate-chloride and methanesulfonate-sulfate electrolytes to enhance the rate of zinc electrodeposition and/or decrease the rate of the hydrogen evolution side reaction. Chapter 6 presents the performance of a zinc-cerium RFB with mixed

methanesulfonate–chloride negative electrolyte compared to that of a conventional zinc-cerium RFB operating with pure methanesulfonic acid electrolyte. Chapter 7 presents a two-dimensional transient model for zinc-cerium RFBs that is validated using our extensive experimental data. Finally, the conclusions reached from this work and recommendations for future work are presented in Chapter 8.

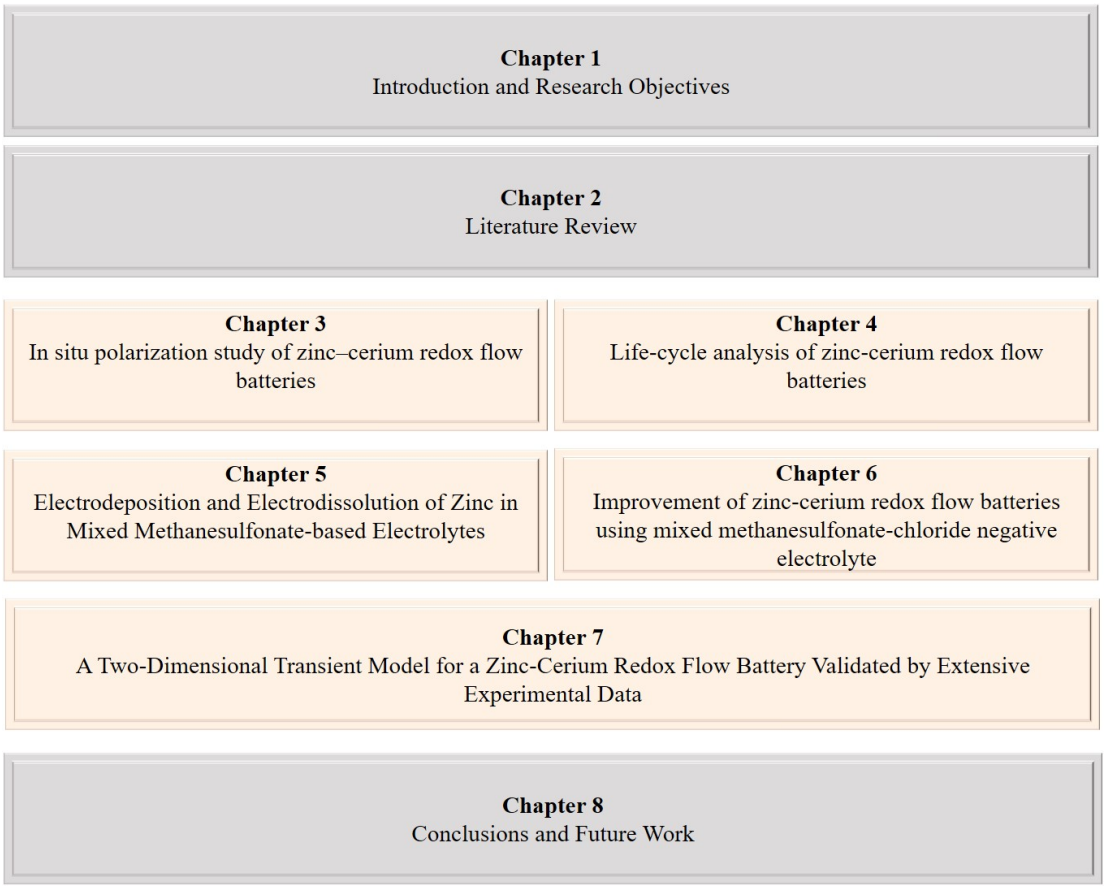

Figure 1.2: Structure of the thesis content.

Chapter 2

Literature Review

2.1 History of Redox Flow Batteries

Early development of full-scale redox flow batteries started in the 1970s [13]. Thaller invented the first iron-chromium RFB in 1974 at the US National Aeronautics and Space Administration (NASA) [13]. NASA conducted pioneering studies on different engineering aspects of RFBs, including analysis of pump losses [14], shunt currents [15], electrode materials [16] and battery cost [17]. This iron-chromium battery relied on an aqueous solution of Cr^{2+}/Cr^{3+} on the negative side and an aqueous solution of Fe^{2+}/Fe^{3+} on the positive side with hydrochloric acid as the supporting electrolyte. The resulting open-circuit voltage of this battery was 1.0 V [13]. Although the iron-chromium system could operate with low-cost carbon felt electrodes, it suffered from low reversibility of the Cr^{2+}/Cr^{3+} redox reaction, excessive hydrogen evolution and severe cross-contamination [18]. Consequently, research on iron-chromium systems was discontinued by NASA in 1984 [19]. Nevertheless, the Electrotechnical Laboratory (ETL) in Japan continued to work on iron/chromium batteries and was able to improve its performance by modifying the felt electrodes to reduce hydrogen evolution and by operating with a single electrolyte, a cheaper membrane and a re-balancing system to adjust the state-of-charge (SOC) in long-term operation of the battery [20]. A 60 k W iron-chromium RFB was developed by Kansai Electric Power Co., Inc. (KEPCO) and Sumitomo Electric Industries, Ltd. (Sumitomo Electric) in 1989 [21, 22].

The concept of using vanadium as the active species in redox flow batteries appeared for the first time in a patent by A. Pelligri and P.M. Spaziante in 1978 [23]. However, the first vanadium redox flow battery (VRFB) was developed and demonstrated by Rychcik and Skyllas-Kazacos at the University of New South Wales in 1988 [24]. These VRFBs made

use of four different oxidation states of vanadium in aqueous solutions: V(II)/V(III) on the negative side and V(IV)/V(V) on the positive side resulting in a standard open-circuit voltage of 1.26 V.

Vanadium RFBs have several advantages over iron-chromium RFBs [18]. Firstly, the cell potential of VRFBs is higher than that of iron-chromium RFBs resulting in a significantly higher energy output. VRFBs do not have the severe cross-contamination problem of iron-chromium RFBs since vanadium species are used in both half-cells. In the event of cross-contamination in all-vanadium RFBs, the solution can be regenerated simply by recharging the electrolytes. On the other hand, in systems with different metals such as iron-chromium RFBs, the mixed liquids must be entirely replaced or removed for external treatment. Moreover, much less hydrogen evolution was found to occur at the negative electrode in VRFBs due to the higher potential of the V(II)/V(III) redox reaction compared to that of the Cr^{2+}/Cr^{3+} reaction. With this success, most RFB researchers shifted their attention to the all-vanadium system [18].

In 1989, a method was developed by Kashima Kita Electric Power Corp. and ETL to recover vanadium from petroleum and heavy fuels [25]. With this technology, several Japanese companies were able to manufacture larger-scale VRFBs such as 450 kW/900 k W h system in 1996 [26] and a 100 kW/800 k W h system in 2000 [18]. Since that time, VRFBs have been introduced onto the market by several global companies [27–34]. In recent years, a 60 MW h demonstration project was completed by Sumitomo in Japan, followed by an on-going project on the largest RFB facility of 800 M W h by Rongke Power in China [35].

Although VRFBs have been successfully commercialized and undergone significant improvements, their energy density is still limited due to the low vanadium solubility in the utilized electrolyte [4]. Thus, a large amount of electrolyte is required to achieve high output energies. Moreover, vanadium is costly so that the electrolyte constitutes the major part of the battery capital costs [4]. Consequently, this has severely limited the viability of VRFBs to meet the cost requirements of a grid-scale energy storage system and so has also hindered its penetration into the broader market. A significant amount of research has thus been focused on improving the performance of all-vanadium RFBs or developing redox flow batteries based on other chemistries and with different designs to improve the energy density and lower the production costs. Before introducing these various types, we briefly describe the key components of RFBs in the next section to provide the necessary background for understanding the different types of RFBs.

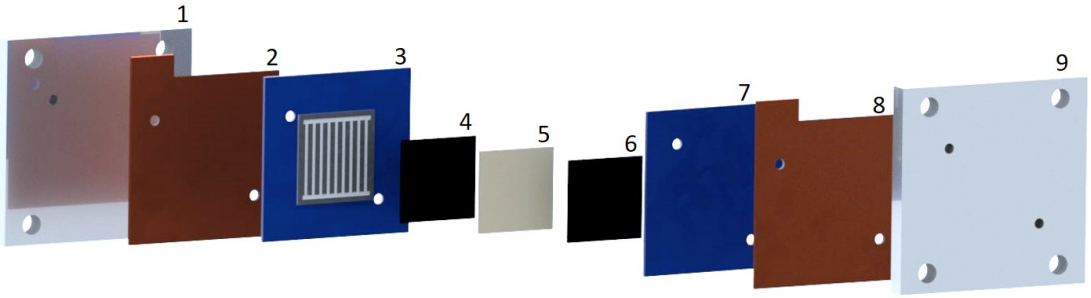

Figure 2.1: Components of redox flow batteries. End plates (1, 9), current collectors (2, 8), flow fields (3, 7), electrodes (4, 6), and membrane (5).

2.2 Components of Redox Flow Batteries

Figure 2.1 shows a schematic of the components typically used in a single cell of a redox flow battery. As shown, a single cell of an RFB typically consists of end-plates, flow fields, current collectors, positive and negative electrodes separated by a membrane. Two electrolytes containing electroactive species flow through each compartment of the battery between the corresponding electrode and the membrane. The choice of these materials, particularly the electrode, membrane and electrolyte significantly affect the overall performance of the battery. The positive and negative electrodes provide the active sites for the redox reactions occurring in the battery and can affect the kinetics and reversibility of the employed redox couples. Additionally, the structure of the electrode can affect the mass transfer and activation overpotentials which directly influence the voltage efficiency of the battery [9]. Flow fields can be employed in conjunction with electrodes to promote the mass transfer rates in the system. The membrane must be selective, durable, conductive and low-cost. While the membrane separates the two half-cells of the battery and must prevent the mixture of the electrolytes, it should be permeable to the charge-carrier species. The background electrolyte must provide high solubility for the employed electroactive species and must not promote any chemical or electrochemical reactions other than the reaction of interest. Additionally, the acidity, viscosity and conductivity of the electrolyte affect the choice of the materials and the design of the battery. The employed electroactive species must undergo a kinetically fast and reversible redox reaction and ideally no side reactions. Additionally, the species should be readily available and inexpensive. In the next section

various types of redox flow batteries categorized based on the choice of their components are presented.

2.3 Different Types of Redox Flow Batteries

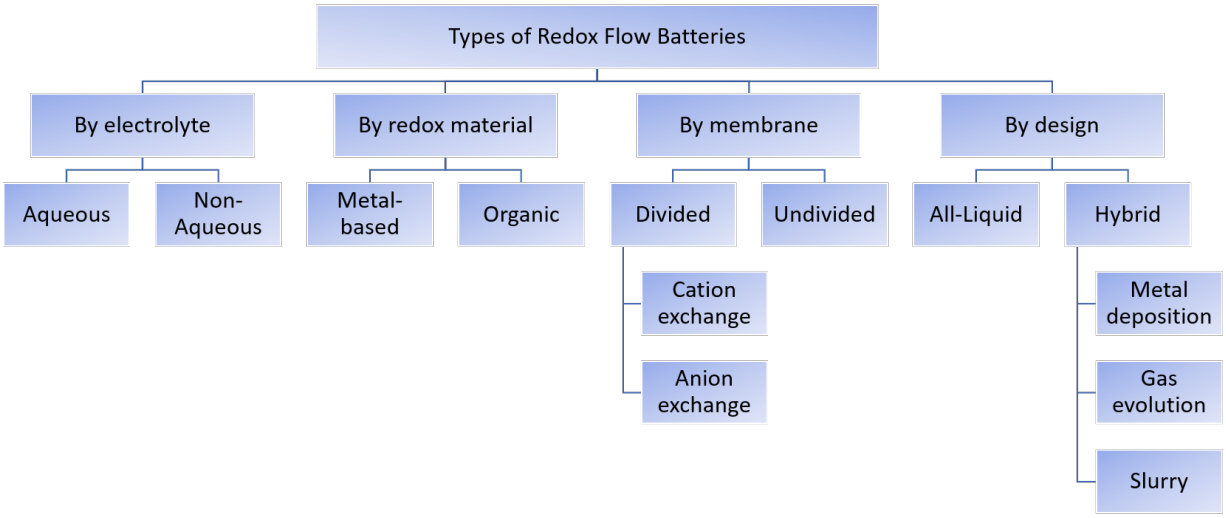

Figure 2.2: Different types of redox flow batteries.

RFBs can be categorized in many ways based on different criteria (Figure 2.2). As mentioned before, conventional systems such as iron-chromium and all-vanadium RFBs, store the active material entirely in the electrolyte. In other words, the electroactive species is in a dissolved form in both its oxidized and reduced states. Hence, such batteries are categorized as all-liquid aqueous redox flow batteries. These systems are desirable since the energy and power densities achievable are completely decoupled. The energy density is dictated by the tank size and the electrolyte volume while the power density only depends on the size of the stack of cells each of which contains bipolar plates, membranes and flow channels/frames connected in series. Table 2.1 summarizes some of the proposed all-liquid

Table 2.1

All-Liquid Aqueous Redox Flow Batteries			
Redox species	Cell Voltage (V)	Challenges	Reference
Cr^{3+}/Cr^{2+}–Fe^{3+}/Fe^{2+}	1.2	• Requires re-balancing system to compensate for H_2 evolution side reaction • Cross-contamination • Low reversibility of Cr^{2+}/Cr^{3+} reaction	[18]
Cr^{3+}/Cr^{2+}–Br^{2+}/Br	1.44	• Corroding environment of HBr • Requires the use of complexing agent to capture Br_2 which results in a two-phase electrolyte.	[36]
Cr^{3+}/Cr^{2+}–CrO_4^{2-}/Cr^{3+}	1.77	• High overpotential for Cr^{3+} reduction • O_2 evolution side reaction • Chromate and dichromate ions are extremely poisonous and carcinogenic	[37]
V^{3+}/V^{2+}–VO_2^+/VO^{2+}	1.4	• High cost of vanadium • Low energy density	[24]
V^{3+}/V^{2+}–$ClBr^{2-}/Br^-$	1.3	• Requires the use of complexing agent to capture Br_2 which results in a two-phase electrolyte	[38]
V^{3+}/V^{2+}–Ce^{4+}/Ce^{3+}	1.87	• Requires expensive platinized-titanium positive electrodes	[39]
V^{3+}/V^{2+}–Mn^{2+}/Mn^{3+}	1.66	• Occurrence of Mn(III) disproportionation reaction	[40]
V^{3+}/V^{2+}–Fe^{3+}/Fe^{2+}	1.02	• Low energy density	[41]
TiO^{2+}/Ti^{3+}–Fe^{3+}/Fe^{2+}	0.72	• Low energy density • Voltage drop through operation	[42]
TiO^{2+}/Ti^{3+}–$ClBr^{2-}/Br^-$	1.1	• Corroding environment of HBr • Requires the use of complexing agent to capture Br_2 which results in a two-phase electrolyte.	[43]
I_2/I^-–IO_3^-/I_2	0.66	• Dissolution of I_2 • Extensive blockage of the cell	[43]
S/S_2^{2-}–Br_2/Br^-	1.5	• Formation of H_2S and Br_2 • Precipitation of sulfur species	[44]
Np^{4+}/Np^{3+}–NpO_2^{2+}/NpO_2^+	1.29	• Hazardous electroactive electrolyte • Requires radiation shielded environment	[45]

aqueous RFBs along with their cell voltage and principal operating challenges still to be resolved.

In hybrid redox flow batteries, the electrochemical reaction of one of the half-cells involves either deposition of a metal on the electrode (e.g., Zn, Fe), evolution of a gas (e.g., H_2, O_2) or the electrochemical reactions on both sides occur on electrically conductive solid particles suspended in an aqueous electrolyte (semi-flow) (Figure 2.3). Flow batteries involving metal deposition can be divided into two groups: zinc-based and single metal. As evident by its name, a zinc-based hybrid RFB employs the Zn/Zn(II) redox reaction as the negative half-cell. A variety of other active materials can be used for the positive half-cell. Table 2.2 summarizes some of the important zinc-based hybrid RFBs. Single metal hybrid RFBs, on the other hand, utilize the same type of metal in both the negative and positive half-cells. All-iron and all-copper hybrid RFBs are examples of this type and are included in Table 2.2. The overall design of hybrid RFBs with a metal negative electrode is similar to that of all-liquid RFBs with the exception that it must accommodate the deposition process. However, since the electroactive metal is plated on the negative electrode during charge in hybrid RFBs, the power and energy densities are not completely independent of each other. Thus, the energy density of such systems depends on the surface area of the electrode in addition to the tank size and electrolyte volume [11].

Hydrogen redox flow batteries have been developed by replacing O_2 reduction that occurs in conventional hydrogen-oxygen fuel cells with a liquid solution containing an electroactive species. H_2 is provided to the system as a compressed gas [46, 47]. Similar to hydrogen-oxygen fuel cells, this system requires a platinum catalyst to enhance the kinetics of the hydrogen redox reaction. Hydrogen-halogen [48], hydrogen-vanadium [49], hydrogen-iron [50] and hydrogen-cerium [51] RFBs are examples of this type.

Redox flow batteries with an oxygen positive electrode have been developed by replacing the hydrogen redox reaction in conventional fuel cells with a liquid solution containing an electroactive species. This type has been proposed with the goal of decreasing the weight of redox flow batteries. Vanadium-air RFBs are the only systems in this category that have been investigated to date [52]. Unfortunately, these initial experiments showed that the charge and voltage efficiencies of such cells were low due to cross-contamination of vanadium and its corrosive effect on the positive electrode. This problem led to the proposal of another system in which oxygen reduction was only utilized during the discharge process to oxidize V(II) to V(III) while reduction of V(III) was done in a separate system during charge by oxidation of an organic compound [53]. However, this design is complex and more expensive than that of conventional hybrid RFBs.

As mentioned previously, another group of hybrid RFBs involves the use of slurries.

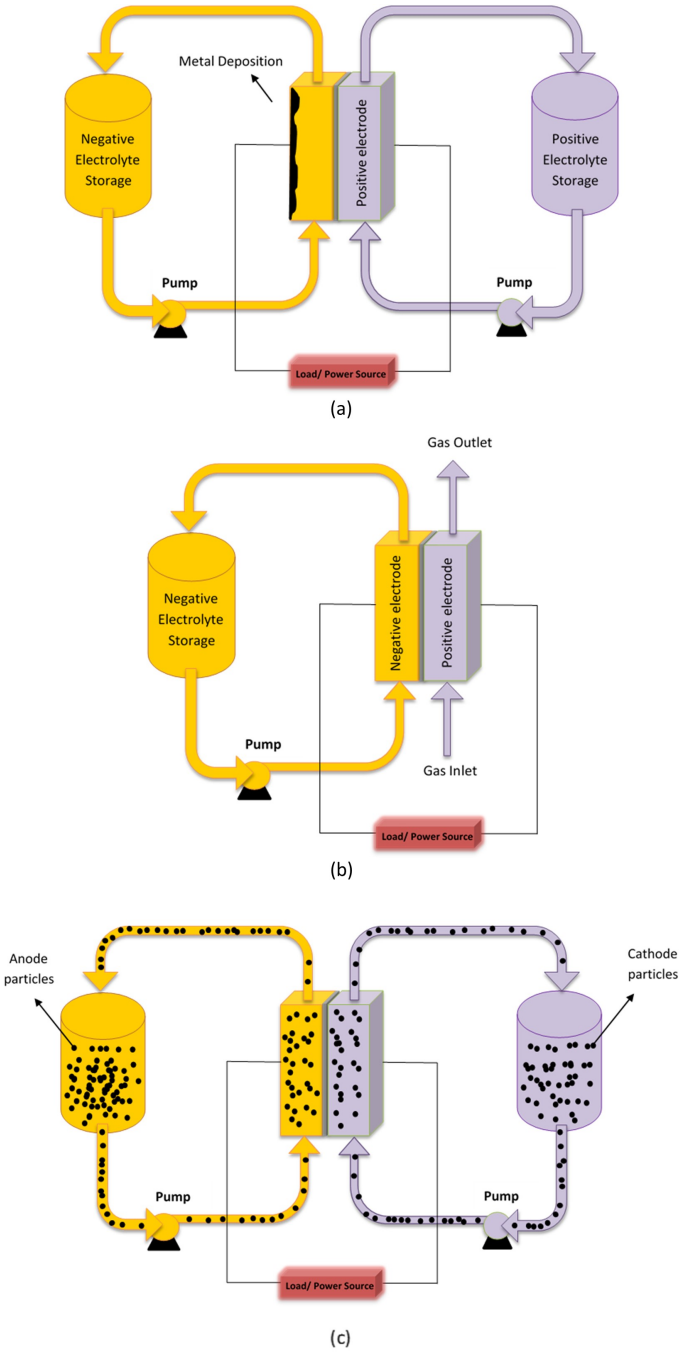

Figure 2.3: Schematic of different hybrid RFBs involving (a) metal deposition, (b) gas redox reaction and (c) slurry electrodes.

Table 2.2

Flow Batteries with Metal Deposition			
Redox species	Cell Voltage (V)	Challenges	Reference
Zinc-Based Flow Batteries			
$Zn^{2+}/Zn–Br_2/Br$	1.82	• Corroding environment of HBr • Requires the use of complexing agent to capture Br_2 which results in a two-phase electrolyte.	[54]
$Zn^{2+}/Zn–Cl_2/Cl$	1.80	• Corroding environment of HCl • Due to high cathode potential, titanium-based electrodes are required • Slow Cl_2–Cl kinetics at titanium-based electrodes	[55]
$Zn^{2+}/Zn–ClBr_2/Br$	1.80	• Similar to zinc chloride RFBs.	[56]
$Zn^{2+}/Zn–VO_2/VO_2^+$	1.76	• Capacity fade due to hydrogen evolution • Cross-contamination	[57]
$Zn^{2+}/Zn–Ce^{4+}/Ce^{3+}$	2.04 - 2.48	• Requires expensive platinized-titanium positive electrodes • O_2 evolution side reaction • H_2 evolution side reaction	[58]
$Zn^{2+}/Zn–I^-/I_3^-$	1.3	• Precipitation of I_2 • Dendrite formation	[59]
Single Metal Flow Batteries			
$Fe^{2+}/Fe–Fe^{3+}/Fe^{2+}$	1.2	• Slow deposition/dissolution reaction • H_2 evolution side reaction	[60]
$CuCl/Cu–Cu^{2+}/CuCl$	0.368	• Low energy density • Dendrite formation	[61]

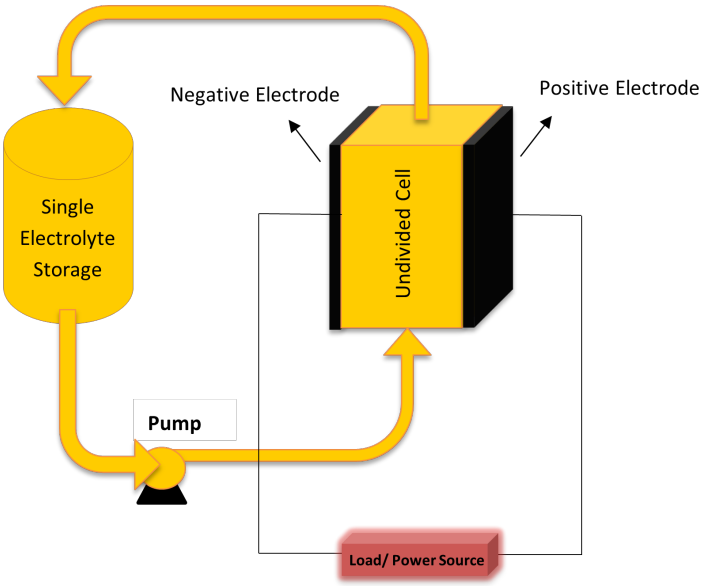

Figure 2.4: Schematic of an undivided membrane-less redox flow battery.

These systems have been proposed with the goal of combining the advantages of conventional RFBs with metal anode hybrid RFBs. Slurries are made by suspending electrically conductive solid particles in an aqueous electrolyte. This yields an electrolyte with a continuous and dynamic percolation network that is capable of electronic conduction. In the case of hybrid RFBs with negative metal electrodes, these conductive particles act as the negative electrode on which metal is deposited during charge. Since the deposited metal circulates with the conductive particles, the energy and power densities are decoupled so that this important advantage of RFBs is retained. In addition, this design simplifies the maintenance process since the cell does not have to be disassembled if an electrode has to be replaced during operation. Most of the previous studies on slurry electrodes have been done for lithium batteries [62, 63]. However, a similar concept has been used to design flowable electrodes for all-iron RFBs [64]. A suspension of Ag-doped polyaniline has also been used in zinc/PANI batteries, which are adaptable to zinc-based hybrid RFBs [65]. A significant challenge with these systems is the rheological limitations due to the higher viscosity of the flowing electrolyte which leads to large pumping losses.

Redox flow batteries are generally designed with an ion-exchange membrane to reduce the cross-contamination between the two half-cells. The employed membranes could be a cation-exchange or anion-exchange membrane. Cation-exchange membranes contain fixed negatively charged ions and hence possess selective permeability to positively charged ions.

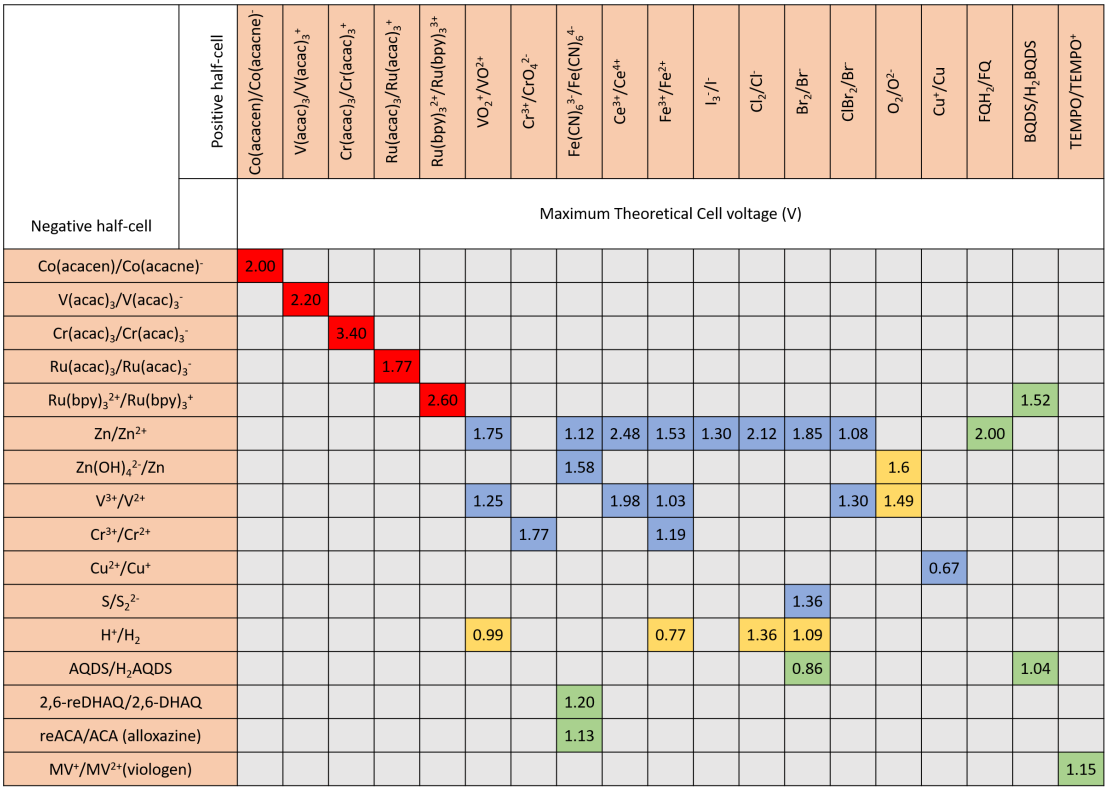

Figure 2.5: List of selected chemistries investigated for use in redox flow batteries. Red refers to non-aqueous systems, blue refers to aqueous systems, green indicates systems where at least on half-cell is organic-based and yellow demonstrates the systems involving gas evolution in one of the half-cells.

Anion-exchange membranes behave oppositely, as their name suggests. In an attempt to reduce the membrane resistivity and high cost of RFBs, some of the mentioned batteries are designed to be membrane-less with a single electrolyte containing the electroactive species for both half-cell reactions (Figure 2.4). Membrane-less zinc-cerium [66], zinc-nickel [67] and lead acid battery [68] are examples of such systems. This design reduces the battery cost and internal resistances. Nevertheless, the use of a single electrolyte may trigger self-discharge or occurrence of undesired side reactions.

RFBs can also be categorized based on the type of the redox couple employed in the system (metallic versus organic). Organic electroactive species are typically less expensive than metal-based species and their redox properties can be tailored by modifying their chemical structures [7]. Nevertheless, they can undergo modification because of electron

gain or loss and degrade over long-term use [69]. Alternatively, RFBs can be identified based on the employed background electrolyte (aqueous versus non-aqueous). In typical RFBs, an aqueous solution is employed due to its lower cost and higher safety. Nonaqueous electrolytes are capable of dissolving redox couples that are commonly unstable in aqueous solutions and thus they offer the possibility of a wider working potential range and higher cell voltages [70]. Nevertheless, nonaqueous electrolytes are commonly expensive and can present safety hazards [71]. Finally, RFBs can be categorized based on the chemistry of the redox reaction. Figure 2.5 provides a list of selected chemistries investigated for use in RFBs.

2.4 Models of Redox Flow Batteries

In addition to experimental studies, mathematical models of redox flow batteries with different chemistries have been developed. The first mathematical model was developed for the iron-chromium redox couple investigated by NASA [72]. It was used to predict the optimum electrode thickness and solution flow rate. Furthermore, the model accounted for the hydrogen evolution side-reaction and showed that the cell geometry and electrolyte flow rate could affect the rate of this reaction and hence the charge efficiency. Transport of the dissolved species due to migration was neglected and convection only in the direction parallel to the electrode surface was considered in this model.

Later, several steady-state models were developed for zinc-bromine redox flow batteries and compared in a subsequent review article [73]. These models could predict the effect of design parameters and operating conditions such as separator thickness, positive electrode thickness, solution flow rate, applied current on cell voltage and the initial electrolyte composition on battery performance. However, these models neglected transient effects as well as the formation of a second phase due to the sequestration of the bromine in the positive half-cell compartment [73].

In recent years, a dynamic two-dimensional model was developed for all-vanadium RFBs [74] and later improved to include temperature effects and hydrogen and oxygen evolution side reactions [75–77]. Vanadium cross-over through the membrane and the resulting capacity loss were also included in another study [78]. Zero-dimensional and three-dimensional isothermal models were later developed for vanadium RFBs [79,80]. The effect of concentration on ion mobility [81] and the incorporation of the Donnan effect [82] in mathematical models of all-vanadium RFBs have also been reported. Three-dimensional transient [83] and steady-state [84] models have also been presented to describe the performance of quinone-bromide RFBs and a two-dimensional model has been developed for

vanadium-cerium RFBs [85]. When models have been validated, they have been fitted to experimental data from a single galvanostatic charge/discharge cycle of a redox battery or polarization curve of a battery at a certain state-of-charge. To date, no multi-physics models have been developed to describe the performance of zinc-cerium RFBs albeit the need to develop a validated mathematical model for these systems has been noted various times in the literature [86, 87].

2.5 Zinc-Cerium Redox Flow Batteries

Zinc-cerium redox flow batteries are relatively new systems developed by Plurion Inc. in 2000s [58] and later studied by other groups [88–90]. As mentioned previously, this system takes advantage of the relatively large difference in the electrode potentials of the Zn/Zn(II) and Ce(III)/Ce(IV) redox reactions. Hence, this system offers one of the highest open-circuit voltages (2.4 V) among conventional RFBs, which can lead to high energy densities when the electrolyte contains high concentrations of the electroactive species. Nevertheless, the large electrode potential difference between the zinc and cerium redox reactions necessitates a careful selection of materials to prevent degradation and suppress side reactions, particularly hydrogen and oxygen evolution. To this end, a number of experimental analyses have been reported so far on the zinc half-cell [91–96], cerium half-cell [97–106] and full-cell zinc-cerium RFBs [12, 107], a summery of which is provided in the following sections.

2.5.1 Negative side of zinc-cerium RFBs

Leung et al. [91] characterized the zinc electrodeposition/electrodissolution reaction in methanesulfonic acid electrolytes for use in zinc-cerium RFBs. The optimum Zn(II) and acid concentrations, operating temperature, applied current density and electrolyte flow rate were found by extracting the charge and voltage efficiencies of a parallel plate flow cell involving zinc redox reaction on the negative side and electrolysis of water on the positive side over a single charge/discharge cycle. Additionally, the morphology of the zinc deposits formed from MSA-based electrolytes at the optimum operating conditions were studied and showed no signs of dendrite formation even after long hours of deposition. In all cases, the system charge efficiency was less than 95% (from 70% to 94% depending on the operating conditions), due to the hydrogen evolution side reaction.

The same authors later investigated the use of additives such as cetyltrimethyl ammonium bromide (CTAB), lead methanesulfonate, indium oxide and butyltriphenyl phospho-

nium chloride (BTPC) for corrosion inhibition of the zinc deposit [92]. Although CTAB and BTPC were found to inhibit zinc corrosion by 40%, they simultaneously reduced the rate of zinc electrodeposition due to their strong blocking effect. The inorganic additives (lead methanesulfonic and indium oxide) slowed down the corrosion during the first few hours of electrodeposition but were ineffective over longer durations ($> 10\,hr$).

Nikiforidis et al. [93, 94] evaluated the performance of several carbon composite negative electrodes including polyvinylidene fluoride (PVDF), uncured high density polyethylene (HDPE-2), high density polyethylene (HDPE-2), polyvinyl ester (PVE), conductive polymer–acid-cure (BAC2) and 20 w% polyvinylidene difluoride (PE20) for the Zn(II)/Zn redox reaction in a methanesulfonic acid electrolyte. Three-electrode half-cell studies revealed that the PVDF, PVE and HDPE-2 carbon composite substrates remain stable over long cycles of zinc electrodeposition/electrodissolution while the other ones significantly deteriorate. Later Nikiforidis et al. [95] fabricated an indium-modified graphite electrode with the goal of HER suppression during the Zn(II)/Zn redox reaction. Half-cell studies revealed that the modified electrode performs better in terms of charge and voltage efficiencies compared to the "as received" graphite electrode due to the reduction in HER rate. No further full-cell studies were performed with the fabricated indium-modified electrode.

2.5.2 Positive side of zinc-cerium RFBs

Leung et al. [98] investigated the Ce(III)/Ce(IV) redox reaction in methanesulfonic acid electrolyte for use in zinc-cerium RFBs. They found that the Ce(III)/Ce(IV) redox reaction on a platinum disc electrode behaves as a quasi-reversible reaction and its overall performance depends strongly on the MSA background concentration. At higher MSA concentrations, oxygen evolution occurs only at very positive potentials. Thus, the oxidation of Ce(III) is the dominant reaction relative to oxygen evolution if higher MSA concentrations are used in the positive electrolyte. Additionally, in agreement with prior literature [108], the solubility of Ce(III) rises as the MSA concentration is reduced, whereas the solubility of Ce(IV) is affected in the opposite way. Thus, a compromise in the MSA level must be made to maintain high solubility of both cerium species in the electrolyte. Moreover, it was shown that the reversibility and kinetics of the Ce(III)/Ce(IV) redox couple improves at higher operating temperatures of 40-70°C. Based on these results, the authors obtained the following optimum conditions for the Ce(III)/Ce(IV) redox reaction: 0.8 $\mathrm{mol\,dm^{-3}}$ cerium(III) methanesulfonate in 4.0 $\mathrm{mol\,dm^{-3}}$ MSA at 70°C.

Due to the highly oxidative environment on the positive side, the choice of the electrode material for the Ce(III)/Ce(IV) reaction is critical. Consequently, this has been the focus

of much of the research related to the positive side. A range of positive electrode materials including platinised titanium mesh, graphite, carbon–polyvinyl ester, reticulated vitreous carbon and carbon felt were evaluated for the cerium redox reaction through polarization and galvanostatic studies [12]. Both carbon felt and platinised titanium mesh electrodes showed high efficiency toward the Ce(III)/Ce(IV) reaction. Nevertheless, carbon electrodes degraded after only a few cycles possibly due to oxidation by Ce(IV). Hence, platinised-titanium positive electrodes were reported as the optimum electrode material.

Nikiforidis and co-workers [99, 101] studied the performance of Pt and Ir-Pt electrodes for the cerium redox reaction in a three-electrode cell system. Not surprisingly, they found that the voltage efficiency dropped due to the higher rate of oxygen evolution at current densities higher than the mass transfer limiting value. This decrease in voltage efficiency could also partly be attributed to the higher ohmic resistance at higher current densities. Additionally, electrodes with higher platinum loading achieved higher voltage efficiencies. The samples with mixed platinum-iridium metal performed similarly to the platinum-only samples especially when tested at higher temperatures. Although carbon-based electrodes are prone to degradation in the presence of Ce(IV), the performance of Ce(III)/Ce(IV) redox reaction on carbon paper [106] and thermally modified graphite electrodes [105] were also investigated in a three-electrode cell configuration. Cyclic voltammetry studies revealed that the performance of Ce(III)/Ce(IV) on both electrodes is comparable to that on platinum-based electrodes. It should be noted, however, that the amount of Ce(IV) concentration produced during cyclic voltammetry tests in these studies was not likely large enough to cause the expected electrode degradation.

Arenas et al. [103] conducted a detailed polarization study of the performance of different Pt/Ti electrode structures with regard to the Ce(IV)/Ce(III) reduction reaction. The polarization analysis was done to compare the mass-transfer limitations and performance of four positive electrode materials (i.e. platinized titanium plate, mesh, micromesh and felt) for cerium conversion. They concluded that Pt/Ti micromesh electrodes are more advantageous than the currently used Pt/Ti expanded mesh electrodes for Ce-based redox flow batteries [103] due to the improved mass transfer rates provided by these electrodes. The authors also characterized these four types of electrodes in terms of their permeability and pressure drop in a later work [104].

Na and co-workers [109] fabricated a SnO_2-modified graphite felt electrode for use as the positive electrode material for the cerium redox reaction. Half-cell CV experiments conducted in 0.05 $\mathrm{mol\,dm^{-3}}$ Ce(III)-methanesulfonate and 1.0 $\mathrm{mol\,dm^{-3}}$ MSA showed a smaller peak separation and anodic/cathodic current ratio closer to 1 (better reversibility) for the cerium redox reaction when carried out on SnO_2-modified graphite felt electrodes compared to an unmodified GF and acid-treated GF. The same authors published another

study in which graphite felt was modified with WO_3 nanowall arrays and used in a lead-cerium redox flow battery [110]. The positive electrolyte contained 1.0 mol dm^{-3} MSA and 1.0 mol dm^{-3} Ce(III) methanesulfonate. In both of these studies, no comment was made on the corrosion of the carbon in the presence of cerium. Again, it is important to note that cyclic voltammetry tests carried out in solutions containing Ce(III) produce only small concentrations of Ce(IV) over one cycle and may not lead to corrosion of the carbon electrode that occurs in the presence of higher concentrations of Ce(IV). Corrosion would likely be observed during continuous battery operation once sufficient amounts of Ce(IV) have been produced.

In order to improve the reversibility and kinetics of the Ce(III)/Ce(IV) redox couple and solubility of both cerium species, the use of a mixed-electrolyte media has also been investigated as a potential remedy [100, 102]. The addition of moderate concentrations (0.5 – 1 mol dm^{-3}) of hydrochloric acid to the base MSA electrolyte has been shown to significantly improve the reversibility and kinetics of the Ce(III)/Ce(IV) redox reaction [102]. Moreover, the diffusion coefficient of Ce(III) was also found to be enhanced in these mixed electrolytes [102]. Although the presence of sulfate rather than chloride in mixed methanesulfonate media also has a positive influence on the Ce(III)/Ce(IV) reaction, its effect does not appear to be as strong [102]. One beneficial effect is an increase in the solubility of Ce(IV) to 1.0 mol dm^{-3} in 2 mol dm^{-3} methanesulfonate / 0.5 mol dm^{-3} sulfate solution [100], while it is less than 0.5 mol dm^{-3} in a 2.5 mol dm^{-3} pure MSA electrolyte [108].

2.5.3 Full-cell studies of zinc-cerium RFBs

Leung et al. [12] characterized the performance of a divided bench-scale zinc-cerium redox flow battery by extracting the charge and voltage efficiencies of the battery over single charge-discharge cycle at different operating conditions. The optimum operating conditions of the battery was found to be 0.8 mol dm^{-3} cerous methanesulfonate dissolved in 4 mol dm^{-3} MSA on the positive side and 1.5 mol dm^{-3} zinc methanesulfonate in 1 mol dm^{-3} MSA on the negative half at elevated temperatures of 40-60°C. Lower MSA concentrations are needed in the negative electrolyte to maintain high zinc deposition/dissolution efficiencies due to competition from hydrogen evolution. At this optimum condition, the battery could be operated at current densities as high as 80 mA cm^{-2} with charge efficiency of 70% and voltage efficiency of 60% [88]. The discharge cell potential was 1.8 V, which is equivalent to an energy density of 350 W h kg^{-1}. In addition to single galvanostatic cycle experiments, authors conducted life-cycle experiments over several charge/discharge cycles and showed that a zinc-cerium RFB could operate for a lifetime between 25-30 hours

over 57 cycles with charge times lasting 15 minutes at a current density of 50 $mA\,cm^{-2}$. The same team later investigated the performance of a membrane-less single compartment zinc-cerium RFB [66]. Elimination of the expensive ion-exchange membrane from RFBs is a very attractive option since it would significantly reduce the cost of materials, simplify the design of the battery and reduce the ohmic resistance across the cell. As mentioned previously, a high MSA concentration is required to achieve high Ce(IV) solubility, while at high MSA concentrations the efficiency of zinc deposition/dissolution reaction decreases due to excessive hydrogen evolution. Thus, in a membrane-less battery where a single electrolyte is used, a compromise must be made between a high Ce(IV) solubility and high efficiency of the Zn/Zn(II) redox reaction. Consequently, the membrane-less zinc-cerium RFBs developed in the work of Leung et al. was operated at lower acid concentrations (~ 0.2 – $0.5\ mol\,dm^{-3}$) and lower Ce concentrations ($0.2\ mol\,dm^{-3}$ – $0.4\ mol\,dm^{-3}$ Ce(III)) [66, 111]. The undivided battery reportedly achieved a current efficiency of 90% and energy efficiency of 75% at 20 $mA\,cm^{-2}$.

Another full-cell study [107] on a divided bench-scale zinc-cerium RFB focused on the effect of operating conditions on the performance of zinc-cerium RFBs and reported comparable results to the above-mentioned study. A different optimum composition of $0.59\ mol\,dm^{-3}$ ceric methanesulfonate and $0.08\ mol\,dm^{-3}$ cerous methanesulfonate in 3.5 $mol\,dm^{-3}$ MSA on the positive side and $2.5\ mol\,dm^{-3}$ zinc methanesulfonate in $1.5\ mol\,dm^{-3}$ MSA on the negative half-cell of the battery was suggested to achieve high output efficiencies, although a low applied current density of 10 $mA\,cm^{-2}$ was used in this study.

In addition to experimental work, Arenas et al. [112] theoretically approximated the cell voltage as a function of discharge current density in an idealized zinc-cerium RFB by calculating the kinetic overpotentials from the Butler-Volmer equation and estimating the ohmic drop in the battery. From this approximation, they found that the use of porous electrodes is highly advantageous for battery performance and that large electrode spacing significantly increase voltage losses in the battery. It should be noted that these conclusions are valid for any RFB system.

2.6 Summary

In this chapter, the history and development of redox flow batteries was reviewed and the key components of this technology were presented. Additionally, the different types of RFBs developed to date were systematically categorized and described. A brief summary of the models developed for understanding and predicting the performance of RFBs was

also presented. The chapter also provided a literature review focused on zinc-cerium redox flow batteries with respect to its negative half-cell, positive half-cell and full-cell operation.

The majority of the work done on the negative side of the system has focused on reducing the rate of hydrogen evolution to increase the charge efficiency of zinc electrodeposition/electrodissolution. The strategies included the use of corrosion inhibitors in the negative electrolyte and the development of alternative negative electrodes. Based on these results, the use of additives such as indium oxide effectively reduces the rate of HER in the first few hours of electrodeposition, but the effect fades away at longer deposition times. In terms of alternative negative electrodes developed for corrosion inhibition, the work done on indium-modified electrodes is promising but requires further investigation to understand its effectiveness in a bench-scale RFB over long hours of operation. In the meantime, any approach capable of enhancing the efficiency of the Zn/Zn(II) reaction would be beneficial for improvement of zinc-cerium RFBs.

The majority of the work done on the positive side of zinc-cerium RFBs has been on the development of electrode materials capable of withstanding the highly oxidative nature of cerium species. Platinized-titanium mesh and micromesh electrodes are recommended due to their durability and high efficiency. Nevertheless, the high cost of these electrodes reduces the commercial attractiveness of zinc-cerium RFBs. Hence, development of low-cost and efficient electrode materials and electrocatalysts for the Ce(III)/Ce(IV) reaction is highly needed. It is obviously very important to thoroughly study the corrosion of the positive electrode material in presence of both Ce(III) and Ce(IV) species when evaluating its durability for zinc-cerium RFBs.

In terms of the full-cell studies on zinc-cerium redox flow battery, the prior work focused on determining the optimum operating conditions in terms of electrolyte composition, applied current density, temperature and flow rate. A detailed description of the sources of performance loss in zinc-cerium RFBs and an analysis of their cycle life would be beneficial for further development of these systems.

Chapter 3

In Situ Polarization Study of Zinc–Cerium Redox Flow Batteries[1]

3.1 Introduction

The full-cell experiments on redox flow batteries have typically involved charge-discharge cycling of the battery under galvanostatic or potentiostatic conditions. These experiments give valuable information on the coulombic, voltage and energy efficiencies of the battery. Nevertheless, these charge-discharge experiments cannot directly sort out the mechanisms responsible for losses in battery efficiency [114]. In general, the limitations in battery performance can be attributed to a variety of processes such as activation polarization, ohmic polarization and concentration polarization. Activation losses are associated with kinetic limitations of the charge-transfer reactions, while ohmic losses are caused by the electrical resistances in the electrolyte, membrane and electrical contacts. Concentration polarization occurs when the rate of mass transport of reactants to/from the electrode limits the production of current [114]. Polarization curves can be analyzed to identify the contributions of the aforementioned overpotentials and to shed light on the causes of the efficiency loss at different current densities.

Although *in situ* two-electrode polarization experiments on full-cell batteries can be used to measure the overall losses in a battery, they cannot provide information on the individual contributions from the negative and positive electrodes. Fortunately, this problem can be easily overcome in RFBs (unlike conventional batteries) by inserting reference

[1]This chapter is adapted from my published work [113].

electrodes on each side of the cell. This approach was used in several earlier studies on all-vanadium RFBs. Langner et al. [115] and Derr et al. [116] placed Ag/AgCl reference electrodes at the each of the inlets to the battery, while Aaron et al. [114, 117] inserted dynamic hydrogen electrodes with a Pt wire between two layers of cation-exchange membranes. A more complex four-point design with four Pt wire pseudo-reference electrodes has also been suggested [118]. Sun et al. [119] combined polarization and EIS experiments to break down the polarization at each electrode further to its components, although they encountered complications with some of their EIS data due to pump noise at low frequencies and distorted high frequency arcs in the response of the positive electrode.

Despite its value, little analysis of full-cell zinc-cerium polarization curves to identify the source of losses in RFBs has been reported. As mentioned in the previous chapter, Leung et al. [12] conducted polarization experiments on a full-cell zinc-cerium RFB to compare the performance of different electrode materials for the positive half-cell of the battery. Although reference electrodes were inserted in the battery setup, the half-cell electrode potentials were not monitored during the polarization experiments. The reference electrodes were used only to monitor half-cell electrode potentials during one galvanostatic charge/discharge cycle of the battery to compare the performance of carbon felt and platinized titanium positive electrode. Another polarization study was done in the work of Arenas et al. [103]. As explained previously, they conducted a detailed polarization study of the performance of different Pt/Ti electrode structures with regard to the Ce(IV)/Ce(III) reduction reaction. The polarization analysis was done to compare the mass-transfer limitations and performance of four positive electrode materials (i.e. platinized titanium plate, mesh, micromesh and felt) for cerium conversion.

In this work, we carry out *in situ* polarization and EIS experiments on a full-cell zinc-cerium RFB with reference electrodes inserted at the electrolyte entrances on both sides of the battery to investigate, for the first time, the sources of voltage loss in zinc-cerium RFBs and to decouple the contribution of negative and positive redox reactions to the overall loss. The goals of this work are to determine the sources of voltage loss (i.e., contributions due to kinetic, ohmic and mass transfer) in a bench-scale zinc-cerium redox flow battery and to characterize the contribution of each half-cell reaction to the overall voltage drop in the battery. This information is crucial for optimizing battery performance and for elucidating the pathways that enhance the system efficiency. We first investigate the overall voltage loss in the battery and identify the contributions of kinetic, ohmic and mass-transfer overpotentials to the total loss by combining data from the polarization and EIS experiments. Following that, we use the monitored positive and negative electrode potentials to resolve the contribution of individual electrodes to the overall voltage drop. An *in situ* kinetic study using the Butler-Volmer equation is also conducted to estimate

the kinetic parameters of the positive and negative electrode reactions. Finally, the effects of an alternative negative electrolyte on the kinetics of the Zn/Zn^{2+} redox couple and electrolyte flow rate on the mass transfer in positive and negative half-cells of an operating RFB are investigated through *in situ* polarization experiments. The alternative negative electrolyte is a mixed methanesulfonate-chloride solution which is developed as part of this thesis and will be discussed further in more detail in Chapter 5 and Chapter 6.

3.2 Experimental

3.2.1 Reagents

All solutions used in the experiments were prepared with ultra-pure water (resistivity of $\sim$ 18 MΩ cm) and analytical grade reagents. Appropriate amounts of high purity zinc oxide (Zochem Inc.) were mixed with 70% methanesulfonic acid (Alfa Aesar) to prepare the zinc(II) methanesulfonate solutions. The mixed methanesulfonate-chloride electrolytes were prepared by combining 99% pure anhydrous zinc chloride (Fisher Scientific) with the zinc(II) methanesulfonate solutions. In the case of cerous methanesulfonate, 99% pure cerium(III) carbonate (Treibacher Industrie AG) was mixed with methanesulfonic acid in the appropriate amounts. All of these solutions were colorless with no precipitates. To determine the concentration of Ce(IV) in the positive electrolyte and hence the state of the charge during battery operation, 99% pure ammonium iron(II) sulfate hexahydrate (Sigma- Aldrich) was titrated into the Ce(IV)-containing solution which also contained ferroin (1,10-phenanthroline iron(II) sulfate) (Alfa Aesar) as a colorimetric redox indicator.

3.2.2 Battery setup

A bench-scale single-cell zinc-cerium redox flow battery was constructed which consisted of a copper current collector (McMaster-Carr), a 6 mm-thick polyvinyl ester (PVE) carbon (TDM Fuel cells) negative electrode, a three-dimensional platinized titanium mesh positive electrode with a loading level of 7 mg cm^{-2} Pt (Metakem GmbH), a Nafion 117 membrane (Fuel Cell Store), two 6 mm-thick acrylic flow channels (acrylic sheets from CIP Wholesale) and four rubber silicone gaskets (CS Hyde Company). These components were stacked in such a way that the electrodes, flow channels and the membrane were separated by the gaskets. Both positive and negative electrodes had an active surface area of 2 cm $\times$ 4.5 cm.

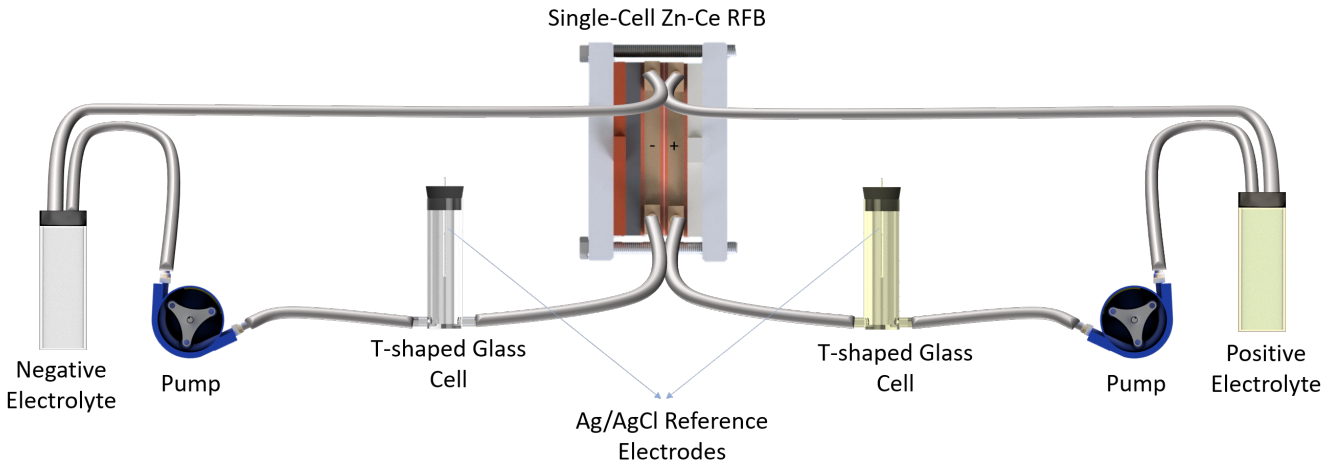

Figure 3.1: Components of the battery setup used in this study.

The negative electrolyte in its fully discharged state contained 1.5 mol dm^{-3} zinc methanesulfonate in 1 mol dm^{-3} methanesulfonic acid in all experiments except those in which a mixed methanesulfonate-chloride negative electrolyte was used. The mixed electrolyte composition was 0.9 mol dm^{-3} zinc methanesulfonate and 0.6 mol dm^{-3} zinc chloride in 1 mol dm^{-3} methanesulfonic acid. In its fully discharged state, the positive electrolyte contained 0.8 mol dm^{-3} cerous methanesulfonate in 4 mol dm^{-3} methanesulfonic acid in all of the tests. The electrolytes were stored in separate external 30 cm^3 reservoirs and pumped into the cell using a model BT100-1L Longer peristaltic pump with two channel heads (model YZ1515) and Viton tubing (McMaster-Carr). The electrolytes were circulated through a temperature bath (Neslab RTE-8) throughout the battery runs to maintain their temperature at 50°C throughout the experiments. Note that due to the improved reversibility of the Ce(III)/Ce(IV) redox reaction at higher temperatures, zinc-cerium RFBs are commonly operated at a temperature of 50°C which has been found to be optimum [12, 98]. Prior to each experiment, the Nafion membrane was pre-treated by immersion in the following sequence of solutions: 3 wt. % H_2O_2, DI water, 0.5 mol dm^{-3} H_2SO_4 solution and DI water again to eliminate any traces of H_2SO_4. The duration of each immersion step was 1 hr at 80°C.

To monitor the negative and positive electrode potentials *in situ* during battery operation, the design shown in Figure 3.1 was employed. As shown in Figure 3.1, two Ag/AgCl reference electrodes (Pine Research Instrumentation) were placed adjacent to the inlet of each flow channel and in the path of the two electrolytes by employing two custom-made T-shaped glass cells. On the negative side (zinc half-cell), the Ag/AgCl reference electrode

directly contacted the negative solution circulated through the battery. On the positive side, we observed that direct contact of the reference electrode with the positive electrolyte led to damage of the Ag/AgCl reference electrode over time due to cerium ions which had diffused through the ceramic frit of the reference electrode and into its inner chamber. Consequently, the reference electrode was placed inside a hollow cylindrical glass holder that was sealed on one end with a Nafion membrane. The holder was filled with 4 $\mathrm{mol\,dm^{-3}}$ MSA, which had the same MSA concentration as in the positive solution but with no cerium. The Nafion membrane provided a barrier to prevent the damage of the reference electrode by cerium ions. The potential drop across this Nafion membrane barrier added to the set-up was found to be $\sim 8 \times 10^{-4}$ V, which was negligible given that the electrode potentials measured in our experiments were all larger than 0.5 V.

3.2.3 Electrochemical tests

All electrochemical polarization experiments were conducted using an Autolab PGSTAT 30 potentiostat/galvanostat. The polarization studies involved first charging the battery galvanostatically for 45 minutes at 50 $\mathrm{mA\,cm^{-2}}$ to reach a state-of-charge (SOC) of 50%. This was confirmed by titration of the positive electrolyte to contain 0.4 $\mathrm{mol\,dm^{-3}}$ Ce(IV) at 50% SOC. Following this step, the battery was discharged at the specific current density for 30 seconds and allowed to rest for 20 seconds at its OCV before applying the next desired current density in the polarization curve. The cell potentials measured over each 30-second period were averaged to provide a value at each current density in the polarization curve. Using the reference electrodes incorporated in the setup, the negative and positive electrode potentials were also monitored and averaged over the 30-second period at each current density. The concentration of Ce(IV) was regularly checked by titration and adjusted (if necessary) throughout the experiment to ensure that a 50% SOC was maintained.

Electrochemical impedance spectroscopy (EIS) was carried out in potentiostatic mode using a BioLogic VMP3 impedance analyzer on a 2-electrode bench-scale zinc-cerium redox flow battery over a frequency range from 150 kHz to 0.1 Hz and a 0.01 V sinusoidal perturbation amplitude about different set potentials. Before each measurement, the electrode was polarized at the desired potential for 30 seconds to achieve a steady state current. This procedure was repeated at different potentials to obtain the impedance spectrum at each point along the polarization curve.

3.3 Results and Discussion

3.3.1 Zinc-cerium full-cell polarization and EIS tests

Figure 3.2a shows the polarization curve of the zinc-cerium redox flow battery while operating at 50% SOC, 50°C and a flow rate of 65 $\mathrm{ml\,min^{-1}}$. The open-circuit voltage (OCV) is $\sim$ 2.37 V, which is close to the expected theoretical value of 2.4 V. From the polarization curve, mass transport begins to affect battery performance at current densities above 65 $\mathrm{mA\,cm^{-2}}$ whereupon the cell voltage begins to drop much more steeply. At current densities lower than 65 $\mathrm{mA\,cm^{-2}}$, the kinetic and ohmic overpotentials are the predominant contributors to the voltage loss.

With the information provided in Figure 3.2a, the approximate battery cell voltage can be determined as a function of current density at 50% SOC. However, with this method, the contributions of the various sub-processes to the voltage loss cannot be identified. In order to further isolate the contributions of kinetic, ohmic and mass transfer effects to the total voltage loss of the battery, two-electrode EIS experiments were conducted on the battery at various overpotentials. As noted previously, the approach of combining EIS and polarization experiments to identify the sources of voltage loss was previously used by Sun et al. [119] for all-vanadium RFBs. These measurements were conducted on each half-cell during battery operation using an *in situ* reference electrode (three-electrode EIS). However, *in situ* EIS measurements on each electrode during battery operation using a reference electrode is complicated by the fact that the pumping of the electrolytes through the chambers leads to considerable pulsation noise in the output signal. Sun et al. [119] eliminated this noise by reducing the flow rate below 1.5 $\mathrm{ml\,min^{-1}}$. Additionally, the previous study on all-vanadium RFB revealed that distorted EIS arcs in the responses of the electrodes on the positive side were observed at high frequency which prevented this technique from accurately estimating the resistances of each of the electrodes [119]. On the other hand, 2-electrode EIS experiments on full batteries do not suffer from these problems and so can be used to gain valuable information regarding the overall kinetic and ohmic losses without the mentioned complications. Note that we did not conduct EIS at low frequencies to extract the mass transfer resistance since the long duration of the tests that are required would significantly change the SOC of the battery from 50% during the course of the measurements.

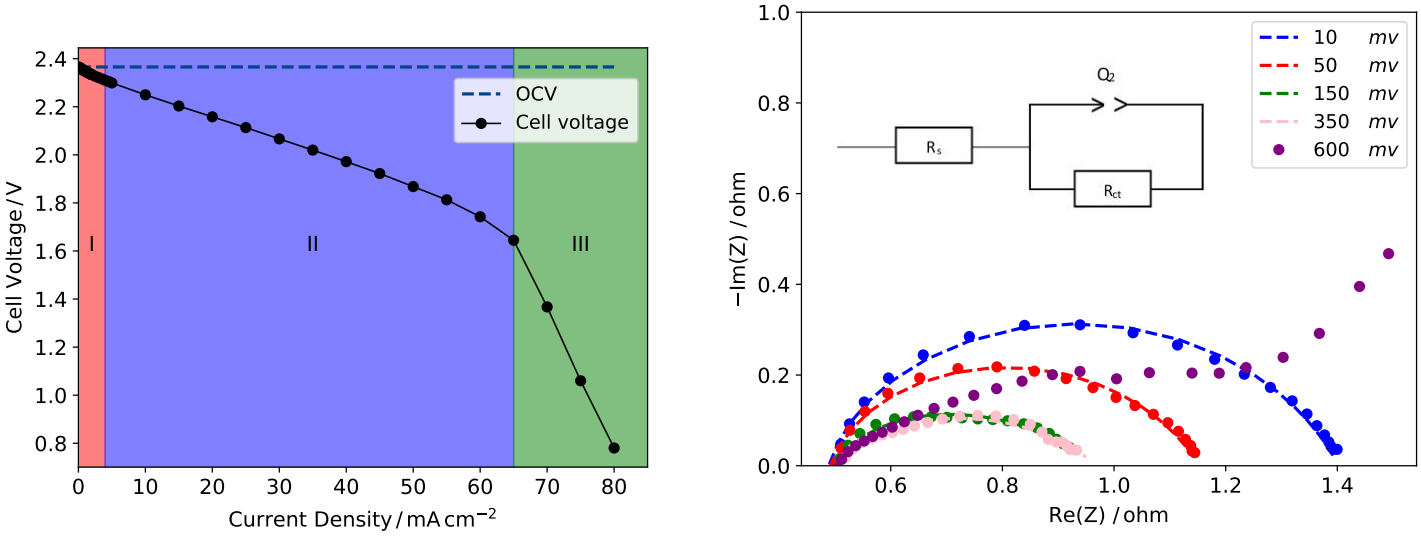

(a) (b)

Figure 3.2: (a) OCV-current density and cell voltage-current density polarization curve of Zn-Ce RFB obtained at 50% SOC and 50°C. Regions I, II and III correspond to the current densities where activation, ohmic and mass transfer first take effect, respectively. (b) Selected Nyquist impedance plots obtained at different overpotentials. The dashed lines show the curves fitted to the data using the equivalent circuit model shown in the plot.

Figure 3.2b presents the Nyquist impedance plots of the full-cell battery at different overpotentials. In order to extract the charge transfer resistance R_{ct} and the ohmic resistance R_s of the battery, the data have been fitted to the Randles equivalent circuit shown in Figure 3.2b. The ohmic resistance obtained from the high-frequency intercept with the x-axis represents the combined voltage drop across the electrolyte, membrane and the electrical contacts in the battery and changes insignificantly throughout the experiment. The area-specific resistance (ASR) of this battery is found to be 4.5 $\Omega\,cm^{-2}$ which is consistent with the previously reported ASR values for RFBs with similar designs. ASRs of 9.2 $\Omega\,cm^{-2}$ for a Zn-Ce RFB [12], 4.2 $\Omega\,cm^{-2}$ for a vanadium-cerium RFB [120] and 5.4 $\Omega\,cm^{-2}$ for an all-vanadium RFB [121] have been reported. The kinetic resistances were experimentally measured up to a current density of 33 mA cm^{-2}. Beyond this current density, mass transfer effects become significant at low frequencies during the EIS experiments and become convoluted with charge transfer effects, making the estimation of R_{ct} difficult. An example of such an occurrence at an overpotential of 600 mV is shown in

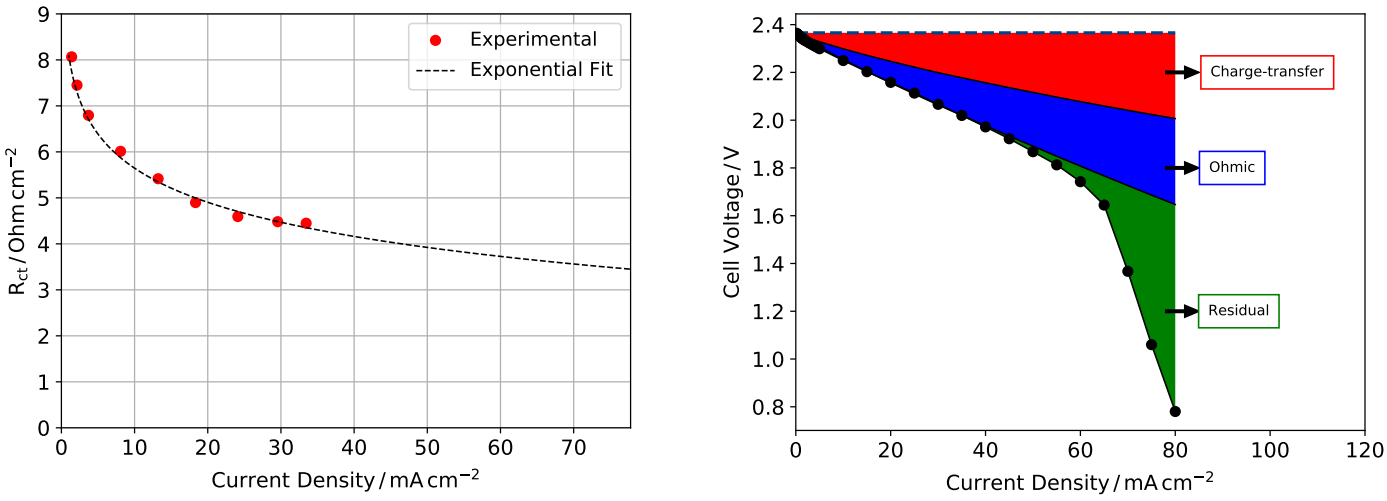

(a) (b)

Figure 3.3: (a) Charge-transfer resistances extracted from fitting the EIS spectrum to a Randles equivalent circuit at different currents (red dots). The exponential function fit to the experimental data is shown as the dashed line. (b) Resolved sources of overpotential contributing to the voltage drop in the system at 50% SOC and 50°C.

Figure 3.2b. Sun et al. [119] observed a similar low-frequency mass transport impedance at current densities higher than 16 mA cm^{-2} and estimated R_{ct} at higher current densities by simple extrapolation. We have followed the same approach by fitting to the relationship between R_{ct} and current, as shown in Figure 3.3a. The charge transfer resistance is found empirically to decrease exponentially as the current density increases (Figure 3.3a). The dependence of overpotential η_{ct} corresponding to charge transfer resistance on current can be obtained by integration over this relationship between R_{ct} and current since the charge transfer resistance is described as:

$$\frac{d\eta_{ct}}{di} = R_{ct}. \tag{3.1}$$

With the above procedure, the charge transfer and ohmic components of the overall cell voltage are determined. By subtracting these two resistances from the overall voltage drop, a residual is found which should mainly correspond to the mass transfer losses. Nevertheless, we call this source "residual" since the mass transfer resistance has not been

measured directly from experiments. Figure 3.3b shows the resolved components of the voltage loss. From this figure, it can be deduced that the charge transfer overpotential is responsible for 56.8% and 50.16% of the voltage loss in the battery at current densities of 25 $\mathrm{mA\,cm^{-2}}$ and 50 $\mathrm{mA\,cm^{-2}}$, respectively. Since $\mathrm{R_{ct}}$ is found to drop exponentially as the current density increases, it decreases more steeply at low and intermediate current regions. Obviously, enhancement of the charge transfer reaction would be very helpful in decreasing the cell voltage loss especially when battery operates at low to mid-range current densities where mass transfer effects do not yet play a role in battery operation. In previous studies, zinc-cerium RFBs were operated at current densities of 10 $\mathrm{mA\,cm^{-2}}$ [89], 15-30 $\mathrm{mA\,cm^{-2}}$ [122] and 50 $\mathrm{mA\,cm^{-2}}$ [12]. Based on the results in Figure 3.3b, all of these current densities fall in the low-to-intermediate range where mass transfer effects are negligibly small.

Ohmic effects are responsible for a voltage drop of ~ 0.11 V at a current density of 25 $\mathrm{mA\,cm^{-2}}$ (ASR of 4.5 $\Omega\,\mathrm{cm^{-2}}$). The battery used in this study is designed with 6 mm-thick acrylic flow channels. Since the negative electrode used for zinc deposition is planar, the electrode-membrane gap is 6 mm in this bench-scale RFB. Improvement in the design of the battery by lowering the electrode-membrane gap would reduce the ohmic drop in the system. The large contribution of the electrode-membrane gap to the battery ohmic drop was also discussed in a previous study [112]. Additional sources of ohmic loss are the voltage drop across the Nafion membrane and the electrical contacts. The residual overpotential which mainly involves losses due to mass transfer resistances occurs entirely at higher current densities. These losses are responsible for the steep drop in the cell voltage when the battery operates at high current densities.

3.3.2 *In situ* monitoring of negative and positive electrodes

In the previous section, the cell voltage of a bench-scale zinc-cerium RFB was measured as a function of current density and the contribution of each sub-process to the voltage loss was resolved. However, as noted, the separate contributions of the processes occurring in each compartment of the RFB to the total loss could not be determined since it was not possible to obtain noise-free EIS data using a 3-electrode setup. Nevertheless, it is possible to obtain a measure of their contributions from DC polarization experiments during battery discharge conducted using a 3-electrode system with Ag/AgCl reference electrodes inserted in the electrolyte inlet on each side. The insertion of reference electrodes enables us to monitor the polarization of each electrode as a function of the cell current density during a full-cell polarization experiment. The battery discharge cell voltage measured during the

polarization test contains the contributions of the positive electrode, negative electrode and ohmic drop across the battery [120], i.e.,

$$E_{cell} = E_{pos} - E_{neg} - \sum IR \tag{3.2}$$

The evolution of the negative electrode potential E_{neg} and positive electrode potential E_{pos} monitored during the battery polarization experiment is shown in Figure 3.4a. Since the reference electrodes are located outside the electrochemical cell close to the entrance of the battery, the ohmic losses in the operating RFB differ from those operating during the *in situ* measurements of the positive and negative electrode potentials. For our purposes here, we define the corrected full cell discharge cell voltage as

$$E_{\text{cell,corrected}} = E_{pos,meas} - E_{neg,meas} \tag{3.3}$$

where $E_{pos,meas}$ and $E_{neg,meas}$ are the measured positive and negative electrode potentials, respectively. If the ohmic losses associated with the measurements of $E_{pos,meas}$ and $E_{neg,meas}$ are negligible, this corrected cell voltage should be the same as the value obtained by subtracting the ohmic potential loss determined via EIS experiments from the total cell voltage obtained from polarization experiments on the full cell (discussed in the previous section).

Thus, $E_{\text{cell,corrected}}$ can be obtained in two different ways, as was done in previous studies on the all-vanadium and Ce-V systems [114, 119, 120]. A comparison of the $E_{\text{cell,corrected}}$ values of the Zn-Ce RFB found by polarization/EIS of the full cell and from the separate measurements of the negative and positive electrode potentials during polarization is shown in Figure 3.4b. The values determined using the two methods are in excellent agreement, confirming the validity of both procedures for finding the $E_{\text{cell,corrected}}$. This also confirms that the ohmic losses associated with the measurements of $E_{pos,meas}$ and $E_{neg,meas}$ are negligibly small.

The individual electrode contributions to the voltage loss during discharge are shown in Figure 3.4c. The voltage losses at the negative electrode are higher than those at the positive electrode at low and mid-range current densities. However, at higher current densities particularly where mass transfer limitations become dominant, most of the voltage loss occurs at the positive electrode where the reduction of Ce(IV) to Ce(III) takes place. The small contribution of the negative half-cell to the voltage loss in this region is expected since it involves the oxidation of Zn metal to Zn(II) during the discharge phase. Since zinc metal is attached to the electrode surface and is already available on the substrate, its oxidation never becomes limited by mass transfer of reactants (zinc metal) to the electrode

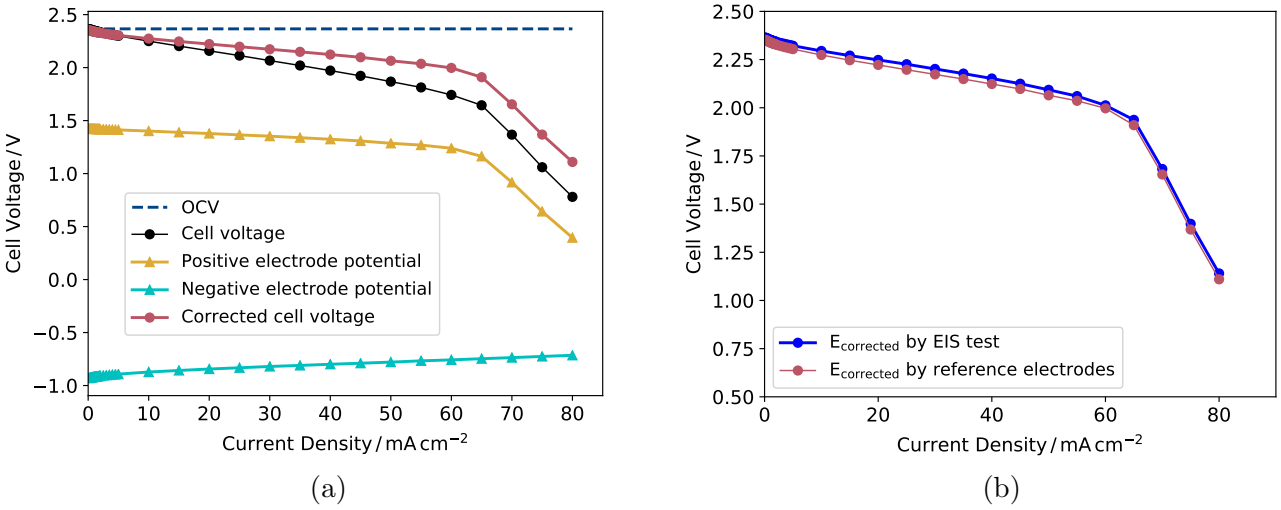

(a) (b)

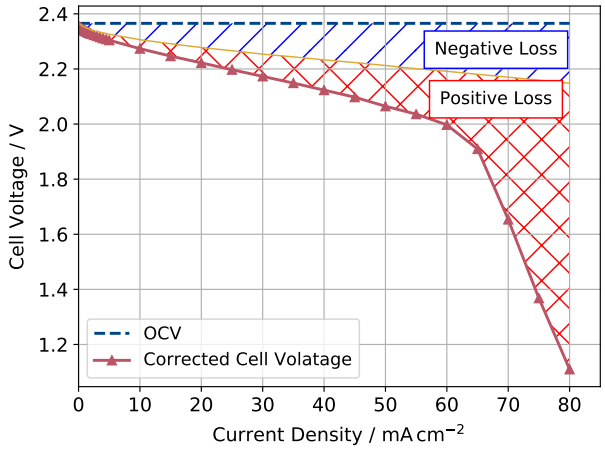

(c)

Figure 3.4: (a) The OCV, cell voltage, positive electrode potential and negative electrode potential measured as a function of current density during full-cell polarization at 50% SOC, 50°C and flow rate of $\sim$ 65 mL min^{-1}. The corrected (IR-free) voltage shown is obtained from measurement of the individual electrode potentials. (b) Comparison between the E_{cell}, corrected obtained using 2-electrode polarization/EIS technique on full-cell and 3-electrode measurement of the individual electrode potentials. (c) Zinc-cerium RFB polarization curve showing the resolved losses attributed to the negative (blue) and positive (red) sides of the RFB obtained from individual electrode potentials measured against Ag/AgCl reference electrodes.

surface regardless of the current density. However, on the positive side, mass transfer eventually limits the rate of the reduction of Ce(IV) to Ce(III) which are both dissolved species when the current becomes high enough. The positive and negative OCVs are found to be 1.42 V and -0.93 V versus Ag/AgCl, respectively, both of which are close to the standard equilibrium potentials of zinc and cerium redox reactions. As evident in Figure 3.4a, the negative and positive polarization curves are asymmetric, indicating that each electrode contributes differently to the overall battery loss. Since the potential and OCV of each electrode are known at each current density, the negative and positive contributions to the overpotential can be determined as follows:

$$\eta_{neg} = E_{neg} - E^{ocv}_{neg} \tag{3.4}$$

$$\eta_{pos} = E_{pos} - E^{ocv}_{pos} \tag{3.5}$$

The variation of η_{pos} and η_{neg} with current density is shown in Figure 3.5a. At current densities less than 58 mA cm^{-2}, the magnitude of η_{neg} is higher than that of η_{pos} at each current density. For example, $|\eta_{neg}|$ at 25 mA cm^{-2} is $\sim$ 0.1 V, while $|\eta_{pos}|$ is only $\sim$ 0.057 V. Once the current density increases above 58 mA cm^{-2}, $|\eta_{neg}|$ continues to increase linearly, but $|\eta_{pos}|$ begins to rise very sharply. Thus, when 80 mA cm^{-2} is reached, $|\eta_{pos}|$ has grown to $\sim$ 1.03 V and $|\eta_{neg}|$ only to $\sim$ 0.22 V, demonstrating that the loss of cell voltage (see Figure 3.2a) at high current densities is due mostly to the positive overpotential.

While the contribution of mass transfer to the cell voltage loss becomes important at very high current densities, the kinetics of the positive and negative redox reactions in zinc-cerium RFBs can be investigated *in situ* by analyzing the individual electrode potentials versus Ag/AgCl reference electrodes obtained at low overpotentials during polarization experiments. Figure 3.5b shows the logarithm of the discharge current density versus overpotential for both negative and positive electrodes within the kinetic-controlled region and so is limited to overpotentials less than 0.140 V corresponding to the current densities below 40 mA cm^{-2}. In order to obtain the exchange current density i_0, β_a and β_c for each electrode reaction, the Butler-Volmer equation (Equation 3.6) is fitted to the experimental data using a non-linear least-square method that makes use of the trust region reflective algorithm (TRF).

$$i = i_0 \left[\exp(\frac{2.3(\eta)}{\beta_a}) - \exp(-\frac{2.3(\eta)}{\beta_c}) \right] \tag{3.6}$$

Based on this approach, the exchange current density for zinc oxidation is estimated

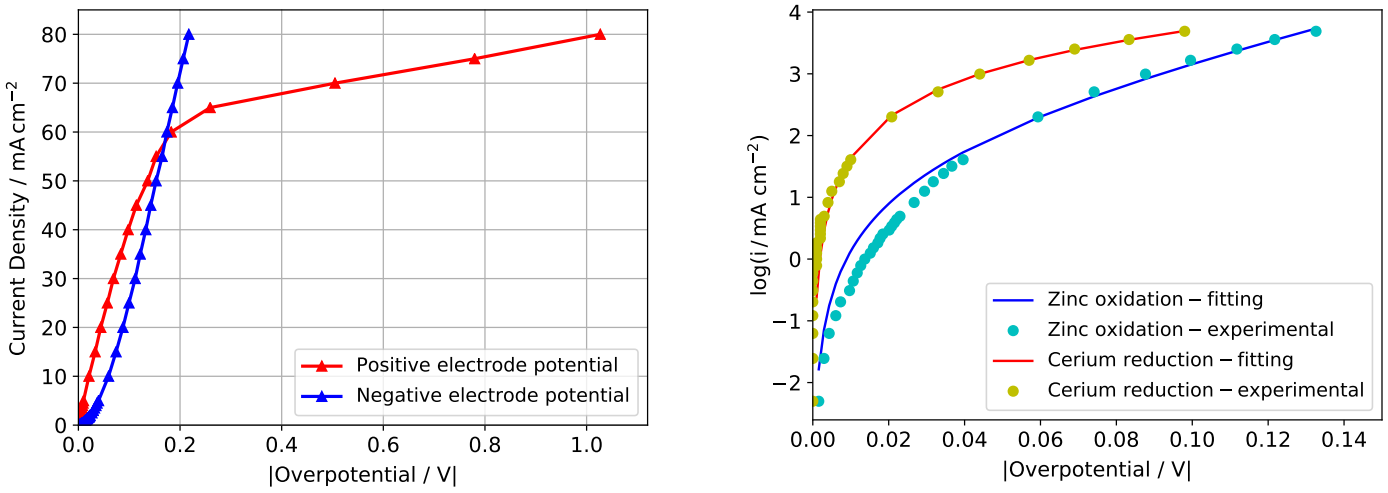

(a) (b)

Figure 3.5: (a) Variation of positive and negative electrode overpotentials with current density at 50% SOC, 50°C and flow rate of $\sim$ 65 mL min^{-1}. (b) Semi-log plot of current density versus overpotential for both positive and negative electrodes during full-cell polarization tests using Ag/AgCl reference electrodes. The dots show the experimental data. The solid lines show the results obtained by fitting the Butler-Volmer equation to the experimental data.

to be $\sim$ 7.4 mA cm^{-2}. This value is consistent with our *ex situ* experiments presented later in Chapter 5 on the Zn/Zn^{2+} system which yielded an exchange current density of $\sim$ 11.3 mA cm^{-2} for zinc oxidation and reduction in an electrolyte containing 1.5 mol dm^{-3} zinc methanesulfonate in 1 mol dm^{-3} methanesulfonic acid at 50°C. Additionally, Leung et al. [12] reported a corrosion study based on measurements of the zinc mass loss in MSA electrolytes and obtained exchange current densities on the order of 10^{-3} A cm^{-2}.

The exchange current density for the discharge reaction at the positive electrode (i.e., Ce(IV) reduction) is estimated to be $\sim$ 24.2 mA cm^{-2}. The exchange current density values reported in the literature from half-cell polarization experiments lie in the range from 1.75 – 11.2 mA cm^{-2}, depending on the platinum loading of the electrode material [89, 100, 123]. These values are of the same order of magnitude, although somewhat lower, than the exchange current density found here for Ce(IV) reduction. It should be noted that the earlier experiments were carried out using an electrolyte with compositions different than the composition of 0.4 mol dm^{-3} Ce(IV), 0.4 mol dm^{-3} Ce(III) and 4

mol dm^{-3} methanesulfonic acid used in this study.

From the exchange current densities found above, we conclude that kinetics of Ce(IV) reduction is faster than that of zinc oxidation during discharge. This is consistent with the results in Figure 3.5a indicating that most of the performance loss can be attributed to the negative electrode and η_{neg} is much larger in magnitude than η_{pos} at low and intermediate current densities. Thus, improvement in the kinetics of the Zn/Zn(II) would be beneficial for enhancing the discharge voltage and lowering the magnitude of η_{neg}, especially for operation at low to mid-range current densities.

3.3.3 Effect of mixed methanesulfonate-chloride negative electrolyte

One possible strategy for improving the kinetics of the Zn/Zn(II) redox reaction is to use an alternative negative electrolyte to the standard methanesulfonate solutions that have typically been used. In our studies presented later in Chapters 5 and 6, we will show that the use of a mixed methanesulfonate-chloride electrolyte on the negative side of the zinc-cerium RFBs enables the battery to operate with higher voltage and charge efficiencies as well as a longer life-cycle than that possible with methanesulfonate-only electrolytes. Thus, it would be useful to investigate the effect of this alternative negative electrolyte on the battery polarization curve. We provide the results related to this alternative electrolyte here to show the improvement in the battery discharge cell voltage with this alternative electrolyte while the memory of the described *in situ* techniques is still fresh to the reader.

Figure 3.6 demonstrates the change in the cell discharge polarization curve when a mixed methanesulfonate-chloride electrolyte with composition of 0.6 mol dm^{-3} $ZnCl_2$ and 0.9 mol dm^{-3} ZnMSA in 1 mol dm^{-3} MSA is used on the negative side of the battery. It is important to note that the total Zn(II) concentration of 1.5 mol dm^{-3} and MSA concentration of 1 mol dm^{-3} remain unchanged from that of the methanesulfonate-only electrolyte used previously in this study. Figure 3.6a shows the contribution of individual electrodes to the overall voltage loss. Since we made no changes to the composition of the positive electrolyte and the operating parameters, the response of the positive electrode and its contribution to the overall voltage loss is almost the same as shown previously, as expected. On the other hand, the contribution of the negative electrode to the overall battery loss has decreased significantly compared to the previous case when a methanesulfonate-only solution is used. As can be seen in Figure 3.6a, the losses at the negative electrode are no longer higher than those at the positive electrode at low and intermediate current densities. Furthermore, Figure 3.6b shows that the negative overpotential is now less

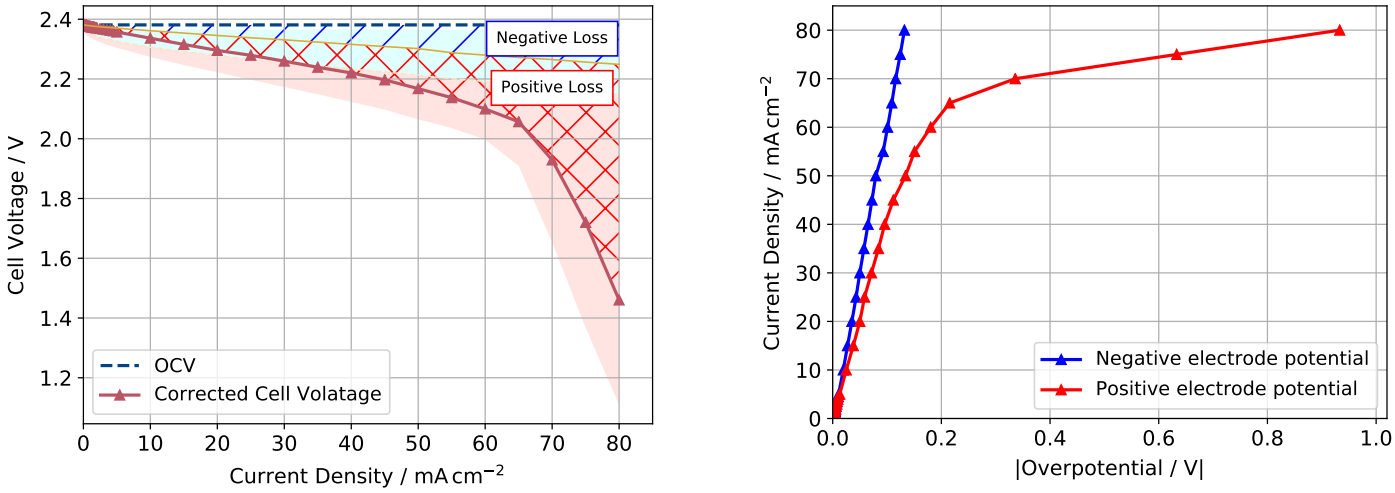

(a) (b)

Figure 3.6: Experimental results of a zinc-cerium RFB operating with mixed MSA-chloride negative electrolyte with composition of 0.6 mol dm^{-3} $ZnCl_2$ and 0.9 mol dm^{-3} ZnMSA in 1 mol dm^{-3} MSA. The remaining operating conditions are the same as for those shown in Figure 3.5. (a) Zinc-cerium RFB polarization curve with isolated negative and positive losses obtained from individual electrode potentials measured against Ag/AgCl reference electrodes. The blue and red areas correspond to the losses from the negative and positive electrode, respectively. The shaded areas in light blue and red correspond to the data shown previously in Figure 3.4c. (b) Positive and negative electrode overpotentials measured at each current density.

than the positive overpotential at all applied current densities and the plot of the negative overpotential has shifted significantly to the left compared to that observed in the methanesulfonate-only electrolyte (Figure 3.5a). For example, the negative overpotential with the methanesulfonate-only electrolyte is ~ 0.1 V at 25 mA cm^{-2}, but drops to ~ 0.043 V at the same current density when the mixed negative electrolyte is employed.

The above results demonstrate the significant reduction in the voltage loss arising from the negative half-cell in the mixed methanesulfonate-chloride solution. In order to confirm that this effect is due to the enhanced kinetics of the zinc redox reaction, the kinetics of the Zn/Zn(II) reaction is investigated by fitting the Butler-Volmer equation (Equation 3.6) to the experimental electrode potentials similar to that done previously. Figure 3.7 shows the experimental and fitted results for a plot of the dependence of the current density

on the negative electrode potential in the mixed methanesulfonate-chloride electrolyte. This fitting procedure yields an exchange current density for zinc oxidation of $\sim$ 53.4 mA cm^{-2} , which is significantly higher than the exchange current density found previously for Zn/Zn(II) in the methanesulfonate-only negative electrolyte. This confirms that the reduction in the voltage losses due the negative half-cell is indeed due to the enhanced kinetics of the zinc redox reaction. This result is also consistent with that of our half-cell study shown later in Chapter 5 on mixed methanesulfonate-chloride electrolytes which shows that the exchange current density for the Zn/Zn^{2+} redox couple rises as the chloride concentration is increased.

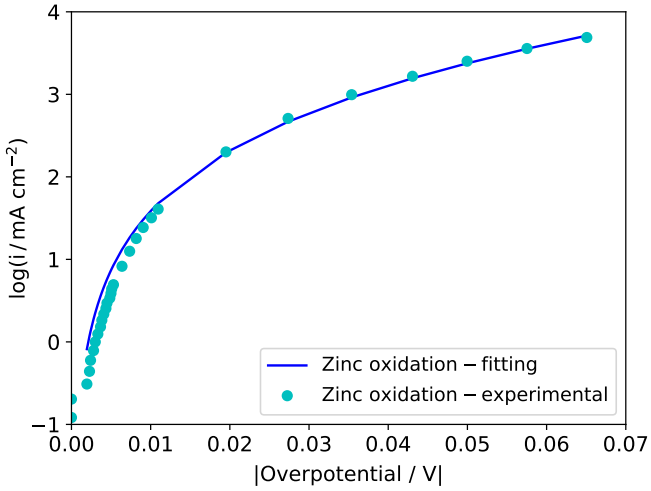

Figure 3.7: Semi-log plot of current density versus overpotential measured at the negative electrode with mixed methanesulfonate-chloride electrolyte during full-cell polarization tests at 50% SOC, 50°C and flow rate of $\sim$ 65 mL min^{-1} while using Ag/AgCl reference electrodes. The dots show the experimental data. The solid line shows the results obtained by fitting the Butler-Volmer equation to the experimental data.

3.3.4 Effect of electrolyte flow rate

As shown in section 3.3.2, mass transfer effects particularly on the positive side make a significant contribution to the overall voltage loss in the Zn-Ce RFB in addition to the kinetic overpotential on the negative side particularly at high current densities. Since the electrolyte flow rate affects the supply of ions to and from the electrode, the cell discharge

voltage is expected to rise in the mass transfer region when the battery is operated at a higher flow rate. Figure 3.8 compares the full-cell battery polarization curves along with the positive and negative electrode potentials achieved at flow rates of 45, 65 and 85 mL min^{-1}.

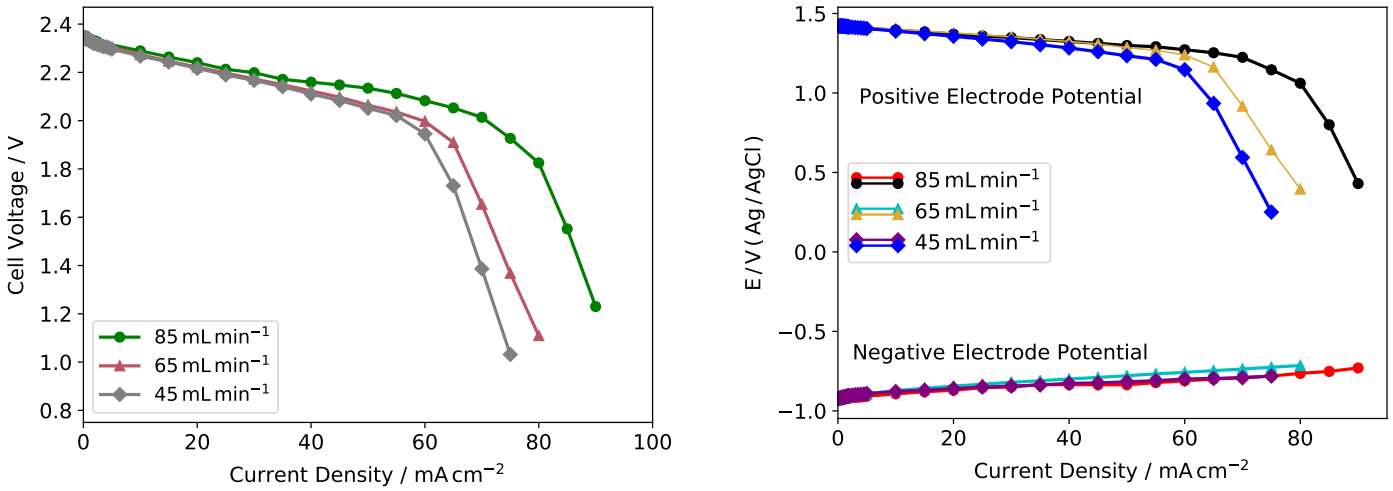

(a) (b)

Figure 3.8: (a) The IR-free cell discharge voltage of battery operated at flow rates of 45, 65 and 85 mL min^{-1} at 50% SOC and 50°C. (b) Variation of positive and negative electrode potentials versus Ag/AgCl reference electrodes with current density monitored *in situ* during full-cell polarization at flow rates of 45, 65 and 85 mL min^{-1}.

As shown in Figure 3.8a, a larger cell voltage is attained in the mass-transfer region when the battery is discharged while operating at the higher flow rate. For example, at 75 mA cm^{-2}, a cell voltage of $\sim$ 1.93 V is achieved at 85 mL min^{-1}, which is 900 mV and 560 mV larger than the values of $\sim$ 1.03 V and $\sim$ 1.37 V obtained when flow rates of 45 and 65 mL min^{-1} are used, respectively. From Figure 3.8b, we confirm that the increase in battery discharge cell voltage at the higher flow rate is rooted in the enhanced mass transfer of dissolved cerium on the positive side since the increase of the flow rate raises the positive electrode potential at high current densities, but has virtually no effect on the negative electrode potential. This result is consistent with that of section 3.3.2 where a significant portion of the voltage loss was shown to be attributable to the cerium half-cell at high current densities. As discussed previously, the positive electrode used in this study

is a platinized-titanium (Pt-Ti) expanded mesh. A previous study has shown that the use of a Pt-Ti micromesh or a Pt-Ti felt electrode on the positive side improves mass transfer rates and leads to higher limiting current densities [103].

3.4 Conclusions

The contributions of the kinetic, ohmic and mass transfer overpotentials to the overall performance loss during discharge of a Zn-Ce redox flow battery have been resolved by conducting *in situ* polarization and EIS experiments on a bench-scale single-cell Zn-Ce RFB. The largest contributors to the performance loss of the battery at low and intermediate current densities are the kinetic overpotentials. At a current density of 25 $\mathrm{mA\,cm^{-2}}$, the kinetic and ohmic overpotentials resulted in losses of ~ 0.14 V and ~ 0.11 V, respectively, of the cell voltage from the OCV. Additionally, mass transfer limitations at high current densities result in a steep drop in the cell discharge potential. By insertion of two Ag/AgCl reference electrodes in the battery setup, the contribution of each electrode to the overall voltage loss was analyzed. This analysis revealed that the kinetic losses at the zinc negative half-cell are responsible for most of the voltage drop at low and intermediate current densities, while limitations to the mass transfer of Ce(IV) and/or Ce(III) on the positive side are the main reasons for the sharp potential drop at high current densities.

The exchange current densities for zinc oxidation and cerium reduction during discharge were estimated by fitting the Butler-Volmer equation to the measured potentials of the individual electrodes at low overpotentials. The exchange current density for zinc oxidation was estimated to be ~ 7.4 $\mathrm{mA\,cm^{-2}}$, while the corresponding value for cerium reduction was found to be ~ 24.2 $\mathrm{mA\,cm^{-2}}$. The lower exchange current density for zinc oxidation confirmed that the slower kinetics of the negative half-cell limited the battery performance at low and mid-range current densities.

The experiments were repeated for an alternative mixed methanesulfonate-chloride negative electrolyte, which will be shown later in Chapters 5 and 6 to improve battery performance. The results obtained with this mixed electrolyte showed a significant enhancement in the exchange current density for zinc oxidation to ~ 53.4 $\mathrm{mA\,cm^{-2}}$ and a large shift in the overpotentials on the negative side to lower values as a function of current density. In addition, we showed that mass transfer on the positive side was improved by increasing the flow rate of both electrolytes through the battery, resulting in a higher cell discharge voltage in the mass-transfer limiting region.

Chapter 4

Life-Cycle Analysis of Zinc-Cerium Redox Flow Batteries[1]

4.1 Introduction

In order to pinpoint the cause of battery capacity fade, the evolution of the performance of the negative and positive redox reactions over the course of the battery life-cycle must be monitored. As shown in the previous chapter, the negative and positive electrode potentials of an RFB can be monitored *in situ* by inserting reference electrodes on each side of the cell. In addition to monitoring the half-cell potentials and full-cell voltage of the battery, valuable information can also be extracted by measurement of the changes in the negative and positive electrolyte compositions over the course of the cycles. As mentioned earlier, the electrolyte solutions in RFBs are stored in separate external reservoirs and pumped into the cell during operation. Thus, the electrolytes are accessible for measurement throughout RFB operation. In all-vanadium RFBs, the V(IV) concentration has been determined by potentiometric titration using a potassium permanganate solution to measure the SOC of the battery during operation [125, 126]. *In situ* monitoring of Ce(III) and Ce(IV) concentrations was carried out in a batch electrochemical system involving a Ce(III)/Ce(IV) redox couple by colorimetric titration with pure ammonium iron(II) sulfate hexahydrate to determine the Ce(III)/Ce(IV) equilibrium potential as a function of their concentrations and reaction rate constants [127]. In the case of the zinc-cerium system, the concentration of Ce(IV) was measured by the same method (colorimetric titration with pure ammonium iron(II) sulfate hexahydrate) at the end of a single charge-discharge cycle

[1] This chapter is adapted from my published work [124].

to determine the conversion rate at the positive electrode [12]. Although knowledge of the change in the acid concentration on one or both sides of a zinc-cerium RFB over the course of its life would be useful, no such measurements have been reported to date.

In the previously reported life-cycle analyses of zinc-cerium RFBs, the battery was subjected to a number of charge/discharge cycles until the capacity of the battery faded and no useful discharge could be achieved. However, to the best of our knowledge, the potential of each electrode has not actually been monitored over the entire battery life-cycle to identify which half-cell limits its capacity during the course of operation and to directly relate this to performance degradation and failure. In this current study, our aim is to measure and analyze the negative and positive half-cell electrode potentials over the entire life-cycle of a zinc-cerium RFB in order to identify the role of the negative and positive redox reactions in the capacity fade of the battery. Additionally, we monitor the change in the proton concentration in the negative electrolyte and Ce(IV) concentration in the positive electrolyte during the cycles by titration. The proton concentration is measured using colorimetric titration following a procedure described in a previous study [128]. It is important to emphasize that the focus of the present work is to closely analyze the half-cell electrode potentials over the battery life-cycle and not to maximize the lifetime of the battery. This information is useful for identifying future research directions aimed at enhancing the zinc-cerium RFB life-cycle. Based on our experimental results, we conclude that the use of anion exchange membranes would be preferable to that of conventionally employed cation exchange membranes. Accordingly, we also describe the results of experiments using a number of commercially available anion-exchange membranes in our RFB and report on the resulting battery performance.

4.2 Experimental

4.2.1 Reagents

Zinc(II) methanesulfonate solutions for use on the negative side of the battery were prepared by mixing high purity zinc oxide (Zochem Inc.) with 70% methanesulfonic acid (Alfa Aesar) in appropriate amounts to form a colorless solution with no precipitates. Cerous methanesulfonate used in the positive side of the battery was prepared by mixing 99% pure cerium(III) carbonate (Treibacher Industrie AG) with 70% methanesulfonic acid in proper quantities, also resulting in a colorless solution free of precipitates. In all cases, ultra-pure water with resistivity of $\approx 18\ \mathrm{M\Omega\,cm}$ was used.

To determine the concentration of protons in the negative electrolyte, samples were titrated colorimetrically with a standard solution of sodium hydroxide (Fisher Scientific) until the end-point indicated by methyl red (Ricca Chemical) was reached. Although the negative electrolyte also contains hydrolyzable zinc ions which can potentially interfere with the proton titration, a previous study on the determination of the free acid concentration in the presence of metal ions revealed that this interference is minimal and that the presence of zinc(II) ions does not affect the location of the end-point [128]. As a check, the pH was measured during each titration. As expected, it was found to sharply rise at a point that closely coincided with the observed color change during the titration. In order to determine the Ce(IV) concentration in the positive electrolyte, the positive electrolyte was titrated with 99% pure ammonium iron(II) sulfate hexahydrate (Sigma-Aldrich) using ferroin (1,10-phenanthroline iron(II) sulfate) (Alfa Aesar) as a colorimetric redox indicator. To monitor the change in the concentration of protons and Ce(IV) during the multi-cycle experiments, 0.2 cm^3 samples were collected from the negative and positive electrolytes after each charge/discharge cycle and used for titration. Such small samples were removed in order to minimize the cumulative loss of electrolyte volume in the reservoirs over the course of these experiments. The effect of this volume change was taken into account when determining the proton and Ce(IV) concentrations.

4.2.2 Battery setup and operation

A bench-scale single-cell zinc-cerium redox flow battery composed of a 6 mm-thick polyvinyl ester (PVE) carbon (TDM Fuel Cells) negative electrode, two 6 mm-thick acrylic flow channels (acrylic sheets from CIP Wholesale), a three-dimensional platinized titanium mesh positive electrode with a Pt loading level of 7 mg cm-2 (Metakem GmbH), a copper current collector (McMaster-Carr), four rubber silicone gaskets (CS Hyde Company) and a membrane was constructed, as shown in Figure 4.1. The following membranes were tested in the battery: i) cation exchange - Nafion 117 (Fuel Cell Store) and ii) anion exchange - Selemion AMV-N, ASV-N, AAV (hydrocarbon-based membranes purchased from Bellex International Corporation) and Fumatech FAPQ-375-PP, FAP-375-PP and FAP-450 (fluorinated-based membranes purchased from the Fuel Cell Store). Both the positive and negative electrodes had an apparent active surface area of 2 cm $\times$ 4.5 cm.

The negative and positive electrolytes in their fully discharged state contained 1.5 $mol\,dm^{-3}$ zinc methanesulfonate in 1 $mol\,dm^{-3}$ methanesulfonic acid and 0.8 $mol\,dm^{-3}$ cerous methanesulfonate in 4 $mol\,dm^{-3}$ methanesulfonic acid, respectively. The electrolytes were pumped from two external 30 cm^3 tanks using a model BT100-1L Longer peristaltic

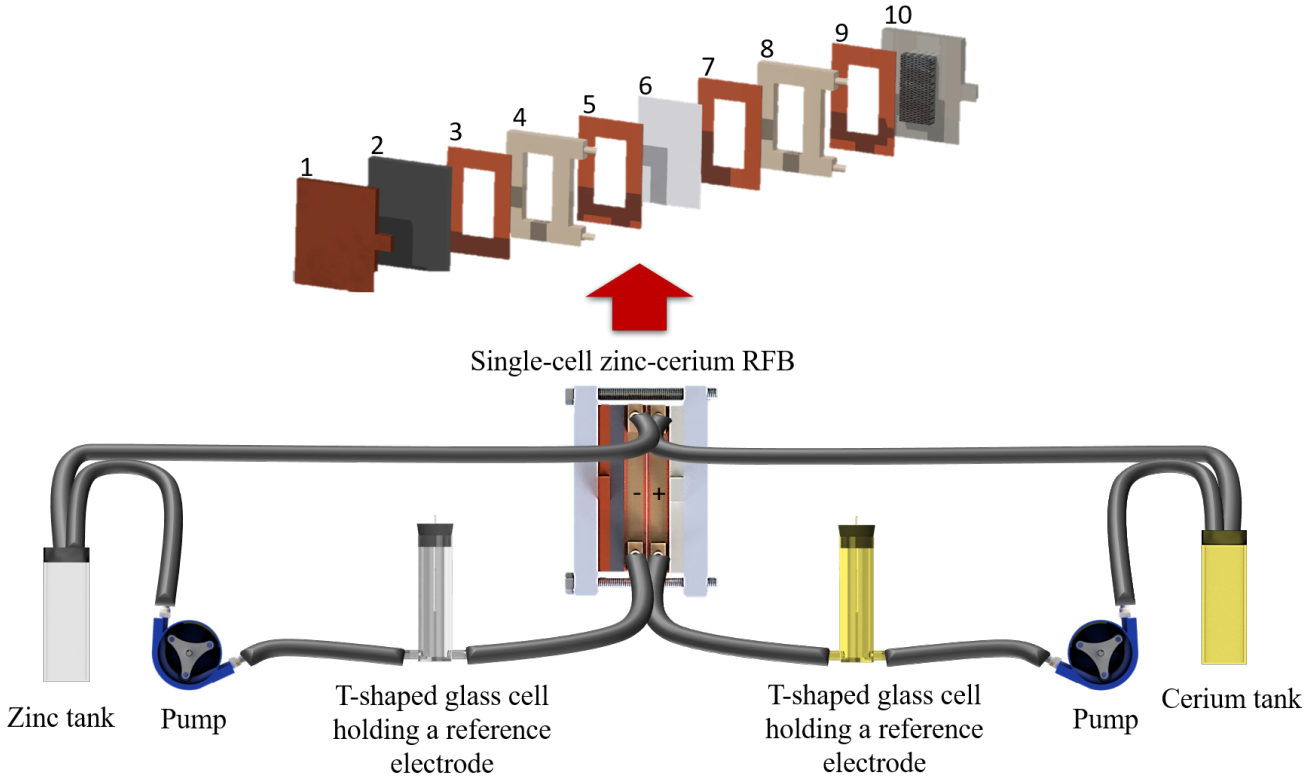

Figure 4.1: Components of the battery setup used in this study. The electrochemical cell consists of: copper current collector (1), PVE negative electrode (2), silicone rubber gaskets (3, 5, 7, 9), acrylic flow channels (4, 8), membrane (6) and positive platinised titanium mesh electrode (10).

pump with two channel heads (model YZ1515) and Viton tubing (McMaster-Carr). Previous experiments with our battery set-up showed that the highest charge efficiencies were achieved if the electrolyte flow rate was set to 60-70 mL min^{-1}. Consequently, an electrolyte flow rate of 65 mL min^{-1} was used throughout this study. A temperature bath (Neslab RTE-8) was employed to maintain the electrolyte temperature at 50°C or 40°C throughout the experiments. The Nafion 117 membrane was pre-treated before each experiment by soaking in the following sequence of solutions: 3 wt.% H_2O_2, DI water, 0.5 mol dm^{-3} H_2SO_4 solution and DI water again each for the duration of 1 hr at 80°C. Based on the manufacturer recommendations, the anion exchange membranes were used as received without any pre-treatment.

The negative and positive electrode potentials were monitored *in situ* during battery operation by placing two Ag/AgCl reference electrodes (Pine Research Instrumentation) close to the inlets of flow frames on each side of the battery by using two custom-made T-shaped glass cells, as shown in Figure 7.1. The reference electrode on the negative side was in direct contact with the circulating zinc solution. On the other hand, a Nafion barrier was used on the positive side between the reference electrode and the circulating positive electrolyte since cerium ions were found over time to diffuse through the ceramic frit of the Ag/AgCl reference electrode into the inner chamber and damage it. The placement of the reference electrode inside a hollow cylindrical holder sealed with a Nafion membrane provided a barrier between the reference electrode and cerium species and prevented the diffusion of cerium ions into the reference electrode. This holder was filled with a 4 mol dm^{-3} MSA solution, which is the same concentration of MSA in the positive electrolyte, but without cerium. The potential drop across this Nafion membrane barrier against cerium was measured to be only $\approx 8 \times 10^{-4}$ V. Since the electrode potentials measured in our experiments were all larger than 0.5 V, this value is considered to be negligible.

An Autolab PGSTAT 30 was used to galvanostatically cycle the battery at current densities of 25 or 50 mA cm^{-2}. The battery was charged for the duration of 1 hour during each cycle and discharge was terminated when the cell voltage dropped to the cut-off value of 0.5 V. At each cycle, the charge efficiency was determined from the ratio of the discharge capacity to the charge capacity and the voltage efficiency was calculated as the ratio of the average cell voltage measured during discharge to the average cell voltage measured during charge.

4.3 Results and Discussion

4.3.1 Life-cycle analysis with *in situ* reference electrodes

Figure 4.2a shows the charge/discharge profiles obtained for the battery operating with a Nafion 117 membrane over cycles having charge times of 1 hr at 25 mA cm^{-2} and 50°C. The charge/discharge experiment was able to continue for a maximum number of 12 cycles before it was no longer possible to satisfactorily discharge the battery, i.e. the charge efficiency dropped to less than 20%. The life-cycle of the battery strongly depends on both the charge duration and applied current density. For example, in previous analysis of zinc-cerium RFBs operating with the much shorter charge duration of 15 minutes, longer cycles of 57 at 50 mA cm^{-2} [12] was reported. Furthermore, at a given current density, the life-span and maximum number of cycles of the battery also depend on the ratio of the

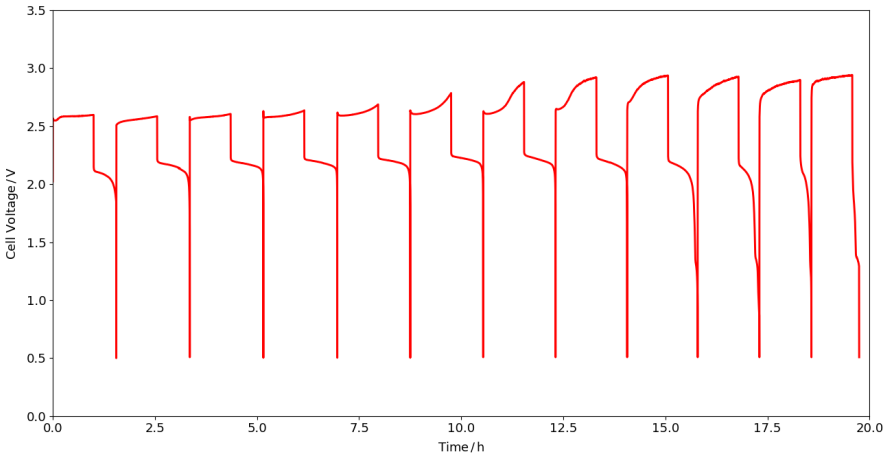

(a)

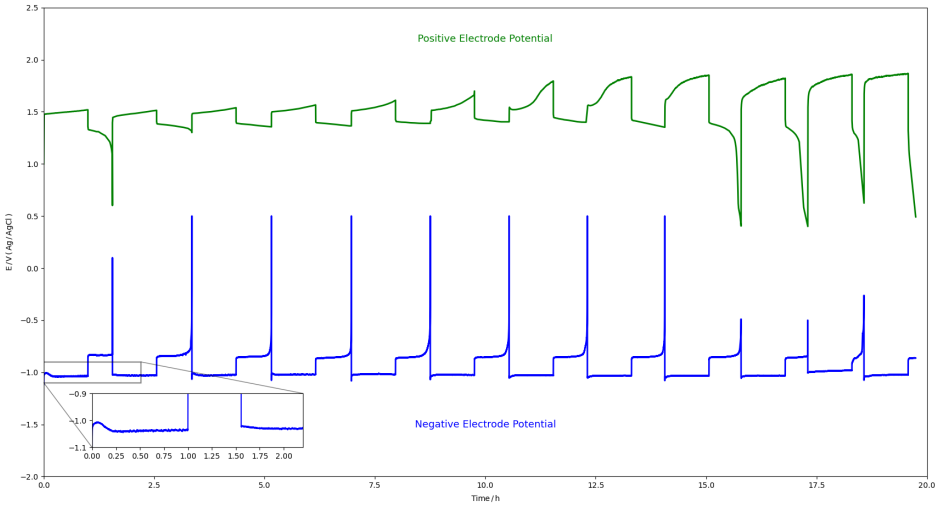

(b)

Figure 4.2: Performance of a zinc-cerium RFB operating with 30 cm^3 of 1.5 mol dm^{-3} zinc methanesulfonate negative electrolyte in 1 mol dm^{-3} methanesulfonic acid and 30 cm^3 of 0.8 mol dm^{-3} cerous methanesulfonate in 4 mol dm^{-3} methanesulfonic acid positive electrolyte separated by a Nafion 117 membrane. (a) Charge-discharge profiles at 25 mA cm^{-2} and 50°C with a 1-hour charge duration. (b) Corresponding potentials of the positive and negative electrodes measured versus Ag/AgCl reference electrode during the battery operation shown in (a). (Inset, Figure 4.2b) Zoomed image of the response of the negative electrode during the first cycle to highlight the delay in attaining a stable electrode potential.

electrolyte volume to the surface area of each electrode. The larger this ratio, the greater is the maximum number of cycles before failure occurs [12, 122]. In this experiment, we deliberately use a long charge duration of 1 hr and a relatively small volume of 30 cm^3 in order to reduce the number of cycles required for battery failure since the point of the study is to investigate and more clearly delineate the phenomena that cause battery failure. The average charge and discharge cell voltages, charge and voltage efficiencies measured during each cycle are listed in Table 4.1. Note that the voltage efficiencies achieved in this work at 25 $mA\,cm^{-2}$ are higher than that obtained and reported in our other work at the same current density [122] since we reduced the ohmic resistance in the battery by providing better electrical connections in the system. Figure 4.2b presents the corresponding positive and negative electrode potentials relative to the Ag/AgCl reference electrode monitored *in situ* during the same battery operation presented in Figure 4.2a. The limiting redox reaction during each cycle can be determined from Figure 4.2b by identifying which electrode potential changes rapidly at the end of discharge. The limiting reaction identified during each cycle is also included in Table 4.1. With the combined information provided in Figures 4.2a and 4.2b, the role of each half-cell in the battery performance loss can be closely monitored.

As indicated in Figure 4.2b, both the negative and positive electrode potentials change sharply at the end of the first discharge cycle, suggesting that the negative and positive redox reactions jointly limit the battery performance at this point during operation. In the positive half-cell, the electrode potential decreases gradually throughout much of the first discharge cycle before dropping very sharply at the very end. A sharp change in the potential of one of the electrodes at the end of a galvanostatic cycle can be an indication that the corresponding electrolyte has become completely or nearly depleted of a reactant for the electrode reaction that is occurring. However, our titration data presented later in Figure 4.3 reveal that 0.12 $mol\,dm^{-3}$ Ce(IV) still remain in the bulk positive electrolyte at the end of the first discharge cycle despite the fact that the positive electrode potential has dropped sharply. This sharp change in potential is likely caused by either mass transfer or kinetic limitations arising from depletion of the bulk Ce(IV) concentration as discharge continues (both kinetics and mass transfer rates are dependent upon reactant concentration). In a previous study on an all-vanadium RFB, it was also reported that the depletion of the bulk concentration of the reactant species as discharge continues could result in mass transfer limitations and consequently a sharp drop in the battery discharge cell voltage [129]. For reasons that will be discussed later, the concentration of Ce(IV) is higher at the end of each discharge during subsequent cycles and the reduction of Ce(IV) is no longer the limiting redox reaction in the system.

On the negative side, the rise in the electrode potential at the end of the first discharge

cycle can be attributed not to this part of the cycle but to what occurred during the first charge. Since zinc is deposited onto a bare PVE surface at the start of the initial charge cycle, an additional barrier that must be overcome by this reaction is a nucleation overpotential that makes it easier for the hydrogen evolution side reaction to compete and decreases the amount of metal that can deposited. Since hydrogen evolution is not reversible, only zinc oxidation contributes to discharge at this electrode and the portion of the current that hydrogen evolution consumes leads to a loss in the overall discharge capacity of the battery. It appears that at about the same point in time during the subsequent discharge when Ce(IV) reduction on the positive side becomes limited, enough zinc deposit has been stripped from the negative electrode that its electrode potential shifts sharply in the positive direction in search of a second anodic reaction to accommodate the demand for current.

Table 4.1 also shows that the first cycle exhibits lower charge and voltage efficiencies than those that immediately follow. This is also immediately evident from Figure 4.2b where the discharge time is noticeably shorter during the first cycle than during subsequent ones. A similar improvement in battery performance after the initial cycles has been reported in previous life-cycle studies on zinc-cerium RFBs [12,122] and can be observed in other zinc-based batteries [130,131]. A galvanostatic cycling study of the Zn/Zn(II) redox reaction on a carbon composite electrode at an applied current density of 25 $\mathrm{mA\,cm^{-2}}$ in an MSA solution found that the electrode potential of a zinc electrode during charge quickly attains a stable value except during the first cycle and that the charge efficiency was lower in the first cycle than in the cycles that immediately followed [93]. Additionally, in a previous study on the electrodeposition of zinc onto different substrates in a rechargeable zinc alkaline battery, the HER was found to occur to a larger extent during the first cycle than subsequent ones [130]. Similarly, our results show that the zinc electrode potential during charge attains a stable potential after $\approx$ 10 minutes in the first cycle, whereas it almost immediately stabilizes during subsequent cycles. The delay in attaining a stable electrode potential during the initial charge is shown in the inset to Figure 4.2b. This delay in attaining a stable potential on the negative electrode in the first cycle should lower the resulting charge and voltage efficiencies associated with the Zn/Zn(II) reaction relative to the levels reached in the cycles that immediately follow. Note that the exchange current density of the HER is dramatically higher on a carbon substrate (6.8×10^{-4} $\mathrm{mA\,cm^{-2}}$ on vitreous carbon [132]) than on a zinc surface (3.16×10^{-8} $\mathrm{mA\,cm^{-2}}$ [133]). Thus, the HER would be expected to occur at a higher rate during the initial part of each charge cycle before a zinc layer covers the underlying carbon-based substrate.

From the second to the eighth cycle, only the potential of the negative electrode changes abruptly at the end of discharge, indicating that this reaction is now solely responsible for

the sharp decrease in the discharge cell voltage (Figure 4.2b). As noted above, the onset of hydrogen evolution lowers the discharge capacity of the battery, which limits the amount of Ce(IV) that can be reduced back to Ce(III) on the positive side. Also, since hydrogen evolution on the negative side consumes more current than the oxygen evolution side reaction on the positive side during each charge, the amount of zinc deposited continually falls below the stoichiometric amount expected if it were to keep pace with the amount of Ce(IV) produced. Since hydrogen evolution is not reversible, the discharge capacity becomes limited by the amount of zinc deposited during charge. This also throws the positive electrode reactions during charge and discharge out of balance and leads to the increase of the Ce(IV) concentration in the positive electrolyte from cycle to cycle. As can be seen in Figure 4.2a and Table 4.1, this change is accompanied by the continual rise in the cell voltage during charge, particularly near the end of each cycle. Furthermore, this effect grows stronger from cycle to cycle. The average cell voltage increases from ≈ 2.58 V in the first cycle to ≈ 2.91 V in the final cycle. Figure 4.2b shows clearly that this increase in the charge cell voltage can be attributed entirely to the positive electrode potential since the negative electrode potential remains almost unchanged during charge. This rise in the electrode potential for the oxidation of Ce(III) to Ce(IV) becomes perfectly understandable in view of the continual build-up of the Ce(IV) concentration and the consequent reduction in the Ce(III) concentration from cycle to cycle.

As can be seen in Figure 4.2b, from the ninth cycle to the final cycle, the responses revert back to that of the first cycle where both the negative and positive electrode potentials change sharply at the end of discharge. As shown in Table 4.1, the charge efficiency of the battery drops gradually over the first 9 cycles, but then drops much more steeply over the last 4 cycles. In the final cycle, the cerium electrode potential drops by ≈ 1 V immediately at the start of discharge, resulting in a very low charge efficiency and termination of the battery life. In order to gain further insight into the behavior of the system just prior to the battery failure, we carried out a separate set of experiments in which the charge/discharge experiment shown in Figure 4.2 was repeated, but now measured the Ce(IV) and H^+ concentrations remaining in the positive and negative electrolytes, respectively, after each charge/discharge cycle by titrimetric analysis. This entailed the removal of 0.2 cm^3-volume samples from each electrolyte after each cycle. Thus, the volume of each electrolyte was reduced by a total of 2.4 cm^3 (or 8% of the volume of each electrolyte) by the end of the battery life. The battery performance over this life-cycle was found to be the same as that shown in Figure 4.2 when no electrolyte was removed for titrimetric analysis, indicating that the reduction of electrolyte volume to carry out the titrations had no effect on the behavior of the system.

Figure 4.3 presents the Ce(IV) concentration measured in the positive electrolyte after

Table 4.1: Average charge and discharge cell voltages and charge and voltage efficiencies extracted from Figure 4.2a at each cycle. The limiting redox reaction at each cycle is also determined from Figure 4.2b.

Cycle number	Average charge voltage (V)	Average discharge voltage (V)	Voltage efficiency (%)	Charge efficiency (%)	Limiting Redox Reaction
1	2.58	2.06	80	56	Both
2	2.56	2.14	84	80	Zinc
3	2.58	2.17	84	80	Zinc
4	2.60	2.18	84	81	Zinc
5	2.62	2.19	84	79	Zinc
6	2.65	2.21	83	79	Zinc
7	2.70	2.20	82	77	Zinc
8	2.80	2.17	78	75	Zinc
9	2.85	2.04	72	73	Both
10	2.85	1.91	67	51	Both
11	2.84	1.90	67	27	Both
12	2.91	1.59	54	17	Cerium

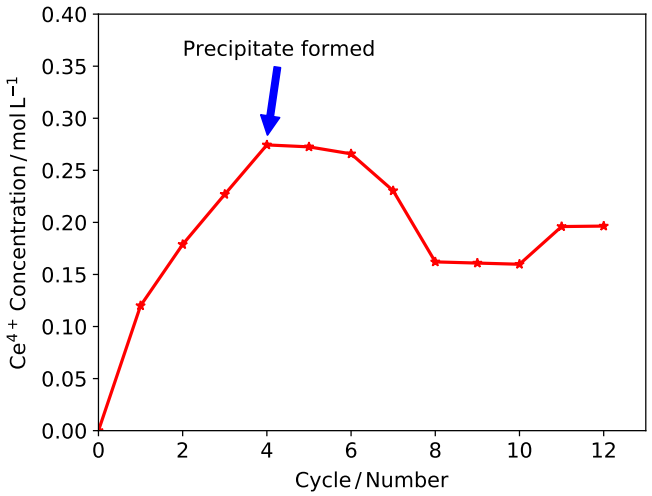

Figure 4.3: Concentration of Ce(IV) after each cycle shown in Figure 4.2a obtained from titration.

each charge/discharge cycle. The Ce(IV) concentration continually grows to a maximum of 0.26 mol dm^{-3} over the first 4 cycles, which confirms the accumulation of Ce(IV) on the positive side due to the limiting amount of zinc deposit formed on the negative electrode that terminates discharge prematurely, as explained previously. As indicated in Figure 4.3, the appearance of particles in the positive compartment presumably due to the precipitation of Ce(IV) is first observed to occur at some point during the fourth cycle. Moreover, the amount of precipitate visible in the positive electrolyte continues to grow over the subsequent cycles. After the fourth cycle, the soluble Ce(IV) concentration remains unchanged before dropping and leveling off between 0.15 and 0.2 mol dm^{-3} for the remainder of the battery life. These trends in the Ce(IV) concentration are governed by the Ce(IV) solubility and precipitation of Ce(IV). Precipitation of Ce(IV) during the charge-discharge cycling of zinc-cerium RFBs has also been reported in a number of previous studies [89, 134, 135]. Nikiforidis [89] reported the precipitation of cerium on the positive side of the zinc-cerium RFBs upon prolong battery cycling, although he could not confirm the exact crystal structure of the precipitate by XRD since it did not correlate with the available literature data for either CeO_2 or Ce_2O_3. Kreh et.al [134] reported that the Ce(IV) solubility depends strongly on the MSA concentration and increases with acid concentration. In solutions that originally contained 1.8 mol dm^{-3} Ce(III) in a relatively low MSA concentration of 1 mol dm^{-3}, the authors observed the formation of a solid yellow precipitate with the structure of $Ce(CH_3SO_3)_2(OH)_2H_2O$ after enough Ce(III) was oxidized to Ce(IV). In our present study, the initial concentration of MSA of 4 mol dm^{-3} in the positive electrolyte was high enough to ensure that all of the Ce(IV) and Ce(III) remain soluble at the start of the cycles. Nevertheless, after a few cycles, a yellow precipitate of Ce(IV) was observed. As reported in prior research [134], the concentration of Ce(III) and Ce(IV) largely depends on the acid concentration with Ce(III) being more soluble at low acid concentrations and Ce(IV) at higher acid concentration. Thus, one reason contributing to the precipitation of Ce(IV) could be related to change in the acidity of the positive half-cell. In order to confirm this effect, we titrated a sample of the negative electrolyte after each cycle to determine the H^+ concentration in the negative electrolyte.

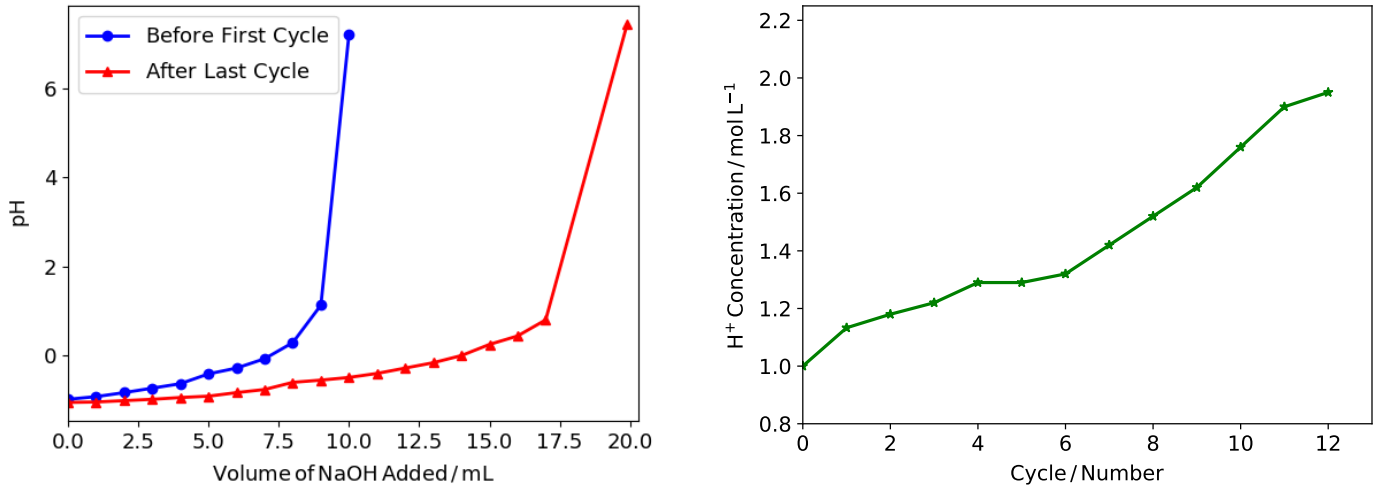

(a) (b)

Figure 4.4: (a) pH titration curve obtained from the negative electrolyte solution before the first cycle (fresh solution) and after the last cycle. (b) H^+ concentration measured by titrating a sample from the negative electrolyte after each complete charge/discharge cycle shown in Figure 3.2.

Figure 4.4a shows a comparison between the pH titration curves obtained for a fresh negative solution containing 1.5 mol dm^{-3} zinc methanesulfonate in 1 mol dm^{-3} methanesulfonic acid before the cycling experiment and after the last cycle. As can be seen, the volume of the NaOH needed for neutralization has almost doubled. Figure 4.4b presents the acid concentration on the negative side of the battery obtained from titration after each cycle. The results clearly demonstrate the significance of H^+ transport and the enhancement in the H^+ concentration on the negative side of the battery over the course of the cycles. The H^+ has increased to $\approx$ 2.0 mol dm^{-3} by the last cycle from the initial concentration of 1.0 mol dm^{-3}.

The increased concentration of protons on the negative side and thus dilution of the acidity on the positive half-cell can be attributed to a combination of several phenomena. In order to maintain electroneutrality, H^+ ions are drawn from the positive side to the negative side during charge to balance the consumption of cations at the negative electrode and the conversion of Ce(III) to Ce(IV) at the positive electrode. Obviously, H^+ are driven in the opposite direction during discharge. However, because more coulombs are passed during charge than discharge in each cycle, this results in the net transfer of H^+ into the negative

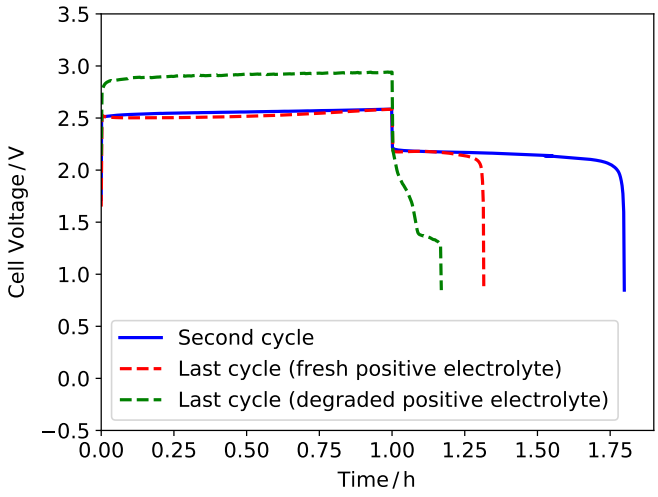

Figure 4.5: Charge/discharge cycle of the battery at the end of its life-cycle with fresh positive electrolyte replacing the degraded one (dashed line) compared with the charge/discharge cycle curve of the second cycle (solid line).

electrolyte over each cycle. Secondly, a large proton concentration difference exists between the negative and positive half-cells of the battery. The negative electrolyte initially contains only 1.0 mol dm^{-3} MSA to minimize hydrogen evolution while still providing sufficient ionic conductivity. This is the optimum value found for the negative electrolyte composition based on prior studies [12]. On the positive side, however, an optimum concentration of 4 mol dm^{-3} MSA [12] is necessary to ensure that all of the Ce(IV) and Ce(III) remain soluble. This large concentration difference serves as a strong driving force for the diffusive transport of H^+ from the positive compartment to the negative compartment of the battery. Additionally, the ionic strength of the negative electrolyte is initially $\approx$ 5.5 mol dm^{-3} which is lower than the level of $\approx$ 8.8 mol dm^{-3} estimated for the positive electrolyte. The resulting osmotic pressure difference between these two electrolytes leads to the transfer of water from the negative side to the positive side of the battery, as has been observed in vanadium RFBs [136]. All of these effects lead to the increase in proton concentration on the negative side and dilution of the acid concentration on the positive side.

As shown in Figure 4.2 and Table 4.1, the Ce(III)/Ce(IV) redox reaction is solely limiting during the very last cycle and the battery fails due to the large accumulation and precipitation of Ce(IV). Nevertheless, it should be realized that the performance in the negative half-cell is also severely degraded due to the increased proton concentration and

in turn higher rate of HER. This has been demonstrated in a separate experiment in which the degraded positive electrolyte is replaced with a fresh positive solution containing 4 mol dm^{-3} MSA that contains no precipitate at the start of the 12$^{\text{th}}$ charge-discharge cycle (also the final cycle before failure). Figure 4.5 shows the charge/discharge voltage response of the battery during this final cycle. Also included for comparison is the response during cycle 2 when the charge efficiency is still high and the response during the last cycle in the case when the degraded positive electrolyte is not replaced with a fresh one. As can be seen, even with a fresh positive electrolyte in which Ce(III) is not depleted and no build-up of Ce(IV) and precipitation have occurred, the charge efficiency of the system is still severely limited. This can only be due to the excessive H^+ concentration and resulting HER on the negative side. On the other hand, the voltage efficiency is not strongly affected. Thus, the problems arising from enhanced proton concentration on the negative side and thus dilution of acid concentration on the positive side are two-fold: enhancement of the rate of HER side reaction at the negative electrode and the precipitation of Ce(IV) in the positive electrolyte.

The analysis in this section gives a fuller picture of the reasons behind the performance loss and eventual failure of the battery. At a current density of 25 mA cm^{-2} and 50°C and prior to the last few cycles, the charge efficiency of the battery is limited solely by the zinc redox reaction at the negative electrode. The conversion of Ce(IV) to Ce(III) during the discharge phase is cut short by the amount of zinc deposit that can be oxidized and thus Ce(IV) accumulates in the positive half-cell as confirmed by the titration data on the positive half-cell of the battery. The accumulation of Ce(IV) results in higher cell voltage during charge and loss of voltage efficiency. Additionally, the titration data on the negative compartment of the battery demonstrates the enhancement in the proton concentration. This leads to two further problems. Firstly, the increased acidity of the negative electrolyte results in an excessive rate of hydrogen evolution and reduction in the battery charge efficiency and secondly the dilution of the acid concentration on the positive side contributes to Ce(IV) precipitation. The combination of these two effects limits the battery performance and results in the eventual capacity fade of the battery.

4.3.2 Effect of applied current density and temperature on battery life-cycle

In the previous sections, the causes of the performance fade and ultimate failure of a zinc-cerium RFB operated at 25 mA cm^{-2} and 50°C were identified and explained. It is of interest to determine whether alteration of the operating current density and temperature

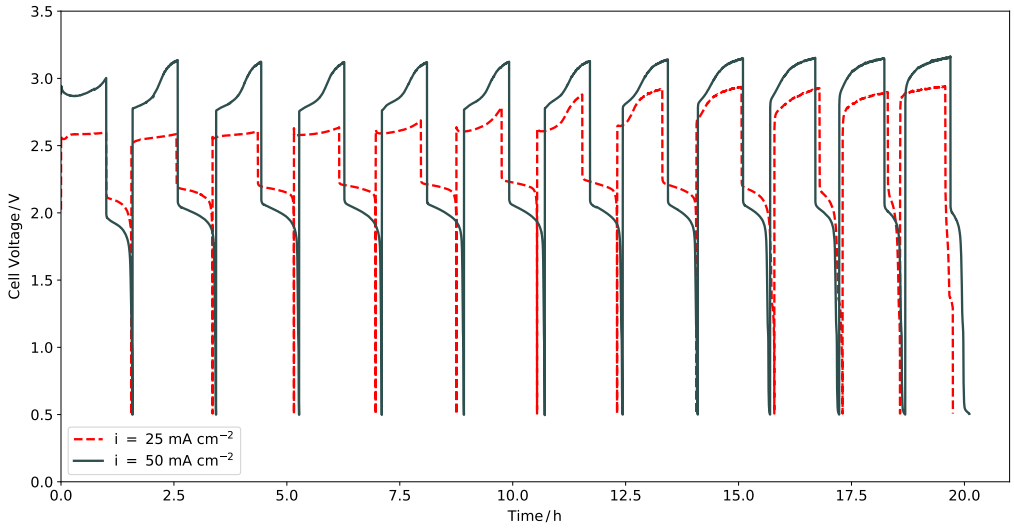

(a)

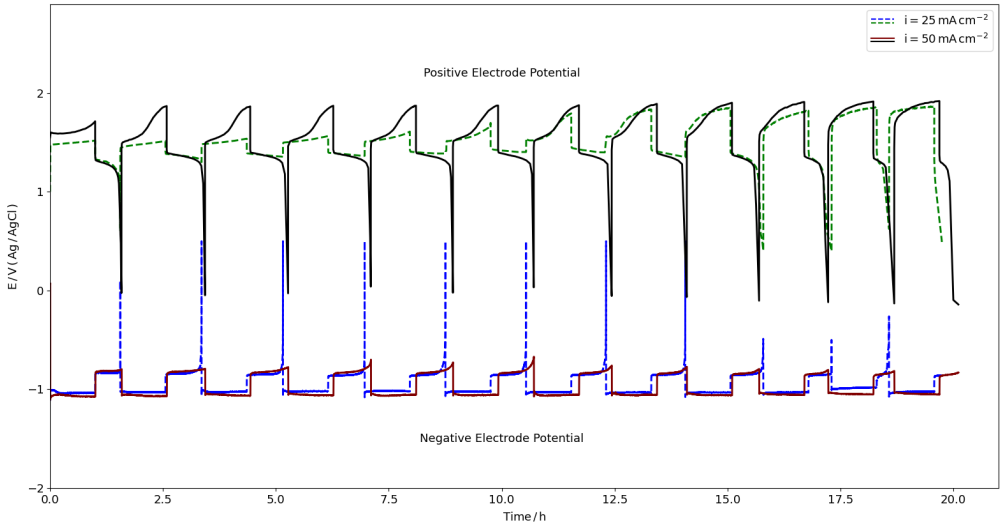

(b)

Figure 4.6: Charge-discharge profiles at current densities of 25 mA cm^{-2} and 50 mA cm^{-2} at 50°C. Charge duration is 1-hour per cycle in both cases. (b) Corresponding potentials of the positive and negative electrodes measured versus Ag/AgCl reference electrode during the battery operation shown in (a).

will affect the life-cycle of the battery and alter the role of each half-cell from that identified previously.

When the applied current density is increased two-fold to 50 mA cm^{-2}, the battery operates for the same number of cycles before it fails. At 50 mA cm^{-2}, the voltage efficiency decreases compared to that at 25 mA cm^{-2} due to the higher ohmic resistance in the battery. The average voltage efficiency over the 12 cycles at 50 mA cm^{-2} is $\approx$ 62%, whereas an average voltage efficiency of $\approx$ 77% is achieved at 25 mA cm^{-2}. The cell voltage and positive electrode potential in particular increase much more during charge, reflecting considerably more severe polarization at 50 mA cm^{-2} than at the lower current density, while the response of the negative electrode during charge remains largely unchanged by the change in current density. On the other hand, the average columbic efficiency over the 12 cycles improves slightly from $\approx$ 65% at 25 mA cm^{-2} to $\approx$ 67% at 50 mA cm^{-2}. Enhancement in the charge efficiency of the battery at higher current densities has also been reported in a previous galvanostatic study of a single charge-discharge cycle of zinc-cerium RFB [12]. The slightly larger charge efficiency at the higher current density of 50 mA cm^{-2} can be attributed to the differences in the effect of current density on the rates of zinc corrosion and zinc electrodeposition [137]. Since an increase in the applied current density tends to raise the rate of Zn(II) reduction relative to that of zinc self-discharge and corrosion [137, 138], such a change would be expected to raise the charge efficiency.

As shown in Figure 4.6, when the current density increases by two-fold to 50 mA cm^{-2}, the positive electrode potential drops sharply at the end of each discharge cycle throughout the battery life, whereas the negative electrode potential never rises sharply, showing that the system is now limited by the positive half-cell reaction rather than the zinc half-cell reaction. We believe that this stems from the stronger mass transfer influence on Ce(IV) reduction on the positive side at the high current density of 50 mA cm^{-2}. This is consistent with a previous polarization study of a zinc-cerium RFB containing a Pt/Ti mesh electrode operating at a current density of 50 mA cm^{-2} and flow velocity of 1.4 cm s^{-1} (close to 1.2 cm s^{-1} used in the current study) [103]. On the positive side, Ce(III) and Ce(IV) are both soluble species, while the reaction on the negative side during discharge involves the dissolution of solid zinc that is already attached to the surface of the electrode. Thus, mass transfer effects at high current densities should particularly affect the positive redox reaction. The combination of the higher polarization of the positive electrode during charge and discharge leads to a lower voltage efficiency of the battery at the higher current density. The proton concentration in the negative electrolyte at the end of the life-cycle of the battery operated at 50 mA cm^{-2} is measured by titration to be $\approx$ 1.9 mol L^{-1}, showing a significant increase in the proton concentration on the negative side, similar to the case of 25 mA cm^{-2} discussed previously. As observed previously at the lower current density,

cerium precipitation is observed in the positive compartment by the end of the life-cycle. Whereas the reactions at both electrodes are limiting throughout the battery life-cycle at the higher current density of 50 $\mathrm{mA\,cm^{-2}}$ (as opposed to zinc being the only limiting reaction when lower current density of 25 $\mathrm{mA\,cm^{-2}}$ is applied), the same combination of problems, i.e. precipitation of Ce(IV) in the positive electrolyte and large rise in the proton concentration in the negative electrolyte is responsible for the capacity fade of the battery.

When the operating temperature of the electrolyte is lowered from 50°C to 40°C at a current density of 25 $\mathrm{mA\,cm^{-2}}$, the charge and voltage efficiencies drop by $\approx 3\%$ and $\approx 7\%$, respectively. This is in line with a previous galvanostatic study of the zinc-cerium system conducted over one charge/discharge cycle, which showed that the battery charge efficiency is reduced at a lower temperature [12]. The decline in voltage efficiency can be attributed to the slower electrode kinetics and lower solution conductivity at the lower temperature. As shown in Figure 4.7, the zinc redox reaction is limiting during all the cycles at 40°C, as in the case of 50°C at the same current density, whereas the cerium redox reaction only limits the performance of the battery during the final cycles. Also, discharge is cut short by reduction in the amount of zinc deposit available for oxidation so that the positive electrolyte becomes increasingly depleted of Ce(III) as the cycling proceeds. The proton concentration measured at the end of the life-cycle of the battery operated at 40°C is $\approx 2\ \mathrm{mol\,L^{-1}}$, showing the similar rise in the acid concentration in the negative electrolyte observed previously. Note that the 1 $\mathrm{mol\,dm^{-3}}$ increase in the acid concentration at 40°C occurs after ≈ 24 hours while the same increase occurs after ≈ 20 hours of operation at 50°C. The battery is capable of operating for a little longer at 40°C, although the precipitation of Ce(IV) and significant increase in the acid concentration on the negative side remain the main problems associated with the capacity fade of the battery.

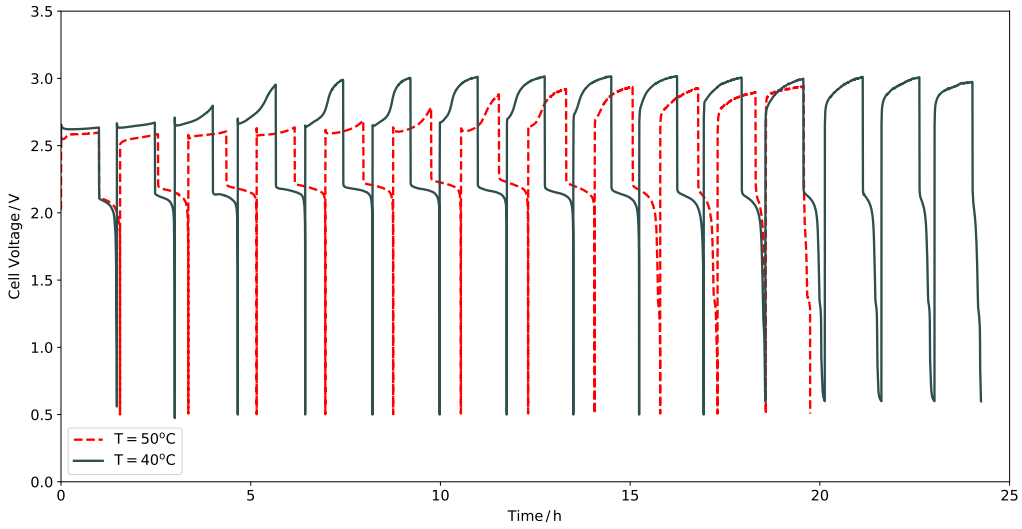

(a)

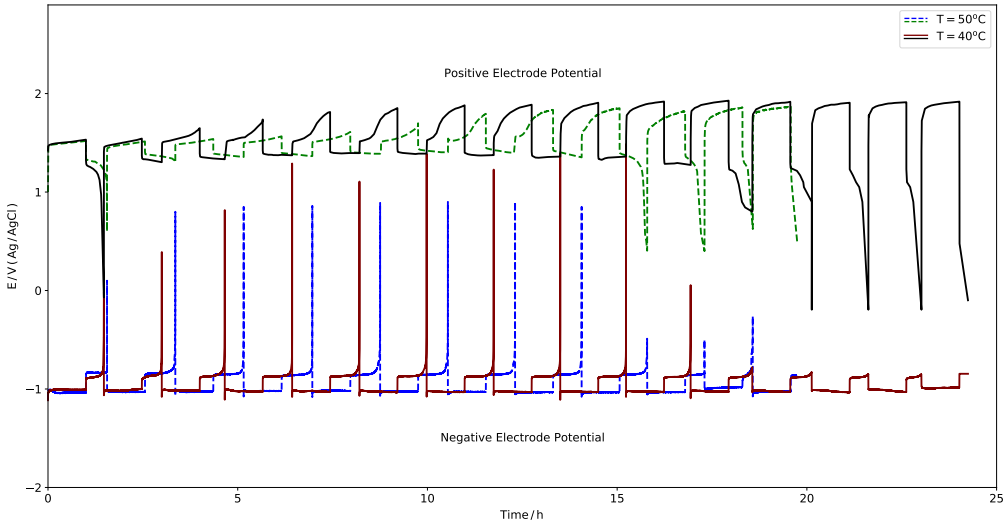

(b)

Figure 4.7: (a) Charge-discharge profiles at temperatures of 50°C and 40°C at 25 mA cm^{-2}. Charge duration is 1-hour per cycle in both cases. (b) Corresponding potentials of the positive and negative electrodes measured versus Ag/AgCl reference electrode during the battery operation shown in (a).

4.3.3 Anion exchange membrane

As has been discussed, mitigation of battery fade and failure requires suppression of the diminution of the acidity on the positive side and rise of the acidity and excessive hydrogen evolution on the negative side. As will be shown in the following chapters, one approach to reduce HER is to use an alternative negative electrolyte. We will show that by using a mixed methanesulfonate-chloride solution instead of methanesulfonic acid-only solutions on the negative side, the zinc charge efficiency increases significantly, which in turn reduces the rate of the Ce(III) depletion and extends the battery life-cycle. Furthermore, another problem due to mass transfer limitations observed in the previous sections can be reduced by employing electrodes with higher porosity, e.g., micromesh or felt Pt/Ti positive electrode, instead of the Pt/Ti mesh electrode employed in the present study [103]. In this section, we address the other problem stemming from the rise of the proton concentration in the negative electrolyte. Although the use of an alternative mixed electrolyte [122] promotes zinc deposition over hydrogen evolution, it could only reduce the extent and delay battery fade and failure. Accordingly, we evaluate the performance of a zinc-cerium RFB with a number of commercially available anion exchange membranes. To date, zinc-cerium RFBs have been operated using cation exchange membranes, specifically Nafion 117, due to their greater stability and durability. To the best of our knowledge, no previous study has been reported on the use of anion-exchange membranes in zinc-cerium RFBs possibly due to their limited availability, stability and durability when this battery chemistry was first introduced. Note that the anion exchange membranes tested in the present study have not been specifically optimized for this system.

Perhaps the biggest concern with anion exchange membranes is their chemical resistance, particularly in the strongly oxidizing environment in the positive compartment. Among the anion exchange membranes that we assessed, AMV-N, AAV, FAPQ-375-PP and FAP-450 degraded quickly in the early cycles. Since these membranes appear to be stable in the presence of Ce(III), Zn(II) and MSA, it is reasonable to infer that they deteriorated due to the formation of highly oxidizing Ce(IV) during the first cycle. The battery was able to operate with another anion exchange membrane ASV without any problem during the first few cycles, but became unstable thereafter. By the end of the battery life, the ASV membrane was significantly degraded and torn. On the other hand, Fap-375-PP AEM was able to withstand the highly oxidative environment of zinc-cerium RFB in order to complete a full life-cycle analysis. Fap-375-PP AEM is a fluorinated anion exchange membrane designed to have high mechanical and chemical stability in acidic environments [139].

Figure 4.8 compares the cell voltages and half-cell electrode potentials of a zinc-cerium

RFB operating with Fap-375-PP AEM at 25 $mA\,cm^{-2}$ and 50°C to one operating with Nafion 117 CEM at the same operating conditions. Additionally, the charge efficiencies during the charge/discharge cycles are extracted from Figure 4.8a and presented in Figure 4.9. The battery with the Fap-375-PP AEM membrane exhibits lower voltage efficiency during each of the cycles than does the one operating with Nafion 117, which is not surprising given the considerably lower ionic conductivity of Fap-375-PP AEM (≈ 0.01 $S\,cm^{-1}$ [139]) compared to Nafion 117 (≈ 0.18 $S\,cm^{-1}$ [140]). This corresponds to areal resistances of $\approx 0.7\ \Omega\,cm^2$ in Fap-375-PP AEM (thickness of 70 µm) and $\approx 0.1\ \Omega\,cm^2$ in Nafion 117 (thickness of 183 µm). Thus, at an operating current density of 25 $mA\,cm^{-2}$, the ohmic potential drop across Fap-375-PP AEM is estimated to be 0.02 V, whereas it is only 0.003 V across Nafion 117. However, as shown in Figure 4.8a, the battery with Fap-375-PP AEM is able to operate for a much longer duration and many more cycles. In particular, it can operate for $\approx$ 50 hours and 33 cycles compared to $\approx$ 20 hours and 12 cycles in the case of Nafion 117 before the charge efficiency drops to 20%. Interestingly, the charge efficiency of the battery when Fap-375-PP AEM is employed drops gradually over the 33 cycles compared to the abrupt drop in the charge efficiency when the cation exchange membrane is used (Figure 4.9). As in the previous cases in this study, evidence of Ce(IV) precipitate was observed when the positive electrolyte was examined after battery failure. However, one significant difference between the two cases is the condition of the membrane after battery failure. Once Nafion 117 is rinsed off to remove any precipitate, subjected to the pre-treatment procedure discussed in the experimental section and then re-installed in the battery, the original battery performance can be restored. However, this is not possible in the case of Fap-375-PP, which suggests that it has been chemically damaged by its exposure to the positive electrolyte.

The half-cell electrode potential responses shown in Figure 4.8b reveal that as in the case with the use of Nafion at the same current density, the negative electrode reaction is limiting throughout the run except during the final cycles. About halfway during the run, the positive electrode potential begins to drop significantly during discharge, indicating that reaction at this electrode now is also limiting the battery operation presumably because of the drop in Ce(IV) concentration due to Ce(IV) precipitation and the resulting slower rate of Ce(IV) reduction. The similarities with the previous results suggest that the same problems observed when Nafion 117 is used arise when Fap-375-PP AEM is employed, only at a slower rate. FAP-375-PP AEM has slowed the rate of increased acidity in the negative electrolyte and thus extended the life of the battery, but a gradual increase in the acidity of the negative half-cell still occurred. Indeed, titrimetric analysis of the negative half-cell solution at the end of the battery life with Fap-375-PP AEM shows that the acid concentration on the negative side has increased to ≈ 1.9 $mol\,dm^{-3}$ from the initial $\approx$ 1

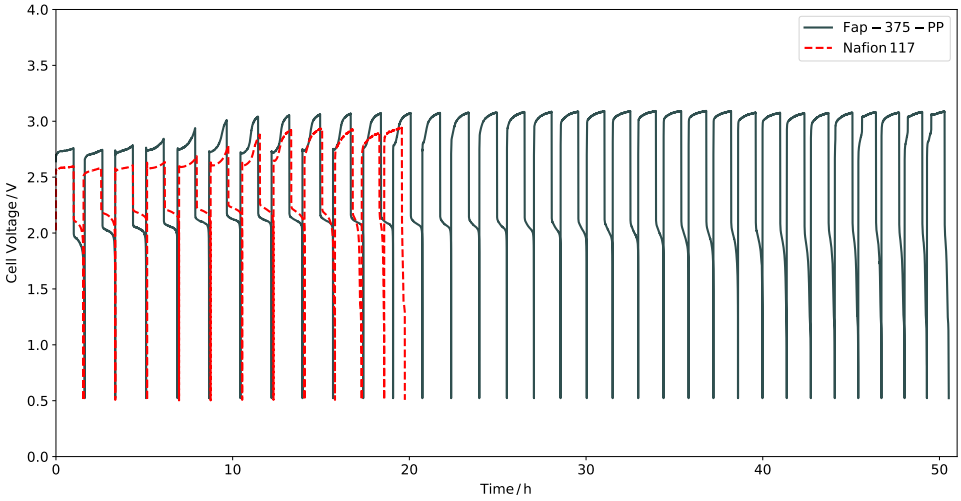

(a)

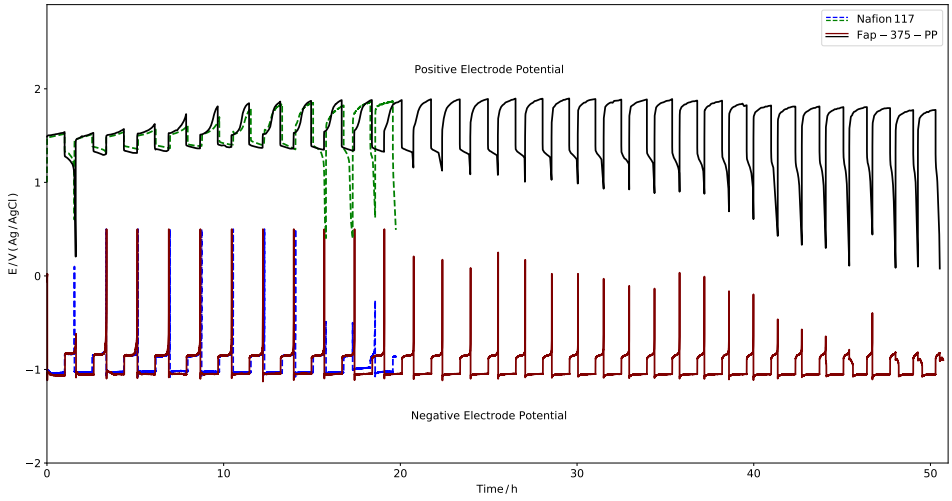

(b)

Figure 4.8: (a) Charge-discharge profiles at 25 mA cm^{-2} and 50°C with a 1-hour charge duration using Fap-375-PP anion exchange membrane compared with Nafion 117 cation exchange membrane. (b) Corresponding potentials of the positive and negative electrodes measured versus Ag/AgCl reference electrode during the battery operation shown in (a) for both Fap-375-PP AEM and Nafion 117 CEM.

mol dm^{-3} concentration. It is important to emphasize that this increase of 0.9 mol dm^{-3} in the acid concentration occurs over $\approx$ 50 hours, while the increase of $\approx$ 1 mol dm^{-3} in the case of Nafion 117 takes place over only $\approx$ 20 hours of operation. The leakage of protons in a number of other anion exchange membranes has also been reported in previous studies on electro-membrane processes for acid recovery [141–144]. Note that among the AEMs evaluated in our study, AVV and FAP-450 are designed to have low proton transfer rate. Unfortunately, they degraded quickly in the presence of Ce(IV) and could not be used for operation of the battery. Since the only anion present in the zinc-cerium system is methanesulfonate ($CH_3SO_3^-$), a suitable anion exchange membrane should easily permit the transport of methanesulfonate through membrane as a charge carrier. Otherwise, the transport of cations across the membrane will occur to maintain electroneutrality. The observation that a significant amount of H^+ has been transported from one side of Fap-375-PP AEM to the other suggests that the membrane is not highly permeable to methanesulfonate. Consequently, the development of a suitable anion exchange membrane that can readily permit the transport of methanesulfonate ions and/or the formulation of alternative electrolytes with high cerium and zinc solubilities that contain other anionic charge carriers would be very advantageous

Although the Fap-375-PP AEM assessed in the present study does not prevent proton leakage, its use leads to a significant improvement in the life-cycle over that achieved using Nafion 117. On the other hand, the apparent chemical degradation of Fap-375-PP AEM is a significant problem. The results of this study point to the critical need for the development of anion exchange membranes that are chemically stable in Ce(IV)-containing solutions and minimize proton transfer.

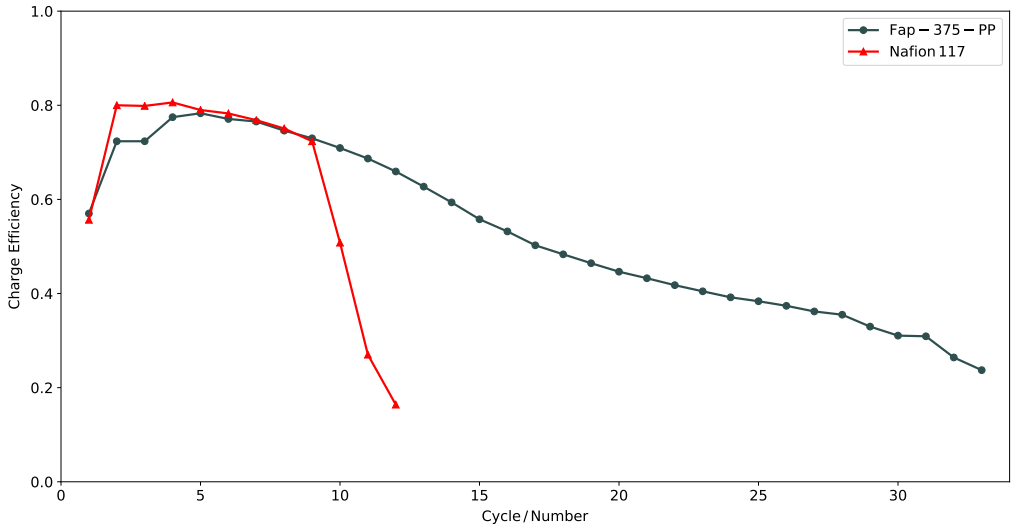

Figure 4.9: Charge efficiency per cycle for a zinc-cerium RFB operated with Fap-375-PP AEM compared to that using Nafion 117 extracted from Figure 4.8.

4.4 Conclusions

The role of the zinc and cerium redox reactions in the performance fade and ultimate failure of a zinc-cerium redox flow battery was investigated by *in situ* monitoring of the positive and negative electrode potentials during battery life-cycle analysis and titrimetric analysis of the positive and negative electrolytes for the Ce(IV) and H^+ concentrations, respectively.

At a current density of 25 mA cm^{-2}, the charge efficiency of the battery is limited by the occurrence of hydrogen evolution during charge which reduces the amount of deposit that is available for oxidation during discharge. This in turn prevents the complete conversion of Ce(IV) to Ce(III) during the discharge phase that would otherwise occur. This leads to the continual depletion of Ce(III) and build-up of Ce(IV) over time and a gradual rise in the cell voltage during charge as the cycling proceeds. Titration of the negative and positive electrolytes also confirms the continual increase in the Ce(IV) concentration on the positive side by the end of each discharge over the first few cycles and the rise of the H^+ concentration in the negative electrolyte throughout the entire life-cycle of the battery. The

dilution of the acidity on the positive side eventually leads to the precipitation of Ce(IV) since its solubility depends strongly on the MSA concentration. The rise in the proton concentration in the negative compartment significantly increases the rate of the hydrogen evolution side reaction. The combination of these phenomena leads to the capacity fade and ultimately the failure of the battery. The same factors occur at the higher applied current density of 50 $\mathrm{mA\,cm^{-2}}$ and lower operational temperature of 40°C.

In an attempt to reduce the enhancement in the acidity of the negative half-cell, the performance of a zinc-cerium RFB was evaluated using a number of commercially available anion exchange membranes as replacements for the Nafion 117 cation exchange membrane conventionally used in zinc-cerium RFBs. Among the AEMs tested, Fap-375 could withstand the highly oxidizing environment of the battery for a full life-cycle analysis. Fap-375 AEM enhanced the life-cycle of the battery by two-fold. However, it could only slow, but not prevent, the problem with proton enhancement in the negative compartment of the battery. This analysis revealed that the use of anion exchange membranes with extremely low proton leakage and high stability in the presence of Ce(IV) is key for the ultimate success of zinc-cerium redox flow batteries.

Chapter 5

Electrodeposition and Electrodissolution of Zinc in Mixed Methanesulfonate-Based Electrolytes[1]

5.1 Introduction

As concluded in our voltage analysis work in Chapter 3, the slower kinetics of the Zn/Zn(II) redox reaction compared to that of Ce(III)/Ce(IV) reaction results in larger overpotentials at low to intermediate applied current densities. Hence, improvement in the kinetics of the Zn/Zn(II) reaction should enhance the voltage efficiency of the battery at these applied current densities. Additionally, our life-cycle analysis in Chapter 4 showed that at these applied current densities, the discharge process is generally limited by the Zn/Zn(II) reaction, which cuts short the complete conversion of Ce(IV) to Ce(III) during the discharge phase. Increasing the rate of Zn(II) reduction relative to that of hydrogen evolution should result in more zinc deposit during the charge phase and consequently a longer discharge phase. This longer discharge phase results in the higher conversion of Ce(IV) to Ce(III) and thus lower rate of accumulation in the system. Hence, faster Zn/Zn(II) kinetics relative to HER is also beneficial for increasing the battery charge efficiency and life-cycle. Previous approaches of employing corrosion inhibitors as additives in the negative electrolyte was

[1]This chapter is adapted from my published work [145].

reported to be effective only during initial hours of electrodeposition, but this effect then fades away over time [92]. In this work, we perform extensive half-cell studies to identify an alternative negative electrolyte that is capable of increasing the rate of the Zn(II)/Zn reaction. In addition to identifying a promising alternative electrolyte for this purpose, half-cell studies are done in the present chapter to examine the performance of the new negative electrolyte under different operating conditions.

The Zn/Zn(II) half-cell reaction has been studied in methanesulfonic [91, 112], sulfuric [91, 146–148] and chloride [148–150] baths. However, to the best of our knowledge, no study on this system in a mixed electrolyte has been reported. The standard rate constant reported in pure chloride solutions is 8.78×10^{-3} cm s^{-1} [151], which is about an order of magnitude higher than the value of 0.16×10^{-3} cm s^{-1} obtained in MSA-only electrolytes [93]. This reflects the beneficial role of chlorides in enhancing the kinetics of the Zn/Zn(II) redox reaction. Based on the well-known behavior of metal deposition systems in general, we expect that the addition of chloride ions to the base MSA electrolyte will be beneficial to zinc deposition. It has been reported that the presence of chloride in zinc electrowinning baths leads to lower polarization resistance and higher charge efficiency of zinc deposition [152]. Additionally, cyclic voltammetry experiments have shown that the overpotential is reduced and the cathodic peak potential is shifted in the positive direction when zinc deposition is carried out in chloride-only baths rather than sulfate-only electrolytes [148]. Chloride ions have also improved the deposition performance of other metals and alloys such as nickel [153], copper [154], chromium [155], indium [156] and Co-Ni alloys [157]. Thus, it is reasonable to investigate the use of chloride ions to facilitate zinc deposition.

In terms of the effect of electrolyte composition on zinc electrodissolution, a thermometric study has shown that both chloride and sulfate tend to promote the oxidation of zinc in acidic media and should be considered as corrosive anions although it was not possible to easily differentiate between their relative strengths as corrosion promoters [158]. Although the effect of chloride on zinc dissolution in highly acidic methanesulfonate-based electrolytes has not been reported to date, halogen ions including chloride have been shown to increase the rate of the Zn(II)/Zn(Hg) reduction and oxidation reaction when they are added to a $NaClO_4$ base electrolyte [159, 160].

In this experimental study, we use a 3-electrode system to determine the electrolyte composition and operating conditions that optimize the kinetics of zinc electrodeposition and electrodissolution in mixed-electrolyte media with particular emphasis on methanesulfonate/chloride solutions. Since the ultimate aim is to determine the optimum operating conditions for a zinc-cerium RFB, we apply compositions that are typically used for this application. Here we examine the alternative electrolyte for eventual use in either undivided (background electrolyte with low acidity) or divided (background electrolyte with high

acidity) zinc-cerium RFBs. The undivided zinc-cerium RFBs are operated at lower acid concentrations ($\sim$ 0.2 mol dm^{-3} – 0.5 mol dm^{-3} MSA base electrolyte) [66, 111], while the negative side of a divided zinc-cerium RFB typically contains a higher acid concentration of $\sim$ 1 mol dm^{-3} MSA. Thus, in order to address both possible situations, we investigate Zn electrodeposition/electrodissolution in two sets of solutions containing either 0.2 mol dm^{-3} or 1 mol dm^{-3} MSA base electrolyte. In particular, the effects of temperature, acid concentration and Zn(II) concentration on the behavior of the Zn/Zn(II) system in mixed-electrolyte media are determined.

5.2 Experimental

For these experiments, a custom-made three-electrode water-jacketed glass cell (Adams & Chittenden Scientific Glass) was employed. The capacity of the cell is $\sim$ 200 mL and the outer cell has the dimensions of 110 mm diameter $\times$ 55 mm height. This cell was connected to a circulating bath (Neslab RTE-8) to control the electrolyte temperature throughout the experiments. All electrochemical experiments were carried out using an EPP-400 potentiostat (Princeton Applied Research). The reference electrode was a saturated glass body calomel electrode (Fisher Scientific) and the counter electrode was a graphite rod (6.15 mm diameter $\times$ 50 mm long). All electrode potentials reported herein correspond to the SCE scale. The working electrode was a glassy carbon (GC) disk of 3 mm diameter (area $\sim$ 0.071 cm^2). The GC electrode tip has a PTFE holder that was fitted to the EDI101 rotator and CTV speed control unit (Radiometer Analytical) for the rotating disk electrode (RDE) experiments. The GC electrode was polished manually with 0.05 µm alumina powder (Buehler) on a MicroCloth polishing pad (Buehler) for several minutes to a mirror finish prior to each experiment. The electrode was then rinsed thoroughly with ultra-pure water (resistivity $\sim$ 18 MΩ cm). It has been shown that the ferricyanide/ferrocyanide redox reaction is sensitive to the cleanliness and preparation method of GC electrodes [161]. Thus, the cleanliness of the GC electrode was assessed by carrying out a cyclic voltammetry scan first from 0.6 to 0 V *vs* SCE and then reversing back to 0.6 V at a scan rate of 100 mV s^{-1} in a solution containing 1 mmol dm^{-3} ferricyanide and 1 mol dm^{-3} KCl and measuring the separation between the cathodic and anodic potential peaks for the ferricyanide/ferrocyanide redox couple. Ideally the separation should be close to 60 mV, as expected for a 1-electron reaction. We measured the peak separation using our clean GC electrode to be 69 mV, which is close to the reported value. After each test with ferricyanide, the electrode surface was again rinsed thoroughly with water.

All solutions used for the zinc deposition/dissolution experiments were prepared with

analytical grade reagents and ultra-pure water (resistivity $\sim 18\ \mathrm{M\Omega\,cm}$). To prevent possible interference from the oxygen reduction reaction, the solutions were purged with nitrogen gas prior to each deposition experiment for 10 minutes and the subsequent experiments were conducted under a blanket of nitrogen gas. The zinc(II) methanesulfonate solutions were prepared by dissolving the appropriate amounts of high purity zinc oxide (Zochem Inc.) in 70% methanesulfonic acid (Alfa Aesar), while sodium methanesulfonate solutions were prepared by dissolving sodium carbonate decahydrate (Alfa Aesar) in 70% methanesulfonic acid. The resulting solutions were colorless with no sign of any precipitate forming. Anhydrous zinc chloride (99% purity; Fisher Scientific) and zinc sulfate heptahydrate (98% purity; Alfa Aesar) were added to these solutions in order to introduce the chloride and sulfate ions into the mixed-electrolyte media. In order to compare the mixed-electrolyte media with pure chloride and sulfate baths, solutions were also made with hydrochloric acid (Sigma Aldrich) and sulfuric acid (Sigma Aldrich) instead of methanesulfonic acid. Solutions that contain MSA, HCl and H_2SO_4 have a pH close to zero. In order to increase the pH of the solutions to higher values (pH 4) for the RDE experiments, $0.5\ \mathrm{mol\,dm^{-3}}$ sodium methanesulfonate, sodium chloride (EMD Millipore) and sodium sulfate (EMD Millipore) were added to the sulfonic-, chloride- and sulfate-based solutions, respectively, followed by the appropriate amounts of MSA, HCl and H_2SO_4, respectively. The kinematic viscosity of the solutions was measured using a Cannon-Fenske viscometer tube. The pH of the solutions was measured with an Orion (420A) pH meter.

The electrochemical techniques conducted included cyclic voltammetry, linear polarization and galvanostatic deposition/dissolution under unstirred conditions and linear sweep voltammetry using a rotating disk electrode. Zinc deposition onto the GC electrode was carried out galvanostatically for 30 seconds at a constant current density of $25\ \mathrm{mA\,cm^{-2}}$, followed by zinc dissolution with the same current density. To prevent excessive oxidation of the electrode surface, zinc dissolution was halted when the potential shifted to values more positive than -0.5 versus SCE. For the morphology study, deposition onto a glassy carbon plate (Alfa Aesar) was carried out. The plate was taped with an insulating polyester tape (Cole-Parmer) to ensure that the area of the working electrode exposed to the solution was 0.5 cm $\times$ 0.5 cm. In this case, zinc deposition was done galvanostatically at a current density of $50\ \mathrm{mA\,cm^{-2}}$ for 1 minute. The images of the deposits were taken with a scanning electron microscope model Zeiss FESEM 1530.

5.3 Results and Discussion

Table 5.1 shows the compositions of the different electrolytes investigated in this study. As can be seen, MSA is the base acid in most of the samples. MSA is less corrosive than hydrochloric acid and sulfuric acid, but has comparable conductivity [162]. Moreover, only moderately high concentrations of chloride are suitable for the electrolyte to be used in a membrane-less zinc-cerium RFB due to the possibility of chlorine gas forming in the presence of Ce(IV). Also, it has been reported that the solubility of Ce(III) in sulfate baths is considerably lower than in MSA media [108]. With these considerations, MSA is the better choice as the base electrolyte.

Table 5.1: Electrolyte compositions investigated in this study

Low acid concentration			
Base electrolyte ($mol\,dm^{-3}$)	ZnMSA ($mol\,dm^{-3}$)	$ZnCl_2$ ($mol\,dm^{-3}$)	$ZnSO_4$ ($mol\,dm^{-3}$)
0.2 MSA	0.7	0	0
0.2 MSA	0.5	0.2	0
0.2 MSA	0.5	0	0.2
0.2 MSA	0.3	0.4	0
0.2 MSA	0.3	0	0.4
0.2 HCl*	0	0.7	0
0.2 H_2SO_4*	0	0	0.7
High acid concentration			
1.0 MSA	1.5	0	-
1.0 MSA	1.3	0.2	-
1.0 MSA	1.2	0.3	-
1.0 HCl*	0	1.5	-

* For comparison

Since undivided zinc-cerium RFBs are usually operated at lower acid concentrations [66, 111], a 0.2 $mol\,dm^{-3}$ MSA base electrolyte containing a total of 0.7 $mol\,dm^{-3}$ Zn(II) is used for one series of voltammetry experiments (Table 5.1). The total Zn(II) concentration is kept fixed in order to fairly compare the results obtained in the various solutions. For

this series of experiments, solutions with mixed methanesulfonate/sulfate have also been prepared since it has been reported that the solubility of Ce(IV) increases in the mixed methanesulfonate/sulfate system [100] which would be beneficial for an undivided zinc-cerium RFB. On the other hand, divided zinc-cerium RFBs operate at much higher Zn(II) concentrations (1.5 mol dm^{-3} ZnMSA in 1 mol dm^{-3} MSA [12]). Thus, 1 mol dm^{-3} MSA base electrolytes containing a total of 1.5 mol dm^{-3} Zn(II) are used for another series of voltammetry experiments (Table 5.1).

5.3.1 Effect of mixed methanesulfonate/chloride electrolyte

Figure 6.1 shows the cyclic voltammograms obtained in the different mixed methanesulfonate/chloride electrolytes with a total of 0.7 mol dm^{-3} Zn(II) in 0.2 mol dm^{-3} MSA (Table 5.1) at 25°C on a static glassy carbon electrode. The potential is swept first from -0.5 to -1.3 V *vs* SCE and then reversed back to -0.5 V at a scan rate of 20 mV s^{-1}. A nucleation loop appears during the cathodic scan obtained in each solution which is typical of that observed during metal electrodeposition. In each case, an oxidation peak during the reverse scan arises due to the anodic stripping of Zn(II) into the solution from the metal coating deposited during the previous cathodic portion of the scan.

The voltammograms clearly show that the addition of chloride ions to the electrolyte significantly increases the cathodic and anodic current densities at any particular potential during the scans and decreases the nucleation overpotential (NOP). The NOP is the difference between the nucleation potential E_{nu} (point A) at which cathodic current is first observed during the scan and the crossover potential E_{co} (point B) at which the current switches from cathodic to anodic during the reverse scan and represents the degree of polarization of the cathode [163]. As shown in Table 5.2, the reduction in the NOP obtained in the mixed methanesulfonate/chloride electrolytes containing a total of 0.7 mol dm^{-3} Zn(II) relative to that in the MSA-only solution reaches as high as 50 mV. The amount of zinc deposited during the cathodic portion of each scan can be determined by measurement of the anodic charge (Q_{an}) during the reverse scan. Analysis of the CVs in Figure 6.1 shows that the amount of zinc deposited has increased by 57% and 129% when 0.2 and 0.4 mol dm^{-3} chloride ion, respectively, replace MSA in the electrolyte (Table 5.2). Note that the total Zn(II) concentration is kept fixed at 0.7 mol dm^{-3} in these solutions so that these differences can be attributed to the amount of chloride present.

A similar trend is observed in the cyclic voltammograms in Figure 5.2 obtained in the different mixed methanesulfonate/chloride electrolytes listed in Table 5.1 which contain a total of 1.5 mol dm^{-3} Zn(II) in 1 mol dm^{-3} MSA (typical composition of the negative

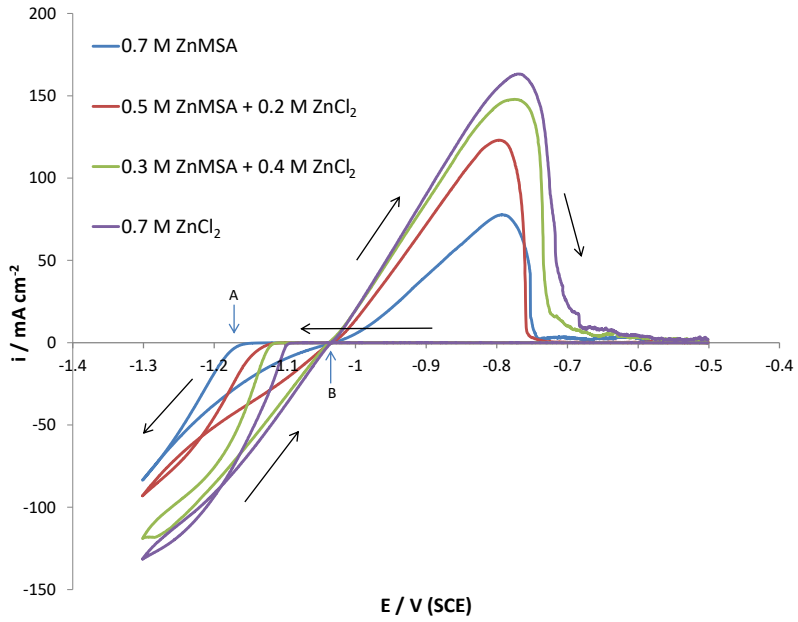

Figure 5.1: Cyclic voltammograms on a glassy carbon electrode (~ 0.071 cm^2) in different mixed methanesulfonate/chloride media with 0.2 mol dm^{-3} MSA base electrolyte at 25°C and a scan rate of 20 mV s^{-1}.

half-cell in divided RFBs). As shown in Table 5.2, the NOP decreases by 90 mV when 0.3 mol dm^{-3} chloride ion replaces 0.3 mol dm^{-3} of the MSA in the electrolyte. Furthermore, Q_{an} increases by 113% relative to the value obtained in the 1.5 mol dm^{-3} ZnMSA solution when MSA is replaced by 0.2 mol dm^{-3} chloride and by 179% when it is replaced by 0.3 mol dm^{-3} chloride.

Due to the highly acidic environment of the studied electrolytes, hydrogen evolution (HER) also accompanies zinc deposition during cathodic polarization. In order to determine if the higher cathodic current density obtained in the mixed methanesulfonate/chloride media is due to zinc deposition or hydrogen evolution, the charge efficiency (CE) over each of the voltammograms has been determined and included in Table 5.2. The charge efficiency is calculated as the ratio of the charge passed during the anodic portion of the scan to that obtained during the cathodic portion. Table 5.2 shows that higher charge efficiency is achieved in the mixed-electrolyte media than in the MSA-only electrolyte. Thus, the mixed methanesulfonate/chloride electrolyte does not appear to promote the HER and the higher current densities observed in the presence of chloride can be attributed to an increase in the zinc deposition/dissolution rate.

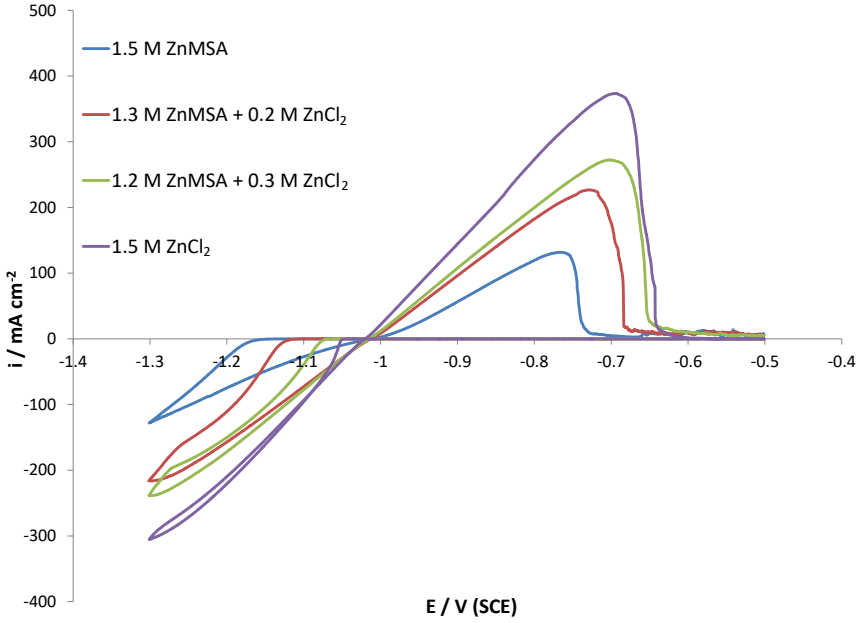

Figure 5.2: Cyclic voltammograms on a glassy carbon electrode (~ 0.071 cm^2) in different mixed methanesulfonate/chloride media with 1.0 mol dm^{-3} MSA base electrolyte at 25°C and a scan rate of 20 mV s^{-1}.

Although a higher concentration of chloride ions in the mixed-electrolyte media improves the zinc half-cell reaction kinetics, it would be preferable to maintain the Cl^- concentration at lower levels in a membrane-less zinc-cerium RFB due to the concern that it could be oxidized by Ce(IV) also present in the electrolyte. Thus, based on the results of this section, a composition of 0.5 mol dm^{-3} ZnMSA/0.2 mol dm^{-3} $ZnCl_2$ in 0.2 mol dm^{-3} MSA is chosen for subsequent analysis as an electrolyte in an undivided RFB (see section 3.4). For a divided zinc-cerium RFB, higher chloride concentrations can be used with the MSA base electrolyte. Thus, for this application, we focus on the composition of 1.2 mol dm^{-3} ZnMSA/0.3 mol dm^{-3} $ZnCl_2$ in 1 mol dm^{-3} MSA. Although not included here, experiments have also been conducted in solutions containing more $ZnCl_2$ (i.e., 1.0 mol dm^{-3} ZnMSA/0.5 mol dm^{-3} $ZnCl_2$ in 1 mol dm^{-3} MSA), but little further change in the electrode response from that obtained in 1.2 mol dm^{-3} ZnMSA/0.3 mol dm^{-3} $ZnCl_2$ in 1 mol dm^{-3} MSA was observed. Thus, no further experiments in electrolytes containing more than 0.3 mol dm^{-3} $ZnCl_2$ have been conducted.

Table 5.2: Effect of electrolyte composition on E_{nu}, NOP, Q_{an} and CE of zinc deposition in mixed electrolyte solutions compared to pure methanesulfonate, chloride and sulfate solutions.

0.2 mol dm^{-3} MSA base electrolyte				
Composition (mol dm^{-3})	E_{nu} (V)	-NOP (mV)	Q_{an} (mA s)	CE (%)
0.7 ZnMSA	-1.15	120	42.9	85
0.5 ZnMSA+ 0.2 $ZnCl_2$	-1.11	80	67.4	93
0.3 ZnMSA + 0.4 $ZnCl_2$	-1.11	70	98.4	89
0.7 $ZnCl_2$	-1.09	60	114.2	88
0.5 ZnMSA+ 0.2 $ZnSO_4$	-1.17	130	27.1	88
0.3 ZnMSA+ 0.4 $ZnSO_4$	-1.17	130	25.2	85
0.7 $ZnSO_4$	-1.18	130	31.3	89
1.0 mol dm^{-3} MSA base electrolyte				
1.5 ZnMSA	-1.15	140	73.4	83
1.3 ZnMSA+ 0.2 $ZnCl_2$	-1.11	100	156.1	94
1.2 ZnMSA + 0.3 $ZnCl_2$	-1.07	50	204.8	90
1.5 $ZnCl_2$	-1.05	30	277.7	87

5.3.2 Effect of mixed methanesulfonate/sulfate electrolyte

Figure 5.3 shows cyclic voltammograms of the Zn/Zn(II) system in different mixed methanesulfonate/sulfate electrolytes and the corresponding pure electrolytes containing a total dissolved Zn(II) concentration of 0.7 mol dm^{-3} in 0.2 mol dm^{-3} MSA (Table 5.1). As Table 5.2 shows, the presence of sulfate ions has a different effect from that of chloride by leading to a slight increase in E_{nu} ($\sim$ 20 mV), reflecting a larger overpotential and more difficult onset of zinc electrodeposition in mixed methanesulfonate/sulfate electrolyte compared to the pure ZnMSA electrolyte. Although the charge efficiencies are comparable in both pure and mixed electrolytes, the current density throughout the cathodic portion of the scan and the anodic charge reflecting the amount of zinc deposited are lower in the sulfate-containing solutions. Thus, although a mixed methanesulfonate/sulfate electrolyte would have some benefits in an undivided zinc/cerium RFB since it enhances the Ce(IV) solubility [100], our results show that the kinetics of the Zn/Zn(II) redox reaction will suffer.

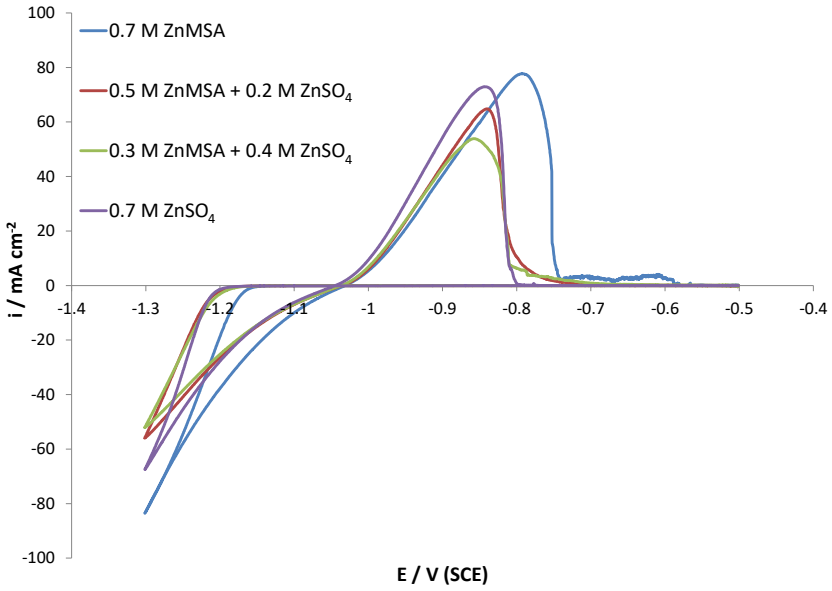

Figure 5.3: Cyclic voltammograms on a glassy carbon electrode (~ 0.071 cm^2) in different mixed methanesulfonate/sulfate media with 0.2 mol dm^{-3} MSA base electrolyte at 25°C and a scan rate of 20 mV s^{-1}.

The CVs in these previous two sections clearly show that the addition of chloride ions to the MSA base electrolyte leads to larger cathodic and anodic current densities and more zinc deposition compared to that obtained in the pure MSA and sulfate-containing electrolytes. Also, the effect of the anions on the overpotential for zinc deposition on glassy carbon electrode increases in the following order: $Cl^- < CH_3SO_3^- < SO_4^-$. As previously mentioned, chloride ions have been shown to enhance the electrodeposition of other metals as well. One proposed mechanism for this effect is the bridging effect of chloride ions [156, 164]. In this mechanism, the chloride ions adsorb on the electrode substrate and facilitate the electron transfer between the metal cations and the electrode by forming bridges between them [156].

Another important factor is the strength of the interaction between Zn(II) and the various ligands present which must be overcome in order to discharge and deposit the metal. Consequently, the more stable a zinc ion-pair or complex is, the slower should be the rate of zinc nucleation and deposition. One measure of the strength of such an interaction is the magnitude of the stability constant for its formation. The stability constant for the formation of the $ZnCl^+$ complex at zero ionic strength is $10^{0.96}$ [165]. On the other

hand, the stability constant for the formation of $ZnSO_4$ complex at zero ionic strength is $10^{2.38}$ [165]. Based on this criterion, it should be easier to discharge Zn(II) and deposit metal in the former than the latter electrolyte. This can explain the lower overpotential for Zn(II) reduction in a mixed methanesulfonate/chloride bath compared to a mixed methanesulfonate/sulfate electrolyte. No data were found in the literature for the stability constant of zinc methanesulfonate complexes. However, it has been reported that methanesulfonate ions are stronger complexing agents than chloride for other metals such as lead and cadmium [166]. Additionally, a previous study on nickel deposition has shown that the overpotential for Ni(II) reduction increases in the sequence $ClO_4^- < CH_3SO_3^- < SO_4^-$, which leads to the expectation that nickel-methanesulfonate complexes are less thermodynamically favored than nickel-sulfate complexes and more than those containing chloride [167]. In this study, we have found a similar trend in the overpotential for Zn(II) reduction and thus propose that the stability of zinc-methanesulfonate complexes is also higher than that of zinc-chloride complexes, leading to the mixed methanesulfonate/chloride bath being the most favorable electrolyte for deposition.

5.3.3 Determination of exchange current density

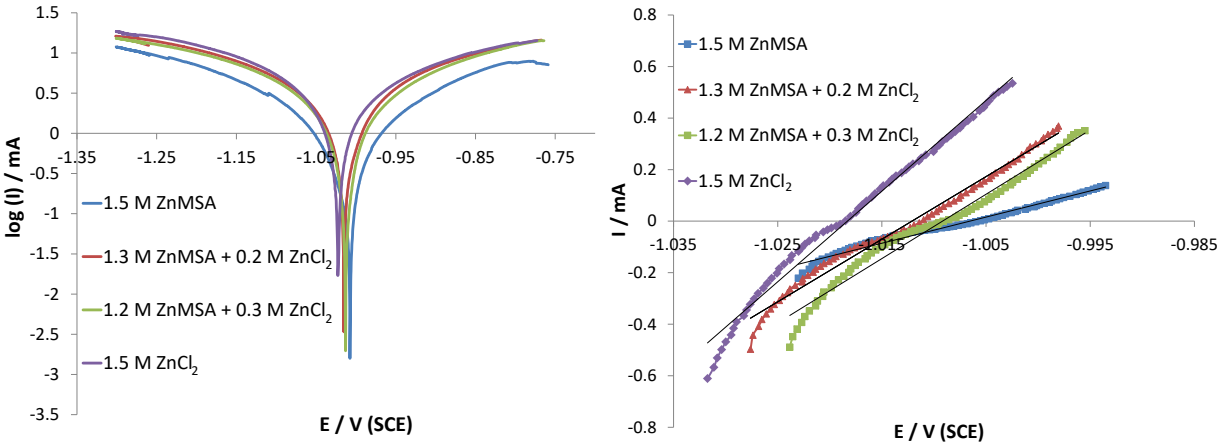

(a) (b)

Figure 5.4: (a) Semi-log plot of current versus potential on a glassy carbon electrode ($\sim$ 0.071 cm^2) immersed in different mixed methanesulfonate/chloride media obtained at a scan rate of 2 $mV\,s^{-1}$. (b) Linear polarization measurements for zinc on a glassy carbon electrode obtained at a scan rate of 0.167 $mV\,s^{-1}$.

Our results in Table 5.2 suggest that the addition of chloride enhances the kinetics of the Zn/Zn(II) redox reaction. Thus, we have conducted polarization experiments to determine the change in the values of exchange current densities upon addition of chloride to the solution. Figure 5.4a is obtained by scanning the potential at a sweep rate of 2 $\mathrm{mV\,s^{-1}}$ up to 0.250 V in both directions from the open-circuit potential for each electrolyte shown in Table 5.3. The Butler-Volmer equation (Eqn 5.1) has been fitted to the experimental data to obtain the exchange current density (i_0), β_a and β_c. A non-linear least-square method that makes use of the trust region reflective algorithm (TRF) has been used to do this fitting.

$$i = i_0 \left[\exp\left(\frac{2.3(E - E_{ocp})}{\beta_a}\right) - \exp\left(-\frac{2.3(E - E_{ocp})}{\beta_c}\right) \right] \tag{5.1}$$

As Table 5.3 shows, the exchange current density increases from 11.3 $\mathrm{mA\,cm^{-2}}$ to 21.7 $\mathrm{mA\,cm^{-2}}$ upon addition of 0.2 $\mathrm{mol\,dm^{-3}}$ $ZnCl_2$ and rises to 24.0 $\mathrm{mA\,cm^{-2}}$ when 0.3 $\mathrm{mol\,dm^{-3}}$ $ZnCl_2$ is added. The highest exchange current density was found for the pure $ZnCl_2$ solution. These values are in the same range ($\approx 10^{-3}$ $\mathrm{A\,cm^{-2}}$) as reported values for the Zn/Zn(II) reaction in pure chloride and MSA electrolytes [92, 168]. As Table 5.3 shows, the β_c and β_a extracted from Figure 5.4a are all larger than the expected value for a two-electron transfer (60 $\mathrm{mV\,decade^{-1}}$). However, they are in agreement with the values reported in previous studies on zinc deposition and dissolution reaction in pure MSA solutions [94].

For the linear polarization technique, a potential sweep rate of 0.117 $\mathrm{mV\,s^{-1}}$ was used and the potentials were limited to 0.010 V from the open-circuit potential. In this range of overpotential, current changes linearly with voltage (Figure 5.4b). Similar to the results found from fitting the Butler-Volmer equation to the experimental data, the exchange current densities increase as the chloride concentration is raised. The difference between the values obtained by these two methods has also been reported in a previous study on zinc redox reaction in pure MSA electrolyte [94] and is attributed to the occurrence of hydrogen evolution reaction particularly at higher overpotentials.

5.3.4 Determination of diffusion coefficients for Zn(II)

In order to study the possible effect of chloride and sulfate ions on the transport properties of Zn(II), we conducted a series of linear sweep voltammetry experiments on a rotating GC electrode in various Zn(II)-containing solutions over the potential range where zinc deposition occurs. As mentioned previously, zinc deposition is accompanied by HER in all

Table 5.3: Open-circuit potential (E_{ocp}), $-\beta_c$ and β_a along with the exchange current density (i_0) calculated from fitting the Butler-Volmer equation to experimental data and use of the linear polarization method.

Composition ($mol\,dm^{-3}$)	Fitting of Butler-Volmer Equation				Linear polarization
	E_{ocp} (V)	$-\beta_c$ ($mV\,decade^{-1}$)	β_a ($mV\,decade^{-1}$)	i_0 $mA\,cm^{-2}$	i_0 $mA\,cm^{-2}$
1.5 ZnMSA	-1.008	177	170	11.3	5.4
1.3 ZnMSA + 0.2 $ZnCl_2$	-1.011	170	170	21.7	12.7
1.2 ZnMSA + 0.3 $ZnCl_2$	-1.014	200	200	24.0	15.2
1.5 $ZnCl_2$	-1.023	181	200	27.0	21.9

the electrolytes considered so far in this study due to their acidic conditions. This greatly complicates the accurate determination of the diffusion coefficient of Zn(II) using the Levich equation since the limiting current plateaus for its reduction do not clearly appear in the linear sweep voltammograms obtained in these solutions. Consequently, we have chosen to measure the Zn(II) diffusion coefficients in less acidic electrolytes that contain lower Zn(II) concentrations to ensure that it is possible for the measured current to be controlled by diffusion of Zn(II) alone. Table 5.4 shows the composition of the electrolytes used for estimation of the diffusion coefficients. The pure MSA and mixed electrolyte solutions are adjusted to pH 4 by adding 0.5 $mol\,dm^{-3}$ NaMSA and the appropriate amount of MSA. Solutions with pure chloride and sulfate ions have also been characterized for comparison. 0.5 $mol\,dm^{-3}$ NaCl or Na_2SO_4 are added to these solutions and the pH is adjusted to 4 using the appropriate amount of HCl or H_2SO_4.

Figure 5.5a shows the cyclic voltammograms obtained in the different mixed methanesulfonate/chloride electrolytes containing a total of 0.02 $mol\,dm^{-3}$ Zn(II) (Table 5.4) at 25°C on a static glassy carbon electrode. In these experiments, the potential is swept first from -0.8 to -1.4 V *vs* SCE and then reversed back to -0.8 V at a scan rate of 20 $mV\,s^{-1}$. Similar to that observed previously in the more concentrated solutions, the addition of chloride shifts the E_{nu} to more positive values and increases the current density and amount of zinc deposited. As reported previously [91], the limiting current density i_L is an important factor in the charge/discharge of RFBs. Operation at current densities higher than i_L leads to excessive hydrogen evolution and hence a lower charge efficiency when the battery is being re-charged. Figure 5.5b shows the electrode responses obtained at 1600 rpm for the same compositions shown in Figure 5.5a. As can be seen, these plots show that the limiting current density for Zn(II) reduction is increased significantly by the

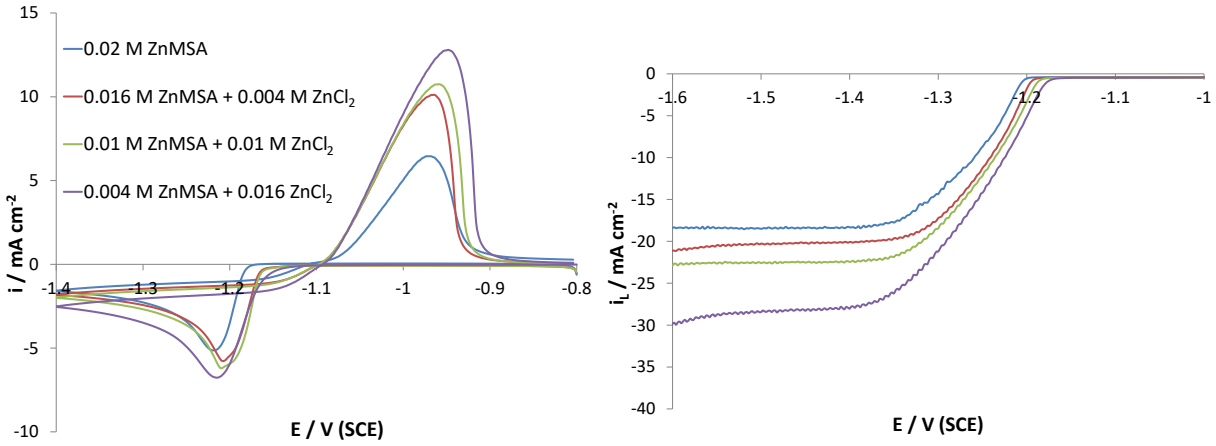

(a) (b)

Figure 5.5: (a) Cyclic voltammograms on a glassy carbon electrode (~ 0.071 cm^2) immersed in different mixed methanesulfonate/chloride media at 25°C obtained at a scan rate of 20 mV s^{-1}. (b) Comparison of linear sweep voltammograms for RDE rotating at 1600 rpm for the same compositions shown in Figure 5.5a. Scan rate = 20 mV s^{-1}.

presence of chloride (e.g., an increase from $\sim$ -18 mA cm^{-2} to $\sim$ -29 mA cm^{-2} as the $ZnCl_2$ concentration is raised from 0 to 0.016 mol dm^{-3}) despite the fact that the total amount of Zn(II) in solution remains unchanged. A similar trend is observed at the other rotation speeds.

Linear sweep experiments over the potential range from -1.0 V to -1.9 V *vs* SCE at a scan rate of 20 mV s^{-1} on an RDE operating at rotation speeds of 400, 900, 1600, 2500 and 3600 rpm have been conducted for each composition given in Table 5.4. Figure 5.6a shows an example of the set of linear sweep voltammograms obtained in one of the solutions (0.01 mol dm^{-3} ZnMSA/0.01 mol dm^{-3} $ZnCl_2$ in 0.5 mol dm^{-3} NaMSA) at pH 4. The current density for the mass transport-limited reaction of an electroactive species at a rotating disk electrode is described by the Levich equation [169]

$$i_L = 0.620nFD^{2/3}\omega^{1/2}v^{-1/6}c \tag{5.2}$$

where n is the number of transferred electrons (2 in this case), F is the Faraday constant, D is the diffusion coefficient, ω is the rotation speed expressed in rad s^{-1}, v is the kinematic viscosity and c is the concentration of the electroactive species. Figure 5.6b shows a plot of i_L versus $w^{1/2}$ according to the Levich equation for the solution considered in Figure

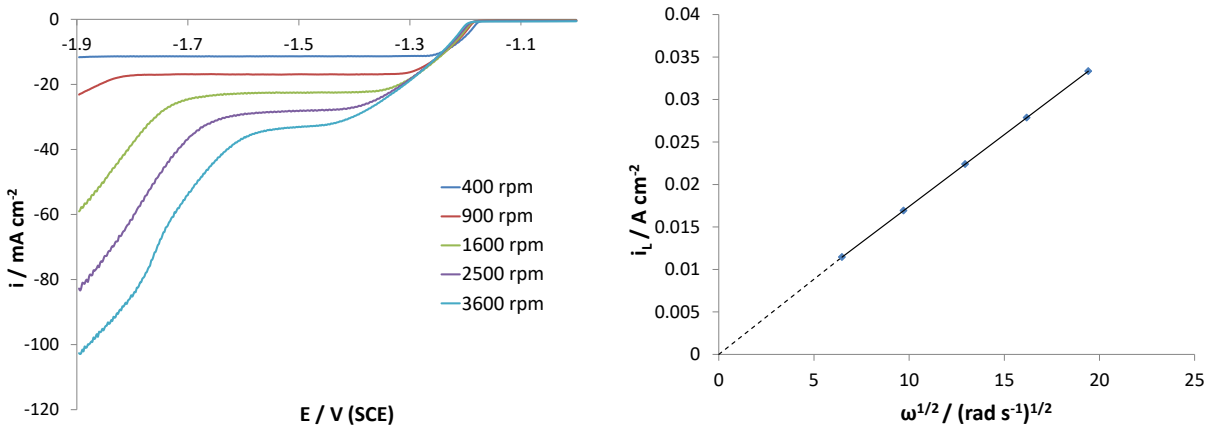

(a) (b)

Figure 5.6: (a) Linear sweep voltammograms for Zn(II) reduction on a glassy carbon electrode (~ 0.071 cm^2) obtained at a scan rate of 20 mV s^{-1} and different rotation speeds in 0.01 mol dm^{-3} ZnMSA/0.01 mol dm^{-3} $ZnCl_2$ and 0.5 mol dm^{-3} NaMSA at pH 4. (b) Plot of limiting current density versus $\omega^{1/2}$ according to the Levich equation obtained in the same solution.

5.6a. As predicted by the Levich equation, the plot is linear and passes through the origin. Although not included here, similar results are obtained for the other solutions. Table 5.4 shows the diffusion coefficients obtained from the slope of the best straight line plot for various electrolytes. Also included in the table are the corresponding kinematic viscosities measured directly in our study. The dimensionless Schmidt number which is the ratio of the dynamic viscosity of the electrolyte to the diffusion coefficient is also included in this table. This number is important for characterizing the flow conditions and is relevant to the design of redox flow batteries. The diffusion coefficient of zinc in pure methanesulfonate, sulfate and chloride solutions is found to be 4.6×10^{-6} cm^2 s^{-1}, 4.4×10^{-6} cm^2 s^{-1}, 8.6×10^{-6} cm^2 s^{-1}, respectively. The values obtained in the sulfate- and chloride-only solutions are in good agreement with those reported previously [91, 149]. In a previous study [100] the diffusion coefficient of Zn(II) in a pure methanesulfonate solution was found to have a somewhat higher value of 7.5×10^{-6} cm^2 s^{-1} than that reported here although it should be noted that this earlier measurement was conducted in a solution with a different concentration (0.01 mol dm^{-3} ZnMSA in 0.5 mol dm^{-3} NaMSA). Also, in this earlier study, the kinematic viscosity of the electrolyte was not measured and instead a value from the literature was assumed for the purpose of estimating diffusion coefficient.

Table 5.4: Kinematic viscosity, diffusion coefficient and Schmidt number measured in various mixed electrolytes.

Composition ($mol\,dm^{-3}$)	Kinematic viscosity (10^{-2} $cm^2\,s^{-1}$)	Diffusion coefficient (10^{-6} $cm^2\,s^{-1}$)	Schmidt number
0.02 ZnMSA	1.064	4.6	0.23
0.016 ZnMSA + 0.004 $ZnCl_2$	1.092	5.3	0.21
0.01 ZnMSA + 0.01 $ZnCl_2$	1.076	6.0	0.18
0.004 ZnMSA + 0.016 $ZnCl_2$	1.088	8.3	0.13
0.02 $ZnCl_2$	1.012	8.5	0.12
0.016 ZnMSA + 0.004 $ZnSO_4$	1.052	4.4	0.24
0.01 ZnMSA + 0.01 $ZnSO_4$	1.064	5.1	0.21
0.004 ZnMSA + 0.016 $ZnSO_4$	1.052	5.7	0.18
0.02 $ZnSO_4$	1.360	4.4	0.31

** pH of all solutions adjusted to 4 through additions of 0.5 $mol\,dm^{-3}$ NaMSA to the methanesulfonate solutions and 0.5 $mol\,dm^{-3}$ NaCl or Na_2SO_4 to the chloride- or sulfate-only solutions.

The results in Table 5.4 show that as more ZnMSA is replaced with $ZnCl_2$ in the electrolyte, the diffusion coefficient increases and approaches the value obtained in a solution containing $ZnCl_2$ alone. On the other hand, the diffusion coefficients in the mixed methanesulfonate/sulfate media differ only slightly from the values observed in the sulfate-only or methanesulfonate-only electrolytes.

5.3.5 Effect of temperature

Temperature is one of the important operating variables for redox flow batteries. Whereas the proposed undivided zinc-cerium RFB has been operated at room temperature [66], higher temperatures (40-60°C) have been used for the divided zinc-cerium RFBs [12]. Thus, the effect of temperature on the Zn/Zn(II) system in mixed methanesulfonate/chloride media is compared to that in the MSA-only electrolyte for compositions used on the zinc negative half-cell side of a divided zinc-cerium RFB.

Figure 5.7 shows the cyclic voltammograms obtained in solutions containing 1.2 $mol\,dm^{-3}$ ZnMSA/0.3 $mol\,dm^{-3}$ $ZnCl_2$ in 1 $mol\,dm^{-3}$ MSA compared to those obtained in the MSA-only electrolyte (1.5 $mol\,dm^{-3}$ ZnMSA in 1 $mol\,dm^{-3}$ MSA) at 25, 35 and 45°C. The

values of E_{nu}, NOP , I_{ac} and Q_{an} determined from these plots for both electrolytes at the three temperatures are summarized in Table 5.5. These data show that an increase in temperature leads to a positive shift of E_{nu} in both electrolytes, but has much less effect in the mixed methanesulfonate/chloride solution. An increase of E_{nu} is expected from both thermodynamic and kinetic points of view. The electrode potential for Zn/Zn(II) increases with temperature according to the Nernst equation, while the rate of formation of metal clusters large enough to ensure spontaneous growth should also rise with temperature as given in classical nucleation theory and the Volmer-Weber equation [170]. The data in Table 5.6 indicate that an increase in temperature causes the amount of zinc deposited during the scan to rise and NOP to decline in both electrolytes. However, they also reveal that the rise in E_{nu} and the amount of zinc deposited during the cathodic scan are significantly higher and NOP is always smaller in the mixed system than in the MSA-only electrolyte at each temperature. At 45 °C, the amount of deposited zinc is 50% higher and the NOP is 86% lower when the mixed electrolyte is used than when MSA-only media are used. Although the NOP tends to decrease in magnitude with temperature, the value for the pure MSA electrolyte at 45°C is 93 mV, which is still higher than the value of 50 mV in the methanesulfonate/chloride electrolyte. This highlights the important role that chloride plays in facilitating zinc deposition. In fact, the improved kinetics achieved at 45°C in the pure MSA electrolyte is already observed in the methanesulfonate/chloride solution at room temperature.

To accurately determine the effect of temperature on the charge efficiency of Zn deposition, we also have conducted experiments in which the GC electrode immersed in the solutions of interest is galvanostatically polarized at 25 $mA\,cm^{-2}$ first in the cathodic direction for 30 s and then with the same magnitude of current in the anodic direction. Figure 5.8 shows the resulting response of the electrode potential over this time obtained in the mixed and the MSA-only electrolytes at the three temperatures, while Table 5.6 summarizes the corresponding data for these experiments. The transient curves for both electrolytes show that the electrode is immediately depolarized at the onset of the cathodic polarization until a plateau is reached. This is not surprising given that the nucleation overpotential for zinc deposition should decrease as the zinc deposit begins to build on the GC substrate and is consistent with the features of the cyclic voltammograms shown in Figure 5.7 and Table 5.5. When the polarity is reversed and anodic current is applied, the response of the system is extremely rapid and a plateau is reached almost immediately in both electrolytes regardless of the temperature. This continues for $\sim$ 25–30 s of anodic polarization until all of the zinc metal deposited during cathodic polarization has been stripped, at which point the potential increases very sharply in the positive direction and the experiment is terminated. The curves in Figure 5.8 clearly show that temperature has

a much smaller effect on the electrode response obtained in the mixed electrolyte than in the MSA-only electrolyte, which is consistent with the effects on E_{nu} and NOP observed in the CV scans in Figure 5.7 and listed in Table 5.5. The curves in Figure 5.8 are relevant to battery applications in that they give the response of the negative Zn electrode that might be expected during a short charge/discharge cycle of a system operating at a given current density. Comparison of the curves reveals a number of benefits of using the mixed methanesulfonate/chloride electrolyte rather than the pure MSA electrolyte. The electrode potential reaches a plateau level where the rate of growth or re-dissolution of zinc is constant almost immediately during both the cathodic and anodic (charge and discharge) portions of the cycle at the three temperatures. On the other hand, the electrode potential never levels off to a constant value by the end of the 30–s duration of cathodic polarization in the MSA-only solution at any temperature. Once the polarity of the current is reversed in the anodic direction, the polarization of the electrode continues to gradually rise until the Zn deposit has completely dissolved from the electrode when carried out in the MSA-only electrolyte, whereas the electrode is able to maintain an almost constant potential until the Zn deposit has been removed in the case of the mixed electrolyte.

The operation of a rechargeable battery is most efficient when the polarization of both electrodes is as low as possible during both charge and discharge. Thus, it is desirable for the electrode potential to be as positive as possible during charge when Zn(II) reduction occurs and as negative as possible during discharge when Zn oxidation occurs. The result will be the smallest change in the electrode potential during the course of a complete charge/discharge cycle. When viewed this way, a comparison of the transient curves in Figure 5.8 clearly shows that with the exception of cathodic polarization at 45°C better performance is achieved in the mixed electrolyte than the pure MSA system.

Since the magnitude of the applied current is the same during both stages of these experiments, the charge efficiency for Zn deposition can simply be obtained from the data in Figure 5.8 from the ratio of the elapsed time required to completely strip the Zn deposit from the substrate during the anodic polarization to the period allowed for cathodic polarization (30 s in this case). The sharp rise in the electrode potential observed when the Zn deposit has been removed makes the determination of the charge efficiency from these plots very straightforward. Although the solution conductivity and voltage efficiency both increase as temperature is raised, the charge efficiency for Zn deposition in pure MSA electrolyte has been previously shown to decrease due to the higher rate of the HER [91]. The effect of temperature in the case of mixed electrolytes has not previously been reported. The results in Table 5.6 not only confirm that temperature has a similar effect in the MSA-only electrolyte investigated in our study but that this effect extends to the mixed electrolyte as well. Thus, the larger cathodic current density observed during the

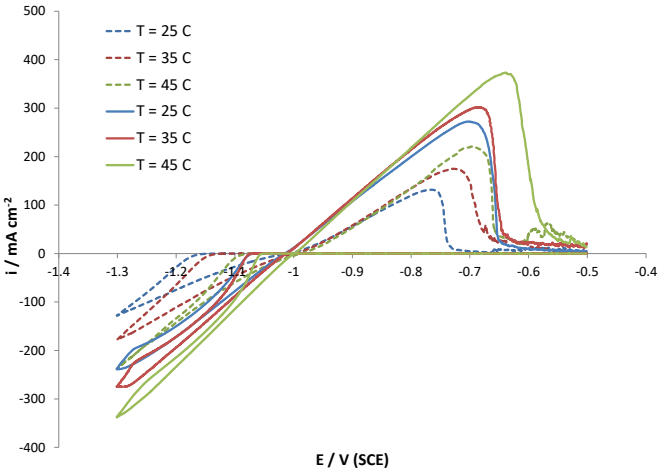

Figure 5.7: Cyclic voltammograms obtained on a glassy carbon electrode ($\sim$ 0.071 cm^2) in mixed methanesulfonate/chloride media (solid line) and MSA-only electrolyte (dashed line) at three different temperatures.

scans in Figure 5.7 as the temperature is raised in both solutions is due to the higher rates of both zinc deposition and hydrogen evolution.

Nevertheless, for the most part, our results clearly show the enhanced performance of the Zn/Zn(II) reaction in mixed-electrolyte media in terms of higher voltage and charge efficiency compared to that achieved in MSA-only electrolyte at each temperature, which leads to a significantly larger energy efficiency. Even with the decrease in the charge efficiency with temperature due to the higher rate of the HER, the energy efficiency at 45°C in the mixed media is still greater than the energy efficiency achieved at room temperature in the pure MSA electrolyte. This observation is particularly important for divided zinc-cerium RFBs that are operated at higher temperatures to enhance the kinetics of the Ce(III)/Ce(IV) reaction. By using the mixed methanesulfonate/chloride electrolyte, the Zn/Zn(II) half-cell performance at 45°C is superior in terms of E_{nu}, NOP, voltage and charge efficiency to that achieved in pure MSA electrolytes at room temperature.

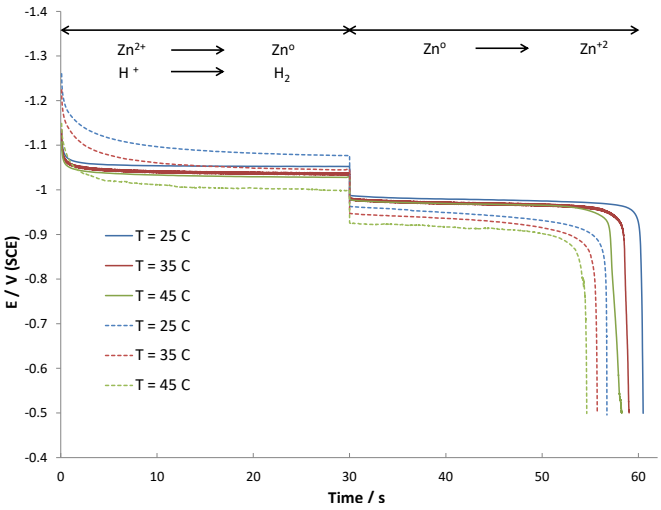

Figure 5.8: Variation of electrode potential with time during galvanostatic cathodic and anodic polarization of glassy carbon electrode ($\sim$ 0.071 cm^2) at 25 $mA\,cm^{-2}$ in mixed methanesulfonate/chloride media (solid line) and MSA-only electrolyte (dashed line) at three different temperatures.

Table 5.5: Effect of temperature, MSA and zinc concentration on E_{nu}, NOP, I_{ac} and Q_{an} of zinc deposition in mixed methanesulfonate/chloride and MSA-only electrolytes. The corresponding figures and compositions for each temperature, MSA and zinc concentration are explained in sections 5.3.5, 5.3.6 and 5.3.7, respectively.

Operating parameter	E_{nu} (V)		-NOP (mV)		I_{ac} ($mA\,cm^{-2}$)		Q_{an} ($mA\,s$)	
	MSA -only	Mixed electrolyte	MSA -only	Mixed electrolyte	MSA -only	Mixed electrolyte	MSA -only	Mixed electrolyte
Temperature (°C)								
25	-1.15	-1.07	140	50	131.6	272.4	73.4	204.8
35	-1.12	-1.07	122	50	174.8	301.9	111.9	230.0
45	-1.08	-1.05	93	50	220.7	373.2	152.9	309.4
MSA concentration ($mol\,dm^{-3}$)								
0.2	-1.15	-1.11	120	80	77.7	123.0	42.9	67.4
0.5	-1.15	-1.12	130	80	113.7	147.0	61.1	85.0
1.0	-1.16	-1.14	150	90	125.1	208.8	64.9	90.0
Zinc concentration ($mol\,dm^{-3}$)								
0.7	-1.15	-1.11	120	80	77.7	123.0	42.9	67.4
1.0	-1.14	-1.10	120	70	98.0	158.6	57.9	118.7
1.5	-1.13	-1.06	120	50	118.8	213.1	74.5	174.7

5.3.6 Effect of methanesulfonic acid concentration

Cyclic voltammograms showing the effect of the addition of different amounts of methanesulfonic acid to a mixed methanesulfonic acid/chloride solution (0.5 mol dm^{-3} ZnMSA/0.2 mol dm^{-3} $ZnCl_2$) and to a pure MSA electrolyte (0.7 mol dm^{-3} ZnMSA) are presented in Figure 5.9. The corresponding data obtained from these plots are given in Table 5.5. The data show that the nucleation potential is largely independent of the MSA concentration and shifts only slightly in the negative direction as the MSA concentration is increased. The NOP is affected more strongly, particularly in the MSA-only solution where it rises from 120 mV to 150 mV as the MSA level is increased from 0.2 mol dm^{-3} to 1.0 mol dm^{-3}. As can be seen, the cathodic current density and amount of zinc deposited during the scans increase in both electrolytes (pure and mixed) when the concentration of the base MSA electrolyte is raised. However, these values always remain higher for the case of the mixed electrolyte. In addition, the onset potential for zinc deposition is more positive and the NOP is significantly lower in the mixed electrolyte than in the MSA-only system.

Figure 5.10 shows the effect of MSA concentration on the electrode potential during the course of galvanostatic cathodic and anodic polarization of the GC electrode at 25 mA cm^{-2} in the mixed and pure MSA electrolytes, while Table 5.6 presents the voltage, charge and energy efficiencies obtained from these experiments. A comparison of these transients shows the clear superiority of the system performance when the mixed electrolyte is used in terms of the lower extent of polarization required to sustain the applied current during both the cathodic and anodic stages, faster attainment of plateau and charge efficiency of Zn deposition.

When the effect of MSA level in each electrolyte is considered, these data reveal that a rise in its concentration leads to more metal deposition, but favors the HER even more. This effect is perfectly understandable given that MSA is the source of H^+ ions. It should be noted that although the charge efficiency decreases as the MSA concentration increases in both solutions, the charge efficiency in the mixed methanesulfonate/chloride media remains higher than in the MSA-only electrolyte at each MSA concentration. Furthermore, although the energy efficiency of zinc deposition decreases with increasing MSA concentrations due to reduction in the charge efficiency, the energy efficiency in the mixed media containing 1.0 mol dm^{-3} MSA is significantly higher than that in pure MSA electrolyte with 0.2 mol dm^{-3} base MSA. Thus, by employing the mixed electrolyte system, it is possible to operate the cell over a wider range of MSA concentrations without the Zn/Zn(II) reaction being negatively affected. Again, this advantage of the mixed electrolyte is particularly important for an undivided zinc-cerium RFB where high MSA concentrations are required to dissolve the Ce(IV). It has been reported that the optimum composition

Table 5.6: Half-cell efficiencies of zinc deposition and dissolution of zinc in mixed MSA/chloride electrolyte and MSA-only electrolytes. The corresponding figures and compositions for each temperature, MSA, zinc concentration and current density are explained in sections 5.3.5, 5.3.6, 5.3.7 and 5.3.8, respectively.

Operating parameter	VE%		CE%		EE%	
	MSA -only	Mixed	MSA -only	Mixed	MSA -only	Mixed
Temperature (°C)						
25	87.7	92.6	86.0	97.3	75.4	90.1
35	89.2	93.0	82.3	94.3	73.5	87.7
45	91.2	93.9	77.3	86.9	70.6	80.6
MSA concentration ($\mathrm{mol\,dm^{-3}}$)						
0.2	81.1	90.9	77.0	95.0	62.4	86.4
0.5	82.9	90.6	76.0	91.7	63.0	83.5
1.0	83.9	93.6	71.3	88.7	59.8	83.0
Zinc concentration ($\mathrm{mol\,dm^{-3}}$)						
0.7	81.1	90.9	77.0	95.0	62.4	86.4
1.0	84.6	91.1	82.3	96.7	69.6	88.1
1.5	86.2	92.0	87.3	97.7	75.3	89.9
Current density ($\mathrm{mA\,cm^{-2}}$)						
5	95.5	97.1	80.0	87.7	76.4	83.1
25	87.7	92.6	86.0	97.3	75.4	90.1
35	84.5	91.0	86.7	92.7	73.2	84.3
45	80.4	87.3	85.0	93.7	68.3	81.8
55	77.6	86.7	84.3	92.3	65.4	80.9

from the point of view of the solubility of cerium species is approximately 0.8 mol dm^{-3} Ce(III) ion in 4.0 mol dm^{-3} MSA [98]. However, at this high MSA concentration, the HER becomes dominant on the zinc side. Thus, for an undivided zinc-cerium RFB, a compromise must be made between a lower hydrogen evolution rate at the zinc side and higher solubility of cerium in the electrolyte. This normally requires that the battery be operated at low MSA concentrations and consequently only at a low Ce(III) concentration ($\sim$ 0.2 mol dm^{-3}) [66]. This leads to a low energy density of 11 W h L^{-1} for an undivided system. Hence, it would be beneficial to achieve higher charge efficiencies for zinc electrodeposition when the solution contains a higher MSA concentration and the battery can produce a higher energy density. As shown in this study, this is possible by using a mixed methanesulfonate/chloride electrolyte, which enables the charge and voltage efficiency for zinc deposition achieved in the presence of 1.0 mol dm^{-3} MSA to be better to that achieved when only 0.2 mol dm^{-3} MSA has been added.

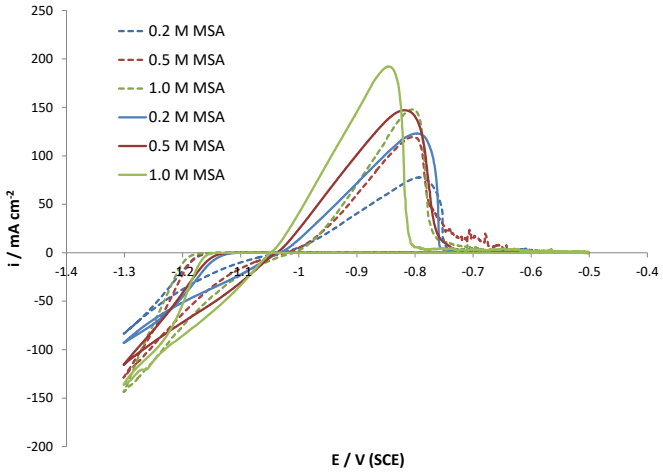

Figure 5.9: Cyclic voltammograms on a glassy carbon electrode ($\sim$ 0.071 cm^2) obtained in 0.5 mol dm^{-3} ZnMSA/0.2 mol dm^{-3} $ZnCl_2$ (solid line) and in 0.7 mol dm^{-3} electrolyte (dashed line) containing three different MSA base concentrations (0.2, 0.5 and 1.0 mol dm^{-3}).

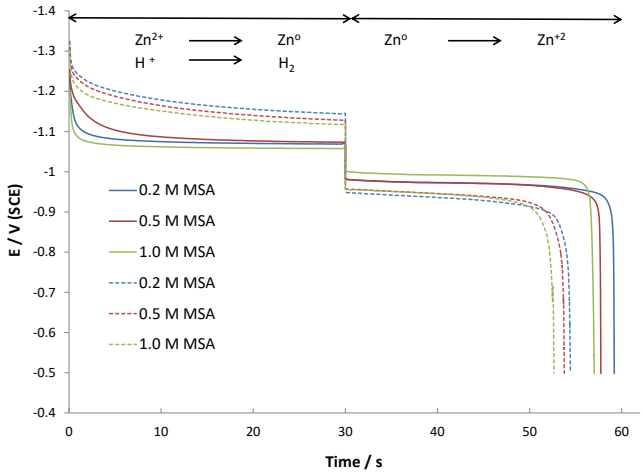

Figure 5.10: Variation of electrode potential with time during galvanostatic cathodic and anodic polarization of glassy carbon electrode (~ 0.071 cm^2) at 25 mA cm^{-2} in 0.5 mol dm^{-3} ZnMSA/0.2 mol dm^{-3} $ZnCl_2$ (solid line) and in 0.7 mol dm^{-3} electrolyte (dashed line) containing three different MSA base concentrations (0.2, 0.5 and 1.0 mol dm^{-3}).

5.3.7 Effect of zinc ion concentration in mixed methanesulfonate /chloride media

In order to investigate the effect of the Zn(II) concentration on the Zn/Zn(II) system, cyclic voltammograms have been obtained in each of the electrolytes listed in Table 5.4. In this series of experiments, the total Zn(II) concentration in the mixed electrolyte is increased from 0.7 mol dm^{-3} to 1.0 mol dm^{-3} and 1.5 mol dm^{-3}, while the molar ratio of methanesulfonate ions to chloride ions is kept fixed at 5:2. Three solutions with 0.7 mol dm^{-3}, 1.0 mol dm^{-3} and 1.5 mol dm^{-3} Zn(II), but in MSA-only electrolytes, are also investigated for comparison purposes. Also, 0.2 mol dm^{-3} MSA has been added to each of these mixed and pure solutions.

Not surprisingly, the cathodic and anodic current density, cumulative charges over the course of the scans of Zn deposition increase as the Zn(II) concentration rises in both electrolytes (Table 5.5). Also, this change causes the nucleation potential to become more positive. More interesting is the comparison of the effect of the Zn(II) concentration in the two types of electrolytes. E_{nu} is more positive, NOP is smaller, while the amount of metal deposited is larger at each Zn(II) concentration when the process is conducted in the mixed methanesulfonate/chloride electrolyte than in the MSA-only electrolyte. Furthermore, the

Table 5.7: Different compositions used to study the effect of Zn(II) concentration in mixed methanesulfonate/chloride and pure MSA electrolytes that also contain 0.2 mol dm^{-3} MSA.

ZnMSA (mol dm^{-3})	$ZnCl_2$(mol dm^{-3})
0.7	0
1.0	0
1.5	0
0.5	0.2
0.714	0.285
1.072	0.42

positive effect of the Zn(II) concentration on the amount of metal deposited is significantly larger in the mixed methanesulfonate/chloride electrolyte than in the MSA-only electrolyte.

Figure 5.12 shows the effect of the Zn(II) concentration on the electrode potential during the course of galvanostatic cathodic polarization and anodic polarization at 25 mA cm^{-2} in the mixed and pure MSA electrolytes. Obviously, zinc deposition becomes increasingly favored over the HER by the increase in the Zn(II) concentration. Previous studies also found that the charge efficiency increases from 78% in 0.5 mol dm^{-3} Zn(II) to 92% in 2.0 mol dm^{-3} Zn(II) when 1.5 mol dm^{-3} pure MSA electrolyte is used [91]. The transients in Figure 5.12 show that this leads to less polarization during reduction in both electrolytes although the effect of the Zn(II) concentration is larger in the MSA-only case. On the other hand, the Zn(II) concentration has no effect on the electrode potential in both solutions as Zn is being oxidized during the anodic polarization. Comparison of the transients also reveals once again the benefits of using the mixed electrolyte over that of the pure MSA electrolyte at each of the Zn(II) levels (less polarization throughout both stages of the cycle, faster attainment of plateau and higher charge efficiency of Zn deposition).

The data in Table 5.6 reveal that at each Zn(II) concentration, the charge and voltage efficiencies are significantly higher in the mixed electrolyte than in the pure MSA solution. It is desirable to use a higher Zn(II) concentration since this reduces the likelihood that mass transfer will affect battery performance at all states-of-charge and permits the battery to be charged at higher current densities. By using the mixed electrolyte rather than the MSA-only solution, it is possible to achieve a higher energy efficiency with lower nucleation overpotential at high Zn(II) concentrations.

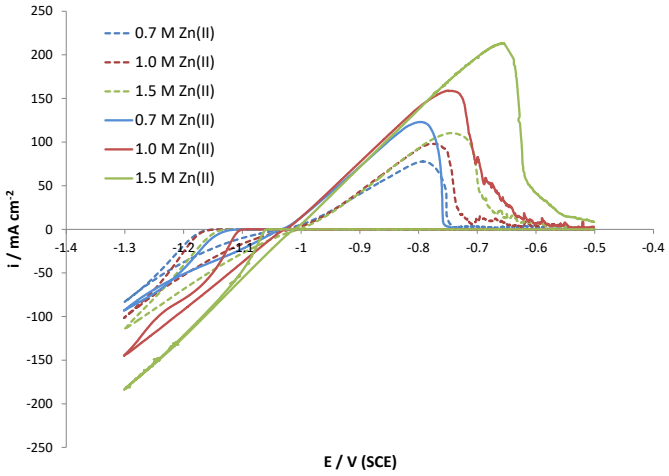

Figure 5.11: Cyclic voltammograms on a glassy carbon electrode ($\sim$ 0.071 cm^2) obtained in mixed methanesulfonate/chloride media (solid line) and MSA-only electrolyte (dashed line) containing 0.7, 1.0 and 1.5 mol dm^{-3} total Zn(II). The solution compositions are listed in Table 5.7.

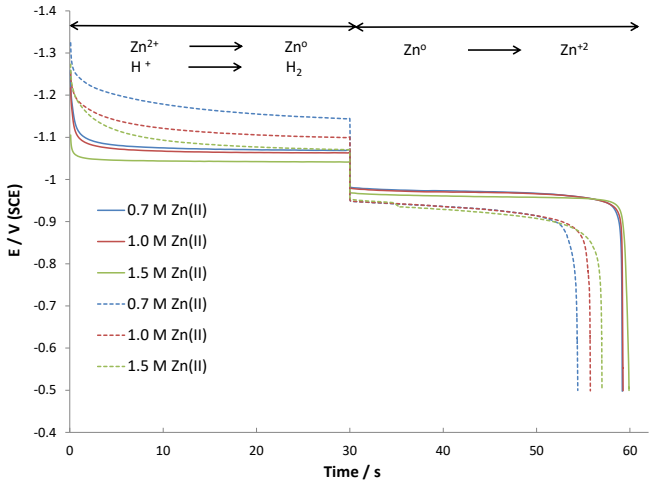

Figure 5.12: Variation of electrode potential with time during galvanostatic cathodic and anodic polarization of glassy carbon electrode ($\sim$ 0.071 cm^2) at 25 mA cm^{-2} in mixed methanesulfonate/chloride media (solid line) and MSA-only electrolyte (dashed line) containing 0.7, 1.0 and 1.5 mol dm^{-3} total Zn(II). The solution compositions are listed in Table 5.7.

5.3.8 Effect of current density

Figure 5.13 shows the effect of current density on the charge/discharge of the zinc redox reaction in solutions containing 1.2 mol dm^{-3} ZnMSA/0.3 mol dm^{-3} $ZnCl_2$ in 1 mol dm^{-3} MSA compared to those obtained in the MSA-only electrolyte (1.5 mol dm^{-3} ZnMSA in 1 mol dm^{-3} MSA). Similar to previous studies [91], higher energy efficiency is found at a moderate current density of 25 mA cm^{-2}. The corresponding data in Table 5 show that the voltage efficiency decreases in both types of electrolytes as the current density is increased. Although the VE% is very high at a low current density of 5 mA cm^{-2}, the resulting charge efficiency is the lowest, which is due to the high self-discharge of zinc [137, 138]. As the current density is raised above 25 mA cm^{-2}, the current efficiency slightly decreases but is generally independent of the applied current density, which is in agreement with the previous literature [171]. The data in Table 5.6 reveal that regardless of the applied current density, the CE, VE and the resulting EE are higher in the mixed electrolyte than in the pure MSA media and the highest energy efficiency is obtained at a current density of 25 mA cm^{-2}.

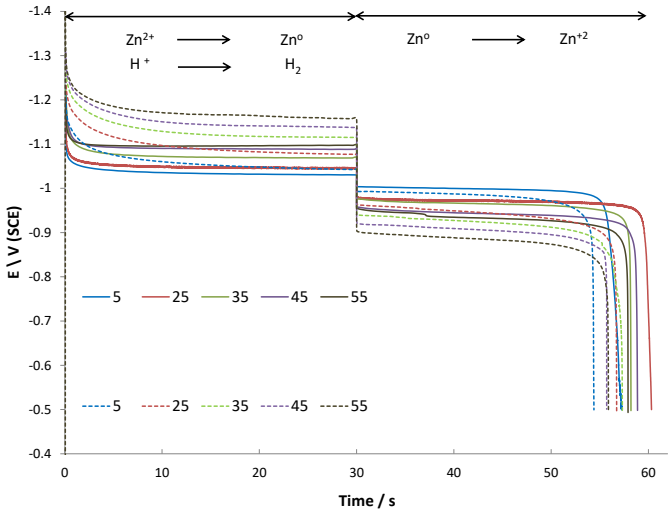

Figure 5.13: Variation of electrode potential with time during galvanostatic cathodic and anodic polarization of glassy carbon electrode ($\sim$ 0.071 cm^2) in mixed methanesulfonate/chloride media (solid line) and MSA-only electrolyte (dashed line) at different applied current densities. Current densities are in mA cm^{-2}.

5.3.9 Deposit morphology

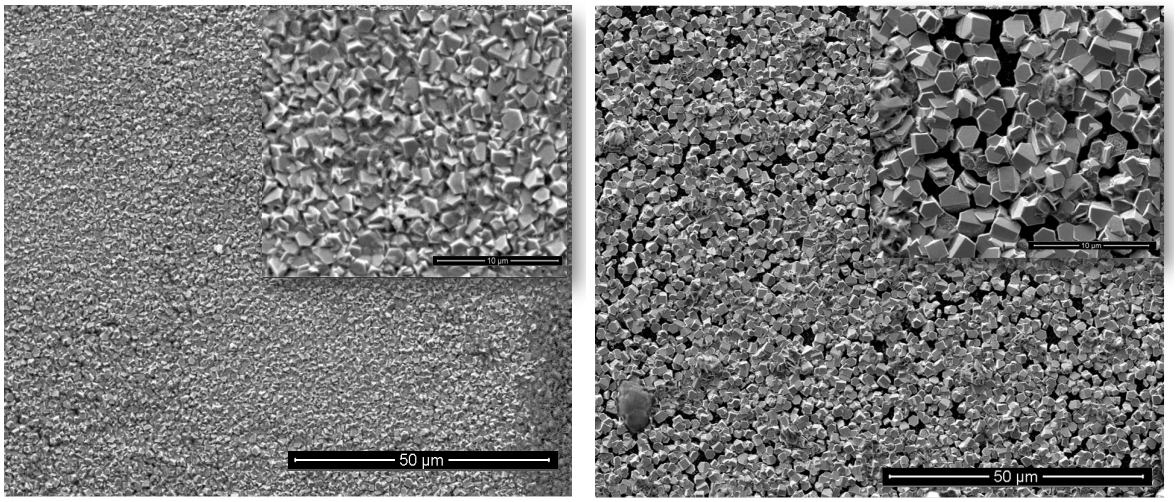

(a) (b)

Figure 5.14: The SEM images of zinc deposited from (a) 0.5 mol dm^{-3} ZnMSA/0.2 mol dm^{-3} $ZnCl_2$ and (b) 0.7 mol dm^{-3} ZnMSA onto glassy carbon plate ($\sim$ 0.25 cm^2). The deposition was done galvanostatically under constant current of 50 mA cm^{-2} for 1 minute.

Figure 5.14 shows the micrographs of zinc deposited from solutions containing 0.5 mol dm^{-3} ZnMSA/0.2 mol dm^{-3} $ZnCl_2$ compared to those obtained in the MSA-only electrolyte (0.7 mol dm^{-3} ZnMSA). The base electrolyte was 0.2 mol dm^{-3} MSA for both solutions. During deposition, the parallel hydrogen evolution reaction resulted in hydrogen bubbles covering many sites on the electrode surface. At some sites, these hydrogen bubbles could potentially undercut and dislodge part of the zinc deposit. The poor surface adhesion of zinc onto glassy carbon electrode and the incomplete coverage of the GC electrode surface by zinc deposits have also been reported in a previous study on the comparison of different carbon materials for the negative side of the zinc-cerium redox flow batteries [94]. It should be noted that the use of carbon composite materials such as polyvinyl ester (PVE) and polyvinylidene difluoride (PVDF) largely solves these problems [94].

For both electrolytes, the deposited zinc is made up of hexagonal grains that are randomly oriented on the electrode surface. This type of morphology for zinc deposits have also been reported in various previous studies [91, 148]. By comparing the two images, it is

clear that the addition of chloride has resulted in denser deposits with a more packed morphology. This is supported by our results in Table 5.5 which showed that regardless of the operating parameters, the anodic charge (which corresponds to the amount of deposited zinc) is significantly higher in mixed electrolytes than in the pure MSA media.

5.4 Conclusions

Cyclic voltammetry and polarization experiments show that the introduction of moderate concentrations of chloride ions to MSA-based electrolytes leads to a significant increase in the rate and amount of Zn deposition, positive shift in the nucleation potential, reduction in the nucleation overpotential and enhanced exchange current densities. On the other hand, the addition of sulfate ions into the MSA-based electrolyte leads to a lower rate of Zn deposition, slightly higher nucleation overpotential and similar charge efficiency to that attained in MSA-only electrolytes.

The use of a mixed MSA-chloride mixed electrolyte has also been found to improve the transport properties of Zn(II). The diffusion coefficient of Zn(II) is found to be 6.0×10^{-6} $cm^2\,s^{-1}$ in 0.01 $mol\,dm^{-3}$ ZnMSA/0.01 $mol\,dm^{-3}$ $ZnCl_2$ compared to 4.6×10^{-6} $cm^2\,s^{-1}$ in 0.02 $mol\,dm^{-3}$ ZnMSA. Both potentiostatic and galvanostatic experiments conducted at 25, 35 and 45°C show that the rate, charge efficiency and voltage efficiency of Zn deposition are higher in the mixed methanesulfonate/chloride solution than in the MSA-only solution at each temperature. Although an increase in the base MSA concentration lowers the charge efficiency for Zn deposition in both pure and mixed MSA electrolytes, the use of a mixed methanesulfonate/chloride system leads to higher charge and voltage efficiency than in pure MSA electrolyte. The microghraph of zinc deposited from a mixed methansulfonate/chloride solution also resulted in more packed morphology compared to the deposits from pure MSA electrolyte.

Chapter 6

Improvement of Zinc-Cerium Redox Flow Batteries Using Mixed Methanesulfonate-Chloride Negative Electrolyte[1]

6.1 Introduction

Our previous half-cell study with mixed methanesulfonate-chloride-based electrolytes on a glassy carbon electrode showed great promise by significantly improving the rate of the zinc redox reaction, reducing the nucleation overpotential (NOP) and increasing the amount of zinc deposited during cathodic polarization [145]. In the present chapter, we aim to test this alternative electrolyte in a bench-scale zinc-cerium redox flow battery and compare the performance of the battery with conventional zinc-cerium RFBs. Note that although a previous half-cell study by Nikiforidis et al. [102] showed that a MSA-chloride electrolyte significantly enhances the reversibility and kinetics of the Ce(III)/Ce(IV) half-cell reaction, we did not employ mixed MSA-chloride on the positive side of the battery since we observed that the presence of chloride and Ce(IV) in the same electrolyte increases the chance of chlorine gas evolution during charge. Hence, full-cell tests in the present work are done in a divided zinc-cerium RFB with alternative mixed methanesulfonate-chloride electrolyte on the negative half-cell and pure MSA electrolyte on the positive half-cell of the battery.

[1] This chapter is adapted from my published work [122].

In what follows, the experimental procedure is first presented in detail. Next, the results of a comprehensive study of this new electrolyte based on half-cell, full-cell and then life-cycle experiments are described. In detail, we first conduct half-cell experiments using a 3-electrode setup to confirm that the expected improvement in the behavior of the zinc redox reaction in a mixed MSA-chloride electrolyte is achieved when glassy carbon is replaced by PVE, which is the commonly used substrate in zinc-cerium RFBs. Then, a bench-scale zinc-cerium RFB is operated with a mixed MSA-chloride electrolyte on the negative side and the resulting charge, voltage and energy efficiencies are compared with that obtained in an RFB containing a standard MSA-only negative electrolyte. Life-cycle galvanostatic experiments are also conducted using the mixed electrolyte as well as standard MSA-only media to compare the duration and number of cycles over which the RFB can operate. The negative and positive electrode potentials are separately monitored during battery operation to better understand which of the half-cell reactions becomes limiting as the cycling continues.

6.2 Experimental

6.2.1 Chemicals

All solutions were prepared with ultra-pure water (resistivity $\sim$ 18 MΩ cm) and analytical grade reagents. The zinc methanesulfonate solutions were prepared by mixing the appropriate amounts of high purity zinc oxide (Zochem Inc.) with 70% methanesulfonic acid (Alfa Aesar). Chloride ions were introduced into these solutions in the form of 99% purity anhydrous zinc chloride (Fisher Scientific). Cerous methanesulfonate solutions were prepared by dissolving 99% purity cerium(III) carbonate (Treibacher Industrie AG) in methanesulfonic acid. The resulting solutions were colorless with no precipitate.

In order to determine the unknown concentration of Ce(IV) after a discharge cycle, the solution containing Ce(IV) was titrated with 99% purity ammonium iron(II) sulfate hexahydrate (Sigma-Aldrich) using a procedure described in the literature [172]. This involved the use of ferroin (1,10-phenanthroline iron(II) sulfate) (Alfa Aesar) as a colorimetric redox indicator.

6.2.2 Half-cell experiments

For half-cell experiments, a standard three-electrode glass cell (Adams & Chittenden Scientific Glass) was employed. Electrochemical experiments were carried out using an Autolab

PGSTAT 30 potentiostat/galvanostat. A saturated Ag/AgCl (Pine Research Instrumentation) electrode was used as the reference electrode and a graphite rod as the counter electrode. All electrode potentials reported herein correspond to the Ag/AgCl scale. A carbon polyvinyl-ester (PVE) composite (TDM Fuel Cell) was used as the working electrode. It was prepared by cutting a cuboid rod with 0.36 cm^2 cross-sectional area exposed to the electrolyte from a 6 mm-thick PVE composite sheet and then sealed with polyester resin (McMaster-Carr) and connected to the potentiostat with an alligator clip. The electrochemical techniques conducted in the half-cell experiments were cyclic voltammetry and cathodic galvanostatic polarization followed by anodic polarization to study Zn deposition/dissolution in an unstirred condition.

6.2.3 Full-cell experiments

For the full-cell experiments, we used a bench-scale two-compartment zinc-cerium redox flow battery similar in design to that described by Leung et al. [12]. Figure 6.1 shows a schematic of the battery components. The cell consisted of a positive electrode, four rubber silicone gaskets (CS Hyde Company), Nafion 117 membrane (Fuell Cell Store), two 6 mm-thick acrylic flow channels (acrylic sheets from CIP Wholesale), negative electrode and a copper current collector (McMaster-Carr). These components were arranged so that the electrodes, flow channels and membrane were separated by the gaskets. The negative electrode was a 6 mm-thick PVE sheet (TDM Fuel cells). The positive electrode was a three-dimensional platinized titanium mesh (Metakem GmbH) fabricated by stacking four 1.5 mm thick platinised titanium mesh layers (surface factor of 1.6) on a 6 mm thick platinised titanium plate. The mesh stack was spot-welded onto the plate. The mesh and the plate were both platinised at a loading level of 7 $mg\,cm^{-2}$ Pt. The active surface area of the positive and negative electrode exposed to the electrolyte had dimensions of 2 cm $\times$ 4.5 cm.

Unless otherwise noted, the negative electrolyte in its fully discharged state contained either 0.9 $mol\,dm^{-3}$ zinc methanesulfonate and 0.6 $mol\,dm^{-3}$ zinc chloride in 1 $mol\,dm^{-3}$ methanesulfonic acid or 1.5 $mol\,dm^{-3}$ zinc methanesulfonate in 1 $mol\,dm^{-3}$ methanesulfonic acid. The fully discharged positive electrolyte consisted of 0.8 $mol\,dm^{-3}$ cerous methanesulfonate in 4 $mol\,dm^{-3}$ methanesulfonic acid. The electrolytes were stored in two external tanks and pumped into the battery using a model BT100-1L Longer peristaltic pump with two channel heads (model YZ1515). Viton tubing (McMaster-Carr) was used to connect the reservoirs to both compartments. The electrolyte volume in each reservoir was maintained at 20 cm^3 in all cases except for the life-cycle analysis experiments where an electrolyte volume of 100 cm^3 was used. The circulating electrolytes were continually pumped through

a constant temperature bath (Neslab RTE-8) to maintain them at 50°C throughout the experiments.

Before each experiment, the Nafion membrane was pre-treated in the following manner: first immersed in 3 wt. % H_2O_2, then rinsed in DI water, followed by immersion in 0.5 mol dm^{-3} H_2SO_4 solution and a final rinse with DI water to remove H_2SO_4 traces. Each of these steps was carried out at 80°C for one hour.

In order to monitor the potentials of each electrode during battery operation in addition to the cell voltage, two Ag/AgCl reference electrodes (Pine Research Instrumentation) were introduced into the set-up, similar to that described by Langner et al. [115]. The reference electrodes were located in the path of the two electrolytes close to the inlet of each flow channel using custom-made T-shaped glass cells. On the zinc side, the reference electrode was maintained in direct contact with the negative electrolyte as it circulated through the RFB. On the positive side, however, we observed that enough cerium ions diffused over time through the porous ceramic frit of the Ag/AgCl reference electrode into its inner chamber and eventually damaged it. A similar problem was reported previously in the case of an all-vanadium RFB [173]. To solve this problem, we incorporated a Nafion membrane as a barrier to prevent damage by cerium. For our purposes, we sealed one end of a hollow cylindrical glass holder with a Nafion membrane and filled it with 4 mol dm^{-3} MSA (same as the MSA concentration in the positive electrolyte, but of course with no cerium). The Ag/AgCl reference electrode was then placed inside this holder which was then inserted into the set-up so that only the membrane was in direct contact with the positive electrolyte. In this way, the Ag/AgCl reference electrode was separated from the positive electrolyte by a Nafion membrane. The potential of the Ag/AgCl reference electrode with and without the holder was tested against a second Ag/AgCl reference electrode in a 4 mol dm^{-3} KCl solution. It was found that the potential difference rose from 1×10^{-3} V to 1.8×10^{-3} V when the Ag/AgCl reference electrode was placed inside the holder. Thus, the corresponding potential drop across the Nafion membrane was 8×10^{-4} V. Given that the electrode potentials measured in our experiments are higher than 0.5 V, the effect of separating the reference electrode from the positive electrolyte with the Nafion membrane is negligible.

Charge/discharge of the battery was conducted galvanostatically using an Autolab PGSTAT 30 at current densities of 15, 25 or 30 mA cm^{-2}. In these experiments, the battery was charged for a duration of either 15 minutes or 1 hour. During each charge/discharge cycle, charge was carried out for one of these prescribed durations, while discharge was terminated and the next charge cycle begun when the cell voltage reached a low cut-off value of 0.5 V. If the cell voltage during charge reached 3.4 V, then the battery was considered to no longer have a useful life and the entire charge/discharge experiment was

terminated.

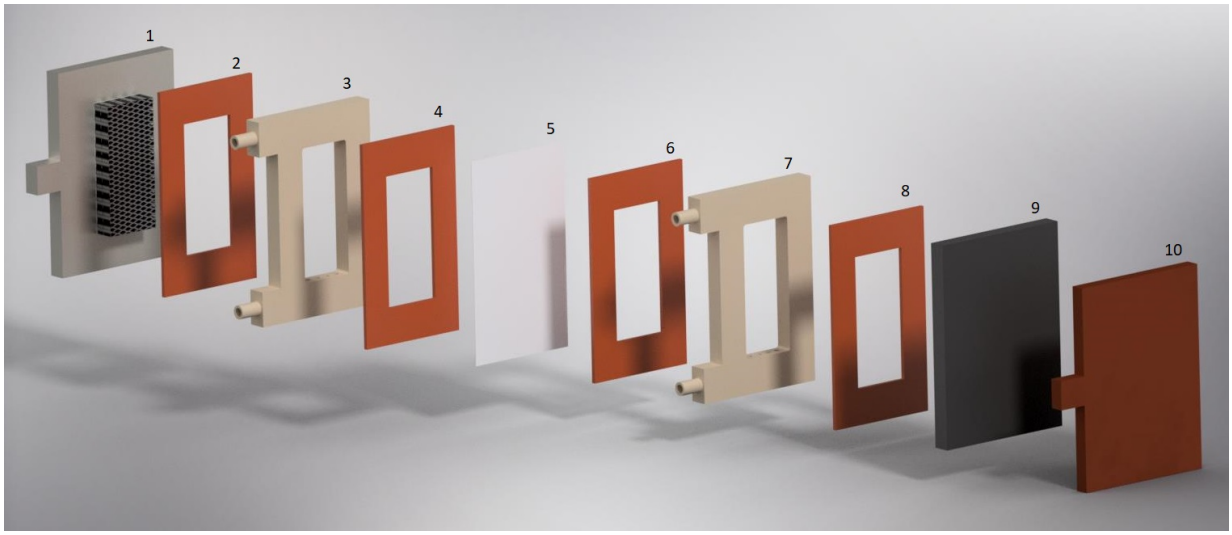

Figure 6.1: Components of the zinc-cerium redox flow battery used in this study: positive platinised titanium mesh electrode (1), silicone rubber gaskets (2, 4, 6, 8), acrylic flow channels (3, 7), Nafion membrane (5), PVE negative electrode (9) and copper current collector (10).

6.3 Results and Discussion

6.3.1 Half-cell experiments

Figure 6.2a shows the cyclic voltammograms for the zinc redox reaction obtained in methanesulfonate-only and mixed methanesulfonate-chloride electrolytes at room temperature on a stationary PVE working electrode (area $\sim 0.36\ \mathrm{cm}^2$). In each case, the solution contains a total of 1.5 $\mathrm{mol\,dm^{-3}}$ Zn(II) in 1 $\mathrm{mol\,dm^{-3}}$ MSA. Each scan is begun at an electrode potential of -0.4 V vs. Ag/AgCl and proceeds in the negative direction to -1.3 V at a rate of 20 $\mathrm{mV\,s^{-1}}$ before returning back to -0.4 V. As evident from the voltammograms, the addition of chloride ions appreciably enhances the anodic and cathodic current densities at any given electrode potential during the scans and decreases the nucleation overpotential. Furthermore, this effect becomes stronger as the amount of $ZnCl_2$ present increases from 0.3 to 0.6 $\mathrm{mol\,dm^{-3}}$. As Table 6.1 shows, when 0.3 $\mathrm{mol\,dm^{-3}}$ $ZnCl_2$ and 0.6 $\mathrm{mol\,dm^{-3}}$

$ZnCl_2$ replace 0.3 mol dm^{-3} ZnMSA and 0.6 mol dm^{-3} ZnMSA, respectively, in the electrolyte, the magnitude of the NOP drops by 84 mV and 109 mV and the anodic charge which reflects the amount of zinc deposited during the cathodic part of the scan increases significantly by 110% and 150%, respectively. For both electrolytes containing chloride ions, a comparable current efficiency (CE) of 95-96% is obtained which is approximately 20% higher than the level reached in the MSA-only solution.

The enhancement in the kinetics of zinc redox reaction in the presence of chloride ions can be quantified by extracting their exchange current densities from polarization experiments. Figure 6.2b presents the polarization curves obtained in the three electrolytes by sweeping the potential up to 0.250 V from the OCP in both directions at a scan rate of 2 mV s^{-1}. Following the same procedure described in the previous chapter [145], the Butler-Volmer equation [174] is fitted to the experimental data of Figure 6.2b using a non-linear least-square method. As shown in Table 6.1, the exchange current density increases from 9.4 mA cm^{-2} in 1.5 mol dm^{-3} ZnMSA to 17.5 mA cm^{-2} in 1.2 mol dm^{-3} ZnMSA + 0.3 mol dm^{-3} $ZnCl_2$ and to 23.6 mA cm^{-2} in 0.9 mol dm^{-3} ZnMSA + 0.6 mol dm^{-3} $ZnCl_2$.

The effect of chloride ions on the electrode potential response has also been studied under galvanostatic conditions and the results are shown in Figure 6.2c. In these experiments, the PVE working electrode is first polarized cathodically under quiescent conditions for 30 seconds at 25 mA cm^{-2} and then anodically with the same magnitude of current. The effect of chloride ion concentration on the corresponding VE, CE and EE is shown in Figure 6.2d. As can be seen, the efficiencies obtained in the mixed methanesulfonate-chloride electrolytes improve remarkably. Specifically, the CE increases by 28% and the VE rises by 13% when 0.3 mol dm^{-3} $ZnCl_2$ replaces 0.3 mol dm^{-3} ZnMSA, which leads to a significant enhancement of 30% in EE. However, a further increase of the amount of $ZnCl_2$ present to 0.6 mol dm^{-3} does not improve the CE any more. This effect of the Cl^- on CE is very similar to the trend observed in the cyclic voltammograms (Table 1). On the other hand, VE is still affected to some degree by the increase in the amount of $ZnCl_2$ added from 0.3 mol dm^{-3} to 0.6 mol dm^{-3} and rises from 83% to 87%. This rise in the amount of $ZnCl_2$ present also leads to a similar small improvement in the NOP values extracted from the CVs (Table 6.1).

Comparison of these data for the zinc redox reaction on the PVE electrode with those of our previous study in Chapter 5 shows that the magnitude of the NOP values are lower and the magnitude of the cathodic/anodic current densities are higher in both the MSA-only and mixed electrolytes when this reaction occurs on a glassy carbon (GC) electrode under the same operating conditions. Nevertheless, a significant enhancement of the Zn/Zn(II) reaction kinetics observed in the mixed methanesulfonate-chloride electrolyte is still observed when the process is carried out on a PVE electrode.

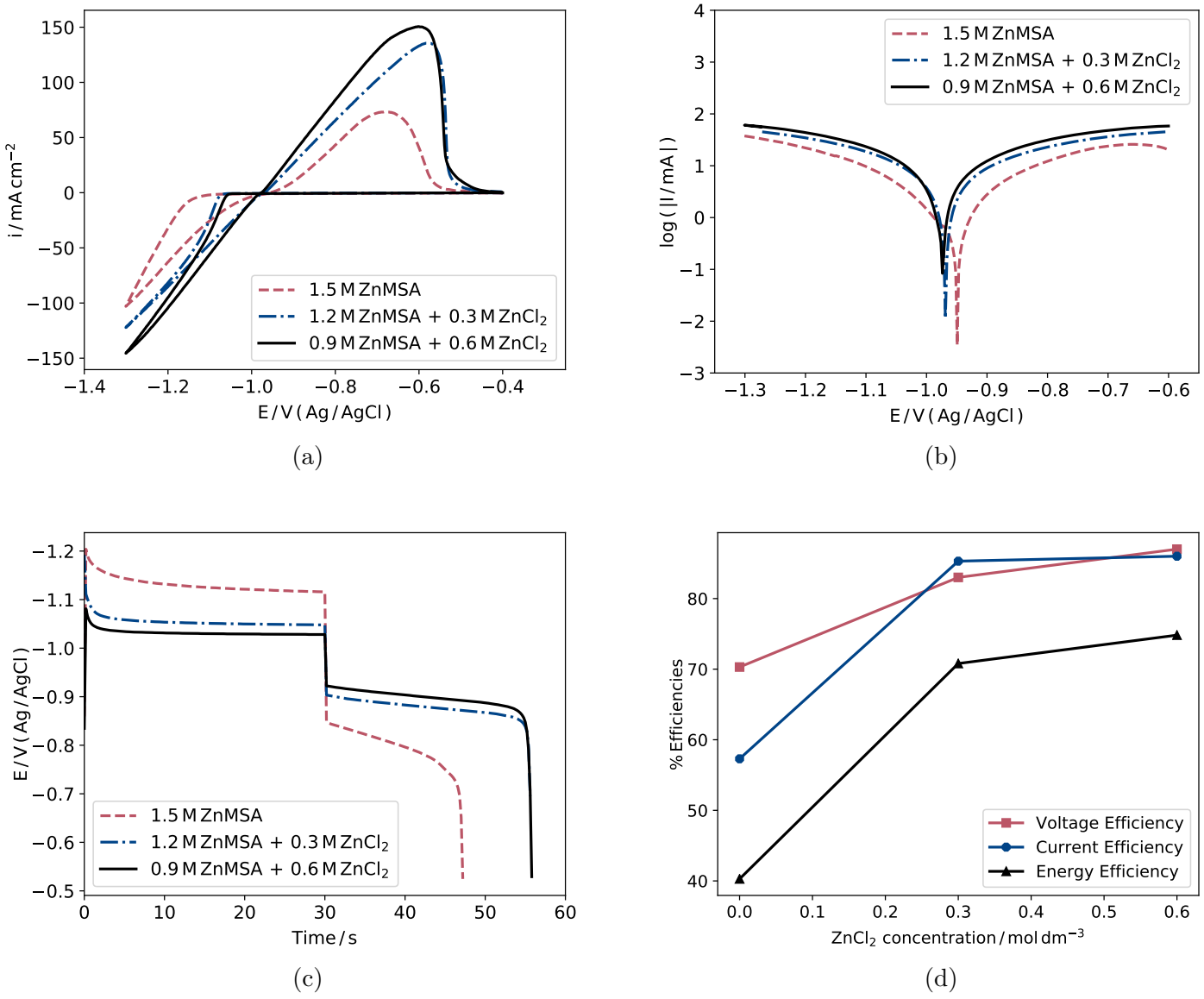

Figure 6.2: Half-cell experiments conducted on a PVE working electrode ($\sim$ 0.36 cm^2) immersed in different electrolytes with 1.0 mol dm^{-3} MSA base solution at room temperature. (a) Cyclic voltammograms obtained at a scan rate of 20 mV s^{-1}. (b) Semi-log plot of current versus potential obtained at a scan rate of 2 mV s^{-1}. (c) Variation of electrode potential with time during galvanostatic cathodic and anodic polarization of PVE electrode at 25 mA cm^{-2}. (d) Voltage, current and energy efficiencies extracted from Figure 6.2c at different chloride concentrations.

Table 6.1: Effect of electrolyte composition on nucleation overpotential (NOP), anodic charge (Q_{an}), current efficiency (CE) and exchange current density (i_0) of zinc redox reaction. NOP, Q_{an} and CE are extracted from cyclic voltammetry plots (Figure 6.2a). i_0 is calculated from fitting the Butler-Volmer equation to the polarization data (Figure 6.2b).

Composition ($mol\,dm^{-3}$)	-NOP (mV)	Q_{an} (mA s)	CE (%)	i_0 ($mA\,cm^{-2}$)
1.5 ZnMSA	180	297.2	74.6	9.4
1.2 ZnMSA+ 0.3 $ZnCl_2$	96	623.5	95.7	17.5
0.9 ZnMSA + 0.6 $ZnCl_2$	71	743.7	95.0	23.6

6.3.2 Battery charge/discharge curve during first cycle

Since the use of a mixed methanesulfonate-chloride electrolyte showed promising results in facilitating the Zn/Zn(II) reaction in half-cell experiments, full-cell experiments have been conducted to evaluate the performance of a bench-scale zinc-cerium RFB operating with a similar mixed electrolyte in the negative compartment. Although an increase in the concentration of $ZnCl_2$ from 0.3 $mol\,dm^{-3}$ to 0.6 $mol\,dm^{-3}$ does not lead to any further improvement of the CE during the half-cell experiments, we choose to use the higher amount of $ZnCl_2$ in the full-cell experiments due to its beneficial effect on the VE. Thus, an electrolyte containing 0.9 $mol\,dm^{-3}$ ZnMSA + 0.6 $mol\,dm^{-3}$ $ZnCl_2$ in 1 $mol\,dm^{-3}$ MSA in its discharged state is employed in the negative side of the RFB during the full-cell experiments. For comparison, the battery is also operated using an electrolyte composition of 1.5 $mol\,dm^{-3}$ ZnMSA in 1 $mol\,dm^{-3}$ MSA on the negative side that has been typically used in previous studies. In both cases, the positive electrolyte with the same composition of 0.8 $mol\,dm^{-3}$ CeMSA in 4 $mol\,dm^{-3}$ MSA when fully discharged is used. Unless stated otherwise, the positive and negative electrolyte volumes are 20 cm^3 and the operating temperature is 50°C.

Figure 6.3a shows a comparison of the charge-discharge profiles obtained for the battery with the MSA-only and mixed MSA-chloride negative electrolytes when operated at a current density of 25 $mA\,cm^{-2}$ for one cycle. In each case, the battery is charged for 1 hour and discharge is terminated when the cell voltage decreases to 0.5 V. The battery operated with 1.5 $mol\,dm^{-3}$ ZnMSA electrolyte exhibits a VE of 60% and CE of 68%. This performance is consistent with that obtained in a previous study on zinc-cerium RFBs by Leung et al who reported a VE of 74% and CE of 63% at a lower current density of 20 $mA\,cm^{-2}$ [12]. Our current results are in line with this earlier one since an increase in the current density would be expected to lead to a lower VE due to the enhancement of the ohmic resistance in the system [12]. On the other hand, the CE tends to rise with

increasing current density up to a threshold, above which it decreases due to enhancement of the side reactions during charge [12].

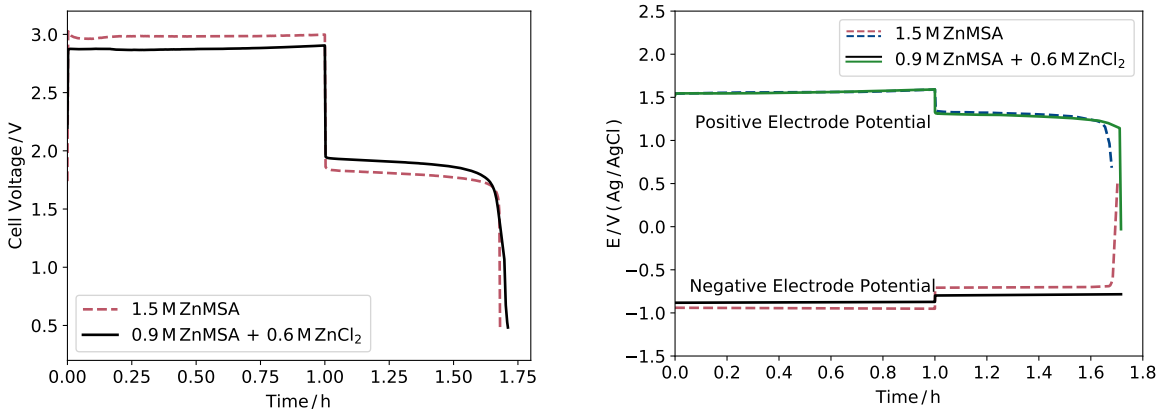

(a) (b)

Figure 6.3: Comparison of the performance of a zinc-cerium RFB operating with a 0.9 mol dm^{-3} ZnMSA + 0.6 mol dm^{-3} $ZnCl_2$ negative electrolyte in its discharge state with that obtained using a 1.5 mol dm^{-3} ZnMSA negative electrolyte. The base electrolyte in both cases is 1 mol dm^{-3} MSA. (a) Charge-discharge profiles at 25 mA cm^{-2} at 50°C with a 1-hour charge. (b) Corresponding potentials of the positive and negative electrodes measured versus Ag/AgCl reference electrode during the battery operation shown in (a).

The results in Figure 6.3a reveal that the switch from the MSA-only negative electrolyte to the mixed methanesulfonate-chloride electrolyte causes the VE to rise significantly, whereas it has only a small positive effect on the CE. The VE increases from 60% to 66% upon the addition of chloride ions. However, based on our half-cell experiments, one would have also expected a similar increase in the CE. In order to understand what has hindered the improvement in CE obtained in the mixed methanesulfonate-chloride electrolyte relative to that in the MSA-only solution, we examine the positive and negative electrode potentials that were also monitored during battery operation by installing reference electrodes in the set-up.

Figure 6.3b shows the potentials of both the positive and negative electrodes measured relative to the Ag/AgCl reference electrodes monitored during the battery charge-discharge cycle. The voltage efficiency of the negative electrode increases by 6% (from 74% to 80%) when the electrolyte is switched from the MSA-only solution to the mixed solution, which

is essentially the same as the improvement in the VE for the full cell. In the case of the MSA-only electrolyte, the zinc electrode potential begins to rise sharply after about 41 minutes of discharge, indicating that no more zinc metal remains on the negative PVE electrode for oxidation. On the other hand, when the mixed MSA-chloride electrolyte is used, no rise in the negative electrode potential is ever observed reflecting that some zinc metal still remains on the electrode for oxidation even at the end of the discharge. This is indeed confirmed when the battery is opened up at the end of the discharge cycle and the negative electrode is examined in each case. A layer of zinc metal is still visible on the PVE electrode when the mixed electrolyte is used, whereas it is completely gone in the case of the MSA-only electrolyte.

As shown in Figure 6.3b, the positive electrode potential remains unaffected by the change in the negative electrolyte composition since the composition of the positive electrolyte and the operating parameters have not been altered. The VE and CE values obtained for the positive electrode are 85% and 68%, respectively. Furthermore, as shown in Figure 6.3b, it is the potential of the positive electrode that drops after 41 minutes of discharge, indicating that the reduction of Ce(IV) to Ce(III) has become limiting by the end of discharge.

6.3.3 Battery charge/discharge curve during first cycle with partially charged positive electrolyte

From the above analysis, we conclude that the reactions at both electrodes are limiting to the system when pure MSA solution is used as the negative electrolyte. On the other hand, when a mixed MSA-chloride electrolyte is employed as the negative solution, the Zn/Zn(II) reaction is no longer the limiting factor and the Ce(III)/Ce(IV) reaction is solely responsible for the drop in the cell voltage. Thus, although we expect improvement in the CE upon addition of chloride to the negative electrolyte, the CE remains unaffected since the Ce(III)/Ce(IV) reaction is the main limiting factor of the system during the first cycle. Based on this idea, the CE of the full cell should have significantly improved if the Ce(III)/Ce(IV) half-cell reaction had not restricted the performance. This supposition can be tested if we measure the performance of the RFB when the limitations due to the cerium half-cell reaction are removed by raising the amount of Ce(IV) present at the start of the charge cycle.

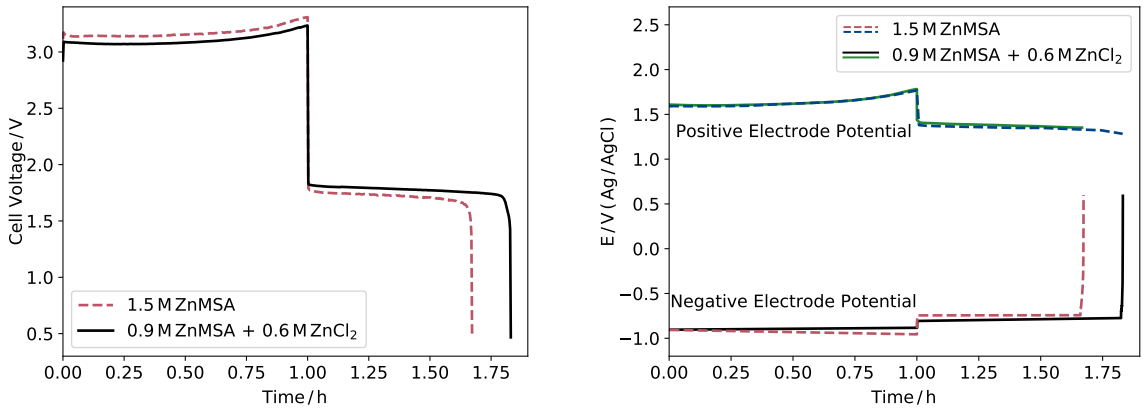

(a) (b)

Figure 6.4: Comparison of the performance of a zinc-cerium RFB operating with a 0.9 mol dm^{-3} ZnMSA + 0.6 mol dm^{-3} $ZnCl_2$ negative electrolyte in its discharge state with that obtained using a 1.5 mol dm^{-3} ZnMSA negative electrolyte. The base electrolyte in both cases is 1 mol dm^{-3} MSA. The positive electrolyte is charged for 30 minutes prior to the experiment. (a) Charge-discharge profiles at 25 mA cm^{-2} at 50°C with a 1-hour charge. (b) Corresponding potentials of the positive and negative electrodes measured versus Ag/AgCl reference electrode during the battery operation shown in (a).

To test the above proposal, a solution containing 0.7 mol dm^{-3} Ce(III) and 0.1 mol dm^{-3} Ce(IV) in 4 mol dm^{-3} MSA is made by charging the battery at 25 mA cm^{-2} for 30 minutes, using an initial positive electrolyte of 0.8 mol dm^{-3} Ce(III) in 4 mol dm^{-3} MSA. The Ce(IV) concentration of 0.1 mol dm^{-3} in the resulting solution is confirmed using the titration method described in the Experimental section. Then, this partially charged positive electrolyte is combined with the mixed MSA-chloride negative solution in its discharged state and the same charge-discharge cycle of 1 hour at 25 mA cm^{-2} used previously is applied to the battery. For comparison, the same procedure is repeated for the case where a fresh MSA-only solution is used on the negative side. Under this condition, the positive electrolyte no longer limits the battery performance and so we should be able to directly determine whether the addition of chloride ions improves the battery CE when the Zn/Zn(II) half-cell is the main limiting factor.

Figures 6.4a and 6.4b present the battery charge-discharge profiles and corresponding electrode potentials, respectively, obtained during the above experiments. As clearly shown, the expected large improvement in the CE is observed when the mixed MSA-

chloride electrolyte is used and the Zn/Zn(II) half-cell reaction is the limiting factor. As shown in Figure 6.4, the CE is increased significantly from 64% to 81% by the addition of Cl^- ions to the negative electrolyte. The electrode responses in Figure 4b confirm that the reduction of Ce(IV) to Ce(III) is not limiting to RFB performance since the positive electrode potential remains essentially unchanged even at the end of the discharge cycle, unlike the behaviour observed in Figure 6.4b. Moreover, the responses of the positive electrode trace each other identically regardless of the composition of the negative electrolyte. The negative electrode potentials, on the other hand, rise sharply at the end of their corresponding discharge cycles indicating that the Zn/Zn(II) reaction is limiting.

6.3.4 Battery charge/discharge curves over longer cycles

From the above experiments, we conclude that the advantage of using mixed MSA-chloride electrolyte can only be fully exploited when the zinc half-cell reaction is the limiting factor. Given that the presence of side-reactions and diffusional transport of protons across the membrane from the positive side to the negative side during charge [12] can shift the limiting reaction, it would be useful to investigate the effect of the mixed methanesulfonate-chloride electrolyte on the performance of the RFB over extended periods of cycling and compare it to that of the conventional MSA-only negative electrolyte.

Figure 6.5a shows the charge-discharge profiles of the battery operated for 5 cycles at 25 $mA\,cm^{-2}$ based on charging for 1 hour during each cycle in the case of both the MSA-only and mixed negative electrolytes. Figure 6.5b presents the corresponding positive and negative electrode potentials monitored during battery operation. As can be seen, when 1.5 $mol\,dm^{-3}$ ZnMSA electrolyte is used in the negative half-cell, the cell voltage required to charge the cell gradually increases as cycling continues. For example, the average charge voltage is 2.98 V during the first cycle, whereas it increases to 3.14 V by the fifth cycle. This trend was also observed in a previous life-cycle study of a zinc-cerium RFB and attributed to the inability to reduce all of the Ce(IV) on the positive side during discharge and the continual build-up of Ce(IV) and loss of Ce(III) from one cycle to the next [12], although no direct proof for this was provided. Examination of Figure 6.5b confirms that this increase in the cell voltage is caused by the rise in the potential of the positive electrode. The reason for this rise can be better understood by considering the responses of both electrode potentials in the case of 1.5 $mol\,dm^{-3}$ ZnMSA electrolyte. As mentioned previously, the reactions at both electrodes are limiting during the first cycle. However, from the second cycle onward, Figure 6.5b shows that the Zn/Zn(II) half-cell reaction is solely responsible for restricting the battery charge efficiency since only the potential of the negative electrode changes sharply at the end of each discharge. More reduction of

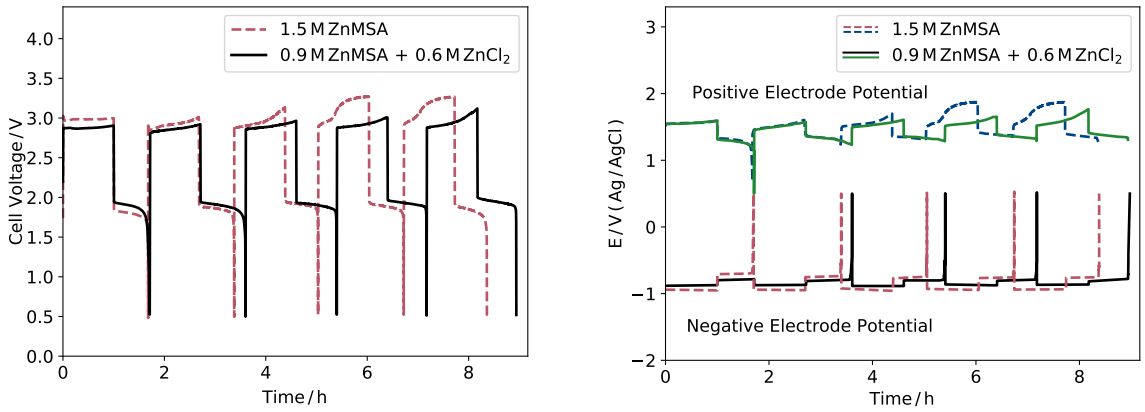

(a) (b)

Figure 6.5: Comparison of the performance of a zinc-cerium RFB operating with a 0.9 mol dm^{-3} ZnMSA + 0.6 mol dm^{-3} $ZnCl_2$ negative electrolyte in its discharge state with that obtained using a 1.5 mol dm^{-3} ZnMSA negative electrolyte. The base electrolyte in both cases is 1 mol dm^{-3} MSA. (a) Charge-discharge profiles for battery operated for 5 cycles at 25 mA cm^{-2} and 50°C with a 1-hour charge per cycle. (b) Corresponding potentials of the positive and negative electrodes measured versus Ag/AgCl reference electrode during the battery operation shown in (a).

Ce(IV) to Ce(III) would have occurred if the discharge cycle had not been cut short by complete depletion of the zinc deposit at the negative electrode. Consequently, not all of the Ce(IV) on the positive side is reduced back to Ce(III) during each discharge. Since less Ce(III) is available for oxidation with each successive charge cycle, battery charge becomes more difficult and thus the charge voltage increases over time. At the same time, the charge efficiency for zinc deposition at the negative electrode drops to 63% by the fifth cycle compared to 68% during the first cycle, which is due to the increased acidity in the negative half-cell as explained previously.

As evident from Table 6.2 and Figure 6.5, both the CE and VE of the battery are significantly higher when the mixed MSA-chloride electrolyte is used in the negative compartment. As in the case of the MSA-only electrolyte, the Zn/Zn(II) reaction still limits the performance of the battery. However, since the presence of chloride ions facilitates the Zn/Zn(II) redox reaction and increases the charge efficiency, each discharge can proceed longer before the cut-off cell voltage of 0.5 V is reached. This, of course, provides more time for the reduction of Ce(IV) to Ce(III) to take place. Consequently, less Ce(IV) accu-

mulates over time than in the case of the MSA-only electrolyte and so the cell voltage does not have to rise to as high values during charge. It should be noted that more Ce(IV) can be reduced to Ce(III) during discharge when the mixed MSA-chloride electrolyte is used on the negative side. However, not all of the Ce(IV) has been converted back to Ce(III) by the end of each discharge, leading to an increase in the cell voltage from 2.87 V to 2.95 V over the first 5 cycles. However, this rise is clearly smaller than in the case of the MSA-only electrolyte.

Table 6.2: Charge and voltage efficiencies extracted from Figure 6.5a at each cycle.

	1.5 ZnMSA		0.9 ZnMSA + 0.6 $ZnCl_2$	
Cycle number	Charge efficiency	Voltage efficiency%	Charge efficiency%	Voltage efficiency%
1	68	61	68	66
2	69	63	89	66
3	65	63	80	66
4	66	60	77	66
5	63	58	77	66
Average	66	61	78	66

As noted above, the CE in addition to the VE is enhanced by the presence of chloride ions after the first cycle (Figure 6.5 and Table 6.2). The CE increases significantly from 68% in the first cycle to 89% in the second cycle. This improvement is due partly to the better kinetics of the Zn/Zn(II) redox reaction in the mixed methanesulfonate-chloride electrolyte and partly to the fact that the Ce(III)/Ce(IV) reaction is the main limiting factor preventing the complete oxidation of zinc during the first cycle in the case of the mixed electrolyte (whereas both electrode reactions are limiting during the first cycle in the MSA-only electrolyte). Thus, some zinc remains on the negative electrode at the termination of the first discharge. However, the electrode responses in Figure 6.5b suggest that the Ce(III)/Ce(IV) reaction is no longer the limiting reaction by the second cycle and so discharge continues until all of the zinc metal has been oxidized. During the second discharge cycle, the zinc deposit that is oxidized includes metal left over from the first cycle and fresh metal deposited during the second charge. Thus, since more zinc is available for oxidation during the discharge phase of the second cycle, the charge efficiency increases as a result. Another reason for the increase in the CE is due to the presence of Cl^- which facilitates zinc deposition relative to H_2 evolution during charge. From the third cycle onward, the only source of zinc metal oxidized during discharge comes from the deposit formed during the charge of the same cycle since all the zinc has been removed from the electrode during the previous discharge. Thus, for the remaining cycles when the

Zn/Zn(II)) reaction is limiting, the higher CE is due solely to the presence of chloride ions.

6.3.5 Effect of current density on battery performance

The performance of the battery has also been studied at two other current densities in the presence of both the mixed and MSA-only negative electrolytes. Figure 6.6 shows the charge-discharge profiles of the battery operated for 5 cycles at current densities of 15 $mA\,cm^{-2}$ (Figure 6.6a) and 30 $mA\,cm^{-2}$ (Figure 6.6c) along with their half-cell potentials (Figure 6.6b and 6.6d, respectively). A charge duration of 1 hour per cycle is used in these experiments. The large improvement in the performance of the battery in the presence of chloride ions is evident at both current densities.

At the lower current density of 15 $mA\,cm^{-2}$, the discharge voltage quickly drops to the lower cut-off of 0.5 V in the first cycle for the case of MSA-only media, resulting in the immediate termination of the discharge process. On the basis of the potentials of the negative and positive electrodes during the first cycle in Figure 6.6b, it is clear that this problem is due to the rise in the negative electrode potential. In fact, the amount of zinc deposited during the first cycle at the lower current density of 15 $mA\,cm^{-2}$ and duration of 1 hour is not adequate for the battery to discharge properly. Importantly, this is not the case for the battery containing the mixed methanesulfonate-chloride negative electrolyte. The presence of chloride ions enables enough zinc to be deposited during charge that the battery is able to discharge properly with a charge efficiency of 60% after only the first hour of charging at a current density of 15 $mA\,cm^{-2}$. As shown in Table 6.3, the average VE and CE over the 5 cycles are 70% and 54% for the case of MSA-only media, while they are 74% and 73% for the battery with the mixed electrolyte. This reflects the beneficial role of chloride ions in enhancing the amount of deposited zinc, which allows a high CE to be maintained even at a low charge rate.

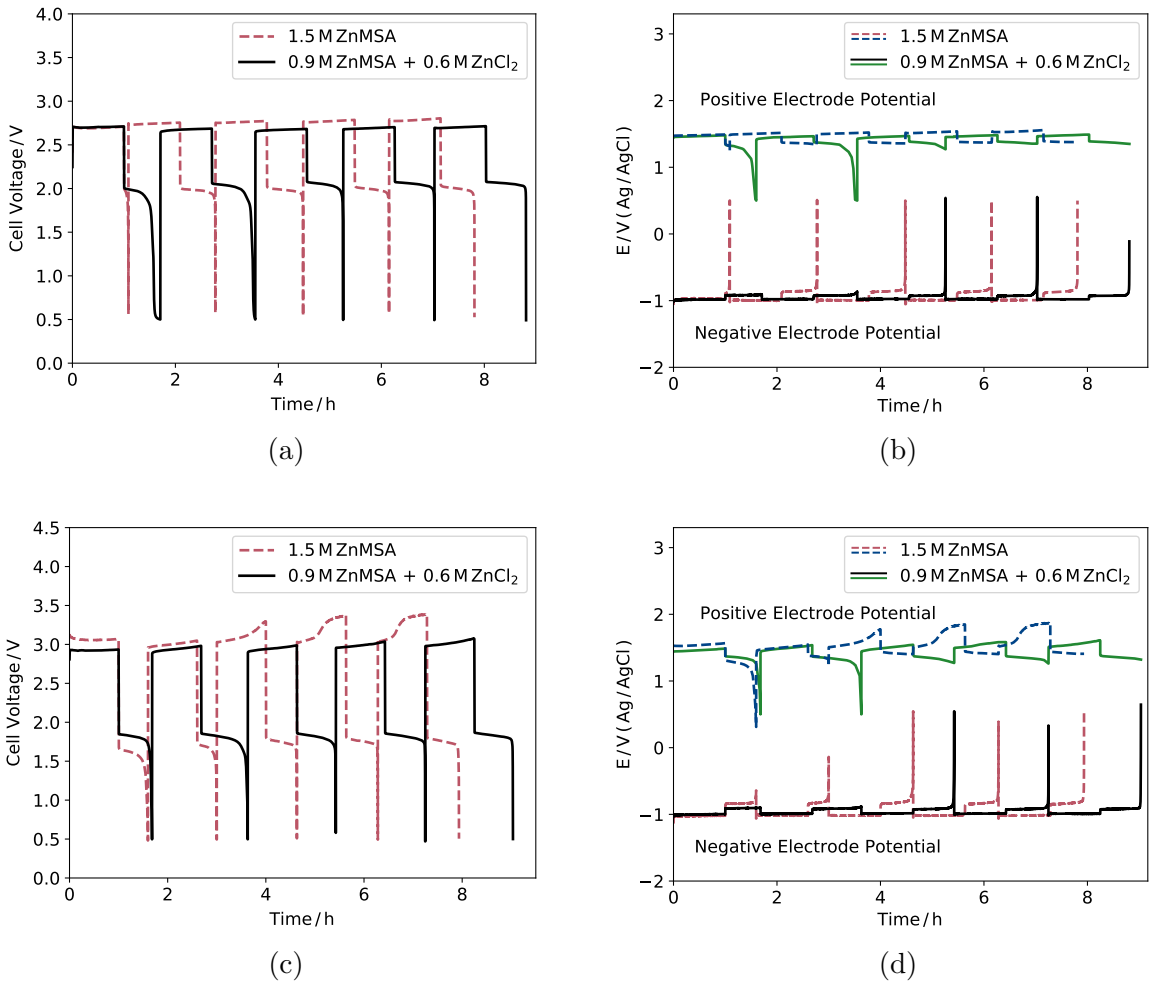

Figure 6.6: Comparison of the performance of a zinc-cerium RFB operating with a 0.9 mol dm^{-3} ZnMSA + 0.6 mol dm^{-3} $ZnCl_2$ negative electrolyte in its discharge state with that obtained using a 1.5 mol dm-3 ZnMSA negative electrolyte. The base electrolyte in both cases is 1 mol dm^{-3} MSA. (a) Charge-discharge profiles for battery operated for 5 cycles at 15 mA cm^{-2} (b) Corresponding potentials of the positive and negative electrodes measured versus Ag/AgCl reference electrode during the battery operation shown in (a). (c) Charge-discharge profiles for battery operated for 5 cycles at 30 mA cm^{-2} (b) Corresponding potentials of the positive and negative electrodes measured versus Ag/AgCl reference electrode during the battery operation shown in (c).

Table 6.3: Average charge and voltage efficiencies of the battery with mixed MSA-chloride negative electrolyte compared to that with pure MSA negative solution extracted from the galvanostatic charge/discharge experiments shown in Figure 6.6.

Electrolyte	i = 15 mA cm^{-2}		i = 30 mA cm^{-2}	
	CE%	VE%	CE%	VE%
0.9 ZnMSA + 0.6 $ZnCl_2$	73	74	80	60
1.5 ZnMSA	54	70	58	54

At the higher current density of 30 mA cm^{-2}, the average VE and CE for the battery containing the MSA-only media on the negative side are 54% and 58%, respectively. When compared to the battery operated at 25 mA cm^{-2}, it can be seen that the average CE has dropped 8% due to the enhanced rate of the HER at higher current densities. As evident from the half-cell electrode potentials in Figure 6.6d, from the first cycle forward, the low CE of the Zn/Zn(II)) redox reaction is responsible for the low battery CE in the case of the MSA-only media. However, in the presence of chloride ions, the battery is able to maintain a high CE throughput the five cycles. As shown in Table 6.3, the average VE and CE for the battery with the mixed electrolyte are 60% and 80%, respectively. This marks the significant advantage of the mixed electrolyte in facilitating the Zn/Zn(II) redox reaction which leads to a more than 20% improvement in the CE at a current density of 30 mA cm^{-2}.

6.3.6 Life-cycle analysis

The trends observed in the above experiment show that not only does the addition of chloride ions improve the battery CE and VE, but suggests that its life-cycle may also be expanded. Consequently, it is important to investigate the effect of the presence of chloride ions on the duration of the battery life.

Figure 6.7 presents the charge-discharge profiles obtained at 25 mA cm^{-2} with a 15-minute charge per cycle in the case of both the mixed methanesulfonate-chloride and conventional MSA-only negative electrolytes. As reported previously [12], the RFB life-cycle depends on the ratio of the electrolyte volume to the area of the working electrode. The higher this ratio, the more cycles can be applied. In the previous life-cycle analysis of this system, the volume of each electrolyte was set to 100 cm^3 [12]. Accordingly, in order to be able to make a fair comparison with this earlier study, we increased the volume of

each electrolyte to 100 cm^3 from 20 cm^3 for this experiment.

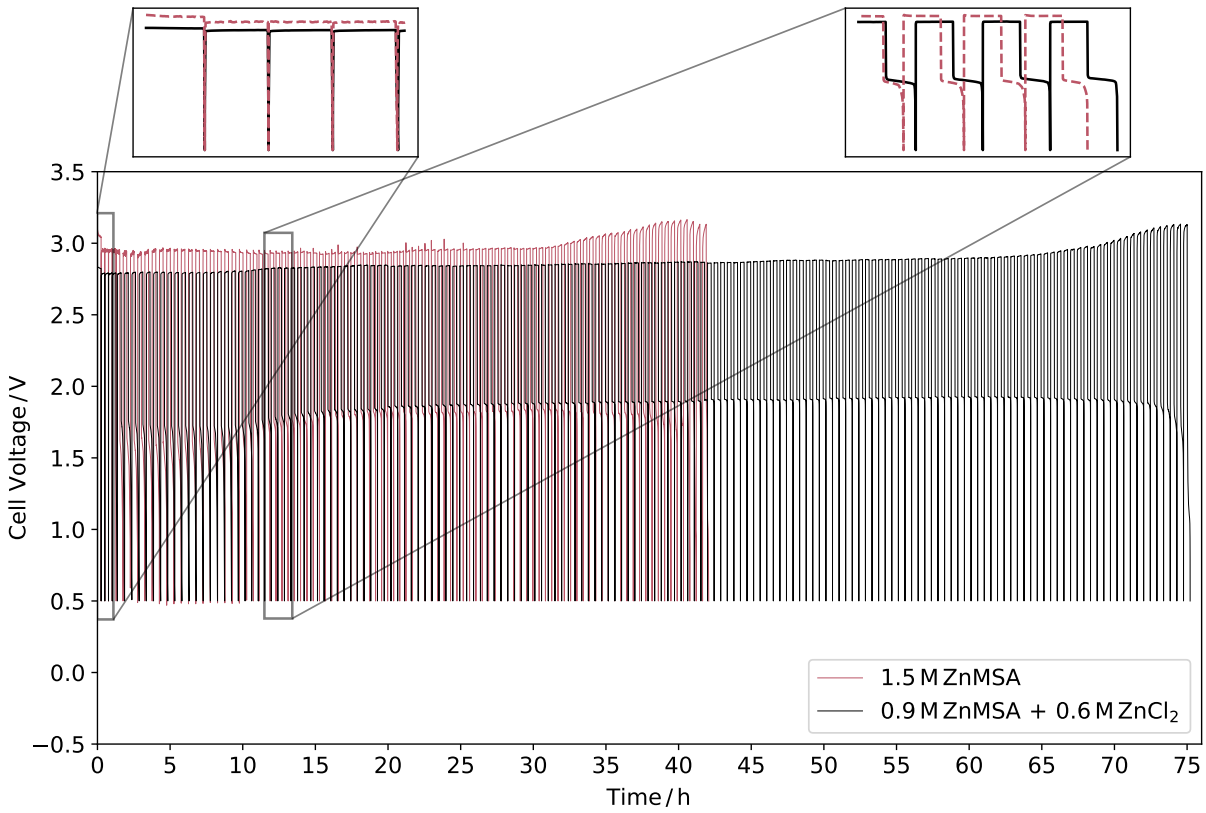

Figure 6.7: Comparison of the life-cycle analysis of a zinc-cerium RFB operating with a 0.9 mol dm^{-3} ZnMSA + 0.6 mol dm^{-3} $ZnCl_2$ negative electrolyte and with a 1.5 mol dm^{-3} ZnMSA negative electrolyte in its discharge state. Charge-discharge cycles at 25 mA cm^{-2} and 50°C with a charge duration of 15 minutes per cycle were applied. The base electrolyte in both cases is 1 mol dm^{-3} MSA. The initial sharp drops in the cell voltage during the early cycles and the normal charge/discharge profiles during the later cycles are shown by inserting the corresponding zoomed images.

As shown for both cases in Figure 6.7, the battery cell voltage drops almost immediately during discharge to the cut-off value of 0.5 V during the early cycles, similar to that reported previously [12]. A zoomed image of the early cycles is inserted in Figure 6.7 to clearly show the sharp drop in the battery cell voltage. This effect can be explained by the fact that the cumulative amount of Ce(IV) produced over the first few charge cycles when only 15

minutes of charge is allowed per cycle is still not sufficient for the battery to discharge properly and thus the cell voltage drops rapidly. After a few cycles, a sufficient amount of Ce(IV) has accumulated by the end of charge that the battery is now able to discharge normally. A zoomed image of the later cycles is also included in Figure 6.7.

For the case of 1.5 mol dm^{-3} ZnMSA in 1 mol dm^{-3} MSA, the battery is able to operate for $\sim$ 42 hours with 97 cycles at a current density of 25 mA cm^{-2}. In a previous life-cycle analysis of the zinc-cerium system [12], the RFB life was found to be $\sim$ 25 hours with 57 cycles when a current density of 50 mA cm^{-2} was used for a charge time of 15 minutes per cycle. The results obtained here appear to be in line with these previous results. Additionally, as shown in Table 6.4, the average CE and VE for the battery operated with the MSA-only electrolyte are 73.5% and 52.8%, respectively. This compares with CE and VE values of 84.9% and 46.2%, respectively, obtained in the previous life-cycle analysis for the same charge duration (15 minutes), but at a higher applied current density (50 mA cm^{-2}). As noted earlier, operation at a lower current density would be expected to increase the VE. Again, comparison of our results with those of the previous study show that they are in good agreement with each other.

Clearly the most noteworthy result shown in Figure 6.7 is the remarkable increase in the battery life observed when chloride ions are added to the negative electrolyte. The battery can now operate for more than 75 hours with 166 cycles, which represents $\sim$ 70% improvement compared to the life of the conventional zinc-cerium RFB. In addition, as presented in Table 6.4, when 0.9 mol dm^{-3} ZnMSA + 0.6 mol dm^{-3} $ZnCl_2$ is used on the negative side, the cell voltage during every cycle is lower during charge and higher during discharge than that observed when the MSA-only electrolyte is used on the negative side. As a result, the CE and VE rise to 83.2% and 62.4%, respectively, leading to a more than 13% improvement in the EE compared to the conventional zinc-cerium RFB. Thus, employing mixed methanesulfonate-chloride electrolytes in the negative half-cell of a zinc-cerium RFBs both extends the battery life-cycle and enhances the CE and VE efficiencies during battery operation.

Table 6.4: Life-cycle analysis of zinc-cerium redox flow battery charged at 25 mA cm^{-2}

Composition (mol dm^{-3})	Average charge voltage (V)	Average discharge voltage (V)	Average CE%	Average VE%	Average EE%
1.5 ZnMSA	2.97	1.57	73.5	52.8	38.8
0.9 ZnMSA + 0.6 $ZnCl_2$	2.87	1.79	83.2	62.4	51.9

6.4 Conclusions

The significant benefits of mixed methanesulfonate-chloride negative electrolyte compared to pure methanesulfonic acid negative electrolyte were explored by performing both half-cell and full-cell experiments. The results of the half-cell experiments are summarized below:

- Cyclic voltammetry and polarization experiments on a polyvinyl ester (PVE) composite electrode showed that the addition of chloride ions significantly increased the amount of deposited zinc, reduced the nucleation overpotential and enhanced the exchange current densities.
- Galvanostatic half-cell studies showed more than 30% improvement in the energy efficiency of the Zn/Zn(II) reaction due to the enhancement in both the charge and voltage efficiencies when chloride ions are added to the electrolyte.

These promising half-cell experiments were used as the basis for full-cell experiments using a bench-scale redox flow battery. A particularly useful aspect of the full cell RFB set-up was the installation of reference electrodes which allowed the potentials of both electrodes to be monitored during battery operation. The results of the full-cell experiments are summarized below:

- During the first cycle, the voltage efficiency of the battery increased when the new mixed MSA-chloride negative electrolyte was used. However, the charge efficiency over the first cycle remained unaffected since the Ce(III)/Ce(IV) redox reaction was the limiting factor during discharge.
- When the battery was operated over many cycles, a dramatic improvement in its charge efficiency in the presence of chloride ions was achieved. This improvement stems from the fact that the Zn/Zn(II) reaction eventually becomes the limiting factor over longer cycles so that the advantage of employing the mixed MSA-chloride electrolyte comes into play.
- In addition to higher charge and voltage efficiencies, the use of the mixed MSA-chloride negative electrolyte also reduced the build-up of Ce(IV) in the positive electrolyte at the end of each cycle since it enabled longer discharge times.

- A significant improvement in the battery life-cycle was observed when the mixed electrolyte was employed compared to that obtained with the conventional pure MSA electrolyte. Whereas the battery containing pure MSA negative electrolyte was able to operate for $\sim$ 42 hours with 97 cycles at a current density of 25 $\mathrm{mA\,cm^{-2}}$, it was able to operate for more than 75 hours with 166 cycles when mixed MSA-chloride was used on the negative side.

Chapter 7

A Two-Dimensional Transient Model for a Zinc-Cerium Redox Flow Battery Validated by Extensive Experimental Data[1]

7.1 Introduction

Despite the attractiveness of zinc-cerium RFBs, no multi-physics model has yet been developed to aid in the understanding of their performance. The need to develop a validated mathematical model for zinc-cerium RFBs has been noted various times in the literature [86, 87]. Hence, the objective of the present chapter is to develop and validate a comprehensive model of a zinc-cerium RFB. In this study, a two-dimensional transient model combining all three modes of transport (migration, diffusion and convection) coupled with electrode kinetics is developed for the first time for zinc-cerium RFBs. The model is then fit to and validated against an extensive set of experimental data obtained in our laboratory comprising full-cell voltages, positive and negative electrode potentials monitored via reference electrodes inserted into the battery set-up and Ce(IV) concentrations in the positive electrolyte measured by colorimetric titration. To the best of our knowledge, this is the most comprehensive comparison carried out between the output of any RFB model and experimental data extracted during actual battery operation. The validated model

[1]This chapter is adapted from my submitted manuscript "Two-dimensional transient model for a zinc-cerium redox flow battery validated by extensive experimental data".

is then used to predict the performance of the battery under different conditions. Based on these simulation results, important recommendations for achieving a high-performance zinc-cerium RFB are provided.

7.2 Experimental

The setup of the bench-scale single-cell zinc-cerium RFB used in the present study is shown in Figure 7.1. The positive electrode employed for the Ce(III)/Ce(IV) redox reaction was a three-dimensional platinized titanium mesh (Figure 7.1b) with a Pt loading level of 7 $\mathrm{mg\,cm^{-2}}$ (Metakem GmbH). The electrode was fabricated by spot-welding a mesh stack consisting of four 1.5 mm thick platinised titanium mesh layers onto a 6 mm thick platinised titanium plate current collector. The negative electrode employed for the Zn/Zn(II) reaction was a planar 6 mm-thick polyvinyl ester (PVE) carbon (TDM Fuel Cells) in contact with a copper current collector (McMaster-Carr) (Figure 7.1c). Both the positive and negative electrodes had an apparent active surface area of 2 cm × 4.5 cm. As shown in Figures 7.1b and 7.1c, a 6 mm-thick acrylic flow channel (acrylic sheets from CIP Wholesale) was used in each compartment. The two half-cells were separated by a Nafion 117 cation exchange membrane. The electrodes, flow channels and membrane were separated by rubber silicone gaskets (CS Hyde Company). The geometric dimensions of the battery employed in the experimental study and used in the model are listed in Table 7.1.

In the fully discharged state, the negative and positive electrolytes contained 1.5 $\mathrm{mol\,dm^{-3}}$ zinc methanesulfonate in 1 $\mathrm{mol\,dm^{-3}}$ MSA and 0.8 $\mathrm{mol\,dm^{-3}}$ cerous methanesulfonate in 4 $\mathrm{mol\,dm^{-3}}$ MSA, respectively. A Longer peristaltic pump with two channel heads (model YZ1515) and Viton tubing (McMaster-Carr) was employed to pump the electrolytes from two external 30 $\mathrm{cm^3}$ reservoirs to the battery. The temperature of both solutions was maintained at 50°C by employing a temperature bath (Neslab RTE-8). In addition to the cell voltage, the positive and negative electrode potentials were measured *in situ* by inserting two Ag/AgCl reference electrodes (Pine Research Instrumentation) close to the inlets of the flow frames on each side of the battery. The battery was galvanostatically cycled at a current density of 25 $\mathrm{mA\,cm^{-2}}$ with a charge duration of 1 hour. The discharge cycle was terminated when the discharge cell voltage dropped to 0.5 V. After each full charge/discharge cycle, a 0.2 $\mathrm{cm^3}$ sample was collected from the positive electrolyte and titrated to determine the Ce(IV) concentration in the positive half-cell. The titration was conducted using 99% pure ammonium iron(II) sulfate hexahydrate (Sigma-Aldrich) with ferroin (1,10-phenanthroline iron(II) sulfate) (Alfa Aesar) as a colorimetric redox indicator.

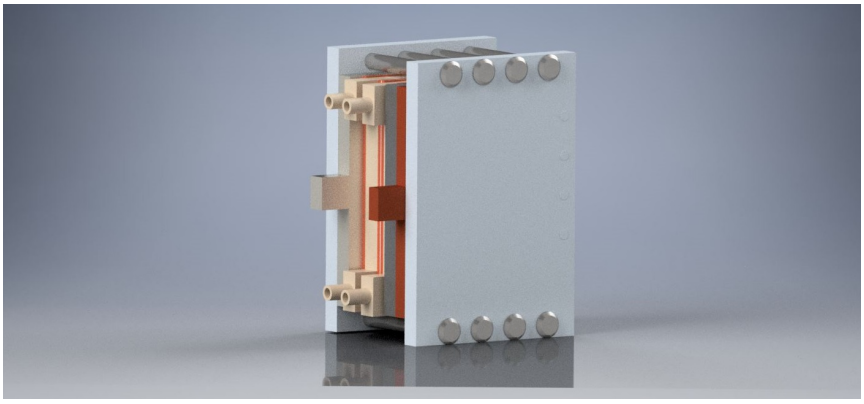

(a)

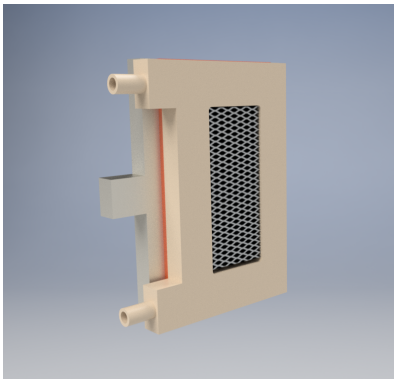

(b)

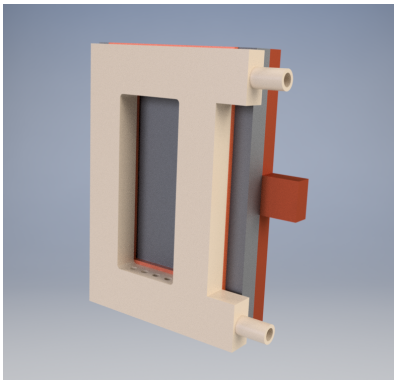

(c)

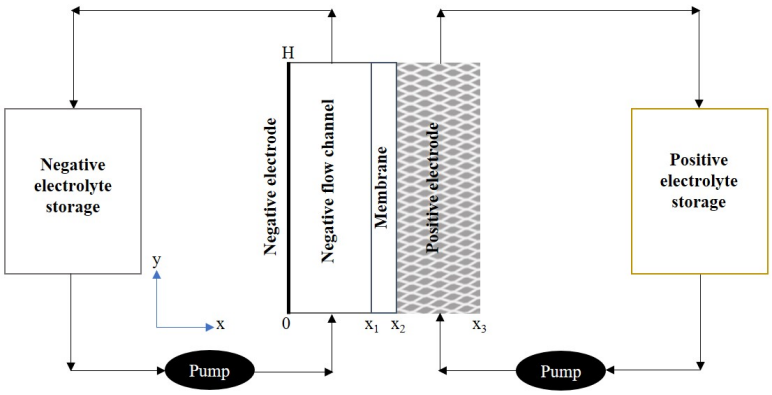

(d)

Figure 7.1: (a) Battery full-cell assembly. (b) Positive half-cell assembly consisting of a 3-dimensional platinized titanium mesh electrode and a flow channel. (c) Negative half-cell assembly consisting of a planar PVE carbon electrode and a flow channel. The carbon electrode is connected to a copper current collector. (d) Schematic of two-dimensional model.

Table 7.1: Battery geometry parameters.

Quantity	Symbol	Value
Electrode height	H	45 mm
Electrode width	L_w	20 mm
Positive electrode porosity	ϵ	0.758
Positive electrode specific surface area	a	150 m^{-1a}
Flow channel thickness	L_f	6 mm
Membrane thickness	L_m	180 µm

[a]Fitted

7.3 Model Assumptions and Equations

Figure 7.1d presents a schematic diagram of the two-dimensional geometry used of the system which includes the main components of a zinc-cerium RFB (i.e., negative and positive electrodes, membrane and storage tanks). The x- and y-directions correspond to thickness and height, respectively. The negative electrode is a planar PVE carbon sheet located at $x = 0$ and the electrolyte flows along the electrode in the space $0 < x < x_1$ between the negative electrode and the membrane located at $x = x_1$. The electrolyte on the positive side flows through a platinized titanium mesh that fills the positive compartment between $x_2 < x < x_3$. Both zinc electrodeposition/electrodissolution and hydrogen evolution are considered to occur at the negative electrode:

$$\begin{aligned} &\mathrm{Zn(II)} + 2\,\mathrm{e^-} \underset{\text{discharge}}{\overset{\text{charge}}{\rightleftharpoons}} \mathrm{Zn} && E = -0.757\ V\ vs.\ SHE \\ &2\,\mathrm{H^+} + 2\,\mathrm{e^-} \xrightarrow{\text{charge}} \mathrm{H_2} && E = 0.0\ V\ vs.\ SHE \end{aligned} \tag{7.1}$$

On the positive electrode, both the Ce(III)/Ce(IV) redox reaction and oxygen evolution occur, i.e.,

$$\begin{aligned} &\mathrm{Ce(III)} \underset{\text{discharge}}{\overset{\text{charge}}{\rightleftharpoons}} \mathrm{Ce(IV)} + \mathrm{e^-} && E = 1.28 - 1.72\ V\ vs.\ SHE \\ &\mathrm{H_2O} \xrightarrow{\text{charge}} \frac{1}{2}\mathrm{O_2} + 2\,\mathrm{H^+} + 2\,\mathrm{e} && E = 1.23\ V\ vs.\ SHE \end{aligned} \tag{7.2}$$

The model accounts for transport of charged species through both electrolytes by diffusion, migration and convection. The following simplifying assumptions are applied to the model:

1. Both electrolytes are incompressible and flow under laminar conditions.
2. Dilute solution theory is applied to both electrolytes.
3. The cation exchange membrane is permeable to protons only. The crossover of other ions and water is neglected. The transfer of water between the two compartments becomes significant when the battery operates for very long durations, but can be neglected over the few cycles investigated in the present study.
4. The effects of gas bubbles produced by the side reactions on the electrolyte volume fraction and electrode ohmic resistance are neglected.
5. Gravity effects are not considered.
6. The battery operates under isothermal conditions.
7. No homogeneous chemical reactions occur in either electrolyte.

7.3.1 Negative electrolyte

On the negative side of the battery, the electrolyte which contains k $=\{\mathrm{Zn(II)}, \mathrm{H^+}, \mathrm{CH_3SO_3^-}\}$ ions, flows through the flow channel between $0 < x < x_1$ (Figure 7.1d). Mass conservation of each of the ions in the negative electrolyte yields:

$$\frac{\partial c_k}{\partial t} + \nabla.\vec{N_k} = 0 \tag{7.3}$$

where $c_k(x, y, t)$ and $\vec{N_k}(x, y, t)$ are the concentration and molar flux of species k, respectively, at location (x, y) within the electrolyte at time t. These fluxes are calculated using the Nernst-Planck equation which includes transport by diffusion, migration and convection:

$$\vec{N_k} = -D_k \nabla c_k - \frac{z_k c_k D_k F}{RT} \nabla \phi_{e,neg} + \vec{v}_{neg} c_k \tag{7.4}$$

where D_k and z_k are the diffusion coefficient and charge of species k, respectively, and $\phi_{e,neg}(x,y,t)$ is the electrical potential within the negative electrolyte. $\vec{v}_{neg}(x,y,t)$ is the velocity of the negative electrolyte and is calculated using the Navier-Stokes equation for an incompressible fluid:

$$\rho\left(\frac{\partial\vec{v}_{neg}}{\partial t}+\vec{v}_{neg}.\nabla\vec{v}_{neg}\right)=-\nabla\vec{P}_{neg}+\mu\nabla^2\vec{v}_{neg} \tag{7.5}$$

where ρ is the constant fluid density, $\vec{P}_{neg}(x,y,t)$ is the pressure vector in the negative electrolyte and μ is the dynamic viscosity of the fluid. Due to the incompressibility assumption, the continuity expression for the fluid becomes:

$$\nabla.\vec{v}_{neg}=0 \tag{7.6}$$

The concentrations of the species within the electrolyte are linked by the electroneutrality condition:

$$\sum_k z_k c_k=0 \tag{7.7}$$

The current density produced by the flux of each charged species k in the electrolyte is:

$$\vec{i}_{e_k}=z_kF\vec{N}_k \tag{7.8}$$

Substitution of Eqn 7.4 into Eqn 7.8 yields:

$$\vec{i}_{e_k}=z_kF(-D_k\nabla c_k)+z_kF(-\frac{z_kc_kD_kF}{RT}\nabla\phi_{e,neg})+z_kF(\vec{v}_{neg}c_k) \tag{7.9}$$

When this quantity is added up over all the charged species, the total current density across the electrolyte is obtained, i.e.,

$$\vec{i}_e=\sum_k\vec{i}_{e_k}=F\sum z_k(-D_k\nabla c_k)-\frac{F^2}{RT}\sum_k z_k^2D_kC_k\nabla\phi_{e,neg} \tag{7.10}$$

7.3.2 Positive electrolyte

As shown in Figure 7.1d, the spacing between x_2 and x_3 that defines the positive compartment is completely filled with a platinized-titanium mesh electrode, unlike the negative side of the battery. The electrolyte, which contains j={Ce(III), Ce(IV), H^+, $CH_3SO_3^-$} ions, flows through the expanded metal mesh. Thus, the conservation of mass on the positive side is different from that given in Eqn 7.3 and instead can be written as:

$$\frac{\partial \epsilon c_j}{\partial t} + \nabla . \vec{N_j} = S_j \tag{7.11}$$

where $S_j(x, y, t)$ is the source term due to the electrochemical reaction occurring on the expanded metal mesh throughout the region between x_2 and x_3. It is given by:

$$S_j = \sum_r \frac{a \nu_{j,r} i_r}{n_r F} \tag{7.12}$$

where r is an index denoting a redox reaction, a is the specific surface area of the expanded mesh and $\nu_{j,m}$ is the stoichiometric coefficient of species j in reaction r written in the reduction direction. Note that the flux term $\vec{N_j}(x, y, t)$ in Eqn 7.11:

$$\vec{N_j} = -D_j^{eff} \nabla c_j - \frac{z_j c_j D_j^{eff} F}{RT} \nabla \phi_{e,pos} + \vec{v}_{pos} c_j \tag{7.13}$$

contains the effective diffusion coefficient D_j^{eff} of species j that accounts for the porosity ϵ of the positive electrode and is related to the molecular diffusion coefficient D_j through the Bruggemann correction:

$$D_j^{eff} = \epsilon^{1.5} D_j \tag{7.14}$$

Additionally, $\phi_{e,pos}$ is the electrical potential within the positive electrolyte.

Due to conservation of charge, the charge entering the electrolyte is equal to the charge leaving the solid electrode in a porous system. Thus,

$$\nabla . \vec{i}_{pos} = \nabla . \vec{i}_{s,pos} + \nabla . \vec{i}_{e,pos} = 0 \tag{7.15}$$

where $\vec{i}_{e,pos}$ and $\vec{i}_{s,pos}$ are the ionic and electronic current densities on the positive side, respectively. The potential $\phi_{s,pos}$ in the positive solid electrode is found using Ohm's law:

$$\vec{i}_{s,pos} = -\sigma_s^{eff} \nabla \phi_{s,pos} \tag{7.16}$$

where σ_s^{eff} is the effective electrical conductivity of the porous electrode related to the conductivity σ_s of the bulk material making up the electrode through the Bruggemann correction:

$$\sigma_s^{eff} = \epsilon^{1.5} \sigma_s \tag{7.17}$$

The velocity term on the positive side obeys Darcy's law, describing fluid flow in a porous medium is given by:

$$\vec{v}_{pos} = \frac{-k_{kc}}{\mu_{dyn}} \nabla P_{pos} \tag{7.18}$$

where μ_{dyn} is the dynamic viscosity of the fluid and k_{kc} is the intrinsic permeability of the platinized-titanium mesh. Due to the incompressibility condition, the continuity equation shown in Eqn 7.6 is also valid on the positive side (i.e., $\nabla . \vec{v}_{pos} = 0$) .

The Ce(III)/Ce(IV) redox reaction and oxygen evolution occur on the solid surfaces of the expanded metal mesh that fills the positive space. The kinetics of the Ce(III)/Ce(IV) reaction is described by the Butler-Volmer equation:

$$i_{Ce} = i_{Ce,0} \left[\frac{c_{Ce(III),s}}{c_{Ce(III)}} \exp\left(\frac{\alpha_{a,Ce} F}{RT} \eta_{Ce} \right) - \frac{c_{Ce(IV),s}}{c_{Ce(IV)}} \exp\left(-\frac{\alpha_{c,Ce} F}{RT} \eta_{Ce} \right) \right] \tag{7.19}$$

where $c_{j,s}(x, y, t)$ is the concentration of species j at the interface of the expanded metal mesh and positive electrolyte and $c_j(x, y, t)$ is the bulk concentration of species j at the same location of the electrode, which is the same as the concentration shown in Eqn 7.13. $\alpha_{a,Ce}$ and $\alpha_{c,Ce}$ are the anodic and cathodic transfer coefficients and $i_{Ce,0}$ is the exchange current density for the Ce(III)/Ce(IV) reaction on the positive side. η_{Ce} is the overpotential for the Ce(III)/Ce(IV) reaction given as:

$$\eta_{Ce} = E_{Ce} - E_{Ce}^{eq} = \phi_{s,pos} - \phi_{e,pos} - E_{Ce}^{eq} \tag{7.20}$$

where E^{eq}_{Ce} is the equilibrium potential for the Ce(III)/Ce(IV) reaction determined using the Nernst equation:

$$E^{eq}_{Ce} = E^{0}_{Ce} + \frac{RT}{nF} \ln\left(\frac{c_{Ce(IV)}}{c_{Ce(III)}}\right) \tag{7.21}$$

E^{0}_{Ce} is the standard potential of the Ce(III)/Ce(IV) reaction and n is the number of electrons transferred during the redox reaction ($n = 1$ in this case). The use of the Butler-Volmer equation according to Eqn 7.19 requires expressions for the Ce(III) and Ce(IV) concentrations at the electrode surface. The relation between the surface and bulk concentrations is obtained by balancing the rate of reaction on the electrode surface with the rate of mass transfer to (or from) the electrode, i.e.,

$$\begin{aligned} &Fk_{m,Ce(III)}(c_{Ce(III)} - c_{Ce(III),s}) = \\ &i_{Ce,0}\left[\frac{c_{Ce(III),s}}{c_{Ce(III)}} \exp\left(\frac{\alpha_{a,Ce}F}{RT}\eta_{Ce}\right) - \frac{c_{Ce(IV),s}}{c_{Ce(IV)}} \exp\left(-\frac{\alpha_{c,Ce}F}{RT}\eta_{Ce}\right)\right] \end{aligned} \tag{7.22}$$

$$\begin{aligned} &Fk_{m,Ce(IV)}(c_{Ce(IV)} - c_{Ce(IV),s}) = \\ &i_{Ce,0}\left[\frac{c_{Ce(IV),s}}{c_{Ce(IV)}} \exp\left(-\frac{\alpha_{c,Ce}F}{RT}\eta_{Ce}\right) - \frac{c_{Ce(III),s}}{c_{Ce(III)}} \exp\left(\frac{\alpha_{a,Ce}F}{RT}\eta_{Ce}\right)\right] \end{aligned} \tag{7.23}$$

where $k_{m,Ce(III)}$ and $k_{m,Ce(IV)}$ are the mass transfer coefficients of Ce(III) and Ce(IV), respectively. $k_{m,i}$ is approximated by relating it to the species diffusion coefficient as follows: $k_{m,i} \approx D_i/d$, where d is the inter-fiber distance in the porous electrode [74–77]. With this approximation, the mass transfer coefficients of Ce(III) and Ce(IV) can be related to each other through their diffusion coefficients:

$$k_{m,Ce(III)} = \frac{D_{Ce(III)}}{D_{Ce(IV)}} \times k_{m,Ce(IV)} \tag{7.24}$$

The Ce(III) and Ce(IV) concentrations at the electrode surface are related to the bulk concentrations by combining Eqns 7.22 and 7.23 to yield:

$$c_{Ce(III),s} = \frac{A_c c_{Ce(IV)}(\frac{k_{m,Ce(IV)}}{k_{m,Ce(III)}}) + (1 + A_c)c_{Ce(III)}}{1 + A_c + A_a} \tag{7.25}$$

$$c_{Ce(IV),s} = \frac{A_a c_{Ce(III)}(\frac{k_{m,Ce(III)}}{k_{m,Ce(IV)}}) + (1 + A_a)c_{Ce(IV)}}{1 + A_c + A_a} \tag{7.26}$$

where

$$A_a = \frac{i_{Ce,0}}{F k_{m,Ce(III)} c_{Ce(III)}} \exp\left(\frac{\alpha_{a,Ce} F \eta_{Ce}}{RT}\right) \tag{7.27}$$

$$A_c = \frac{i_{Ce,0}}{F k_{m,Ce(IV)} c_{Ce(IV)}} \exp\left(-\frac{\alpha_{c,Ce} F \eta_{Ce}}{RT}\right) \tag{7.28}$$

The kinetics of oxygen evolution on the positive electrode during charge is described by the following Butler-Volmer equation:

$$i_{O_2} = i_{O_2,0} \exp\left(\frac{\beta'_{O_2} F}{RT} \eta_{O_2}\right) \tag{7.29}$$

where η_{O_2} is the overpotential associated with the OER and is given by:

$$\eta_{O_2} = \phi_{s,pos} - \phi_{e,pos} - E^0_{O_2} \tag{7.30}$$

where $E^0_{O_2}$ is the formal potential of the OER. The cathodic direction is not included in Eqn 7.29 since oxygen evolution occurs only during battery charge.

7.3.3 Membrane

As noted previously, we assume that the membrane is permeable to only protons in the present model. The crossover of protons maintains electroneutrality of both electrolytes as the electrode reactions occur. The membrane contains a certain concentration c_f of fixed sulfonate sites with negative charge $z_f = -1$. Since H^+ ions are the only mobile species within the membrane, the concentration of c_{H^+} inside the membrane always remains fixed at c_f to maintain electroneutrality. Thus, although the H^+ concentrations in the positive and negative compartments are very different, no concentration gradient exists within the membrane itself. Additionally, no fluid convection through the membrane is considered.

Thus, transport of the protons through the membrane occurs exclusively via migration and is governed by Ohm's law:

$$\vec{i}_m = \sigma_m \nabla \phi_m \tag{7.31}$$

where σ_m is the membrane conductivity and ϕ_m is the membrane potential. Additionally, the Donnan effect is taken into account at the membrane/electrolyte interfaces in the positive and negative compartments in determining σ_m, as will be discussed in Section 7.3.4. This effect arises because of the difference in proton concentration in the membrane and on each side of the membrane/electrolyte interface which leads to an electric potential difference across each interface [175].

7.3.4 Boundary conditions

Figure 7.1d should be recalled for the discussion of the boundary conditions. The Zn/Zn(II) reaction and HER occur at the surface of the negative electrode located at boundary $x = 0$. The following Butler-Volmer equation is used to describe the kinetics of the Zn/Zn(II) reaction [176]:

$$i_{Zn} = i_{Zn,0} \left[\frac{c_{\mathrm{Zn}}}{c_{\mathrm{Zn},ref}} \exp\left(\frac{\alpha_{a,Zn} n F}{RT} \eta_{Zn} \right) - \frac{c_{\mathrm{Zn(II)}}}{c_{\mathrm{Zn(II)},ref}} \exp\left(-\frac{\alpha_{c,Zn} n F}{RT} \eta_{Zn} \right) \right] \tag{7.32}$$

where c_i is the concentration of species i and $c_{i,ref}$ is the reference concentration of species i. $c_{Zn(II),ref}$ is set to 1.5 $\mathrm{mol\,dm^{-3}}$ which matches the total bulk zinc concentration, while $c_{Zn,ref}$ is set to 1 M. α_{Zn} is the transfer coefficient and $i_{Zn,0}$ is the exchange current density associated with the Zn/Zn(II) reaction. As evident from Eqn 7.32, the rate of the Zn/Zn(II) reaction is assumed to be kinetically controlled. This assumption is valid since the available zinc concentration for the negative half-cell reaction is large (1500 $\mathrm{mol\,m^{-3}}$). As shown by the model and discussed later in Section 7.5.1 (Figure 7.4a), very little depletion of Zn(II) occurs at the negative electrode during each discharge cycle throughout battery operation. Thus, the rate of Zn(II) reduction should not be affected by the transport of the reactant to and from the negative electrode. It is important to note the c_{Zn} and $c_{Zn,ref}$ terms in the first term of Eqn 7.32. These terms are included to account for the fact that the negative electrode is coated with only a finite amount of zinc at any time during battery operation. c_{Zn} gives the amount of metal on the electrode surface at any point during discharge/charge. α_{Zn} is the transfer coefficient and $i_{Zn,0}$ is the exchange current

density associated with the Zn/Zn(II) reaction. Moreover, η_{Zn} is the overpotential for the Zn/Zn(II) reaction:

$$\eta_{Zn} = E_{Zn} - E_{Zn}^{eq} = \phi_{s,neg} - \phi_{e,neg} - E_{Zn}^{eq} \tag{7.33}$$

E_{Zn}^{eq} is the equilibrium potential of the Zn/Zn(II) reaction calculated using the Nernst equation:

$$E_{Zn}^{eq} = E_{Zn}^{0} + \frac{RT}{nF} \ln\left(\frac{\mathrm{c_{Zn(II)}}}{\mathrm{c_{Zn(II),ref}}}\right) \tag{7.34}$$

In addition to the zinc redox reaction, hydrogen evolution also occurs on the negative electrode. The current density for this reaction is:

$$i_{H_2} = i_{H_2,0}\left[-\frac{c_{H^+,neg}}{c_{H^+,b}} \exp\left(-\frac{\beta'_{H_2} F}{RT}\eta_{H_2}\right)\right] \tag{7.35}$$

The anodic direction for this reaction is not included in the Butler-Volmer equation above since hydrogen evolution occurs only during battery charge. The overpotential η_{H_2} associated with the HER is given by:

$$\eta_{H_2} = \phi_s - \phi_e - E_{H_2}^{0} \tag{7.36}$$

where $E_{H_2}^{0}$ is the formal potential of the HER.

It is assumed that only protons cross the membrane. Thus, at the interfaces between the membrane and the two electrolytes, the flux of each species other than protons is set to zero, i.e.,

$$\begin{cases} \vec{N}_k.\vec{n} = 0 & @(x = x_1, y) \\ \vec{N}_j.\vec{n} = 0 & @\,(x = x_2, y) \end{cases} \quad \text{(except for protons)} \tag{7.37}$$

At the electrolyte/membrane interface, the membrane potential ϕ_m is related to the electrolyte potential ϕ_e by the Donnan effect:

$$\phi_m = \phi_e + \frac{RT}{F}\ln(\frac{c_{H^+,e}}{c_{H^+,m}}) \quad @\begin{cases}(x = x_1, y) \\ (x = x_2, y)\end{cases} \tag{7.38}$$

where $c_{H^+,m}$ is the proton concentration in the Nafion 117 membrane. Since electroneutrality must be maintained in the membrane, $c_{H^+,m}$ obtained from:

$$c_{H^+,m} = -z_f c_f \tag{7.39}$$

where z_f and c_f are the known charge and concentration of the fixed sulfonate sites in the Nafion membrane, respectively. Additionally, all of the current that passes through the electrolyte must also pass through the membrane, i.e.,

$$\vec{i}_e \cdot \vec{n} = \vec{i}_m \cdot \vec{n} \quad @ \begin{cases} (x = x_1, y) \\ (x = x_2, y) \end{cases} \tag{7.40}$$

The battery considered in this study is operated galvanostatically. Thus, the current density at each electrode is set to the applied current density. Furthermore, we assume that the negative electrode is grounded. This leads to the following conditions:

$$\begin{array}{lll} \phi_s = 0 & @ \quad (0, y) & \\ i = i_{app} & @ \quad (x_3, y) & \text{, (during charge)} \\ i = -i_{app} & @ \quad (x_3, y) & \text{, (during discharge)} \end{array} \tag{7.41}$$

where i_{app} is the magnitude (i.e., positive) of the applied current density.

Since the species concentrations change over time, the boundary conditions for the concentrations at the inlet to each compartment located at $y = 0$ are also transient:

$$\begin{aligned} c_k(x_1 < x < x_2, 0, t) &= c_k^{in}(t) \\ c_j(x_2 < x < x_3, 0, t) &= c_j^{in}(t) \end{aligned} \tag{7.42}$$

where $c_i^{in}(t)$ is the concentration of species i in the inlet to each compartment.

Each electrolyte is continuously recirculated through its own reservoir which is assumed to behave as a perfectly mixed tank. Since the discharge from each battery compartment is fed to its respective reservoir and the outlet stream from each reservoir is pumped back

into its compartment, the following balance equation is obtained for c_k^{in} and c_j^{in}:

$$\begin{aligned}\frac{\partial c_k^{in}}{\partial t} &= \frac{L_w}{V_e}\left(\int\limits_{neg,outlet}\left(\vec{N_k}\cdot\vec{n}\right)dS - \int\limits_{neg,inlet}\left(\vec{N_k}\cdot\vec{n}\right)dS\right)\\ \frac{\partial c_j^{in}}{\partial t} &= \frac{L_w}{V_e}\left(\int\limits_{pos,outlet}\left(\vec{N_j}\cdot\vec{n}\right)dS - \int\limits_{pos,inlet}\left(\vec{N_j}\cdot\vec{n}\right)dS\right)\end{aligned} \tag{7.43}$$

where V_e is the tank volume and L_w is the electrode width. The right hand side of Eqn 7.43 accounts for the change in the average inlet flux and average outlet flux for each species over time.

The fluid velocity at the inlet to each compartment is held constant during operation:

$$\begin{aligned}v(0 < x < x_1, 0, t) &= v_{in}\\ v(x_2 < x < x_3, 0, t) &= v_{in}\end{aligned} \tag{7.44}$$

where v_{in} is:

$$v_{in} = \frac{Q}{L_w L_f} \tag{7.45}$$

where Q is the flow rate, L_f is the channel thickness and ϵ is the porosity of the positive electrode. The same flow rate Q has been used on both sides. At the outlet of each compartment, the diffusional flux of each species is zero:

$$-D_k \nabla c_k.\vec{n} = 0 \quad \text{outlets} \tag{7.46}$$

and the pressure is set:

$$\begin{aligned}P(x_1 < x < x_2, H, t) &= P_{out,neg}\\ P(x_2 < x < x_3, H, t) &= P_{out,pos}\end{aligned} \tag{7.47}$$

Finally, initial conditions are set for the concentration of each species:

$$\begin{cases}c_k(x_1 < x < x_2, y, t = 0) = c_k^0\\ c_j(x_2 < x < x_3, y, t = 0) = c_j^0\end{cases} \tag{7.48}$$

7.4 Simulation Details

The battery operating conditions are listed in Table 7.2, while the transport and electrochemical property values are given in Table 7.3. The compositions and initial concentrations listed in Table 7.2 are the same as those set in the experiments. The positive electrolyte initially contained 0.8 mol dm^{-3} Ce(III) in 4 mol dm^{-3} MSA with no Ce(IV) ions. To avoid the numerical problem of division by zero during the first time step when solving the model equations, the initial Ce(IV) concentration was taken to be a very small value of 0.001 mol dm^{-3}.

With the described model and the model parameters provided in Tables 7.2 and 7.3, the species concentrations and the electric fields are calculated. The battery cell-voltage is then found by:

$$V_{cell} = E_{pos} - E_{neg} \pm |IR_{ohm}| = (\phi_{s,pos} - \phi_{l,pos}) - (\phi_{s,neg} - \phi_{l,neg}) \pm |IR_{ohm}| \qquad (7.49)$$

where the R_{ohm} is the total effective resistance of the electrodes, electrolytes and the membrane of the battery. This value was measured via electrochemical impedance spectroscopy for the cell used in the present study [113].

The model was fit to the experimental data acquired from the battery galvanostatic charge/discharge cycles using three parameters as adjustable parameters: i) specific surface area a of the positive platinized titanium mesh electrode, ii) exchange current density $i_{H2,0}$ of the HER and (iii) mass transfer coefficient $k_{m,Ce(IV)}$ of Ce(IV). A parametric sweep analysis revealed that these three parameters have very distinct effects on the battery response: $i_{H2,0}$ affects the charge efficiency at the negative electrode, $k_{m,Ce(IV)}$ affects the charge efficiency at the positive electrode and a affects the battery voltage efficiency. This behaviour facilitated the fitting process and enabled each of the parameters to be estimated manually one at a time. All the remaining model parameter values were obtained from the literature.

The aforementioned governing equations and boundary conditions with the model parameters were solved via the finite-element method using the COMSOL multi-physics software package. A total of 4150 mesh elements were used in the domain based on mesh refinement checks that compared the cell voltage and concentration for a series of refined meshes. The relative tolerance was set to 10^{-3} and the absolute tolerance to 10^{-4}. The simulation time for 5 charge/discharge cycles with 1-hour charge duration at current density of 25 mA cm^{-2} was $\approx$ 2.5 hours on an Intel(R) Core(TM) i5-7200U CPU, 64-bit operating

system with 8 GB RAM.

Table 7.2: Operating conditions.

Quantity	Symbol	Value
Initial Zn(II) concentration	$c^0_{Zn(II)}$	1.5 $\mathrm{mol\,dm^{-3}}$
Initial H^+ concentration in the negative half-cell	$c^0_{H^+,neg}$	1 $\mathrm{mol\,dm^{-3}}$
Initial $CH_3SO_3^-$ concentration in the negative half-cell	$c^0_{CH_3SO_3^-,neg}$	4 $\mathrm{mol\,dm^{-3}}$
Initial Ce^{3+} concentration	$c^0_{Ce^{3+}}$	0.8 $\mathrm{mol\,dm^{-3}}$
Initial Ce^{4+} concentration	$c^0_{Ce^{4+}}$	0.001 $\mathrm{mol\,dm^{-3}}$
Initial H^+ concentration in the positive half-cell	$c^0_{H^+,pos}$	4 $\mathrm{mol\,dm^{-3}}$
Initial $CH_3SO_3^-$ concentration in the positive half-cell	$c^0_{CH_3SO_3^-,pos}$	6.4 $\mathrm{mol\,dm^{-3}}$
Positive outlet pressure	$P_{out,pos}$	100 Pa [104]
Negative outlet pressure	$P_{out,neg}$	0 Pa
Electrolyte volume	V_e	30 $\mathrm{cm^3}$
Temperature	T	50°C
Applied current density	i_{app}	25 $\mathrm{mA\,cm^{-2}}$
Flow rate	Q	65 $\mathrm{ml\,min^{-1}}$

Table 7.3: Transport and electrochemsitry constants.

Quantity	Symbol	Value
Diffusion coefficient of Zn(II) (50°C)	$D_{\mathrm{Zn(II)}}$	1.165×10^{-9} $\mathrm{m^2\,s^{-1}}$ [93]
Diffusion coefficient of H^+ (50°C)	D_{H^+}	1.230×10^{-8} $\mathrm{m^2\,s^{-1}}$ [177]
Diffusion coefficient of Ce(III) (50°C)	$D_{Ce(III)}$	1.520×10^{-10} $\mathrm{m^2\,s^{-1}}$ [98]
Diffusion coefficient of Ce(IV) (50°C)[1]	$D_{Ce(IV)}$	1.075×10^{-10} $\mathrm{m^2\,s^{-1}}$ [89]
Diffusion coefficient of $CH_3SO_3^-$ (50°C)	$D_{CH_3SO_3^-}$	2.378×10^{-9} $\mathrm{m^2\,s^{-1}}$ [178]
Positive electrode conductivity[2]	$\sigma_{s,pos}$	2×10^6 $\mathrm{S\,m^{-1}}$
Membrane conductivity (50°C)[1]	σ_m	15.95 $\mathrm{S\,m^{-1}}$ [179]
Cerium exchange current density (50°C)	$i_{Ce,0}$	242 $\mathrm{A\,m^{-2}}$ [113]
Zinc exchange current density (50°C)	$i_{Zn,0}$	74 $\mathrm{A\,m^{-2}}$ [113]
HER exchange current density (50°C)[3]	$i_{H_2,0}$	2.21×10^{-5} $\mathrm{A\,m^{-2}}$
OER exchange current density (50°C)[1]	$i_{O_2,0}$	5.08×10^{-6} $\mathrm{A\,m^{-2}}$ [180, 181]
Zinc cathodic electron transfer coefficient	$\alpha_{c,neg}$	0.5 [182]
Zinc anodic electron transfer coefficient	$\alpha_{a,neg}$	0.5 [180]
Cerium cathodic electron transfer coefficient	$\alpha_{c,pos}$	0.33 [183]
Cerium anodic electron transfer coefficient	$\alpha_{a,pos}$	0.27 [183]
HER electron transfer coefficient	β'_{H_2}	0.5 [184]
OER electron transfer coefficient	β'_{O_2}	0.52 [185]
Standard potential of zinc (50°C)	E^0_{neg}	-0.757 V [186]
Standard potential of cerium (50°C)	E^0_{pos}	1.639 V [12]
Standard potential of oxygen (50°C)	$E^0_{O_2}$	1.21 V [186]
Standard potential of hydrogen (50°C)	$E^0_{H_2}$	0.00 V [186]
Fixed charge site concentration	c_f	1.2 $\mathrm{mol\,dm^{-3}}$ [187]
Charge of sulfonate sites	z_f	-1
Ce(IV) mass transfer coefficient[3]	$k_{m,Ce(IV)}$	2.8×10^{-5} $\mathrm{m\,s^{-1}}$
Platinized-titanium mesh permeability	k_{kc}	7.1×10^{-4} $\mathrm{cm^2}$ [104]
Area specific resistance	ASR	4.5×10^{-4} $\Omega\,\mathrm{m^2}$ [113]

[1] Data provided in literature was interpolated to find the property at 50°C.

[2] Conductivity of Ti electrode

[3] Fitted

7.5 Results and Discussion

7.5.1 Model validation

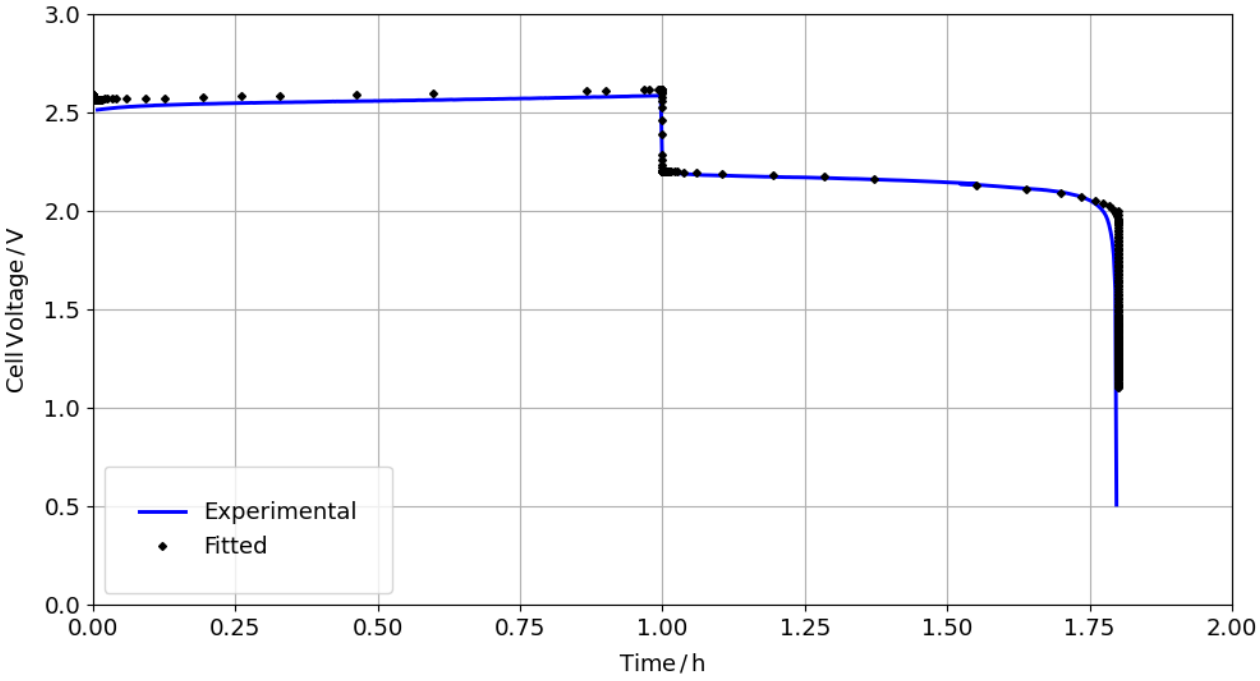

Figure 7.2: Experimental and fitted charge-discharge profile of a zinc-cerium RFB operating at 25 mA cm^{-2} and 50°C with a 1-hour charge duration.

Figure 7.2 presents the experimental and fitted charge-discharge curves of a zinc-cerium RFB operated galvanostatically at a current density of 25 mA cm^{-2} and 50°C with a 1-hour charge duration. From this fitting, the specific surface area of the positive electrode was found to be 150 m^{-1}, which is a reasonable value given that the positive electrode is a 3D mesh substrate. The Ce(IV) mass transfer coefficient was found to be 2.8×10^{-5} m s^{-1}. In a previous experimental study of Ce(IV) reduction on a Pt-Ti mesh electrode, an electrode performance factor (i.e., $k_m \times a$) of 2.46×10^{-3} s^{-1} for Ce(IV) at the same flow velocity of ≈ 1.21 cm s^{-1} was reported. If this factor is used, a Ce(IV) mass transfer coefficient of 1.64×10^{-5} m s^{-1} is obtained at an electrode with a specific surface area of 150 m^{-1}. This

is very close to the fitted value of 2.8×10^{-5} m s^{-1} found in the present study. Finally, the HER exchange current density is found to be 2.21×10^{-5} A m^{-2}. Note that a wide range of values has been reported in the literature for the exchange current density of the HER on carbon-based electrodes. For example, exchange current densities between $\approx 10^{-3}$ - 10^{-5} A m^{-2} [132] have been obtained for HER on graphite-based electrodes. These three fitted parameters were used in all the subsequent calculations.

It should be noted that the battery response shown in Figure 7.2 corresponds to the second charge/discharge cycle during battery operation since the first one serves as a preconditioning step and exhibits lower charge efficiency compared to subsequent ones, as discussed previously [93, 124]. The values of the three parameters noted above were obtained by fitting the model to this second cycle. It has been shown that the zinc electrode potential quickly stabilizes during each battery charge except the first one [93, 124]. Since the exchange current density of HER is significantly higher on a carbon surface than on a zinc substrate [124], a delay in covering the underlying carbon electrode with a zinc layer during the first part of the charge cycle would increase the rate of HER and decrease the zinc redox reaction efficiency. The higher rate of HER during the first cycle compared to subsequent ones has also been reported in other zinc-based batteries [130]. Thus, the first cycle should not be used for the purpose of determining the HER exchange current density that accurately describes battery performance. Indeed, a value for $i_{H_2,0}$ of 6.52×10^{-5} A m^{-2} for the HER is obtained when the model is fitted to the 1^{st} cycle, which is higher than the value of 2.21×10^{-5} A m^{-2} based on the 2^{nd} cycle alone.

Using the fitted parameters, the model simulation was continued for another three charge/discharge cycles and the predicted cell voltages over this additional period are compared to the experimental values. An excellent match between the experimental and computed charge-discharge curves over the first 5 cycles is achieved, as clearly shown in Figure 7.3a. Throughout the present study, the simulations have been limited to examining the performance of the battery over its first five cycles due to the complications arising from precipitation of Ce(IV) in the positive half-cell of the battery over longer battery operation [124], which will be discussed in more detail at the end of this section.

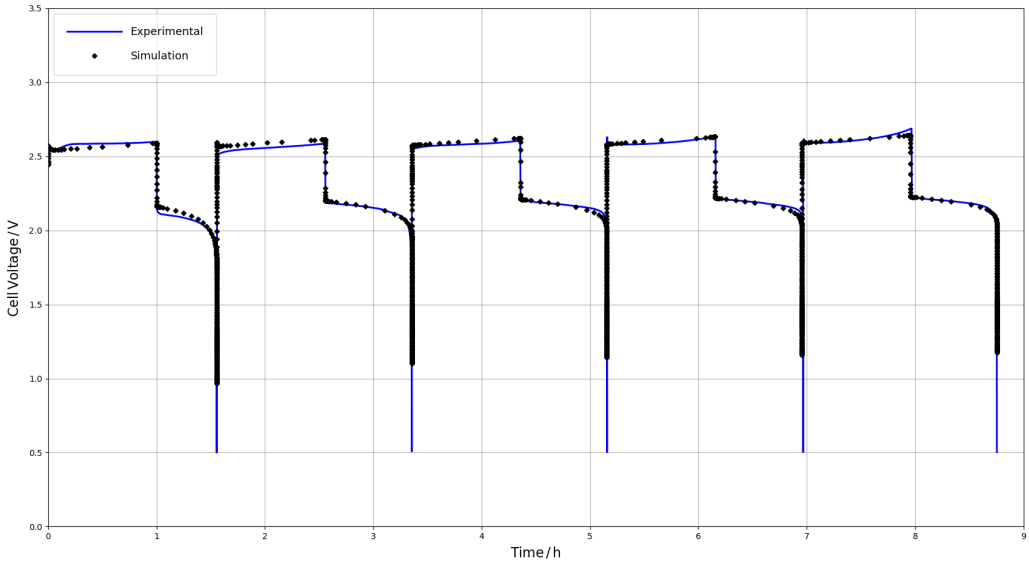

(a)

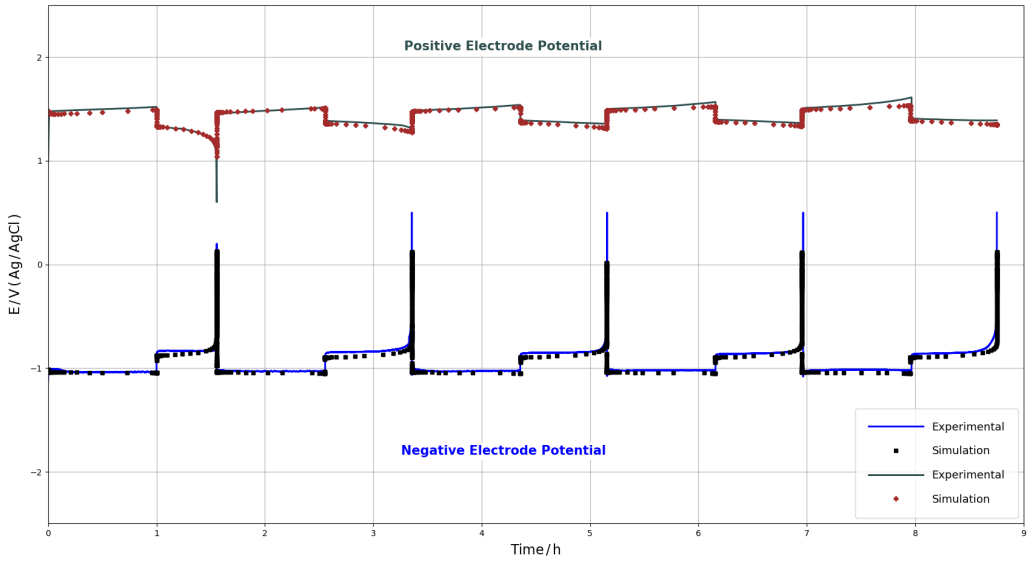

(b)

Figure 7.3: (a) Experimental and simulated charge-discharge profiles of a zinc-cerium RFB operated for 5 cycles at 25 mA cm^{-2} and 50°C with a 1-hour charge duration. (b) Experimental and simulated positive and negative electrode potentials obtained during the full-cell charge/discharge experiments shown in (a).

To further validate the model, the potentials of the negative and positive electrodes measured *in situ* during the charge-discharge experiments shown in Figure 7.3a by insertion of two Ag/AgCl reference electrodes close to the inlets of the flow frames on each side of the battery are compared to the predicted half-cell electrode potentials in Figure 7.3b. As shown in the battery setup in Figure 7.1c, a copper current collector is employed on the negative side and connected to the PVE negative electrode. Thus, the measured negative half-cell electrode potentials contain an extra ohmic resistance that is not explicitly considered in the model. To account for this effect, we directly measured the ohmic resistance between the carbon electrode and the current collector and found it to be $R \approx 0.24\ \Omega$. This ohmic drop (IR) is added to the simulated negative half-cell electrode potential. No correction is made to the experimental positive electrode potentials since the platinized titanium mesh electrode itself also serves as the current collector.

As can be seen in Figure 7.3b, the model predicts the trends in the half-cell electrode potentials extremely well. One important piece of information that can be extracted from the half-cell electrode potential responses is the identity of the redox reaction that limits battery performance during each cycle. This is determined by identifying the electrode potential that changes sharply at the end of each discharge cycle. As shown in the experimental data in Figure 7.3b, the negative electrode potential increases sharply at the end of each discharge cycle under the present operating conditions, while the positive electrode potential only drops at the end of the first discharge cycle. The rise in the negative electrode potential at the end of the discharge cycles stems from the complete removal of zinc by the end of discharge, as confirmed by the subsequent direct inspection of this electrode. This inhibits the complete conversion of Ce(IV) to Ce(III) on the other side and limits battery performance [124]. The role of the half-cell reactions in the performance of the zinc-cerium RFB under different operating conditions has been comprehensively analyzed in the previous chapters [113, 122, 124, 188]. The model indeed predicts the same trend. Figures 7.4a and 7.4b show the change in the calculated bulk Zn(II) concentration in the negative electrolyte and molar surface density of metallic zinc on the negative electrode, respectively, over the 5 cycles. These results show that Zn metal is completely stripped from the surface of the electrode and the Zn(II) concentration reaches its maximum value at the end of each discharge cycle. The model correctly predicts that this leads to the sharp rise of the negative electrode potential (Figure 7.3b), in agreement with the experimental results and observations discussed above. It is also interesting to note that the model confirms that a smaller amount of zinc metal is deposited during the first cycle compared to the subsequent ones, due to the higher rate of HER in the first cycle, as discussed previously.

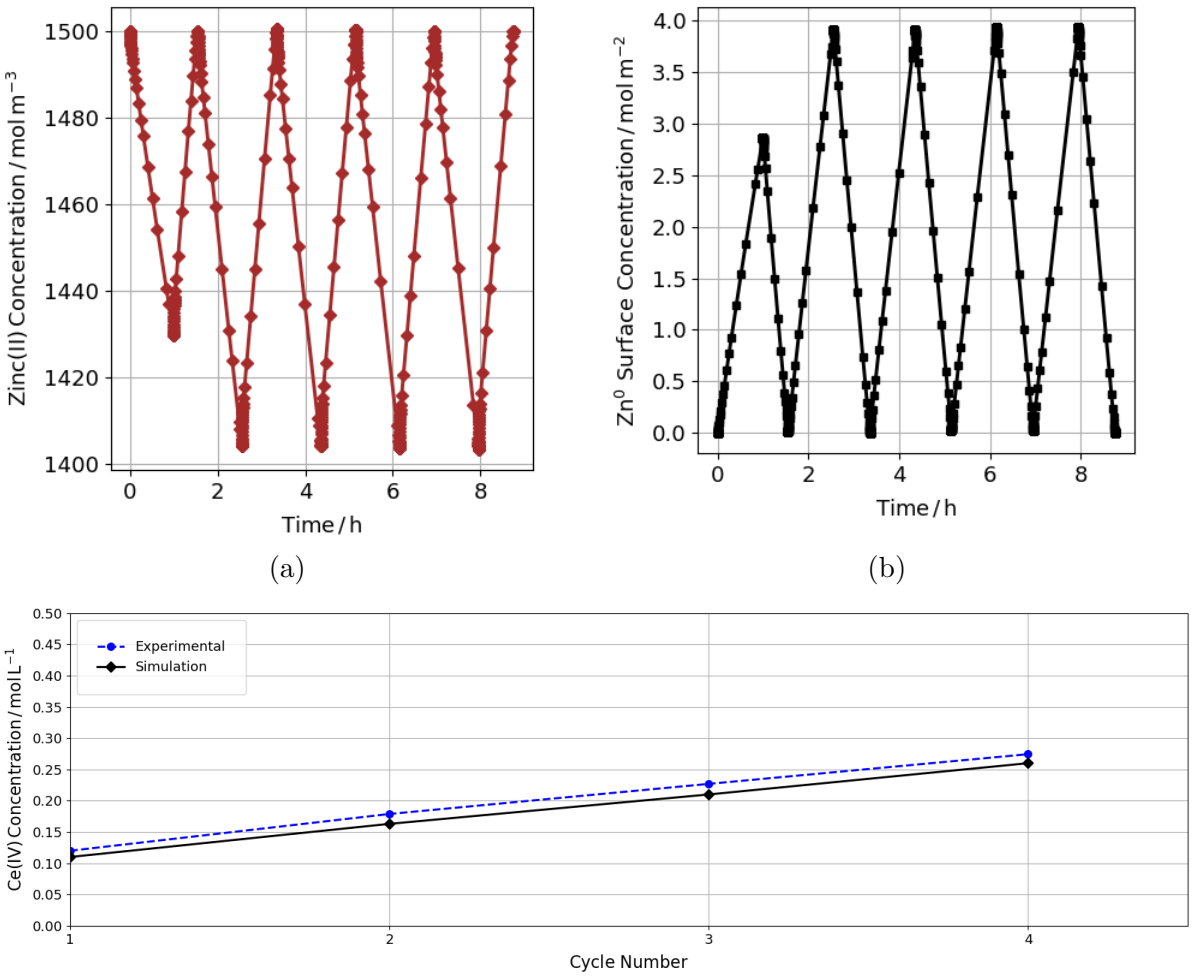

Figure 7.4: Changes in the (a) bulk Zn(II) concentration in the negative electrolyte and (b) surface density of metallic Zn on the negative electrode during the 5 cycles shown in Figure 7.3a. (c) Experimental and simulated Ce(IV) concentrations obtained after each cycle shown in Figure 7.3a (first 4 cycles). The experimental results are obtained by colorimetric titration.

As evident from Figure 7.3b, the Ce(III)/Ce(IV) half-cell reaction is not limiting under the operating conditions of this study, except during the first cycle when the positive

electrode potential drops at the end of the first discharge cycle. This drop in the electrode potential during the first cycle is also accurately captured by the model. In contrast to the situation discussed above regarding the negative side, the drop in the measured positive electrode potential at the end of the first discharge cycle is not due to the complete depletion of Ce(IV). In fact, the titration data shown in Figure 7.4c confirm that 0.12 $\mathrm{mol\,dm^{-3}}$ Ce(IV) still remains in the positive electrolyte at the end of the first discharge cycle despite the fact that the positive electrode potential has dropped sharply. This drop occurs due to the mass transfer limitations at the end of the first discharge cycle, which will be discussed later in Section 7.5.3. On the other hand, the Zn/Zn(II) reaction is limiting during all cycles tested and prevents the complete conversion of Ce(IV) to Ce(III), leading to the accumulation of Ce(IV) in the positive electrolyte from one cycle to the next. This trend is observed in Figure 7.4c which compares the Ce(IV) concentration in the positive electrolyte at the end of each discharge cycle measured by colorimetric titration with the amount predicted by the model. This comparison shows excellent agreement between the experimental data and simulations. The small difference of $\approx$ 0.01 - 0.02 $\mathrm{mol\,dm^{-3}}$ between the experimental and the computedf concentrations may be attributed to the assumption that the solutions behave ideally. Nevertheless, the deviation of the predicted concentrations from the experimental values always remains less than 5%.

As can be seen in Figure 7.4c, the concentrations are shown only up to the 4^{th} charge-discharge cycle of the battery. The effects of the accumulation of Ce(IV) and the resulting imbalance in the system were thoroughly analyzed in the experimental study presented in Chapter 4 [124]. We observed that the accumulated Ce(IV) begins to precipitate from the 4^{th} cycle onward due to its continual build-up and the transfer of H^+ from the positive side to the negative side [124]. The titration data show a concentration of $\approx$ 0.27 $\mathrm{mol\,dm^{-3}}$ at the end of the 5^{th} cycle, whereas the model predicts a higher value at 0.31 $\mathrm{mol\,dm^{-3}}$. Such a difference is reasonable since the model does not include the possibility of Ce(IV) precipitation. Beyond the 5^{th} cycle, the amount of precipitate present in the positive half-cell of the battery grows with time. Due to this precipitation, we have limited the prediction of the model to the first 5 cycles of the battery and have not used this model to predict the performance beyond this cycle. Over the initial five cycles, comparison of the model to our extensive experimental data has shown that the model can accurately describe the trends in the battery full cell voltage, positive and negative electrode potentials as well as the zinc and cerium concentration changes. Consequently, the validated model can be used for further performance predictions and design optimization.

7.5.2 Applied current density

An important operating parameter that affects charge/discharge cycling of the RFBs and can influence the output charge and voltage efficiencies is the applied current density. Figures 7.5a and 7.5c present the simulated full-cell and half-cell electrode potentials obtained at the lower current density of 15 mA cm^{-2}. The previously shown responses at 25 mA cm^{-2} are also included for comparison. These results show a lower charge voltage and higher discharge voltage at 15 mA cm^{-2} than at 25 mA cm^{-2}. The average voltage efficiency over the 5 cycles is 88% at 15 mA cm^{-2}, which is higher than the 83% achieved for the 25 mA cm^{-2}. A higher voltage efficiency is expected at a lower applied current density due to the reduced electrode polarization and ohmic losses. The average charge efficiency, on the other hand, is 70% at 15 mA cm^{-2} over the 5 cycles compared to 75% at 25 mA cm^{-2}. As shown in Figure 7.5c, the Zn/Zn(II) reaction is the limiting reaction in all 5 cycles simulated. Thus, the lower charge efficiency of the system at 15 mA cm^{-2} is predicted to be due to the lower charge efficiency at the negative electrode. Within the range of current densities where Zn/Zn(II) is the limiting redox reaction, an increase in the applied current density raises the rate of Zn(II) reduction relative to that of hydrogen evolution and hence a higher charge efficiency is achieved on the negative side and consequently in the battery. This behavior agrees very well with the trends observed in the previous experimental results of zinc-cerium RFBs [12, 122].

Figures 7.5b and 7.5d presents the battery cell voltage and the half-cell electrode potentials, respectively, at the higher current density of 35 mA cm^{-2}. Consistent with the trends observed in Figure 5a, a higher charge efficiency of 79% and lower voltage efficiency of 79% are attained at 35 mA cm^{-2} than at 25 mA cm^{-2}. Another important point based on these simulations is the rise in the charge cell voltage of the battery during cycling at the higher applied current density of 35 mA cm^{-2}. The average charge cell voltage increases from 2.66 V during the first cycle to 2.72 V during the fifth cycle. As evident in Figure 7.5d, this change stems from the rise in the positive electrode potential. This trend has also been shown in the previous chapters [122, 124]. The build-up of Ce(IV) in the positive electrolyte over the cycles leads to depletion of Ce(III). Hence, a lower amount of Ce(III) is available to charge the battery during the fifth cycle compared to the first cycle, leading to a higher charge cell voltage, that is accurately predicted by the model. Figure 7.5e presents the simulated Ce(IV) concentration accumulated in the positive electrolyte over the 5 cycles at current densities of 15, 25 and 35 mA cm^{-2}. The Ce(IV) concentration rises faster from cycle to cycle as the current density increases. Thus, the rise in the charge cell voltage due to depletion of Ce(III) is predicted to occur more quickly when larger applied current densities are used.

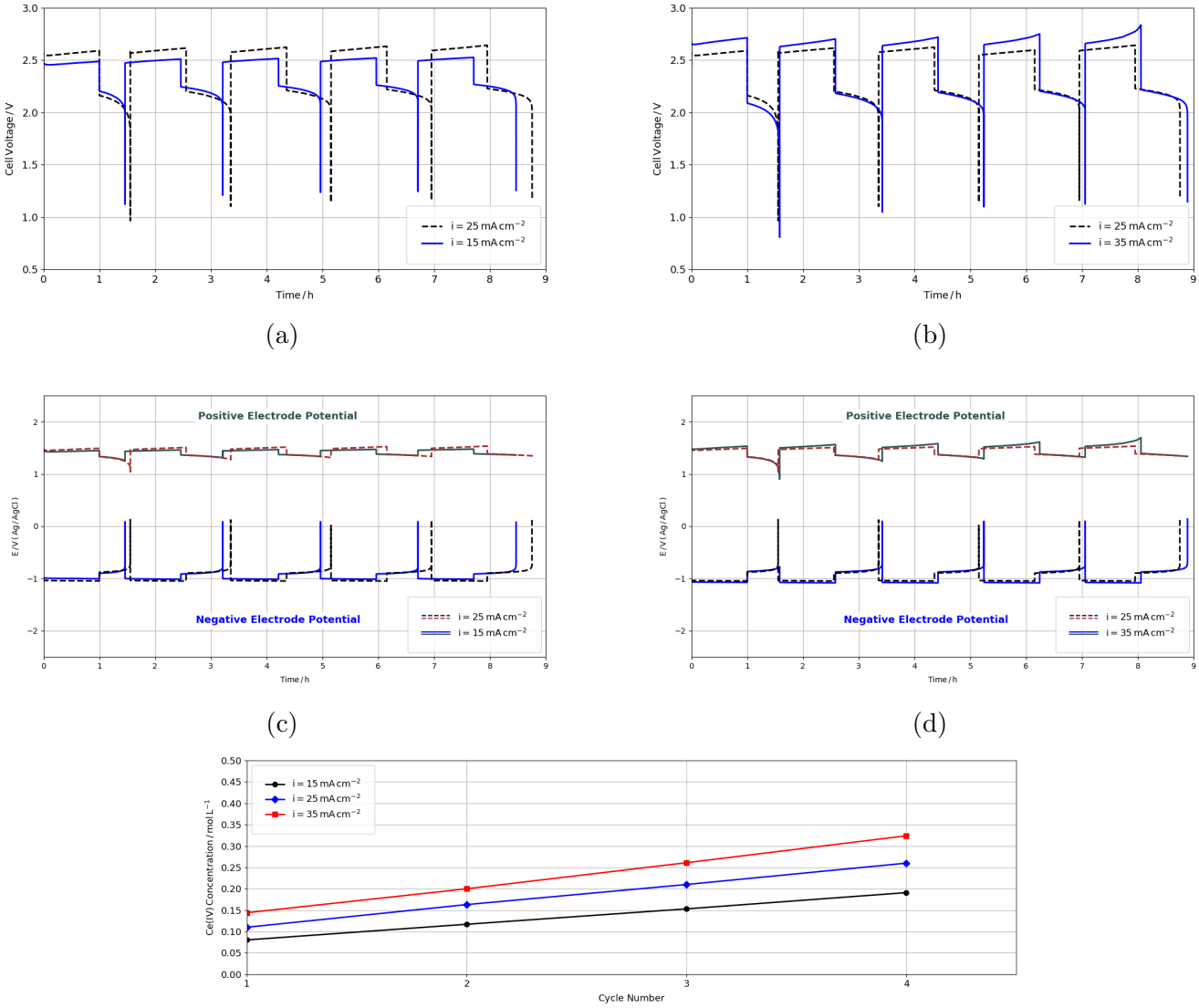

Figure 7.5: Simulated charge-discharge profiles of a zinc-cerium RFB over 5 cycles at (a) 15 and (b) 25 mA cm^{-2} at 50°C with a 1-hour charge duration. The simulated positive and negative electrode potentials in (c) and (d) correspond to the full-cell charge/discharge simulations shown in (a) and (b), respectively. (e) Computed Ce(IV) concentrations remaining after discharge over the first 4 cycles at current densities of 15, 25 and 35 mA cm^{-2}.

7.5.3 Role of mass transfer of Ce(III) and Ce(IV)

The mass transfer of Ce(III) and Ce(IV) to and from the positive electrode plays an important role in achieving a high and stable discharge cell voltage, especially when the system is under mass transfer limiting conditions. Previously, it was shown that the Zn/Zn(II) reaction is solely limiting during all cycles except the first one (when the Ce(III)/ Ce(IV) reaction also becomes limiting) at a current density of 25 mA cm^{-2}. A drop in the positive electrode potential at the end of the first discharge cycle is observed despite the fact that more than 0.1 mol dm^{-3}Ce(IV) is still available in the positive electrolyte. This behaviour can be understood by analysing the role of mass transfer of Ce(III) and Ce(IV) in the battery response.

In the present model, the relation between the bulk and surface cerium concentrations is described in Eqns 7.22 and 7.23 by balancing the rate of the redox reactions with the rate of mass transfer to/from the substrate. Values of $\approx 10^{-5}$ m s^{-1} for $k_{m,Ce(IV)}$ enable an excellent fit of the model to the experimental data. These values are close to those previously reported for the mass transfer coefficient of Ce(IV) at a platinized titanium mesh electrode (given the specific surface area of 150 m^{-1} in the present work) [103]. Note that the Ce(III) mass transfer coefficient is dependent on $k_{m,Ce(IV)}$, as given by Eqn 7.24. Figure 6 presents the simulated single charge/discharge cycle of the battery when $k_{m,Ce(IV)}$ has values in the range of $\approx 10^{-4}$ and $\approx 10^{-6}$ m s^{-1}. For comparison, the previous results at $\approx 10^{-5}$ m s^{-1} are also included. When $k_{m,Ce(IV)}$ is increased from $\approx 10^{-5}$ m s^{-1} to $\approx 10^{-4}$ m s^{-1}, the voltage efficiency is predicted to improve from 78% to 86%, mostly due to the enhancement of the discharge cell voltage (Figure 7.6a). Additionally, the cell voltage during discharge is predicted to become more stable at the higher $k_{m,Ce(IV)}$ value. As expected, this improvement solely stems from the positive half-cell electrode response (Figure 7.6b) since a change in the cerium mass transfer coefficient should not have any effect on the zinc electrode response (Figure 7.6c). The model also predicts that the positive electrode potential no longer drops at the end of the first discharge cycle when Ce(IV) has a $k_{m,Ce(IV)}$ value of $\approx 10^{-4}$ m s^{-1} and its reduction to Ce(III) is no longer the limiting reaction in the system. A specific surface area of 150 m^{-1} used in the present study and a $k_{m,Ce(IV)}$ value of $\approx 10^{-4}$ m s^{-1} yields a $k_{m,Ce(IV)} \times a$ value of $\approx 10^{-2}$ m s^{-1}, which corresponds to the range previously reported for platinized titanium micromesh and felt electrodes [103]. This suggests that the use of platinized titanium micromesh or felt electrodes should remove the mass transfer limitations on the cerium side under the operating conditions tested here compared to the Pt-Ti mesh electrode used in the present study.

As shown in Figure 7.6a, the battery is not able to discharge at all when $k_{m,Ce(IV)}$ has

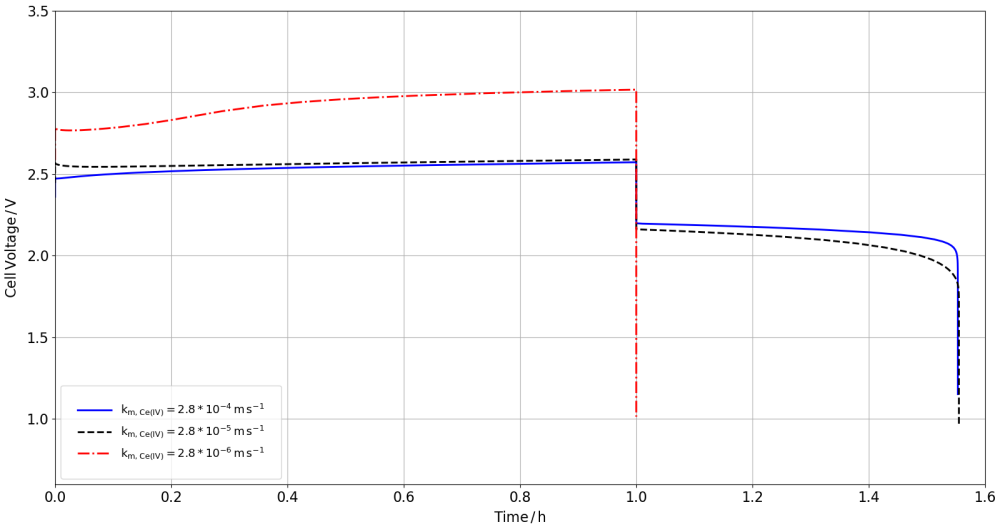

(a)

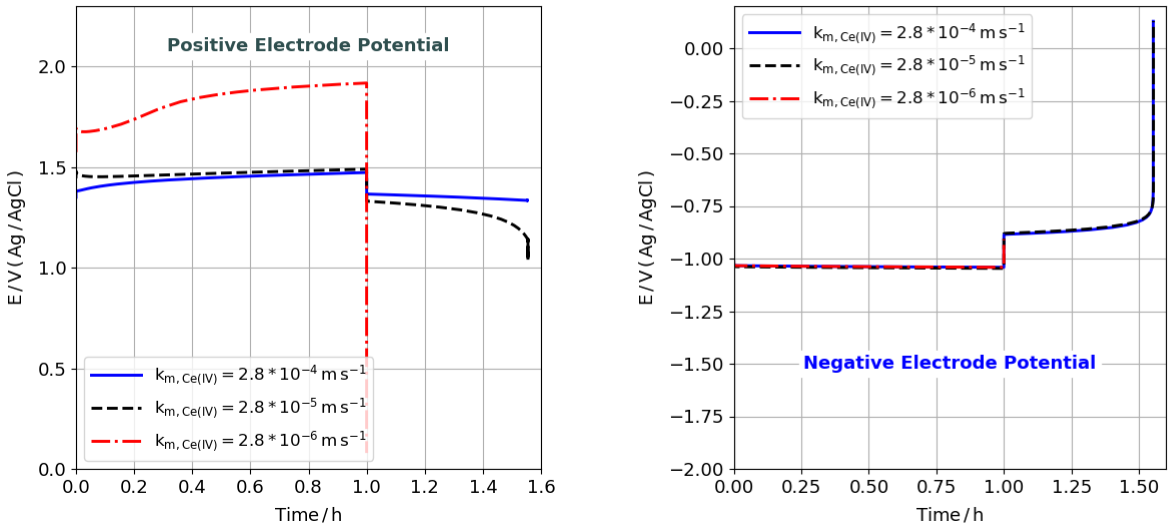

(b) (c)

Figure 7.6: (a) Simulated single charge-discharge profile of a zinc-cerium RFB operated at 25 mA cm^{-2} and 50°C with a 1-hour charge duration with $k_{m,Ce(IV)}$ values of 2.8×10^{-4} , 2.8×10^{-5} and 2.8×10^{-6} m s^{-1}. Simulated (b) positive and (c) negative electrode potentials corresponding to the full-cell charge/discharge experiment shown in (a).

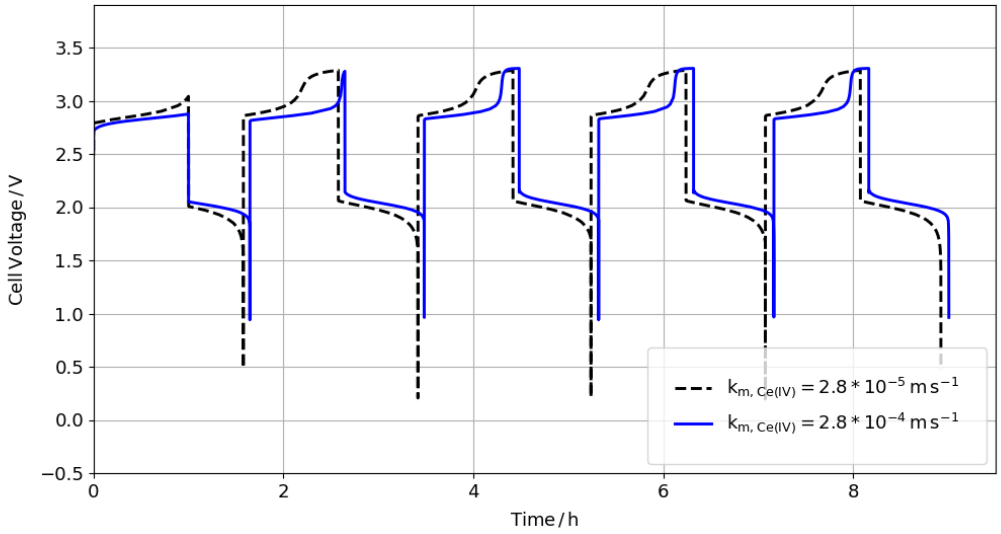

(a)

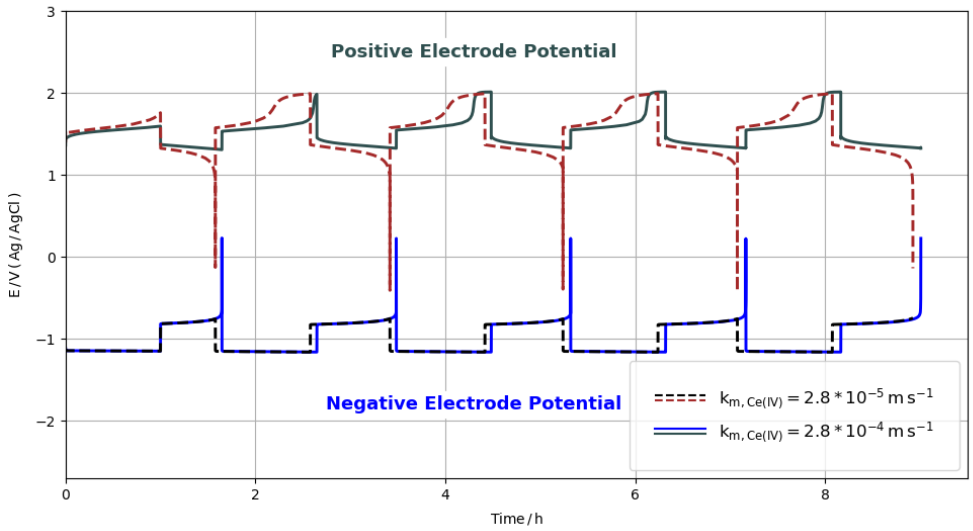

(b)

Figure 7.7: (a) Simulated charge-discharge profiles of a zinc-cerium RFB operated at 60 $mA\,cm^{-2}$ and 50°C with a 1-hour charge duration with $k_{m,Ce(IV)}$ values of 2.8×10^{-4} and 2.8×10^{-5} $m\,s^{-1}$. (b) Simulated positive and negative electrode potentials corresponding to the full-cell charge/discharge experiment shown in (a).

a very small value of $\approx 10^{-6}$ m s^{-1} and so the electrode potential drops immediately due to the limited transfer of Ce(IV) to the electrode substrate during discharge (Figure 7.6b). Note that, $k_{m,Ce(III)}$ is also small when $k_{m,Ce(IV)}$ is low. Although the Ce(III) concentration is large during the first charge cycle, the model predicts that the transfer of Ce(III) to the electrode substrate also becomes difficult enough at very small $k_{m,Ce(III)}$ values that a large charge cell voltage is required, as shown in Figure 7.6a. These effects of very slow mass transfer of Ce(III) and Ce(IV) predicted by the model are in good agreement with previously reported experimental results. Based on a previous experimental study, the Ce(IV) mass transfer coefficient is $\approx 10^{-6}$ m s^{-1} (at 150 m^{-1}) when a platinized titanium plate (planar) electrode is employed for Ce(IV) reduction. Half-cell experiments at a Pt-Ti plate electrode have shown that the electrode potential is less than 0.5 V when Ce(IV) reduction is carried out at 25 mA cm^{-2} [103]. Since this potential is already less than the cut-off discharge voltage during battery operation, acceptable discharge would not be possible at such electrodes at this current density, in agreement with the computed results in the present work.

As discussed previously, the battery is limited by the Ce(III)/Ce(IV) reaction only during the first cycle at 25 mA cm^{-2}. During subsequent charge-discharge cycles at 25 mA cm^{-2}, mass transfer effects on the positive side are less dominant since limitations associated with the Zn/Zn(II) reaction shorten the discharge process and lead to the accumulation of Ce(IV). Hence, the role of cerium mass transfer over multiple cycles is not entirely apparent at this current density. However, this effect becomes more clear when the battery operates at higher applied current densities, where the cerium mass transfer limitations become dominant over successive cycles. Figure 7.9 presents the simulated charge-discharge profiles of the battery operating at a large current density of 60 mA cm^{-2} with $k_{m,Ce(IV)}$ values of 2.8×10^{-5} and 2.8×10^{-4} m s^{-1}. Under these conditions, the battery performance is entirely limited by the Ce(III)/Ce(IV) reaction when $k_{m,Ce(IV)} = 2.8 \times 10^{-5}$ m s^{-1}, as indicated by the drop in the positive electrode potential at the end of each discharge cycle. The negative electrode potential, on the other hand, does not rise at the end of discharge, demonstrating that zinc dissolution has been cut short. Another interesting prediction is that due to the mass transfer limitations, the charge cell voltage rises significantly particularly toward the end of charge when Ce(III) is depleted. The nature of the limiting redox reactions and battery performance change drastically when a higher $k_{m,Ce(IV)}$ value of 2.8×10^{-4} m s^{-1} is used. As this mass transfer coefficient increases, the limiting redox reaction shifts from the Ce(III)/Ce(IV) to Zn/Zn(II) reaction, as evident in Figure 7.7b. The battery discharge process is no longer limited by the supply of Ce(IV) to the electrode surface and the process stops when the zinc metal is completely stripped from the electrode surface. Additionally, at the higher $k_{m,Ce(IV)}$, the cell voltage rises at a

later point during charge compared to the situation at lower $k_{m,Ce(IV)}$ since the depletion of Ce(III) during charge becomes less problematic.

7.5.4 Effect of exchange current density of Zn/Zn(II) reaction

As shown previously, even with improved mass transfer rates on the positive side, the occurrence of the HER on the negative side reduces the amount of zinc that deposits on the electrode during each charge cycle and thus shortens the discharge phase before all the available Ce(IV) in the positive electrolyte can be reduced back to Ce(III). Therefore, any improvement in the rate of Zn(II) reduction and/or inhibition of the HER would be beneficial for the performance of zinc-cerium RFBs. In our experimental work presented in previous chapters, we demonstrated that an alternative mixed methanesulfonate-chloride negative electrolyte increases the exchange current density of zinc redox reaction to 53.4 $\mathrm{mA\,cm^{-2}}$, almost an order of magnitude higher than that achieved in a pure MSA electrolyte (7.4 $\mathrm{mA\,cm^{-2}}$). In this section, the model is used to examine the performance of the battery with this alternative electrolyte in terms of full-cell and half-cell voltages and the cerium and zinc concentration changes. The alternative mixed methanesulfonate-chloride electrolyte is comprised of 0.9 $\mathrm{mol\,dm^{-3}}$ zinc methanesulfonate and 0.6 $\mathrm{mol\,dm^{-3}}$ zinc chloride in 1 $\mathrm{mol\,dm^{-3}}$ MSA electrolyte when the negative electrode is fully discharged. Thus, in addition to the ions listed in the model development section, Cl^- anions at an initial concentration of 0.6 $\mathrm{mol\,dm^{-3}}$ are also included on the negative side. The exchange current density for the Zn/Zn(II) reaction is also changed from the previous value of 7.4 $\mathrm{mA\,cm^{-2}}$ to 53.4 $\mathrm{mA\,cm^{-2}}$. All the other variables are assumed to remain unchanged.

Figure 7.8 presents the simulated full-cell and half-cell potentials corresponding to a battery operating with pure MSA electrolyte and mixed methanesulfonate-chloride solutions. As shown in Figure 7.8a, the model accurately predicts that charge and voltage efficiencies of the battery improve when the RFB operates with the mixed acid electrolyte. The charge efficiency increases from 75% to 80%, while the voltage efficiency is raised from 83% to 85%. Obviously, both improvements stem from enhancement in the Zn/Zn(II) reaction, as shown in Figure 7.8b. The slight increase in the voltage efficiency of the system with the mixed negative electrolyte is due to the enhanced kinetics at the negative electrode, which reduces the activation overpotential for the Zn/Zn(II) reaction. As for the charge efficiency, given the higher exchange current density achieved in the mixed negative electrolyte, a higher amount of Zn(II) ion is deposited during each cycle (Figure 7.9a) which enables a longer discharge before all of the deposited zinc metal is stripped from the negative electrode. Moreover, the prolonged discharge ensures that more Ce(IV) is

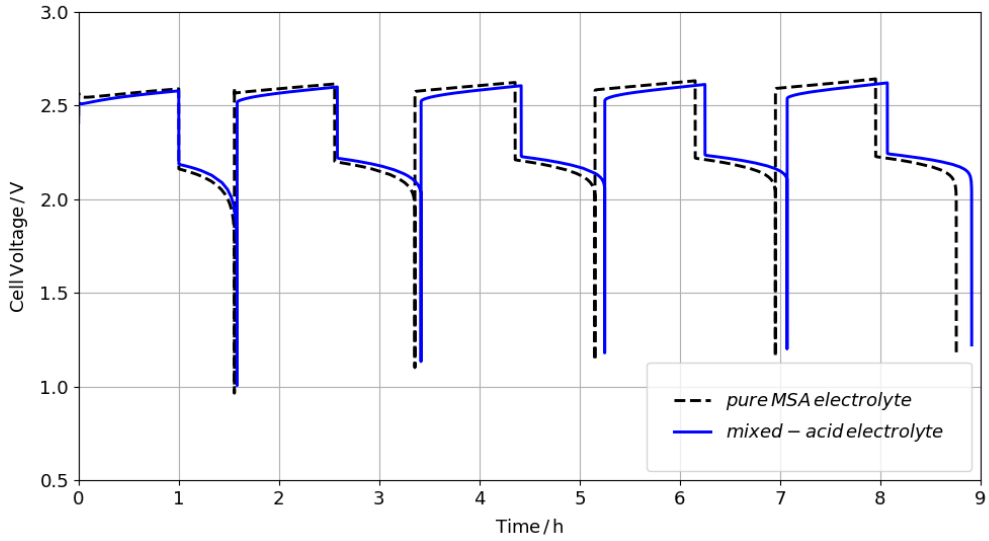

(a)

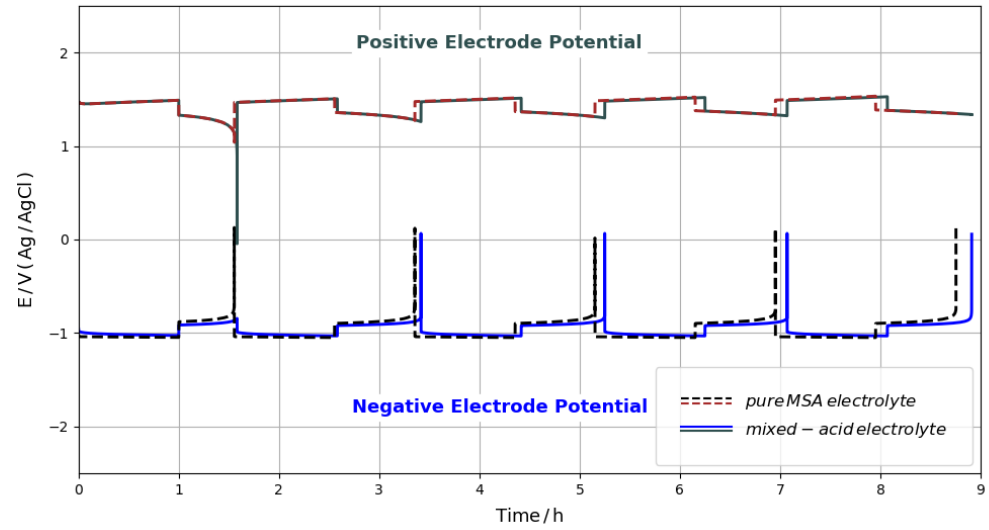

(b)

Figure 7.8: (a) Simulated charge-discharge profiles of a zinc-cerium RFB operating for 5 cycles at 25 mA cm^{-2} and 50°C with a 1-hour charge duration in a mixed methanesulfonate-chloride negative electrolyte and pure MSA electrolyte. (b) Simulated positive and negative electrode potentials corresponding to the full-cell charge/discharge experiments shown in (a).

converted to Ce(III) during each cycle and slows the build-up of Ce(IV) remaining in the positive electrolyte at the end of discharge, as shown in Figure 7.9b.

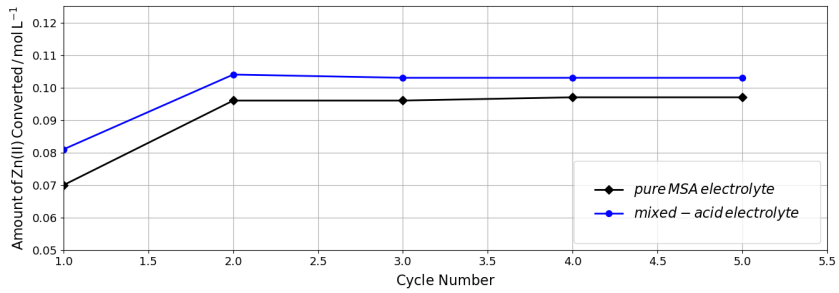

(a)

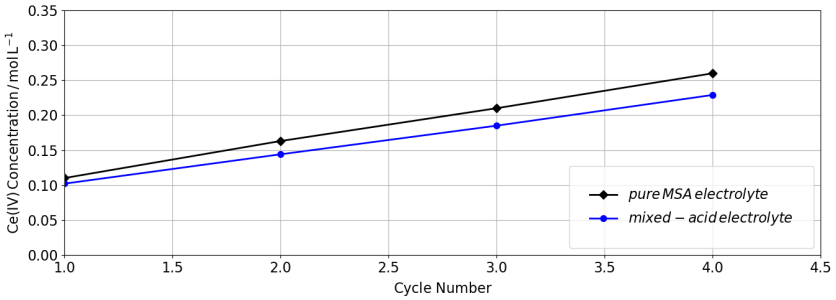

(b)

Figure 7.9: (a) Simulated amount of converted zinc(II) after each cycle. (b) Simulated Ce(IV) concentrations obtained after each cycle.

Although the exchange current density for the Zn/Zn(II) reaction has increased by almost an order of magnitude when the mixed negative electrolyte is used, the model predicts that it still remains the limiting redox reaction and shortens the duration of discharge before all the Ce(IV) can be converted back to Ce(III) (Figure 7.8). Clearly, any further improvement in the electrode kinetics of this reaction beyond that achieved with the mixed negative electrolyte would be beneficial for enhancing the charge efficiency of the battery and reducing the rate of accumulation of Ce(IV). However, even this would only stave off the failure of the battery when subjected to repeated charge-discharge cycles, but not prevent it. If a balance between the two sides of the battery is to be achieved, the HER side reaction must be completely inhibited. However, this is not likely possible, particularly given the continual transfer of H^+ across the membrane from the positive side to the

negative side. The most successful strategy will likely involve a combination of all of these approaches (i.e., promotion of Zn(II) reduction, inhibition of HER and H^+ transfer into the negative electrolyte). Another practical approach would be to periodically reduce the Ce(IV) that accumulates in the positive electrolyte back to Ce(III) in an external catalytic bed in a dual-circuit setup, similar to the concept used in vanadium RFBs [189]. For any of these scenarios, the model developed in the present study can provide highly accurate and useful predictions of the accumulated cerium as well as the negative and positive electrode potentials, full cell voltages and system efficiencies during single or multiple charge-discharge cycles.

7.6 Conclusions

In the present study, a two-dimensional transient model was developed to simulate the operation of a single-cell zinc-cerium RFB. The dynamic model included all three modes of transport (migration, diffusion and convection) coupled with electrode kinetics of the Zn/Zn(II) and Ce(III)/Ce(IV) reactions as well as the hydrogen and oxygen evolution side reactions. The model was validated using an extensive set of experimental data obtained in our laboratory. The experimental full-cell voltages obtained during galvanostatic charge/discharge cycling of the flow battery over multiple cycles were compared to the simulated full-cell voltages under the same operating conditions. Additionally, the computed negative and positive electrode potentials were compared to the experimental values obtained *in situ* using inserted reference electrodes during battery operation. Moreover, the concentration of Ce(IV) obtained from colorimetric titration over multi-cycle experiments was compared to the predicted Ce(IV) concentrations. In all cases, excellent agreement between the predicted values and the experimental data was attained. The validation of the model with the aforementioned experimental data allowed us to not only employ the model to predict the full-cell voltage of the battery but also to closely identify the limiting redox reaction in the system under different operating conditions.

Chapter 8

Conclusions and Future Work

8.1 Conclusions

The present thesis focused on an experimental and modeling study of a class of redox flow batteries based on Zn/Zn(II) and Ce(III)/Ce(IV) chemistry. The content of the thesis was arranged in 8 chapters. In Chapter 1, an overview of the RFB technology was presented and the objectives of the research were discussed. In Chapter 2, a comprehensive literature review of redox flow batteries was provided. Particularly, the historical development, key components and different types of RFBs were described and prior studies conducted on zinc-cerium RFBs were discussed. Based on this literature review, it was suggested that additional work is needed to better understand the performance of zinc-cerium RFBs. Specifically, knowledge is lacking regarding the sources of voltage and capacity loss over long-term operation of these batteries. Additionally, it was shown that fabricating a durable and low-cost electrode for the positive half-cell and developing a strategy for suppressing the hydrogen evolution side reaction on the negative half-cell of the battery would be highly beneficial for further development of these systems.

In Chapter 3, an *in situ* investigation of the sources of performance loss during discharge of a zinc-cerium redox flow battery was described. Polarization and electrochemical impedance spectroscopy (EIS) measurements on a bench-scale zinc-cerium RFB were combined to determine the overpotentials due to kinetic and ohmic effects and provide an estimate of the mass-transfer losses. In order to further evaluate the source of these overpotentials, the contribution of each half-cell was evaluated by insertion of Ag/AgCl reference electrodes at each of the two inlets to the battery. Measurements revealed that most of the losses are due to the kinetic overpotential of the Zn/Zn(II) reaction at low and

intermediate current densities. On the other hand, mass-transfer limitations associated with the Ce(III)/Ce(IV) reaction are solely responsible for the large potential drop at high current densities. Additionally, *in situ* investigation of the kinetics of the negative and positive redox reactions revealed that the exchange current density is $\sim 7.4\ \mathrm{mA\,cm^{-2}}$ for Zn/Zn(II) oxidation and $\sim 24.2\ \mathrm{mA\,cm^{-2}}$ for Ce(IV) reduction. The difference in these values supported the conclusion that the slower kinetics at the negative electrode limits the performance at low and intermediate current densities.

In Chapter 4, the life-cycle of a zinc-cerium redox flow battery was investigated in detail by *in situ* monitoring of the half-cell electrode potentials and measurement of the Ce(IV) and H^+ concentrations on the positive and negative side, respectively, by titrimetric analysis over its entire life . At a current density of $25\ \mathrm{mA\,cm^{-2}}$, the charge efficiency of the battery was found to be initially limited by the Zn/Zn(II) redox reaction, which leads to the incomplete reduction of Ce(IV) to Ce(III) during discharge and the accumulation of Ce(IV) on the positive side. Titration experiments confirmed the accumulation of Ce(IV) on the positive side of the battery and revealed that the proton concentration in the negative electrolyte of the battery increases over the cycles. This increases the rate of hydrogen evolution on the negative side and contributes to Ce(IV) precipitation on the positive side. These effects combine to cause capacity fade and ultimate failure of the battery. In order to mitigate these effects, the battery life-cycle was evaluated when the Nafion 117 cation exchange membrane was replaced with an anion exchange membrane (AEM). Among the AEMs tested, Fap-375-PP was found to be sufficiently stable in the presence of Ce(IV) to complete a full life-cycle analysis. Although a very gradual leakage of protons across this anion exchange membrane was observed and the membrane suffered irreversible damage by the end of a full life-cycle experiment, it significantly slowed the increase in proton concentration on the negative side and extended the life of the system relative to that possible using Nafion 117.

In Chapter 5, zinc electrodeposition and electrodissolution in methanesulfonic acid (MSA) electrolytes mixed with chloride or sulfate were investigated in a 3-electrode cell for eventual use in divided and undivided zinc-cerium redox flow batteries. Cyclic voltammetry and polarization experiments showed that the addition of chloride to MSA-based electrolytes shifted the nucleation potential in the positive direction, lowered the nucleation overpotential and enhanced the kinetics of Zn deposition and subsequent dissolution relative to that achieved when sulfate was added or MSA was the only anion present. In addition, the diffusion coefficient of Zn(II) and the resulting limiting current density for Zn deposition were found to be moderately higher in mixed methanesulfonate-chloride media than when chloride was absent. The effects of temperature, MSA concentration, Zn(II) concentration and current density on the Zn/Zn(II) system were also investigated under

potentiostatic and galvanostatic conditions. Although an increase in temperature and/or MSA concentration tended to lower the charge efficiency for Zn deposition in both mixed and MSA-only electrolytes due to the higher rate of hydrogen evolution, the amount of zinc deposited, charge and voltage efficiency always remained significantly higher in the mixed methanesulfonate/chloride media than the pure MSA media. These experiments showed that the use of a mixed methanesulfonate/chloride media should enable both divided and undivided zinc-cerium RFBs to operate over a wider range of temperatures and MSA concentrations compared to the case with pure MSA electrolyte. The addition of sulfate to MSA-based electrolytes, however, did not improve the performance of the Zn/Zn(II) system relative to that possible in the MSA-only electrolytes.

In Chapter 6, the performance of a zinc-cerium redox flow battery with mixed methanesulfonate (MSA) - chloride negative electrolyte was compared to that of a zinc-cerium RFB with pure MSA electrolyte. Half-cell studies on a polyvinyl-ester carbon electrode confirmed that the addition of Cl^- ions increased the anodic charge and the exchange current density of the zinc redox reaction. Hence, an electrolyte with a composition of 0.9 $mol\,dm^{-3}$ ZnMSA and 0.6 $mol\,dm^{-3}$ $ZnCl_2$ in 1 $mol\,dm^{-3}$ MSA was chosen as the negative electrolyte for use in a bench-scale zinc-cerium RFB. Reference electrodes were also incorporated in the RFB set-up so that the potential of each electrode could be monitored during operation. The results of the full-cell experiments showed that the battery voltage efficiency increased when operating with mixed MSA-chloride electrolyte due to the lower overpotential of the Zn/Zn(II) reaction. Moreover, under the conditions where this reaction was the main limiting factor, the charge efficiency rose significantly when the mixed solution was employed. Additionally, a life-cycle analysis of the battery based on a 15-minute charge period and current density of 25 $mA\,cm^{-2}$ showed that the total operating time and number of cycles increased from 42 hours and 97 cycles, respectively, in the case where the conventional negative electrolyte was used to more than 75 hours and 166 cycles when Cl^- was added. Based on these results, it was concluded that a zinc-cerium RFB with mixed MSA-chloride negative electrolyte has a notably longer life and higher energy efficiency compared to conventional zinc-cerium RFBs.

In Chapter 7, a two-dimensional transient model accounting for three modes of transport (migration, diffusion and convection) coupled with electrode kinetics was developed for zinc-cerium redox flow batteries. The model was validated against the extensive set of experimental data obtained in the previous chapters. This included full-cell voltages, positive and negative electrode potentials monitored via reference electrodes inserted into the battery set-up and Ce(IV) concentrations in the positive electrolyte measured by colorimetric titration over multi-cycle experiments. To the best of our knowledge, this is the most comprehensive comparison carried out between the output of a model and experi-

mental data extracted during operation of a redox flow battery. The validated model was then used to predict the cell voltages and limiting redox reactions during battery operation for different model parameters to provide a guide to further improve the performance of zinc-cerium RFBs.

The contributions of the present thesis can be summarized as follows:

- Determination of the sources of voltage loss (kinetic, ohmic and mass transfer) in zinc-cerium redox flow batteries and decoupling the contribution of the negative and positive redox reactions to this overall loss. This information is crucial for optimizing the battery performance and for elucidating the pathways that enhance the system efficiency.
- Identifying the cause of the capacity fade and battery failure in zinc-cerium RFBs by analyzing the battery life-cycle and further demonstrating the advantage of employing an anion-exchange membrane in place of a cation-exchange membrane in zinc-cerium RFBs.
- Developing an alternative negative electrolyte based on mixed methanesulfonate-chloride media capable of enhancing the rate of the zinc redox reaction relative to hydrogen evolution side reaction. The developed electrolyte is advantageous for potential use in zinc-based acidic batteries.
- Improving the performance of a zinc-cerium RFB in terms of charge and voltage efficiency as well as battery life-cycle by employing the alternative mixed methanesulfonate-chloride electrolyte on the negative half-cell of the battery.
- Developing a transient multi-physics model for zinc-cerium RFBs and validating the model against extensive experimental date. The validated model is capable of predicting the cell voltages and limiting redox reactions during battery operation for different model parameters.

8.2 Future Work

8.2.1 Development of durable anion-exchange membranes

Currently cation-exchange membranes, specifically Nafion membranes, are employed in zinc-cerium RFBs due to their durability in presence of cerium species. Nevertheless, as

shown in Chapter 4, the gradual transfer of protons from the positive electrolyte to the negative electrolyte during battery operation results in continuous increase in the rate of the hydrogen evolution side reaction in these systems. The enhancement in the rate of HER reduces the discharge time and battery charge efficiency over cycles and results in accumulation of Ce(IV) species in the positive electrolyte. Our results in Chapter 4 revealed that the use of anion-exchange membranes in place of cation-exchange membranes is promising for resolving the aforementioned issue and for enhancing the life-cycle of the battery. The membranes tested in the present work were commercially available products that were not optimized for this system and mostly degraded irreversibly over long durations in the presence of Ce(IV). Fabrication of anion exchange membranes with extremely low proton leakage and high stability in the presence of Ce(IV) that can readily permit the transport of methanesulfonate ions is key for the ultimate success of zinc-cerium redox flow batteries.

8.2.2 Investigation of the nature of water and proton transfer mechanisms

The titration data in Chapter 4 showed the rise in concentration of protons on the negative side and thus dilution of the acidity on the positive side over multiple cycles of zinc-cerium RFBs. As explained previously, this phenomenon can be attributed to a combination of several mechanisms. Firstly, due to the onset of HER, the discharge time is shorter than the charge time, which results in the net transfer of H^+ into the negative electrolyte over each cycle. Additionally, the difference in proton concentrations of the two half-cells can result in diffusive transport of protons. Moreover, the difference in the ionic strengths of the two half-cells contributes to the osmotic transfer of a significant amount of water when the battery is operated for many charge-discharge cycles. Greater knowledge regarding the contributions of different transport mechanisms for proton and other species across the membrane (diffusion, migration, osmotic convection and electro-osmotic convection) as well as osmotic and electro-osmotic transfer of water is highly beneficial for finding suitable solutions to the aforementioned problems. Comparable studies have been conducted for all-vanadium RFBs to address the water transfer and vanadium crossover problems [136, 190–192], which have resulted in useful operating recommendations such as utilization of asymmetric flow rates for the two sides of the battery to control the pressure gradient [192] and varying applied current densities between the charge and discharge cycles of the battery [190]. Comparable studies for zinc-cerium redox flow batteries are warranted.

8.2.3 Incorporation of a dual-circuit battery architecture

As explained previously, battery discharge is limited by the Zn/Zn(II) redox reaction at low to intermediate current densities stems from the occurrence of hydrogen evolution during the battery charge cycle. The limitation by the Zn/Zn(II) reaction leads to the incomplete reduction of Ce(IV) to Ce(III) during discharge and the accumulation of Ce(IV) on the positive side. As shown in Chapters 5, 6 and 7, any improvement in the kinetic of the Zn/Zn(II) reaction relative to that of HER would be very beneficial for zinc-cerium RFBs. However, a small efficiency loss from HER should always be expected to occur since complete suppression of HER during zinc electrodeposition in an acidic environment is likely impossible to achieve, particularly if the gradual proton transfer across the membrane occurs. Thus, even at low rates of HER, Ce(IV) is still expected to accumulate on the positive side over long term operation of the battery. A practical solution to this problem would be to periodically reduce the Ce(IV) that accumulates in the positive electrolyte back to Ce(III) in an external catalytic bed in a dual-circuit setup, similar to the concept used in vanadium RFBs [189]. Investigation into the type of catalyst needed for conversion of Ce(IV) to Ce(III) in an external bed and evaluation of the performance of the battery with this dual circuit design would be very beneficial.

8.2.4 Development of positive electrode materials

As mentioned previously, the choice of electrode material for the Ce(III)/Ce(IV) reaction becomes critical due to the highly oxidative and acidic nature of the positive electrolyte. Although the use of the Ce(III)/Ce(IV) reaction is highly attractive due to its large positive potential, the development of low-cost and efficient electrode materials and electrocatalysts for RFBs based on this chemistry has received much less attention than other types such as vanadium-based RFBs. To date, expensive platinum-based electrodes are recommended for use in cerium-based RFBs due to their durability and high efficiency. However, the high cost of these electrodes reduces their appeal. The search for durable and low-cost positive electrode materials should continue. Corrosion studies of any potential new material should be conducted in the presence of high concentrations ($0.5 - 0.8$ mol dm^{-3}) of both Ce(IV) and Ce(III) species. Materials with wide range of potential stability such as Ebonex (a corrosion-resistant titanium oxide ceramic) [193] are potential candidates for further evaluation. In addition to the development of electrode materials for zinc-cerium RFBs, the optimization of the electrode structure with regard to its porosity and permeability is important, particularly at high applied current densities where mass transfer of electroactive species to and from the positive electrode becomes important.

8.2.5 Increasing the solubility of cerium species

Increasing the solubility of cerium species is another important factor that would enable the battery to provide higher energy densities. As mentioned previously, the solubility of Ce(III) rises as the MSA concentration is reduced, whereas the solubility of Ce(IV) is affected in the opposite way. Thus, a compromise in the MSA level must be made to maintain adequate solubility of both cerium species in the electrolyte. Currently, an optimum composition of 0.8 $\mathrm{mol\,dm^{-3}}$ cerium(III) methanesulfonate in 4.0 $\mathrm{mol\,dm^{-3}}$ MSA is used on the positive side of zinc-cerium RFBs. Further work must be done on developing alternative positive electrolytes or new complexing agents for cerium species with the goal of increasing their solubility limit. A review of organic and inorganic complexing agents of cerium ions is provided in the work of Arenas et al [90].

8.2.6 Incorporation of additional phenomena in the transient multi-physics model

In the model described in Chapter 7, water transfer across the membrane is assumed to be negligible and the transfer of protons in the membrane is assumed to exclusively occur via migration. It would be useful to relax these assumptions and incorporate the osmotic and electro-osmotic transfer of water as well as all three modes of proton transfer (diffusion, migration, convection) through the membrane in the present model, particularly for prediction of the performance of the battery over its life-cycle. The development of this model is possible with a concurrent experimental study on the mechanisms of water and proton transfer across the membrane, as described in 8.2.2. Also, as explained previously, the increase in the acidity of the negative half-cell and the dilution of the acidity on the positive half-cell leads to Ce(IV) precipitation over long-term operation of the battery. Incorporation of a complete thermodynamic model for cerium aqueous chemistry that includes Ce(IV) precipitation with the transport model presented in this thesis is essential for improving the accuracy of the model when applied to long-term operation.

References

[1] H. M. Zhang, B. Huang, J. Lawrimore, M. Menne, T. M. Smith, NOAA global surface temperature dataset, version 4.0 (2015).

[2] J. Carle, Climate change seen as top global threat, Pew Research Centre 14 (2015).

[3] J. Eyer, G. Corey, Energy storage for the electricity grid: Benefits and market potential assessment guide, Sandia National Laboratories 20 (10) (2010) 5.

[4] T. Nguyen, R. F. Savinell, Flow batteries, The Electrochemical Society Interface 19 (3) (2010) 54.

[5] C. Ponce-de Leon, A. Frías-Ferrer, J. González-García, D. A. Szánto, F. C. Walsh, Redox flow cells for energy conversion, Journal of power sources 160 (1) (2006) 716–732.

[6] A. Z. Weber, M. M. Mench, J. P. Meyers, P. N. Ross, J. T. Gostick, Q. Liu, Redox flow batteries: a review, Journal of Applied Electrochemistry 41 (10) (2011) 1137.

[7] J. Winsberg, T. Hagemann, T. Janoschka, M. D. Hager, U. S. Schubert, Redox-flow batteries: from metals to organic redox-active materials, Angewandte Chemie International Edition 56 (3) (2017) 686–711.

[8] Á. Cunha, J. Martins, N. Rodrigues, F. Brito, Vanadium redox flow batteries: a technology review, International Journal of Energy Research 39 (7) (2015) 889–918.

[9] K. Amini, J. Gostick, M. D. Pritzker, Metal and metal oxide electrocatalysts for redox flow batteries, Advanced Functional Materials (2020).

[10] P. K. Leung, X. Li, C. Ponce-de Leon, L. Berlouis, C. T. J. Low, F. C. Walsh, Progress in redox flow batteries, remaining challenges and their applications in energy storage, RSC Advances 2 (27) (2012) 10125–10156.

[11] G. L. Soloveichik, Flow batteries: current status and trends, Chemical reviews 115 (20) (2015) 11533–11558.

[12] P. K. Leung, C. Ponce-de Leon, C. T. J. Low, A. A. Shah, F. C. Walsh, Characterization of a zinc–cerium flow battery, Journal of Power Sources 196 (11) (2011) 5174–5185.

[13] L. H. Thaller, Electrically rechargeable redox flow cell, US Patent 3,996,064 (1976).

[14] N. Hagedorn, M. Hoberecht, L. Thaller, NASA redox cell stack shunt current, pumping power, and cell performance tradeoffs (1982).

[15] P. R. Prokopius, Model for calculating electrolytic shunt path losses in large electrochemical energy conversion systems (1976).

[16] J. Giner, L. Swette, K. Cahill, Screening of redox couples and electrode materials (1976).

[17] K. Michaels, G. Hall, Cost projections for redox energy storage systems (1980).

[18] T. Shigematsu, Redox flow battery for energy storage, SEI technical review 73 (2011) 4–13.

[19] N. H. Hagedorn, NASA redox storage system development project (1984).

[20] R. F. Gahn, N. H. Hagedorn, J. S. Ling, Single cell performance studies on the Fe/Cr redox energy storage system using mixed reactant solutions at elevated temperature (1983).

[21] T. Tanaka, T. Sakamoto, N. Mori, K. Mizunami, T. Shigematsu, Development of a redox flow battery, SEI Technical Review 137 (1990) 191.

[22] T. Shigematsu, T. Ito, T. Sakamoto, New energy storage system with redox flow battery, Electrical Review 78 (9) (1993).

[23] A. Pellegri, P. M. Spaziante, Novel halogenation process and apparatus, US Patent 4,172,773 (1979).

[24] M. Rychcik, M. Skyllas-Kazacos, Characteristics of a new all-vanadium redox flow battery, Journal of Power Sources 22 (1) (1988) 59–67.

[25] M. Nakajima, M. Sawahata, S. Yoshida, K. Sato, H. Kaneko, A. Negishi, K. Nozaki, Vanadium redox flow battery with resources saving recycle ability i. production of electrolytic solution for vanadium redox flow battery from boiler soot, Denki Kagaku Oyobi Kogyo Butsuri Kagaku 66 (6) (1998) 600–608.

[26] N. Tokuda, T. Kumamoto, T. Shigematsu, H. Deguchi, T. Ito, N. Yoshikawa, T. Hara, Development of a redox flow battery system, Sumitomo electric technical review (45) (1998) 88–94.

[27] UniEnergy Technologies, http://www.uetechnologies.com/.

[28] Vionx Energy Corp., http://www.vionxenergy.com/.

[29] VanadiumCorp., http://www.vanadiumcorp.com/.

[30] redT Energy, https://redtenergy.com/.

[31] Prudent Energy, http://prudentenergyltd.com/.

[32] VoltStorage, https://voltstorage.com/.

[33] Schmid Group, https://schmid-group.com/en/.

[34] Australian Vanadium, http://www.australianvanadium.com.au/.

[35] L. Arenas, C. P. De León, F. Walsh, Engineering aspects of the design, construction and performance of modular redox flow batteries for energy storage, Journal of Energy Storage 11 (2017) 119–153.

[36] J. D. Giner, H. H. Stark, Redox battery including a bromine positive electrode and a chromium ion negative electrode, and method, US Patent 4,469,760 (1984).

[37] W. Kangro, Verfahren zur speicherung von elektrischer energie, German patent 914264 (1949).

[38] M. Skyllas-Kazacos, Novel vanadium chloride/polyhalide redox flow battery, Journal of Power Sources 124 (1) (2003) 299–302.

[39] Y. Liu, X. Xia, H. Liu, Studies on cerium (Ce^{4+}/Ce^{3+})–vanadium (V^{2+}/V^{3+}) redox flow cell—cyclic voltammogram response of Ce^{4+}/Ce^{3+} redox couple in H_2SO_4 solution, Journal of power sources 130 (1-2) (2004) 299–305.

[40] F. Q. Xue, Y. L. Wang, W. H. Wang, X. D. Wang, Investigation on the electrode process of the Mn(II)/Mn(III) couple in redox flow battery, Electrochimica Acta 53 (22) (2008) 6636–6642.

[41] W. Wang, S. Kim, B. Chen, Z. Nie, J. Zhang, G. G. Xia, L. Li, Z. Yang, A new redox flow battery using Fe/V redox couples in chloride supporting electrolyte, Energy & Environmental Science 4 (10) (2011) 4068–4073.

[42] Y. Y. Wang, M. R. Lin, C. C. Wan, A study of the discharge performance of the Ti/Fe redox flow system, Journal of power sources 13 (1) (1984) 65–74.

[43] M. Skyllas-Kazacos, N. Milne, Evaluation of iodide and titanium halide redox couple combinations for common electrolyte redox flow cell systems, Journal of Applied Electrochemistry 41 (10) (2011) 1233–1243.

[44] S. Ge, B. Yi, H. Zhang, Study of a high power density sodium polysulfide/bromine energy storage cell, Journal of applied electrochemistry 34 (2) (2004) 181–185.

[45] Y. Shiokawa, H. Yamana, H. Moriyama, An application of actinide elements for a redox flow battery, Journal of nuclear science and technology 37 (3) (2000) 253–256.

[46] E. M. Gray, C. Webb, J. Andrews, B. Shabani, P. Tsai, S. Chan, Hydrogen storage for off-grid power supply, International journal of hydrogen energy 36 (1) (2011) 654–663.

[47] P. Jena, Materials for hydrogen storage: past, present, and future, The Journal of Physical Chemistry Letters 2 (3) (2011) 206–211.

[48] R. Yeo, J. McBreen, A. Tseung, S. Srinivasan, J. McElroy, An electrochemically regenerative hydrogen-chlorine energy storage system: electrode kinetics and cell performance, Journal of Applied Electrochemistry 10 (3) (1980) 393–404.

[49] V. Yufit, B. Hale, M. Matian, P. Mazur, N. Brandon, Development of a regenerative hydrogen-vanadium fuel cell for energy storage applications, Journal of The Electrochemical Society 160 (6) (2013) A856–A861.

[50] M. Alon, A. Blum, E. Peled, Hydrogen/iron regenerative fuel cell for grid storage applications, in: Meeting Abstracts, no. 9, The Electrochemical Society, 2013, pp. 477–477.

[51] M. C. Tucker, A. Weiss, A. Z. Weber, Improvement and analysis of the hydrogen-cerium redox flow cell, Journal of Power Sources 327 (2016) 591–598.

[52] H. Kaneko, A. Negishi, K. Nozaki, K. Sato, M. Nakajima, Redox battery, US Patent 5,318,865 (1994).

[53] Y. Wen, J. Cheng, P. Ma, Y. Yang, Bifunctional redox flow battery-1 V(III)/V(II)–glyoxal (O_2) system, Electrochimica Acta 53 (9) (2008) 3514–3522.

[54] P. C. Butler, P. A. Eidler, P. G. Grimes, S. E. Klassen, R. C. Miles, Zinc/bromine batteries, Handbook of Batteries (Ed.: David Linden, Thomas B. Reddy), McGraw-Hill, Ohio (2001).

[55] J. Jorné, J. Kim, D. Kralik, The zinc-chlorine battery: half-cell overpotential measurements, Journal of Applied Electrochemistry 9 (5) (1979) 573–579.

[56] L. Zhang, Q. Lai, J. Zhang, H. Zhang, A high-energy-density redox flow battery based on zinc/polyhalide chemistry, ChemSusChem 5 (5) (2012) 867–869.

[57] C. Tang, D. Zhou, Methanesulfonic acid solution as supporting electrolyte for zinc-vanadium redox battery, Electrochimica Acta 65 (2012) 179–184.

[58] R. L. Clarke, B. Dougherty, S. Harrison, P. J. Millington, S. Mohanta, Cerium batteries, US Patent 7,625,663 (Dec. 1 2009).

[59] Q. Jian, M. Wu, H. Jiang, Y. Lin, T. Zhao, A trifunctional electrolyte for high-performance zinc-iodine flow batteries, Journal of Power Sources 484 (2021) 229238.

[60] L. W. Hruska, R. F. Savinell, Investigation of factors affecting performance of the iron-redox battery, Journal of the Electrochemical Society 128 (1) (1981) 18–25.

[61] L. Sanz, D. Lloyd, E. Magdalena, J. Palma, K. Kontturi, Description and performance of a novel aqueous all-copper redox flow battery, Journal of Power Sources 268 (2014) 121–128.

[62] S. Hamelet, T. Tzedakis, J.-B. Leriche, S. Sailler, D. Larcher, P.-L. Taberna, P. Simon, J.-M. Tarascon, Non-aqueous Li-based redox flow batteries, Journal of The Electrochemical Society 159 (8) (2012) A1360–A1367.

[63] Y. M. Chiang, W. H. Woodford, Z. Li, W. C. Carter, Metal sulfide electrodes and energy storage devices thereof, US Patent 9,583,779 (2017).

[64] T. J. Petek, N. C. Hoyt, R. F. Savinell, J. S. Wainright, Slurry electrodes for iron plating in an all-iron flow battery, Journal of Power Sources 294 (2015) 620–626.

[65] Y. Zhao, S. Si, C. Liao, A single flow zinc/polyaniline suspension rechargeable battery, Journal of Power Sources 241 (2013) 449–453.

[66] P. K. Leung, C. Ponce-de León, F. C. Walsh, An undivided zinc–cerium redox flow battery operating at room temperature (295 K), Electrochemistry Communications 13 (8) (2011) 770–773.

[67] J. Cheng, L. Zhang, Y. S. Yang, Y. H. Wen, G. P. Cao, X. D. Wang, Preliminary study of single flow zinc–nickel battery, Electrochemistry Communications 9 (11) (2007) 2639–2642.

[68] A. Hazza, D. Pletcher, R. Wills, A novel flow battery: A lead acid battery based on an electrolyte with soluble lead(II) part I. preliminary studies, Physical Chemistry Chemical Physics 6 (8) (2004) 1773–1778.

[69] J. Zhang, I. A. Shkrob, R. S. Assary, S. o. Tung, B. Silcox, L. A. Curtiss, L. Thompson, L. Zhang, Toward improved catholyte materials for redox flow batteries: what controls chemical stability of persistent radical cations?, The Journal of Physical Chemistry C 121 (42) (2017) 23347–23358.

[70] R. M. Darling, K. G. Gallagher, J. A. Kowalski, S. Ha, F. R. Brushett, Pathways to low-cost electrochemical energy storage: a comparison of aqueous and nonaqueous flow batteries, Energy & Environmental Science 7 (11) (2014) 3459–3477.

[71] J. Noack, N. Roznyatovskaya, T. Herr, P. Fischer, The chemistry of redox-flow batteries, Angewandte Chemie International Edition 54 (34) (2015) 9776–9809.

[72] P. S. Fedkiw, R. W. Watts, A mathematical model for the iron/chromium redox battery, Journal of The Electrochemical Society 131 (4) (1984) 701–709.

[73] T. Evans, R. E. White, A review of mathematical modeling of the zinc/bromine flow cell and battery, Journal of The Electrochemical Society 134 (11) (1987) 2725–2733.

[74] A. A. Shah, M. J. Watt-Smith, F. C. Walsh, A dynamic performance model for redox-flow batteries involving soluble species, Electrochimica Acta 53 (27) (2008) 8087–8100.

[75] H. Al-Fetlawi, A. A. Shah, F. C. Walsh, Non-isothermal modelling of the all-vanadium redox flow battery, Electrochimica Acta 55 (1) (2009) 78–89.

[76] A. A. Shah, H. Al-Fetlawi, F. C. Walsh, Dynamic modelling of hydrogen evolution effects in the all-vanadium redox flow battery, Electrochimica Acta 55 (3) (2010) 1125–1139.

[77] H. Al-Fetlawi, A. A. Shah, F. C. Walsh, Modelling the effects of oxygen evolution in the all-vanadium redox flow battery, Electrochimica Acta 55 (9) (2010) 3192–3205.

[78] K. W. Knehr, E. Agar, C. R. Dennison, A. R. Kalidindi, E. C. Kumbur, A transient vanadium flow battery model incorporating vanadium crossover and water transport through the membrane, Journal of The Electrochemical Society 159 (9) (2012) A1446.

[79] X. Ma, H. Zhang, F. Xing, A three-dimensional model for negative half cell of the vanadium redox flow battery, Electrochimica Acta 58 (2011) 238–246.

[80] M. Pugach, M. Kondratenko, S. Briola, A. Bischi, Zero dimensional dynamic model of vanadium redox flow battery cell incorporating all modes of vanadium ions crossover, Applied energy 226 (2018) 560–569.

[81] X. L. Zhou, T. S. Zhao, L. An, Y. K. Zeng, X. H. Yan, A vanadium redox flow battery model incorporating the effect of ion concentrations on ion mobility, Applied Energy 158 (2015) 157–166.

[82] Y. Lei, B. W. Zhang, B. F. Bai, T. S. Zhao, A transient electrochemical model incorporating the donnan effect for all-vanadium redox flow batteries, Journal of Power Sources 299 (2015) 202–211.

[83] D. Chu, X. Li, S. Zhang, A non-isothermal transient model for a metal-free quinone–bromide flow battery, Electrochimica Acta 190 (2016) 434–445.

[84] X. Li, Modeling and simulation study of a metal free organic–inorganic aqueous flow battery with flow through electrode, Electrochimica Acta 170 (2015) 98–109.

[85] S. Smith, I. Firdous, Q. Wang, S. Esmalla, W. A. Daoud, A two-dimensional model of the vanadium–cerium redox flow battery, Electrochimica Acta 328 (2019) 135019.

[86] F. C. Walsh, C. Ponce-de Leon, L. Berlouis, G. Nikiforidis, L. F. Arenas-Martínez, D. Hodgson, D. Hall, The development of Zn-Ce hybrid redox flow batteries for energy storage and their continuing challenges, ChemPlusChem 80 (2) (2015) 288–311.

[87] L. F. Arenas, F. C. Walsh, C. P. de León, The importance of cell geometry and electrolyte properties to the cell potential of Zn-Ce hybrid flow batteries, Journal of the Electrochemical Society 163 (1) (2015) A5170.

[88] P. Leung, Development of a zinc-cerium redox flow battery, Ph.D. thesis, University of Southampton (2011).

[89] G. Nikiforidis, Investigations of the zinc-cerium hybrid flow battery, Ph.D. thesis, University of Strathclyde (2012).

[90] L. F. Arenas Martinez, An electrochemical engineering approach to improvements in the zinc-cerium redox flow battery, Ph.D. thesis, University of Southampton (2017).

[91] P. K. Leung, C. Ponce-de Leon, C. T. J. Low, F. C. Walsh, Zinc deposition and dissolution in methanesulfonic acid onto a carbon composite electrode as the negative electrode reactions in a hybrid redox flow battery, Electrochimica Acta 56 (18) (2011) 6536–6546.

[92] P. K. Leung, C. Ponce-de Leon, F. J. Recio, P. Herrasti, F. C. Walsh, Corrosion of the zinc negative electrode of zinc–cerium hybrid redox flow batteries in methanesulfonic acid, Journal of Applied Electrochemistry 44 (9) (2014) 1025–1035.

[93] G. Nikiforidis, L. Berlouis, D. Hall, D. Hodgson, Evaluation of carbon composite materials for the negative electrode in the zinc–cerium redox flow cell, Journal of Power Sources 206 (2012) 497–503.

[94] G. Nikiforidis, L. Berlouis, D. Hall, D. Hodgson, A study of different carbon composite materials for the negative half-cell reaction of the zinc cerium hybrid redox flow cell, Electrochimica Acta 113 (2013) 412–423.

[95] G. Nikiforidis, W. A. Daoud, Indium modified graphite electrodes on highly zinc containing methanesulfonate electrolyte for zinc-cerium redox flow battery, Electrochimica Acta 168 (2015) 394–402.

[96] K. Amini, M. Pritzker, Improved electrolyte for negative side of zinc-cerium redox flow batteries, in: ECS Meeting Abstracts, no. 5, IOP Publishing, 2019, p. 233.

[97] Z. Xie, Q. Liu, Z. Chang, X. Zhang, The developments and challenges of cerium half-cell in zinc–cerium redox flow battery for energy storage, Electrochimica Acta 90 (2013) 695–704.

[98] P. Leung, C. P. De León, C. T. J. Low, F. C. Walsh, Ce(III)/Ce(IV) in methanesulfonic acid as the positive half cell of a redox flow battery, Electrochimica Acta 56 (5) (2011) 2145–2153.

[99] G. Nikiforidis, L. Berlouis, D. Hall, D. Hodgson, Charge/discharge cycles on Pt and Pt-Ir based electrodes for the positive side of the zinc-cerium hybrid redox flow battery, Electrochimica Acta 125 (2014) 176–182.

[100] X. Zhipeng, Z. Debi, F. Xiong, S. Zhang, K. Huang, Cerium-zinc redox flow battery: Positive half-cell electrolyte studies, Journal of Rare Earths 29 (6) (2011) 567–573.

[101] G. Nikiforidis, L. Berlouis, D. Hall, D. Hodgson, An electrochemical study on the positive electrode side of the zinc–cerium hybrid redox flow battery, Electrochimica Acta 115 (2014) 621–629.

[102] G. Nikiforidis, W. A. Daoud, Effect of mixed acid media on the positive side of the hybrid zinc-cerium redox flow battery, Electrochimica Acta 141 (2014) 255–262.

[103] L. F. Arenas, C. P. de León, F. C. Walsh, Mass transport and active area of porous Pt/Ti electrodes for the Zn-Ce redox flow battery determined from limiting current measurements, Electrochimica Acta 221 (2016) 154–166.

[104] L. F. Arenas, C. Ponce de León, F. C. Walsh, Pressure drop through platinized titanium porous electrodes for cerium-based redox flow batteries, AIChE Journal 64 (3) (2018) 1135–1146.

[105] G. Nikiforidis, W. A. Daoud, Thermally modified graphite electrodes for the positive side of the zinc-cerium redox flow battery, Journal of the Electrochemical Society 162 (6) (2015) A809.

[106] G. Nikiforidis, Y. Xiang, W. A. Daoud, Electrochemical behavior of carbon paper on cerium methanesulfonate electrolytes for zinc-cerium flow battery, Electrochimica Acta 157 (2015) 274–281.

[107] G. Nikiforidis, L. Berlouis, D. Hall, D. Hodgson, Impact of electrolyte composition on the performance of the zinc–cerium redox flow battery system, Journal of power sources 243 (2013) 691–698.

[108] R. P. Kreh, R. M. Spotnitz, J. T. Lundquist, Mediated electrochemical synthesis of aromatic aldehydes, ketones, and quinones using ceric methanesulfonate, The Journal of Organic Chemistry 54 (7) (1989) 1526–1531.

[109] Z. Na, X. Wang, D. Yin, L. Wang, Tin dioxide as a high-performance catalyst towards Ce(VI)/Ce(III) redox reactions for redox flow battery applications, Journal of Materials Chemistry 5 (10) (2017) 5036–5043.

[110] Z. Na, X. Wang, D. Yin, L. Wang, Graphite felts modified by vertical two-dimensional wo3 nanowall arrays: high-performance electrode materials for cerium-based redox flow batteries, Nanoscale 10 (22) (2018) 10705–10712.

[111] P. K. Leung, C. Ponce-de León, F. C. Walsh, The influence of operational parameters on the performance of an undivided zinc–cerium flow battery, Electrochimica Acta 80 (2012) 7–14.

[112] L. F. Arenas, F. Walsh, C. P. de León, The importance of cell geometry and electrolyte properties to the cell potential of zn-ce hybrid flow batteries, Journal of The Electrochemical Society 163 (1) (2016) A5170–A5179.

[113] K. Amini, M. D. Pritzker, In situ polarization study of zinc–cerium redox flow batteries, Journal of Power Sources 471 (2020) 228463.

[114] D. Aaron, Z. Tang, A. B. Papandrew, T. A. Zawodzinski, Polarization curve analysis of all-vanadium redox flow batteries, Journal of Applied Electrochemistry 41 (10) (2011) 1175.

[115] J. Langner, J. Melke, H. Ehrenberg, C. Roth, Determination of overpotentials in all vanadium redox flow batteries, ECS Transactions 58 (37) (2014) 1–7.

[116] I. Derr, M. Bruns, J. Langner, A. Fetyan, J. Melke, C. Roth, Degradation of all-vanadium redox flow batteries (VRFB) investigated by electrochemical impedance and x-ray photoelectron spectroscopy: Part 2 electrochemical degradation, Journal of Power Sources 325 (2016) 351–359.

[117] D. Aaron, C.-N. Sun, M. Bright, A. B. Papandrew, M. M. Mench, T. A. Zawodzinski, In situ kinetics studies in all-vanadium redox flow batteries, ECS Electrochemistry Letters 2 (3) (2013) A29–A31.

[118] P. Mazur, J. Mrlik, J. Charvat, J. Pocedic, J. Vrana, J. Dundalek, J. Kosek, A complex four-point method for the evaluation of ohmic and faradaic losses within a redox flow battery single-cell, MethodsX 6 (2019) 534–539.

[119] C.-N. Sun, F. M. Delnick, D. Aaron, A. Papandrew, M. M. Mench, T. A. Zawodzinski, Probing electrode losses in all-vanadium redox flow batteries with impedance spectroscopy, ECS Electrochemistry Letters 2 (5) (2013) A43–A45.

[120] P. Leung, M. Mohamed, A. Shah, Q. Xu, M. Conde-Duran, A mixed acid based vanadium–cerium redox flow battery with a zero-gap serpentine architecture, Journal of Power Sources 274 (2015) 651–658.

[121] M. Kazacos, M. Skyllas-Kazacos, Performance characteristics of carbon plastic electrodes in the all-vanadium redox cell, Journal of the Electrochemical Society 136 (9) (1989) 2759–2760.

[122] K. Amini, M. D. Pritzker, Improvement of zinc-cerium redox flow batteries using mixed methanesulfonate-chloride negative electrolyte, Applied Energy 255 (2019) 113894.

[123] L. Arenas, C. P. De León, F. Walsh, Electrochemical redox processes involving soluble cerium species, Electrochimica Acta 205 (2016) 226–247.

[124] K. Amini, M. D. Pritzker, Life-cycle analysis of zinc-cerium redox flow batteries, Electrochimica Acta 356 (2020) 136785.

[125] B. Tian, C. W. Yan, Q. Qu, H. LI, F. h. Wang, Potentiometric titration analysis of electrolyte of vanadium battery, Battery Bimonthly 4 (2003).

[126] L. Liu, J. Xi, Z. Wu, W. Zhang, H. Zhou, W. Li, X. Qiu, State of charge monitoring for vanadium redox flow batteries by the transmission spectra of V(IV)/V(V) electrolytes, Journal of Applied Electrochemistry 42 (12) (2012) 1025–1031.

[127] P. Trinidad, C. Ponce-de Leon, F. C. Walsh, The use of electrolyte redox potential to monitor the Ce(IV)/Ce(III) couple, Journal of Environmental Management 88 (4) (2008) 1417–1425.

[128] E. Rolia, J. Dutrizac, The determination of free acid in zinc processing solutions, Canadian Metallurgical Quarterly 23 (2) (1984) 159–167.

[129] S. K. Murthy, A. K. Sharma, C. Choo, E. Birgersson, Analysis of concentration overpotential in an all-vanadium redox flow battery, Journal of The Electrochemical Society 165 (9) (2018) A1746–A1752.

[130] X. Wei, D. Desai, G. G. Yadav, D. E. Turney, A. Couzis, S. Banerjee, Impact of anode substrates on electrodeposited zinc over cycling in zinc-anode rechargeable alkaline batteries, Electrochimica Acta 212 (2016) 603–613.

[131] Y. Ito, M. Nyce, R. Plivelich, M. Klein, D. Steingart, S. Banerjee, Zinc morphology in zinc–nickel flow assisted batteries and impact on performance, Journal of Power Sources 196 (4) (2011) 2340–2345.

[132] M. P. J. Brennan, O. Brown, Carbon electrodes: Part 1. hydrogen evolution in acidic solution, Journal of Applied Electrochemistry 2 (1) (1972) 43–49.

[133] D. Pletcher, F. C. Walsh, Industrial electrochemistry, Springer Science & Business Media, 2012.

[134] R. P. Kreh, R. M. Spotnitz, J. T. Lundquist, Mediated electrochemical synthesis of aromatic aldehydes, ketones, and quinones using ceric methanesulfonate, The Journal of Organic Chemistry 54 (7) (1989) 1526–1531.

[135] G. Brodt, J. Haas, W. Hesse, H. U. Jager, Method for electrolytic galvanizing using electrolytes containing alkane sulphonic acid, US Patent 6,811,673 (2004).

[136] C. Sun, J. Chen, H. Zhang, X. Han, Q. Luo, Investigations on transfer of water and vanadium ions across Nafion membrane in an operating vanadium redox flow battery, Journal of Power Sources 195 (3) (2010) 890–897.

[137] J. Pan, Y. Wen, J. Cheng, J. Pan, S. Bai, Y. Yang, Evaluation of substrates for zinc negative electrode in acid PbO_2-Zn single flow batteries, Chinese Journal of Chemical Engineering 24 (4) (2016) 529–534.

[138] J. Pan, Y. Wen, J. Cheng, J. Pan, Z. Bai, Y. Yang, Zinc deposition and dissolution in sulfuric acid onto a graphite–resin composite electrode as the negative electrode reactions in acidic zinc-based redox flow batteries, Journal of Applied Electrochemistry 43 (5) (2013) 541–551.

[139] FuelCell Store, Technical Data Sheet - Fumasep FAP-375-PP.

[140] L. Napoli, J. Franco, H. Fasoli, A. Sanguinetti, Conductivity of Nafion®117 membrane used in polymer electrolyte fuel cells, International Journal of Hydrogen Energy 39 (16) (2014) 8656–8660.

[141] Y. Lorrain, G. Pourcelly, C. Gavach, Influence of cations on the proton leakage through anion-exchange membranes, Journal of Membrane Science 110 (2) (1996) 181–190.

[142] B. J. Robbins, R. Field, S. Kolaczkowski, A. Lockett, Rationalisation of the relationship between proton leakage and water flux through anion exchange membranes, Journal of Membrane Science 118 (1) (1996) 101–110.

[143] Y. Lorrain, G. Pourcelly, C. Gavach, Transport mechanism of sulfuric acid through an anion exchange membrane, Desalination 109 (3) (1997) 231–239.

[144] T. Bai, M. Wang, B. Zhang, Y. Jia, Y. Chen, Anion-exchange membrane with ion-nanochannels to beat trade-off between membrane conductivity and acid blocking performance for waste acid reclamation, Journal of Membrane Science 573 (2019) 657–667.

[145] K. Amini, M. D. Pritzker, Electrodeposition and electrodissolution of zinc in mixed methanesulfonate-based electrolytes, Electrochimica Acta 268 (2018) 448–461.

[146] C. Cachet, R. Wiart, Zinc deposition and passivated hydrogen evolution in highly acidic sulphate electrolytes: Depassivation by nickel impurities (Nov 1990).

[147] I. Zouari, F. Lapicque, An electrochemical study of zinc deposition in a sulfate medium, Electrochimica Acta 37 (3) (1992) 439–446.

[148] J. Yu, H. Yang, X. Ai, Y. Chen, Effects of anions on the zinc electrodeposition onto glassy-carbon electrode, Russian journal of electrochemistry 38 (3) (2002) 321–325.

[149] G. Trejo, Nucleation and growth of zinc from chloride concentrated solutions, Journal of The Electrochemical Society 145 (12) (1998) 4090.

[150] J. Mcbreen, E. Gannon, ChemInform abstract: Electrodeposition of zinc on glassy carbon from zinc chloride and zinc bromide electrolytes, Chemischer Informationsdienst 14 (49) (1983) 47.

[151] L. H. Mendoza-Huízar, C. H. Rios-Reyes, M. G. Gómez-Villegas, Zinc electrodeposition from chloride solutions onto glassy carbon electrode, Journal of the Mexican Chemical Society 53 (4) (2009) 243–247.

[152] H. Nakamura, S. Oue, N. Sogabe, H. Nakano, Effect of chloride ions on the deposition behavior and morphology of zinc at initial stage from electrowinning solution, Journal of MMIJ 131 (5) (2015) 164–169.

[153] J. Yeager, J. P. Cels, E. Yeager, F. Hovorka, The electrochemistry of nickel I. codeposition of nickel and hydrogen from simple aqueous solutions, Journal of the electrochemical society 106 (4) (1959) 328–336.

[154] Z. Nagy, Chloride ion catalysis of the copper deposition reaction, Journal of The Electrochemical Society 142 (6) (1995) L87.

[155] R. L. Pecsok, J. J. Lingane, Polarography of chromium (II), Journal of the American Chemical Society 72 (1) (1950) 189–193.

[156] J. Heyrovský, Retarded electrodeposition of metals studied oscillographically with mercury capillary electrodes, Discussions of the Faraday Society 1 (1947) 212.

[157] J. Vazquez-Arenas, M. Pritzker, Effect of electrolyte and agitation on the anomalous behavior and morphology of electrodeposited Co–Ni alloys, Journal of Solid State Electrochemistry 17 (2) (2012) 419–433.

[158] V. Gouda, M. Khedr, A. S. El Din, Role of anions in the corrosion and corrosion-inhibition of zinc in aqueous solutions, Corrosion Science 7 (4) (1967) 221–230.

[159] J. Blackledge, N.-S. Hush, Mechanism of the Zn(II)/Zn(Hg) exchange: Part 2: catalysis by halide and thiocyanatk ions, Journal of Electroanalytical Chemistry (1959) 5 (6) (1963) 435–449.

[160] E. Ahlberg, H. Anderson, Simulating impedance spectra from a mechanistic point of view: application to zinc dissolution, Acta Chemica Scandinavica(Denmark) 46 (1) (1992) 15–24.

[161] S. Ranganathan, T.-C. Kuo, R. L. McCreery, Facile preparation of active glassy carbon electrodes with activated carbon and organic solvents, Analytical Chemistry 71 (16) (1999) 3574–3580.

[162] M. D. Gernon, M. Wu, T. Buszta, P. Janney, Environmental benefits of methanesulfonic acid, Green Chemistry 1 (3) (1999) 127–140.

[163] Q. B. Zhang, Y. Hua, Effect of Mn^{2+} ions on the electrodeposition of zinc from acidic sulphate solutions, Hydrometallurgy 99 (3-4) (2009) 249–254.

[164] R. de Levie, Anion bridging and anion electrocatalysis on mercury, Journal of The Electrochemical Society 118 (8) (1971) 185C.

[165] L. G. Sillén, A. E. Martell, Stability constants of metallic-ion complexes, Soil Science 100 (1) (1965) 74.

[166] M. Capelato, J. Nobrega, E. Neves, Complexing power of alkanesulfonate ions: the lead-methanesulfonate syste, Journal of Applied Electrochemistry 25 (4) (1995) 74.

[167] F. I. Danilov, I. V. Sknar, Y. E. Sknar, Kinetics of nickel electroplating from methanesulfonate electrolyte, Russian Journal of Electrochemistry 47 (9) (2011) 1035–1042.

[168] D. Baik, D. Fray, Electrodeposition of zinc from high acid zinc chloride solutions, Journal of applied electrochemistry 31 (10) (2001) 1141–1147.

[169] V. G. Levich, Physicochemical hydrodynamics, Prentice hall, 1962.

[170] E. B. Budevski, Deposition and dissolution of metals and alloys. part a: Electrocrystallization, in: Comprehensive treatise of electrochemistry, Springer, 1983, pp. 399–450.

[171] Q. B. Zhang, Y. X. Hua, T. G. Dong, D. G. Zhou, Effects of temperature and current density on zinc electrodeposition from acidic sulfate electrolyte with [BMIM] HSO_4 as additive, Journal of applied electrochemistry 39 (8) (2009) 1207.

[172] P. Patnaik, Dean's Analytical Chemistry Handbook, Vol. 1143, McGraw-Hill New York, 2004.

[173] X. Gao, Vanadium redox flow batteries for large-scale energy storage, Ph.D. thesis, National University of Ireland, Galway (2012).

[174] A. J. Bard, L. R. Faulkner, Electrochemical Methods: Fundamentals and Applications, Vol. 2, Wiley New York, 1980.

[175] F. G. Donnan, The theory of membrane equilibria., Chemical Reviews 1 (1) (1924) 73–90.

[176] Z. Xu, J. Wang, S. C. Yan, Q. Fan, P. D. Lund, Modeling of zinc bromine redox flow battery with application to channel design, Journal of Power Sources 450 (2020) 227436.

[177] S. H. Lee, J. C. Rasaiah, Proton transfer and the mobilities of the H^+ and OH^- ions from studies of a dissociating model for water, The Journal of chemical physics 135 (12) (2011) 124505.

[178] C. L. Yaws, C. Gabbula, Handbook of Thermodynamic and Physical Properties of Chemical Compounds, Knovel, 2003.

[179] S. Slade, S. A. Campbell, T. R. Ralph, F. C. Walsh, Ionic conductivity of an extruded Nafion 1100 EW series of membranes, Journal of the Electrochemical Society 149 (12) (2002) A1556–A1564.

[180] R. Parsons, Handbook of Electrochemical Constants, Butterworth, 1959.

[181] M. H. Miles, E. A. Klaus, B. P. Gunn, J. R. Locker, W. E. Serafin, S. Srinivasan, The oxygen evolution reaction on platinum, iridium, ruthenium and their alloys at 80deg in acid solutions, Electrochimica Acta 23 (6) (1978) 521–526.

[182] G. D. Simpson, R. E. White, An algebraic model for a zinc/bromine flow cell, Journal of the Electrochemical Society 136 (8) (1989) 2137.

[183] J. M. Nzikou, M. Aurousseau, F. Lapicque, Electrochemical investigations of the Ce(m)/Ce(IV) couple related to a Ce(IV)-assisted process for SO_2/NO_x abatement, Journal of applied electrochemistry 25 (10) (1995) 967–972.

[184] G. W. Barton, A. C. Scott, A validated mathematical model for a zinc electrowinning cell, Journal of applied electrochemistry 22 (2) (1992) 104–115.

[185] L. B. Kriksunov, L. V. Bunakova, S. E. Zabusova, L. I. Krishtalik, Anodic oxygen evolution reaction at high temperatures in acid solutions at platinum, Electrochimica acta 39 (1) (1994) 137–142.

[186] S. G. Bratsch, Standard electrode potentials and temperature coefficients in water at 298.15 K, Journal of Physical and Chemical Reference Data 18 (1) (1989) 1–21.

[187] D. M. Bernardi, M. W. Verbrugge, Mathematical model of a gas diffusion electrode bonded to a polymer electrolyte, AIChE journal 37 (8) (1991) 1151–1163.

[188] K. Amini, M. Pritzker, Voltage loss analysis of zinc-cerium redox flow batteries, ECS Meeting Abstracts MA2020-02 (45) (2020) 3732–3732.

[189] J. Piwek, C. Dennison, E. Frackowiak, H. Girault, A. Battistel, Vanadium-oxygen cell for positive electrolyte discharge in dual-circuit vanadium redox flow battery, Journal of Power Sources 439 (2019) 227075.

[190] E. Agar, K. Knehr, D. Chen, M. Hickner, E. Kumbur, Species transport mechanisms governing capacity loss in vanadium flow batteries: Comparing Nafion® and sulfonated radel membranes, Electrochimica Acta 98 (2013) 66–74.

[191] X. Zhou, T. Zhao, L. An, Y. Zeng, L. Wei, Critical transport issues for improving the performance of aqueous redox flow batteries, Journal of Power Sources 339 (2017) 1–12.

[192] K. Knehr, E. Kumbur, Role of convection and related effects on species crossover and capacity loss in vanadium redox flow batteries, Electrochemistry Communications 23 (2012) 76–79.

[193] D. Kearney, D. Bejan, N. J. Bunce, The use of Ebonex electrodes for the electrochemical removal of nitrate ion from water, Canadian Journal of Chemistry 90 (8) (2012) 666–674.